Quantitative Analysis of Challenging Chemical Mixtures by Rotational Spectroscopy

Martin Storm Holdren
Troy, Pennsylvania

B.S. Chemistry and Applied Mathematics, Minor in German
Mansfield University of Pennsylvania, 2016

A Dissertation Presented to the Graduate Faculty of the

University of Virginia

in Candidacy for the Degree of

Doctor of Philosophy

Department of Chemistry
University of Virginia
May 2022

Committee Members:
Brooks H. Pate, Advisor
Robin T. Garrod, Chair
W. Dean Harman
Kevin K. Lehmann
Robert R. Jones

Abstract:

Rotational spectroscopy has long been used for the study of small molecule chemical structure and has only recently found its way into the field of analytical chemistry for larger and more complex molecules. The development of the Fabry-Pérot cavity Fourier transform microwave spectrometer with a pulsed molecular beam source **[1]** allowed for the study of larger molecules and weakly bound clusters of molecules; however, this instrument required stepping through a frequency space over large lengths of time with continuous measurements lasting hours to days to acquire a broadband spectrum **[2]**. It was the invention of chirped-pulse Fourier transform microwave (CP-FTMW) spectroscopy in 2006-2008 **[3,4]** that allowed for acquisition of broadband spectra with high spectral resolution in a factor of >1000 less time and that contains spectral signatures of many species at once. With improvements to the technology backing this instrumentation, complex chemical mixtures containing structural isomers, regioisomers, diastereomers, isotopologues and isotopomers, conformers, and minor impurities can be analyzed without separation techniques making the technique advantageous to pharmaceutical synthetic processes and even real-time quality assurance **[5, 6, 7]**. More recently, rotational spectroscopy has also shown its ability in distinguishing enantiomers and quantifying enantiomeric excess through microwave three-wave mixing (3WM) rotational spectroscopy **[8]** and chiral tag rotational spectroscopy **[9]**.

This dissertation will show how challenging chemical mixtures in a wide array of settings in the analytical field are easily analyzed by the new techniques in rotational spectroscopy. The quantitative limits in determining enantiomeric excess by 3WM rotational spectroscopy will be discussed including the technique's strength in complex mixtures through analysis of components in essential oil mixtures. An additional project will be discussed in which 3WM rotational spectroscopy is used as a technique in designing an instrument for prospective use in biomarker detection in the search of past or present life in various locations within the solar system. In another group of projects, The CP-FTMW instrument is used to show how isotopic impurity levels in the synthesis of deuterated molecules can be quickly analyzed through the use of 'cocktail' reaction mixture analysis. Additional mixture analysis will be shown on deuterated molecules used in a building block strategy for drug design in which quick, quantitative analysis in a new sampling system guides synthetic chemists to produce targets with lower abundances of impurities. This final project includes using the chiral tag rotational spectroscopy technique to determine the enantiomeric excess and absolute configuration of a molecule that is chiral merely by deuterium substitution, showing the strength of rotational spectroscopy in sensing the smallest of structural changes.

[1] Balle, T. J.; Flygare, W. H., Fabry–Perot cavity pulsed Fourier transform microwave spectrometer with a pulsed nozzle particle source. *Review of Scientific Instruments* **1981,** *52* (1), 33-45.

[2] Park, G. B.; Field, R. W., Perspective: The first ten years of broadband chirped pulse Fourier transform microwave spectroscopy. *J Chem Phys* **2016,** *144* (20), 200901.

[3] Brown, G. G.; Dian, B. C.; Douglass, K. O.; Geyer, S. M.; Pate, B. H., The rotational spectrum of epifluorohydrin measured by chirped-pulse Fourier transform microwave spectroscopy. *Journal of Molecular Spectroscopy* **2006,** *238* (2), 200-212.

[4] Brown, G. G.; Dian, B. C.; Douglass, K. O.; Geyer, S. M.; Shipman, S. T.; Pate, B. H., A broadband Fourier transform microwave spectrometer based on chirped pulse excitation. *Rev Sci Instrum* **2008,** *79* (5), 053103.

[5] Neill, J. L.; Yang, Y.; Muckle, M. T.; Reynolds, R. L.; Evangelisti, L.; Sonstrom, R. E.; Pate, B. H.; Gupton, B. F., Online Stereochemical Process Monitoring by Molecular Rotational Resonance Spectroscopy. *Organic Process Research & Development* **2019,** *23* (5), 1046-1051.

[6] Vang, Z. P.; Reyes, A.; Sonstrom, R. E.; Holdren, M. S.; Sloane, S. E.; Alansari, I. Y.; Neill, J. L.; Pate, B. H.; Clark, J. R., Copper-Catalyzed Transfer Hydrodeuteration of Aryl Alkenes with Quantitative Isotopomer Purity Analysis by Molecular Rotational Resonance Spectroscopy. *J Am Chem Soc* **2021,** *143* (20), 7707-7718.

[7] Smith, J. A.; Wilson, K. B.; Sonstrom, R. E.; Kelleher, P. J.; Welch, K. D.; Pert, E. K.; Westendorff, K. S.; Dickie, D. A.; Wang, X.; Pate, B. H.; Harman, W. D., Preparation of cyclohexene isotopologues and stereoisotopomers from benzene. *Nature* **2020,** 581 (7808), 288-293.

[8] Patterson, D.; Doyle, J. M., Sensitive chiral analysis via microwave three-wave mixing. *Phys Rev Lett* **2013,** *111* (2), 023008.

[9] Brooks H. Pate, L. E., Walther Caminati, Yunjie Xu, Javix Thomas, David Patterson, Cristobal Perez, Melanie Schnell, Quantitative Chiral Analysis by Molecular Rotational Spectroscopy. In *Chiral Analysis*, 2 ed.; 2018; pp 679-729.

Table of Contents:

List of Abbreviations:

3WM	Three-wave mixing
Å	Angstrom
AC	Absolute configuration
API	Active pharmaceutical ingredient
atm	Atmosphere (unit of pressure)
Avg	Average
Bn	Benzyl group
CD	Circular dichroism
CDA	Chiral derivatizing agent
CP-FTMW	Chirped-pulse Fourier transform microwave
d_x-	Deuterated ('x' is amount of deuteration)
-D	Deuterium
D	Debye
dB	Decibel
DKIE	Deuterium kinetic isotope effect
DFT	Density Functional Theory
DMAP	4-Dimethylaminopyridine
ee	Enantiomeric excess
EE	Enantiomeric excess (*100%)
EtOD	Deuterated ethanol (O-D)
EtOH	Ethanol
FID	Free induction decay
FT	Fourier transform
fwhm	Full width at half maximum
GC	Gas chromatography
-H	Hydrogen
HIE	Hydrogen isotope exchange
Hz	Hertz
IR	Infrared
JPL	Jet Propulsion Laboratory (NASA)
LOD	Limit of detection
MeOD	Deuterated methanol (O-D)
MeOH	Methanol
MRR	Molecular rotational resonance
MS	Mass spectrometry
nd	No detection
NMR	Nuclear magnetic resonance
Piv	Pivaloyl group
PBu_3	Tributylphosphine
PMe_3	Trimethylphosphine
PO	Propylene oxide

ppm	Parts per million
psi	Pounds per square inch (unit of pressure)
psig	Pounds per square inch gauge
RMS	Root-mean-squared error
TFIP	Trifluoroisopropyl alcohol
TBP	Tributylphosphine
TMP	Trimethylphosphine
Tp	Trispyrazolylborate
TWT	Traveling wave tube [amplifier]
UV-Vis	Ultraviolet-visible
VCD	Vibrational circular dichroism

Chapter 1: Introduction

1.1: *Motivation*

The field of Analytical Chemistry is of great importance to the general public as it plays large roles in the well-being of humankind and nature in areas such as security, quality control, environmental safety, disease diagnosis, medicine, and forensic sciences, among other roles.[1] However, the direction of funded research being done in analytical chemistry tends to gravitate towards biological implications, whether they be in development of instrumentation or in quantitative analysis of pharmaceutical drugs.[2] The challenges being undertaken in this field are often driven by the need for more rapid, selective, and sensitive methods to perform various measurements in this wide variety of environments.[1-3] Analytical instrumentation that is used within the realm of biological importance is constantly improving with technological advancements to rise to these challenges.[3] A hinderance to many current analytical chemistry methods within all of these areas is in the analysis of complex chemical mixtures.

Separation and spectroscopic techniques aim to provide unambiguous measurements for identification and quantitative purposes in this field. Chromatography methods are routinely used to provide 'gold-standard' assurance in areas of quality control and are often paired with mass spectrometry to achieve high detection sensitivity. Chromatography has had a long span of development in separation and analysis of complex chemical mixtures; however, the technique still falters in areas such as chiral analysis and isotopic impurity analysis where molecular structure is so similar that separating multiple components proves to be challenging or impossible. Developing the proper protocol for separating all the components can be time

consuming and chiral separation can take many minutes to hours. The range of possible analytes to be studied is also often limited to selected functional groups.

Within this thesis, spectroscopic approaches to address the areas where the routine analysis by the comfortable choice of chromatography or even NMR analyses fail or struggle will be discussed. Rotational spectroscopy can be used to perform quantitative analysis of highly complex chemical mixtures without prior separation and on a wide range of chemical species that are relevant to roles that analytical chemistry has in society.[4]

1.2: *Chirality and Chiral Analysis*

Chirality is a fundamental property of nature and omnipresent in all forms of life. The word *chirality* derives from the Greek word χειρ (*kheir*) meaning 'hand' and, in our case, referring to 'handedness'.[5, 6] This word is used to describe an asymmetry of a three-dimensional object that makes it distinguishable from its mirror image as they are nonsuperimposable; the object cannot be converted into its mirror image via rotation. The first use of the term 'chirality' was coined by Lord Kelvin at a lecture in 1893 and later published in his book, *The Molecular Tactics of a Crystal*.[7] This intrinsic chemical property was noticed much earlier in 1848 by Louis Pasteur at the early age of 25.[6, 8] Pasteur separated two forms of crystalline tartaric acid salt (found in wine making) which crystalized in mirror image morphologies.[6, 8, 9] It had also been found earlier that century that when these crystals were dissolved in water separately and exposed to a plane-polarized light field, the plane-polarization was rotated in the opposite directions for each of the crystal forms.[6, 8, 9] Pasteur was able to perform this optical rotation technique himself and

concluded that the salt was chiral, existing in two forms that when combined came to be a racemic, or 1:1 ratio, mixture.[6, 8, 9]

The most familiar example of chirality is our hands. Our right and left hands are mirror images of each other and cannot be superimposed without some rearranging of our fingers. Furthermore, examples like the spiral feature of snail shells, the thread on a screw, left- and right-handed scissors, or the direction of a spiral staircase also fit this definition. Chirality is ubiquitous in our lives and ranges wide in size as seen in the range from macro-sized examples like those mentioned above, down to the double helix of DNA and even smaller to the sugars and amino acids that make up all life on Earth. In fact, some of the largest questions in humanity - what is the origin of life and where do we come from – are influenced by chirality.[10, 11] Why is life homochiral, existing almost exclusively with one handedness or the other for biological molecules? Why is this homochirality not the dominated by the opposite handedness and where did this preference of one enantiomer over the other originate?

The pair of mirror image molecules are called enantiomers. The most common example causing handedness in molecules arises from a carbon atom surrounded by four unique substituents in a typical tetrahedral geometry; this carbon is termed a chiral center or asymmetric carbon.[5] In general, these particular molecules have no symmetry and fall into the symmetry point group C_1,[12] although some exceptions like that of meso compounds exits having chiral centers but a plane of symmetry. Multiple chiral centers can exist within a molecule, resulting in unique chiral structures. If one or more, but not all, stereocenters are exchanged, these isomers are called diastereomers where each diastereomer consists of a pair of enantiomers in which all

stereocenters are exchanged as seen in Figure 1.1. Together, these two forms of isomers, diastereomers and enantiomers, fall into a category called stereoisomers.

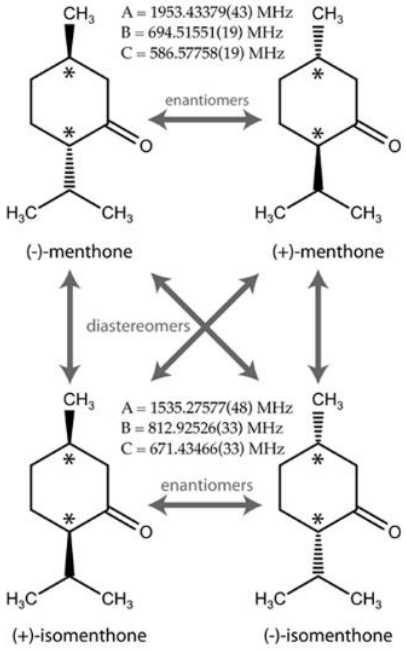

Figure 1.1: A schematic from Figure 2 of Shubert *et al,*[13] which shows the possible chemical structures when having two asymmetric carbons for the molecule, menthone, marked by asterisks. Mirror image structures called enantiomers are given in the (+)/(-) notation (and have the same rotational structural parameters (A, B, and C) that define the distribution of mass) while diastereomers that have unique structures (seen here with a difference in the rotational structural parameters A, B, and C) have different names, menthone and isomenthone, as well as different physical properties. The rotational structural parameters will be defined and discussed in the next section.

Asymmetric carbons are given the nomenclature of the Cahn-Ingold-Prelog system, (S) and (R) (one can think of left- or right-handed). In in biologically related molecules, (D) and (L) or (+) and (-) are often used as nomenclature, particularly as more asymmetric carbons appear in complex molecules.[5] (D) and (L) refer to dextrorotatory and levorotatory and are designated by Fischer projections. (+) and (-) refer to the optical activity of the molecules in the presence of plane polarized light (for $\lambda = 589$ nm) meaning that the given enantiomer in solution rotates plane

polarized light in a clockwise or counterclockwise fashion when the light passes through the solution.[5] Additional forms of chirality exist such as helicity; however, these are out of the scope of this thesis. Enantiomers will have the same physical characteristics such as melting point, bond lengths, density, *etc*.; however, enantiomers will react differently when placed in chiral environments.

While chirality is incredibly important to life and nature, the deeper one delves into the world of chirality, the more challenging it becomes trying to experimentally distinguish between chiral structures and quantify ratios of multiple chiral species. In some instances, knowing the exact chirality/handedness, called the absolute configuration (AC), is needed to create a drug that will properly interact in the body (which itself is a chiral environment). Additionally, it is paramount in pharmaceutical chemistry to quantify the ratio of enantiomers, called the enantiomeric excess (EE). In fact, it is government regulated that there is an assessment of how each enantiomer will react in the body and quantification is needed for each enantiomer in a manufactured drug.[14] While the FDA recognizes that technical challenges of quantifying stereoisomers may provide limitations, they recommend a similar reporting to that of other impurities at levels greater than 0.1% (which they recommend through controlling starting materials where it is often the case that the AC is set for the final chiral drug). These regulations can be found in the FDA's guidance document, *Q6A Specifications: Test Procedures and Acceptance Criteria for New Drug Substances and New Drug Products: Chemical Substances*, section 3.3.1 from the year 2000.

1.3: *Available Techniques in the Field for Chiral Analysis*

Chiral analysis still poses some key challenges for the synthetic and analytical fields of chemistry. All of life is built with chiral molecules, and because of this, humanity needs to understand and be able to quantify certain aspects of chirality. For one, many pharmaceutical drugs need to be designed to be chiral to get proper interactions in the body.[14] Another important feature of chirality for the sake of deep questions, and something I have great interest in, is related to where life came from. Why is life built of chiral molecules and why is life on Earth built of all left-handed amino acids and all right-handed sugars?[10, 15] Where did this homochirality originate?[16] Techniques used within this smaller field of interest are looking beyond Earth to learn more about these questions by sending probes to comets,[17, 18] rovers to Mars,[19-21] and instrumentation to the moons of Jupiter.[22] However, if one were to ask for the perfect technique to solve all the challenges involving chiral analysis, one may be discouraged to find there is no single answer.

The ideal technique would be one that could distinguish between a pair (or multiple pairs) of enantiomers to determine the absolute configuration of a molecule while also being able to quantify any abundances of the various enantiomers and diastereomers present. This technique would also need to achieve these measurements in real-time for rapid monitoring while also having the ability to perform in complex mixtures without prior separation (which can take excesses of time and money). Unfortunately, such a universally applicable technique does not yet exist and current techniques can only check off a few of those requirements and are often limited to only measure either the AC or EE.

The driving problem is that with the possibility of having more than one chiral center in a molecule, the more difficult the analysis becomes. In general, as the number of these chiral centers (N) increases, the number of stereoisomers (enantiomers and diastereomers) will increase by 2^N where there are 2^{N-1} diastereomers and each diastereomer consists of a pair of enantiomers (the presence of meso compounds slightly changes this result, where stereocenters exist, but due to a plane of symmetry, the molecule can be achiral). One can imagine how quickly this can become a challenge for larger and more complex molecules with the currently available techniques.

As was mentioned previously, one of the first techniques used to initially learn about chirality was measuring the optical activity.[6, 8] Linearly polarized light can be passed through a sample of a chiral molecules in solution, and that linear plane will be rotated clockwise or counterclockwise.[5] The rotation demonstrates that there is optical activity caused by the chiral nature of the molecules. The enantiomers will rotate the light equally but in opposite directions while a mixture of enantiomers will rotate the light in the direction directed by the dominantly abundant enantiomer but at reduced effective rotation measured in degrees.[5] The rotation can be used to confirm the AC of a simple sample if compared to a reference sample of known AC. If multiple diastereomers or additional chiral molecules are present in the solution, this simple technique will struggle as each chiral center or chiral species will compound into this effect.

Circular dichroism (CD) techniques can be used at various frequencies of light and are grouped into terms about these ranges. The dichroism itself is a measurement of the difference in absorption of left- and right-circularly polarized light, and therefore, CD instruments will report a plot that shows this differential absorption as $\Delta A = A_L - A_R$ where A is absorption and A_L and A_R

refer to the absorption of left- and right-circularly polarized light, respectively. Two commonly used CD techniques with high structure specificity are vibrational circular dichroism (VCD)[23-26] in the infrared region with vibrational transitions and photoelectron circular dichroism (PECD)[27-29] which uses the angular distribution of photoelectrons ejected from a chiral molecule when blasted with high-energy circularly polarized light to ionize the molecule. VCD and PECD are promising for the analytical side of chiral analysis as they are high-resolution techniques and can find ways to distinguish various diastereomers that can often convolute measurements.[30-34] These techniques also have robust computational predictions for AC and analysis software for EE determinations. [31, 33-36] However, these have their limitations when the sample becomes more complex and rapid monitoring becomes ever more challenging with the increase in time needed to signal average for these techniques to acquire an adequate signal to noise ratio. Intrinsic chiral signals can be 4-5 orders of magnitude weaker than achiral signals for VCD where the CD effect comes from a coupling of the electric and much weaker magnetic dipole moment.[23, 26, 37]

Chiral chromatography can achieve highly reliable quantitative EE measurements and is commonly used by large chemical companies like MilliporeSigma for assessing product quality.[38, 39] Liquid and gas chromatography are performed by using chiral columns containing chiral molecules that slows the elution rate of one of the enantiomers (and multiple diastereomers) flowing through it *via* chiral recognition interactions. This allows all stereoisomers to be separated and analyzed in a chromatogram. This separation technique can be used to achieve high-confidence AC and EE determinations as long as there is a known reference sample to aid in the assessment. Additionally, specific chiral columns are needed for each specific type

of molecule which makes analyzing a large range of molecules difficult. Without a proper column, overlap of signals on the chromatogram can hinder these determinations.

NMR is likely the most popular technique for synthetic chemists. Molecules are placed in a strong magnetic field where a radio pulse disrupts the magnetic alignment of nuclei, such as ^{1}H and ^{13}C. As the disrupted nuclei return into alignment, they emit radiation that is collected and Fourier transformed. Enantiomers will produce the same spectral signatures by NMR; however a chiral derivatizing agent (CDA) can be used to covalently modify the molecule and produce a mixture of diastereomers, which can be spectroscopically resolved.[40, 41] Additionally, chiral solvating agents work in a similar fashion but act through non-covalent interactions rather than forming a chemical bond. These newly created diastereomers will produce slight differences in the spectra for each species that can be calculated for through high-level quantum chemistry; however, reference samples are typically still needed to confirm the difference in absolute configuration and samples typically must be very pure from contamination to yield clear conclusions from the NMR spectra.[41]

Lastly, X-ray diffraction provides a truly gold standard view of molecular absolute structure including that of absolute configuration in chiral species. X-ray light is used and scatters off a crystal of the molecule, and the 3-D crystalline structure can be determined via the diffraction patterns obtained.[42-45] The technique works well for large structures of high purity but becomes challenging if a good crystal cannot be formed such as those of organic oils. X-ray diffraction techniques also struggle for smaller organic molecules due to very small changes in the scattering effects for the lighter elements like C, H, O, and N.[42] In more recent years, powder

X-ray diffraction has gained ground and has also been combined with solid state NMR analysis to provide some great outlooks for AC and EE determinations.[45]

Rotational spectroscopy can now be used to tackle chiral analysis problems as well. Traditional rotational spectroscopy cannot observe distinguishing features for enantiomers, but with some cleverness, diastereomer complexes can be formed in the gas phase by noncovalently "tagging" the chiral analyte with a smaller chiral molecule of known stereochemistry.[46] Alternatively electric dipole properties can be manipulated to extract chiral signatures directly from the molecule without tagging via a newer technique for this field called three-wave mixing rotational spectroscopy that will be discussed below and in detail in the next chapter. Table 1.1 lists the techniques above with brief notes on each of their requirements.

Table 1.1: *Requirements and Drawbacks of Common Chiral Analysis Techniques in the Literature*

Technique	Basic Requirements and Drawbacks
Chiral Gas Chromatography (GC) [17, 18, 38]	- Thermally stable, volatile compounds - Chiral derivatizing agents in some cases - Needs chiral columns tested with known AC - Different column and set-up needed for different classes of molecules
Chiral NMR [40, 41, 47, 48]	- Chiral derivatizing/solvating agents, solvents - External strong magnetic field - Needs tuning for each measurement - High spectral overlap from impurities
Microwave-Three Wave Mixing [a]	- Must have non-zero electric dipole components - Analyte brought into gas phase - Pulsed jet sample introduction introduces large fluctuation error
Chiral Tag Rotational Spectroscopy [46, 49, 50]	- Analyte brought into gas phase - Quantum computations on large, noncovalently bound complexes - Flexible molecules with many conformations can be challenging - Potential for many isomers in analysis
Photoelectron Circular Dichroism [32, 51, 52]	- Synchrotron radiation or femtosecond laser - Velocity-map-imaging - Reliant on mass spectrometry for molecule identification
Vibrational Circular Dichroism (VCD) [23, 25, 31, 53]	- Requires high concentrations - Technique uses a coupling effect of the electric and magnetic dipole moments and therefore much weaker in signal intensity and requires more time signal averaging
X-Ray Crystallography [42, 43, 54]	- Growth of a single, enantiopure crystal [b], where oils will not work - Difficulties in smaller organics due to small scattering effects - Needs prior separation

[a] A Literature review is given in a later section

[b] Powder X-ray diffraction is helping to replace this requirement

1.4: *Rotational Spectroscopy*

What is spectroscopy? Spectroscopy itself is defined as the study of the interaction of light (electromagnetic radiation) with matter.[55] In the natural world, this interaction with matter drives many processes within the universe. All regions of the electromagnetic spectrum, as seen in Figure 1.2, are capable of interacting with matter.

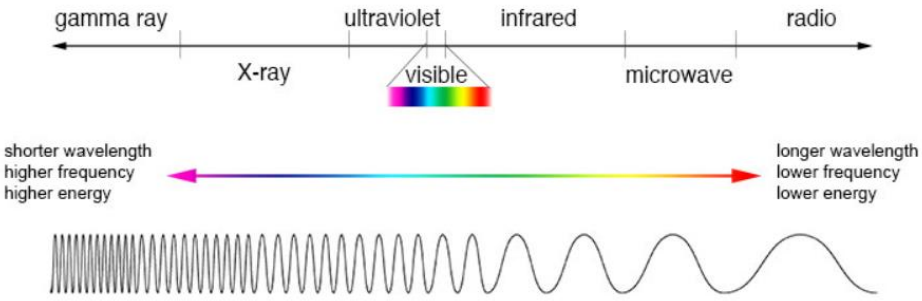

Figure 1.2: The electromagnetic spectrum of light is categorized into named sections that interact with matter in different ways. Various frequencies of light can be used to interrogate important features of the natural world. Image courtesy of Nasa's *Imagine the Universe* (https://imagine.gsfc.nasa.gov/).

Highly energetic (high frequency) light like X-rays and UV light can ionize molecular species and break chemical bonds, tearing apart molecules, DNA and cells, while lower frequency radio waves are used to communicate across large distances without much interaction with the air between. Ultraviolet light can damage skin while infrared light can be felt as heat. Humans can only see such a small fraction of this spectrum with our eyes deemed the visible spectrum, but special tools and instruments are used to access these other regions. The lower frequencies (longer wavelengths) of the microwave region (0.3 GHz – 1000 GHz) can be used to learn a lot about the structure of a molecular species. These lower frequencies can interact with the end-over-end rotational motion of molecules in the gas phase and produce rotational spectra that

yield unique, fingerprint-like signatures for any molecule, conformer, isotopomer, and weakly bound complex with a permanent electric dipole moment. To understand how this is possible, the ability of light to couple with the energy of a species' quantized rotation must be considered.

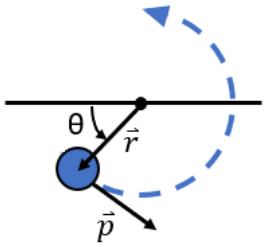

Figure 1.3: A particle orbiting about a center-of-mass with the position vector, $\vec{r}$, moves with linear momentum, $\vec{p}$, and an angular momentum vector pointing toward or away from the observer. The resulting cross product of these two vectors depends on the clockwise or counterclockwise rotation of the particle. Figure is adapted from figures in Peter Bernath's *Spectra of Atoms and Molecules*.[55]

To gain some understanding of the rotational motion of a small object like a molecule, one must first understand angular momentum and the effects of angular momentum in quantum mechanics. Classically, the angular momentum is given by Equation 1.1 where $\vec{r}$ is the position vector and $\vec{p}$ is the linear momentum vector.

$$\vec{L} = \vec{p} \times \vec{r} \tag{1.1}$$

In Figure 1.3, a particle is orbiting in a circle about a point; taken as the cross product of these two values, the angular momentum vector will point towards or away from you depending on if the particle is orbiting clockwise or counterclockwise. The linear momentum is $\vec{p} = m * \vec{v}$ where m is mass of the particle and $\vec{v}$ is the linear velocity vector.[55]

For a rigid molecule rotating end-over-end (ignoring distortion of the molecule from its rotation for the moment) with an angular velocity, $\vec{\omega}$, the system will have an angular momentum given by Equation 1.2. $\boldsymbol{I}$ is the classical inertia tensor that defines the mass distribution of the three dimensional molecule about its center-of-mass. With some linear algebra, an axis system can be defined with the origin at the center-of-mass of the object in which the inertia tensor is diagonalized in Equation 1.3 and 1.4. Equation 1.4 defines a diagonal term that represents one of the principal moments-of-inertia, where $r_{i,\perp}$ is the distance perpendicular from the respective inertial axis for the mass, *m*. This is called the principal axis system and change the labeling in this axis system to a, b, and c to define the mass distribution of the object about each principal inertial axis.

$$\vec{L} = \boldsymbol{I} * \vec{\omega} \tag{1.2}$$

$$\boldsymbol{I} = \begin{pmatrix} I_{xx} & I_{xy} & I_{xz} \\ I_{yx} & I_{yy} & I_{yz} \\ I_{zx} & I_{zy} & I_{zz} \end{pmatrix} \Rightarrow \begin{pmatrix} I_{aa} & 0 & 0 \\ 0 & I_{bb} & 0 \\ 0 & 0 & I_{cc} \end{pmatrix} \tag{1.3}$$

$$I_{aa} = \sum m_i * r_{i,\perp}^2 = \sum m_i (b_i^2 + c_i^2) \tag{1.4}$$

In quantum mechanics, the angular momentum is quantized. Operators are used to obtain the eigenvalues for this quantization to find the rotational kinetic energy. While $\vec{L}$ can be classically broken down into its L_x, L_y, L_z components, in quantum mechanics there will be an uncertainty in the direction, and a vector operator is needed to find the magnitude and direction of the angular momentum. Due to the nature of quantum mechanics, only one directional component of the angular momentum can, in general, be known at one time through the $\hat{L}_z$

operator. Some intuition of the vector's magnitude can be gained through the $\hat{L}^2$ operator. These give the projection of $\vec{L}$ on the z-axis and the square of the length of $\vec{L}$, respectively, which are also both quantized.

The kinetic energy (E_k) of a simple rigid rotor is described by Equation 1.5. By substituting in the components of the moment of inertia and the definition of linear momentum from Equation 1.2, Equations 1.6 and 1.7 are obtained. Here, the nomenclature for the subscripts of the terms are also be simplified.

$$E_k = \frac{1}{2} I \omega^2 \tag{1.5}$$

$$E_k = \frac{1}{2} I_A \omega_A^2 + \frac{1}{2} I_B \omega_B^2 + \frac{1}{2} I_C \omega_C^2 \tag{1.6}$$

$$E_k = \frac{L_A^2}{2\, I_A} + \frac{L_B^2}{2\, I_B} + \frac{L_C^2}{2\, I_C} \tag{1.7}$$

The $\hat{L}_z$ and $\hat{L}^2$ operators are used to find the eigenfunctions of quantized angular momentum which are known as the spherical harmonics at values of ℓ (ℓ + 1) $\hbar^2$ where ℓ is the angular momentum quantum number and $\hbar$ is the reduced Planck's constant. Accounting also for intrinsic spin, the total angular momentum is labeled as $\vec{J}$, which takes on values J (J + 1) $\hbar^2$. In most cases, a specific class of molecule called an asymmetric top which has nonequal principal moments of inertia will be the subject of discussion. The rotational kinetic energy, characteristic of the molecular geometry, is quantized. The energy between rotational states is related to the Bohr condition such that light coupling to the molecular rotation will have energy absorbed at characteristic frequencies of the molecule; this coupling occurs when the oscillating light matches this frequency, $\Delta E = h\nu$, where h is Planck's constant and ν is frequency of rotation. The energy

between these rotational energy levels is determined using the rotational kinetic energy (asymmetric rigid rotor approximation) Hamiltonian, following the treatment in the equations below:

$$\hat{H}_{Rot} = \hat{T}_{Rot} \equiv \hat{T}_{Rot_a} + \hat{T}_{Rot_b} + \hat{T}_{Rot_c} \tag{1.8}$$

Where, $\hat{T}_{linear} \equiv \frac{\hat{P}^2}{2*m}$ and $\hat{T}_{Rot} \equiv \frac{\hat{J}^2}{2*I}$. Equation 1.8 can then be rewritten as:

$$\hat{H}_{Rot} \equiv \frac{\hat{J}_a^2}{2 * I_A} + \frac{\hat{J}_b^2}{2 * I_B} + \frac{\hat{J}_C^2}{2 * I_C} \tag{1.9}$$

$$\equiv A * \hat{J}_A^2 + B * \hat{J}_B^2 + C * \hat{J}_C^2 \tag{1.10}$$

Where these three new constants, A, B, and C, represent the structural information or the distribution of mass. These are called the rotational constants defined in Equation 1.11. The energy eigenvalues (or 'energy levels', in units of Joules and often converted to be in units of MHz or cm^{-1}), in a simple case of a diatomic with only one inertial axis and no net electronic angular momentum, is given in Equation 1.12 following the quantized treatment mentioned above for values of the rotational quantum number, *J.* The transition between two energy levels with the selection rule of $\Delta J = \pm 1$ yields Equation 1.13 in this simplistic case. The energy eigenvalues when considering an asymmetric top molecule with distortion becomes more complicated and many additional terms are needed.

$$A = \frac{\hbar^2}{2*I_A} \qquad B = \frac{\hbar^2}{2*I_B} \qquad C = \frac{\hbar^2}{2*I_C} \tag{1.11}$$

$$E_{Rot}(J) = B * J(J+1) \tag{1.12}$$

$$\nu_{J' \leftarrow J} = E_{Rot}(J') - E_{Rot}(J) = 2B(J+1) \tag{1.13}$$

Molecules can be separated into groupings based on the relationship between their three principal moments-of-inertia: linear molecules, spherical tops, prolate symmetric tops, oblate symmetric tops, and asymmetric tops. Most molecules fall into the category of polyatomic asymmetric tops and will therefore be the main focus of this thesis. Values of *J* will also no longer be enough information to describe an asymmetric top. Asymmetric tops are instead categorized to be between an oblate or prolate symmetric top. A new quantum number *K*, which is the projection of $\vec{J}$ about the unique symmetry axis, bridges between the two extremes. Rotational energy levels are then a correlation between an oblate (K_a) and prolate top (K_c) such that they are reported as $J_{Ka,Kc}$ (ex. $1_{0,1}$ where J=1, K_a=0, K_c=1). In addition, molecules are not truly rigid and can distort as they rotate, so more information is needed in the form of centrifugal distortion constants. These constants won't be discussed in detail here (nor will the total description of the rotational kinetic energy of an asymmetric top), but can be found elsewhere.[55, 56] These constants can be obtained by fitting experimental rotational spectra with software packages like JB95[57], AABS[58, 59] and Pickett's SPCAT/SPFIT[60] by including initial guesses for all constants.

Light will interact with the molecule via its electric dipole moment which acts like an antenna as it receives or radiates light when the light's frequency matches a characteristic frequency of the molecular rotation and following selection rules (probability of the transition using the electric dipole moment operator yielding $\Delta J=0, \pm 1$ and ΔK_a and ΔK_c are discussed later in Equations 1.15-1.17).[56] For rotational spectroscopy, the molecule being subjected to the light must have a nonzero electric dipole moment for this interaction to occur. The light will give a torque on the electric dipole moment as shown in the simple diatomic case in Figure 1.4.

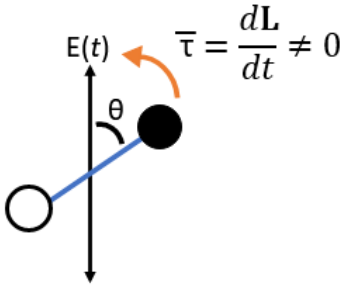

Figure 1.4: A simple diatomic molecule rotating end-over-end in free space is given a torque, $\bar{\tau}$, from the interaction of its electric dipole moment and an electric field, *E(t)*, of incident light as the electric dipole moment at angle, θ, from the electric field polarization moves in line. The change in angular momentum over time will be nonzero.

As the frequency of light becomes resonant with the frequency of rotation, energy can be given to the molecule and produce a time-dependent oscillating electric dipole moment which in turn will produce light as it oscillates in the absence of the incident light (Figure 1.5). This is further explained in detail in Chapter 2.

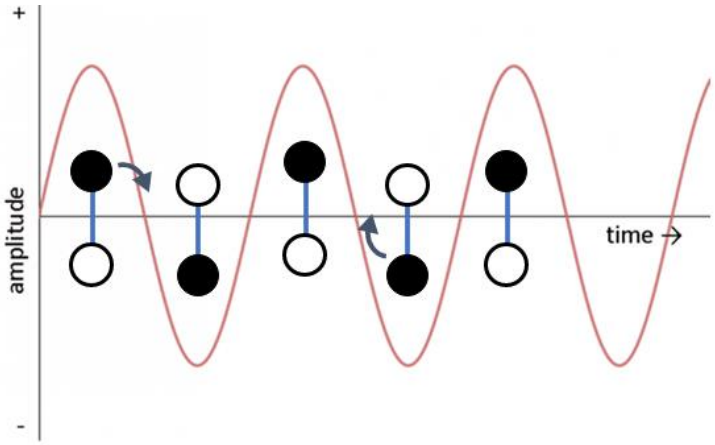

Figure 1.5: The simple diatomic molecule shown in Figure 1.5 is shown here in 5 instances of time as it rotates in pursuit of the incident light, creating a time-dependent oscillating electric dipole moment. An oscillating dipole will thereby produce light in the direction of the incident light field.

The interaction Hamiltonian between the light and electric dipole moment is given in Equation 1.14.

$$\widehat{H}_{Int} = -\vec{\mu} * E(t) \quad (1.14)$$

Where $\vec{\mu}$ is the electric dipole moment that can be broken up into its vector components, μ_a, μ_b, and μ_c, that describes the sum of particles at a position multiplied by their charge and $E(t)$ is the oscillating electric field of the light interacting with the molecule's electric dipole moment. In this formulation, light may interact and produce a torque on each of the three electric dipole moment vector components. This causes each rotational spectrum to consist of three spectra that referred to as the a-, b- and c-type spectra with specific selection rules (and in general with ΔJ=0, ±1) shown in Equations 1.15-17.

$$\text{a-type: } \Delta K_a = 0,\ \Delta K_c = \pm 1 \quad (1.15)$$

$$\text{b-type: } \Delta K_a = \pm 1,\ \Delta K_c = \pm 1 \quad (1.16)$$

$$\text{c-type: } \Delta K_a = \pm 1,\ \Delta K_c = 0 \quad (1.17)$$

For the sake of this dissertaiton, information about the rotational constants is needed to determine the rotational energy levels for a given molecule, and information on the electric dipole moment is used determine the allowed transitions and the intensity pattern of the spectrum produced through the interaction of light with our molecule. Information regarding the

population in each of the energy levels will be discussed later in the thesis when some information about introducing gases via a pulsed supersonic jet expansion are considered.

Spectra are acquired using advanced technologies in microwave spectroscopy that are known for their high resolution such that the fingerprint-like spectra of multiple molecules, conformers, isomers, and isotopomers/isotopologues can all be measured at once without any spectral overlap as seen in the example of methylphenyloxirane in Figure 1.6.

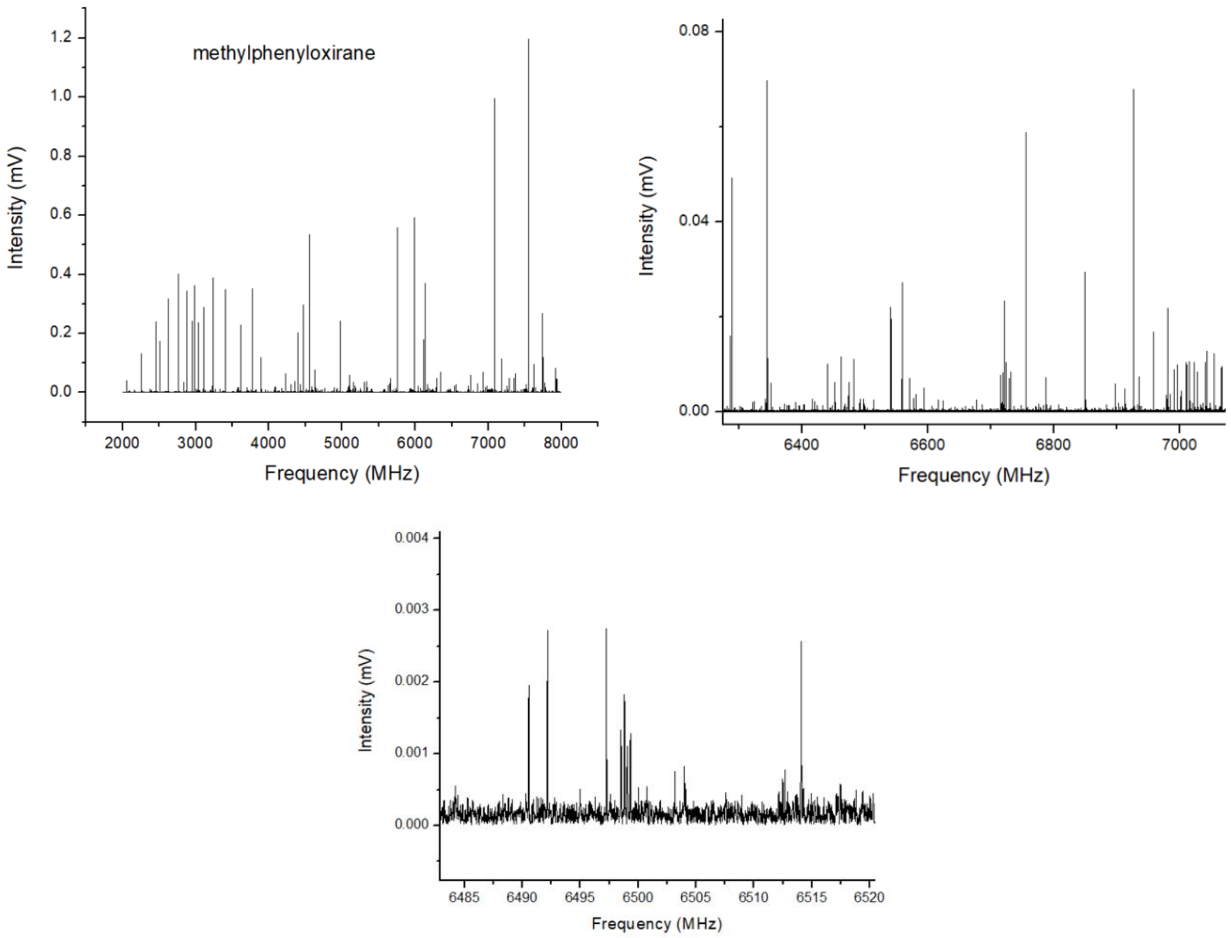

Figure 1.6: A 2-8 GHz spectrum of methylphenyloxirane measured in UVA's Physical Chemistry I Laboratory course during a project to compare various chiral analysis methods. The rotational spectrum collected using a chirped-pulse Fourier transform microwave spectrometer, known for its high spectral resolution, consists of many transitions without spectral overlap, as depicted in the zoomed-in spectra. Spectral fingerprints of conformers of the analyte, isotopologues found in natural abundance, and impurities are all observed through this frequency range.

The rotational spectroscopy technique has been known for its strength in structure determination but until recently, had failed to be useful in differentiating molecules of the same mass distribution, like enantiomers. While a technique of tagging enantiomers with a small chiral molecule will be demonstrated in a later chapter, another approach called three-wave mixing rotational spectroscopy will be employed, which uses just the electric dipole moment information to distinguish enantiomers without the need of a chiral tag.

1.5: *A Brief History of Rotational Spectroscopy*

Spectroscopy using microwaves to investigate molecular structure arose from radar technology development during World War II. Before this, only the measurement of ammonia gas by Cleeton and Williams in 1933 was of great note.[61] In the early experiments post war, simple absorption gas cells were used where light was passed through a molecular gas sample and a detector recorded the absorption features at resonant frequencies. A cavity system of confocal mirrors was introduced later in 1979 by Balle and Flygare, which revolutionized the field. The mirrors allowed more passes of light through a gas sample at resonant frequencies and emission of the molecules was detected; this instrumentation greatly increased sensitivity.[62-64] Additionally, the introduction of the pulsed jet sample injection system aided in rotationally cooling samples such that larger molecular systems could be studied.[62, 64] This cavity system was then automated to allow for the collection of many spectral components over a larger bandwidth with high sensitivity by adjusting the distance between the mirror components in a step-wise fashion.[64] However, the time it took to tune the cavity for larger bandwidths was immense. The

Pate group and collaborators then revolutionized the field of microwave spectroscopy by developing technology capable of producing chirped microwave pulses where a linear sweep of frequencies is sufficiently powered to polarize a molecular sample over larger frequency bandwidths of GHz in size in a single experiment.[64-66] Instead of a tunable cavity system, this new spectrometer relies on high-powered traveling wave tube (TWT) amplifiers, arbitrary waveform generators (AWG), and fast digitizers to generate the chirped pulses and record the large bandwidth of data directly. The sensitivity of chirped pulse Fourier transform microwave (CP-FTMW) spectrometers when coupled with multiple pulsed supersonic jets for sample introduction allows for the detection of hundreds of transitions for many molecular species and complexes in microseconds at great resolution; similar measurements on cavity systems on the other hand can take up to take many days complete the same bandwidth.[64]

Additionally, great interest over the years in looking out into the universe to observe the radio and millimeter/submillimeter emission of molecules has led to the inventions of radio telescopes like the Green Bank Observatory in West Virginia and incredible arrays of many telescopes like that of the ALMA observatory in Chile, where chemical compositions and structure of not only far away galaxies but also the birth of planetary systems are now regularly observed.[67, 68]

1.6: *Predicting the Rotational Spectrum Using Quantum Chemistry Calculations*

To predict a rotational spectrum for molecular species and complexes, treated as a rigid rotor, seven parameters are required. The energy levels are determined by the rotational Hamiltonian with the three structural parameters *A*, *B*, and *C*. The allowed transitions from selection rules and the intensity of the spectrum rely on knowledge of the electric dipole moment (broken up into μ_a, μ_b, and μ_c vector components) and the rotational temperature, T_{Rot}. The relative intensity of the a-, b-, and c-type spectra are proportional to the square of the electric dipole vector components.

The software package Gaussian16[69] can be used to predict *A*, *B*, *C*, μ_a, μ_b, and μ_c. Gaussian16 allows one to draw a ball-and-stick figure of any molecule or complex and then submit a quantum calculation to find minima in a potential energy surface for the total electronic energy (the electronic structure) as atoms of the molecule are moved, where the corresponding minima are the equilibrium structures for the molecule (molecular geometries). The user must give a specified method (using various approximations), basis set ('shapes' used to approximate the electron wavefunctions), and additional effects like electron correlation. There are always trade-offs of what level of theory (method and basis set) to use for a given molecule. It might be true that as you go to higher and higher levels or theory and include more basis functions that you will get closer to the 'correct' answer, but it will take an incredible amount of computing time. A level of theory is often settled on that will finish calculating an optimal geometry in hours or a couple days and still get very close to the true geometry found during experiments.

Some of the useful or typical methods are second order Møller-Plesset perturbation theory (MP2), dispersion corrected Density Functional Theory (DFT), and coupled-cluster (CC) methods. MP2 tends to overestimate the structural parameters and higher order perturbations (MP3, MP4, etc.) take exceedingly more computation time and oscillate around the true answer for the parameter in question.[70] CC methods will yield very accurate results, where CCSD(T) is considered a 'gold-standard' treatment with low relative errors with a tradeoff of being computationally expensive.[70] DFT uses functionals to approximate the electron density of a molecular system where the electron wave functions are input into the functional and the output is the electronic energy of the system. DFT is a relatively quick calculation to run but does require additional corrections to account for dispersion forces and other effects across the molecule.[71] Benchmarking is done to assess the quality of these functionals when compared to experimentally measured rotational parameters.[70-73] A quick, but quite accurate calculation uses the B3LYP functional with D3BJ dispersion correction and a 6-311G++(d,p) or def2TZVP basis set. Future chapters will highlight the successes of the B2PLYPD3 method and the def2TZVP basis set. These levels of theory yield percent errors between experimental fits and theory well below 1% in the rotational constants that have observed in many measurements over the years.

Additionally, and importantly, these calculations can be done on the university's supercomputing cluster, Rivanna, to reduce computational time. Many CPUs and larger amounts of disk space and RAM are used to increase run speeds from a smaller six-core processor computer by factors of 10 or more. Rivanna is a powerful tool as it allows for hundreds of calculations to be run at once to obtain a complete conformer space of some highly flexible molecules.

1.7: *Outline of Dissertation*

I've had the opportunity and pleasure to work on several collaborations with faculty and researchers like David Pratt (University of Vermont), Berhane Temelso and George Shields (Bucknell University), Joe Clark (Marquette University), Shanshan Yu and Deacon Nemchick (Nasa's Jet Propulsion Laboratory), Justin Neil (BrightSpec Inc.) and Dean Harman (University of Virginia). Each of these collaborations have been so interesting and full of exciting chemistry. However, for the sake of cohesion, the focus of this thesis will be the summation of work developing methods for quantitative analysis of challenging chemical mixtures by rotational spectroscopy in the realms of chiral analysis and isotopic purity analysis.

Chapter 1 introduced chiral analysis and the challenges it provides in the context of analytical chemistry. Rotational spectroscopy was introduced as well, along with a short look at its history. Quantum chemistry was also discussed as it provides the backbone to the identification and quantitation by the rotational spectroscopy technique.

Chapter 2 will introduce the three-wave mixing (3WM) rotational spectroscopy technique. This technique was the first approach taken in the field to address chiral analysis challenges by rotational spectroscopy.[74-76] A summary of the measurement principle is discussed and an in-depth work-up of the quantum dynamics describing this technique is provided. Additionally, a brief literature review of the technique is given as it is still in its infancy and only a handful of journal articles have been published on it.

Chapter 3 will provide a look at the quantitative analysis of 3WM. The question of "can the 3WM technique be used to solve the overwhelming challenges of chiral analysis?" will be

addressed. A large dataset and selection of experimental conditions was used to analyze the performance of the technique, its weaknesses and strengths, and to assess its role for the future.

Chapter 4 is a current summation of a collaboration project with Shanshan Yu at the Jet Propulsion Laboratory (NASA/Caltech) to take 3WM into the millimeter wave regime where size, weight, and power of the instrumentation can be reduced in alignment with requirements for a space mission. The 3WM technique, which has inherent strengths in measurements in complex mixtures, was assessed for its measurement capabilities of potential biomarkers in the search for past or present life in our solar system on places like Mars and the moons of Jupiter and Saturn. A prototype instrument named ChiralSpec was designed, constructed, and tested, with success in measuring a chiral signature in the millimeter-wave regime. Future possibilities of the instrument will be discussed as the project is on-going.

Chapter 5 shifts gears from chiral analysis to isotopic purity analysis, which also proves to be challenging by many analytical techniques due to the very subtle changes in chemical structure through isotopic substitution. A collaboration project with the Clark group at Marquette University (Wisconsin) is discussed and shows how rotational spectroscopy can be used to perform quantitative analysis of the synthesis of many isotopic isomers due to its high spectral resolution. A “cocktail” synthesis reaction is used to produce a mixture of all possible isotopic isomers to build a library of measured rotational spectroscopic fingerprints for quick analysis of further syntheses in the direction of real-time quantitative analysis.

Chapter 6 represents another collaboration project in the realm of isotopic impurity analysis, in this case with the Harman group at the University of Virginia. A sampling reservoir

was designed to aid in analyzing selectively deuterated species along with adding improvements in measurement speed and reproducibility such that the analysis could directly inform the synthetic chemists in the mechanism and thermodynamics of their chemistry. Additional kinetics studies using rotational spectroscopy and the new sample cell were done to show how changing the ligand structure on a metal complex used to allow for selective deuteration of the analyte can alter the activation energy of the ligand bond holding the analyte.

Finally, Chapter 7 combines the strengths of rotational spectroscopy in chiral analysis and isotopic impurity analysis by analyzing a stereoselective product of the Harman group's synthesis, namely a molecule that is chiral merely by deuteration. Chiral tagging rotational spectroscopy is implemented to provide high-confidence determinations of absolute configuration and enantiomeric excess while the analyte can also be analyzed for its isotopic impurities at the same time, all without any prior separation. This set of measurements shows a great view of how rotational spectroscopy can provide chemists with the capability to analyze a wide range of analytes in highly complex chemical mixtures.

Chapter 1 References:

1. Ju, H., Grand challenges in analytical chemistry: towards more bright eyes for scientific research, social events and human health. *Front Chem* **2013,** *1*, 5.
2. Merone, G. M.; Tartaglia, A.; Locatelli, M.; D'Ovidio, C.; Rosato, E.; de Grazia, U.; Santavenere, F.; Rossi, S.; Savini, F., Analytical Chemistry in the 21st Century: Challenges, Solutions, and Future Perspectives of Complex Matrices Quantitative Analyses in Biological/Clinical Field. *Analytica* **2020,** *1* (1), 44-59.
3. Trojanowicz, M., Challenges of Modern Analytical Chemistry. *Modern Chemistry & Applications* **2013,** *01* (04).
4. Neill, J. L.; Yang, Y.; Muckle, M. T.; Reynolds, R. L.; Evangelisti, L.; Sonstrom, R. E.; Pate, B. H.; Gupton, B. F., Online Stereochemical Process Monitoring by Molecular Rotational Resonance Spectroscopy. *Organic Process Research & Development* **2019,** *23* (5), 1046-1051.
5. Loudon, M., *Organic Chemistry*. 5 ed.; Roberts and Company Publishers: 2009.
6. Gal, J., Louis Pasteur, language, and molecular chirality. I. Background and dissymmetry. *Chirality* **2011,** *23* (1), 1-16.
7. Barron, L. D., Compliments from Lord Kelvin. *Nature* **2007,** *446*, 505-506.
8. Gal, J., Pasteur and the art of chirality. *Nat Chem* **2017,** *9* (7), 604-605.
9. Klein, J., How Pasteur's Artistic Insight Changed Chemistry. *The New York Times* 2017.
10. Vitalii I. Goldanski, V. V. K., Chirality and cold origin of life. *Nature* **1991,** *352*, 114.
11. Blackmond, D. G., The origin of biological homochirality. *Philos Trans R Soc Lond B Biol Sci* **2011,** *366* (1580), 2878-84.
12. Cotton, F. A., *Chemical Applications of Group Theory*. 3 ed.; John Wiley & Sons, Inc: 1990.
13. Shubert, V. A.; Schmitz, D.; Perez, C.; Medcraft, C.; Krin, A.; Domingos, S. R.; Patterson, D.; Schnell, M., Chiral Analysis Using Broadband Rotational Spectroscopy. *J Phys Chem Lett* **2015,** *7* (2), 341-50.
14. Lien Ai Nguyen, H. H., Chuong Pham-Huy, Chiral Drugs: An Overview. *International Journal of Biomedical Science* **2006**.
15. Pizzarello, S., Molecular Asymmetry in Prebiotic Chemistry: An Account from Meteorites. *Life (Basel)* **2016,** *6* (2).
16. Joyce, G. F., Schwartz A. W., Miller S. L., Orgel L. E., The case for an ancestral genetic system involving simple analogues of the nucleotides. *Proc. Natl. Acad. Sci. USA* **1987,** *84* (Biochemistry), 4398-4402.
17. Thiemann WH, M. U., ESA mission ROSETTA will probe for chirality of cometary amino acids. *Orig Life Evol Biosph.* **2001**.
18. Myrgorodska, I.; Meinert, C.; Martins, Z.; Le Sergeant d'Hendecourt, L.; Meierhenrich, U. J., Molecular chirality in meteorites and interstellar ices, and the chirality experiment on board the ESA cometary Rosetta mission. *Angew Chem Int Ed Engl* **2015,** *54* (5), 1402-12.
19. Alison M. Skelley, J. R. S., Andrew D. Aubrey, William H. Grover, Robin H. C. Ivester, Pascale Ehrenfreund, Frank J. Grunthaner, Jeffrey L. Bada, and Richard A. Mathies, Development and evaluation of a microdevice for amino acid biomarker detection and analysis on Mars. *Proceedings of the National Academy of Sciences of the United States of America* **2005,** *102* (4).
20. Goesmann, F.; Brinckerhoff, W. B.; Raulin, F.; Goetz, W.; Danell, R. M.; Getty, S. A.; Siljeström, S.; Mißbach, H.; Steininger, H.; Arevalo, R. D.; Buch, A.; Freissinet, C.; Grubisic, A.; Meierhenrich, U. J.; Pinnick, V. T.; Stalport, F.; Szopa, C.; Vago, J. L.; Lindner, R.; Schulte, M. D.; Brucato, J. R.; Glavin, D. P.; Grand, N.; Li, X.; van Amerom, F. H. W.; the, M. S. T., The Mars Organic Molecule Analyzer (MOMA) Instrument: Characterization of Organic Material in Martian Sediments. *Astrobiology* **2017,** *17* (6-7), 655-685.

21. Jennifer L. Eigenbrode, R. E. S., Andrew Steele, Caroline Freissinet, Maëva Millan , Rafael Navarro-González, Brad Sutter, Amy C. McAdam, Heather B. Franz, Daniel P. Glavin, Paul D. Archer Jr., Paul R. Mahaffy, Pamela G. Conrad, Joel A. Hurowitz, John P. Grotzinger , Sanjeev Gupta, Doug W. Ming , Dawn Y. Sumner11, Cyril Szopa, Charles Malespin, Arnaud Buch, Patrice Coll, Organic matter preserved in 3-billion-year-old mudstones at Gale crater, Mars. *Science* **2018,** *360*.
22. Creamer, J. S.; Mora, M. F.; Willis, P. A., Enhanced Resolution of Chiral Amino Acids with Capillary Electrophoresis for Biosignature Detection in Extraterrestrial Samples. *Anal Chem* **2017,** *89* (2), 1329-1337.
23. Stephens, P. J., Theory of Vibrational Circular Dichroism. *J. Phys. Chem.* **1985,** *89* (5), 748-752.
24. F.J. Devlin, P. J. S., Conformational Analysis Using ab Initio Vibrational Spectroscopy: 3-Methylcyclohexanone. *Journal of the American Chemical Society* **1999,** *121* (32), 7413-7414.
25. P.J. Stephens, F. J. D., Deterimination of the Structure of Chiral Molecules using Ab Initio Vibrational Circular Dichroism Spectroscopy. *Chirality* **2000,** *12*, 172-179.
26. He, Y.; Wang, B.; Dukor, R. K.; Nafie, L. A., Determination of absolute configuration of chiral molecules using vibrational optical activity: a review. *Appl Spectrosc* **2011,** *65* (7), 699-723.
27. Ritchie, B., Theory of the angular distribution of photoelectrons ejected from optically active molecules and molecular negative ions. *Physical Review A* **1976,** *13* (4), 1411-1415.
28. Bowering, N.; Lischke, T.; Schmidtke, B.; Muller, N.; Khalil, T.; Heinzmann, U., Asymmetry in photoelectron emission from chiral molecules induced by circularly polarized light. *Phys Rev Lett* **2001,** *86* (7), 1187-90.
29. Garcia, G. A.; Nahon, L.; Lebech, M.; Houver, J.-C.; Dowek, D.; Powis, I., Circular dichroism in the photoelectron angular distribution from randomly oriented enantiomers of camphor. *The Journal of Chemical Physics* **2003,** *119* (17), 8781-8784.
30. Abbate, S.; Castiglioni, E.; Gangemi, F.; Gangemi, R.; Longhi, G., NIR-VCD, vibrational circular dichroism in the near-infrared: experiments, theory and calculations. *Chirality* **2009,** *21 Suppl 1*, E242-52.
31. Sherer, E. C.; Lee, C. H.; Shpungin, J.; Cuff, J. F.; Da, C.; Ball, R.; Bach, R.; Crespo, A.; Gong, X.; Welch, C. J., Systematic approach to conformational sampling for assigning absolute configuration using vibrational circular dichroism. *J Med Chem* **2014,** *57* (2), 477-94.
32. Beaulieu, S.; Ferré, A.; Géneaux, R.; Canonge, R.; Descamps, D.; Fabre, B.; Fedorov, N.; Légaré, F.; Petit, S.; Ruchon, T.; Blanchet, V.; Mairesse, Y.; Pons, B., Universality of photoelectron circular dichroism in the photoionization of chiral molecules. *New Journal of Physics* **2016,** *18* (10).
33. Kastner, A.; Lux, C.; Ring, T.; Zullighoven, S.; Sarpe, C.; Senftleben, A.; Baumert, T., Enantiomeric Excess Sensitivity to Below One Percent by Using Femtosecond Photoelectron Circular Dichroism. *Chemphyschem* **2016,** *17* (8), 1119-22.
34. Goetz, R. E.; Isaev, T. A.; Nikoobakht, B.; Berger, R.; Koch, C. P., Theoretical description of circular dichroism in photoelectron angular distributions of randomly oriented chiral molecules after multi-photon photoionization. *J Chem Phys* **2017,** *146* (2), 024306.
35. Tools for Discoveries of Life. http://www.btools.com/vcd_general.htm.
36. Turchini, S., Conformational effects in photoelectron circular dichroism. *J Phys Condens Matter* **2017,** *29* (50), 503001.
37. Prasad L. Polavarapu, J. H., Chiral Analysis Using Mid-IR Vibrational CD Spectroscopy. *Analytical Chemistry* **2004,** *76* (3), 61 A-67 A.
38. Zhang, Y.; Wu, D.-R.; Wang-Iverson, D. B.; Tymiak, A. A., Enantioselective chromatography in drug discovery. *Drug Discovery Today* **2005,** *10* (8), 571-577.
39. Ribeiro, A. R.; Maia, A. S.; Cass, Q. B.; Tiritan, M. E., Enantioseparation of chiral pharmaceuticals in biomedical and environmental analyses by liquid chromatography: an overview. *J Chromatogr B Analyt Technol Biomed Life Sci* **2014,** *968*, 8-21.

40. Parker, D., NMR determination of enantiomeric purity. *Chem. Rev.* **1991,** *91* (7).
41. Wenzel, T. J.; Chisholm, C. D., Assignment of absolute configuration using chiral reagents and NMR spectroscopy. *Chirality* **2011,** *23* (3), 190-214.
42. Parsons, S., Determination of absolute configuration using X-ray diffraction. *Tetrahedron: Asymmetry* **2017,** *28* (10), 1304-1313.
43. J.M. Bijvoet, A. F. P., and A. J. van Bommel, Determination of the absolute configuration of optically active compounds by means of X-rays. *Nature* **1951,** *168*.
44. Flack, H. D.; Bernardinelli, G., The use of X-ray crystallography to determine absolute configuration. *Chirality* **2008,** *20* (5), 681-90.
45. Watts, A. E.; Maruyoshi, K.; Hughes, C. E.; Brown, S. P.; Harris, K. D. M., Combining the Advantages of Powder X-ray Diffraction and NMR Crystallography in Structure Determination of the Pharmaceutical Material Cimetidine Hydrochloride. *Crystal Growth & Design* **2016,** *16* (4), 1798-1804.
46. Brooks H. Pate, L. E., Walther Caminati, Yunjie Xu, Javix Thomas, David Patterson, Cristobal Perez, Melanie Schnell, Quantitative Chiral Analysis by Molecular Rotational Spectroscopy. In *Chiral Analysis*, 2 ed.; 2018; pp 679-729.
47. Neill, J. L.; Douglass, K. O.; Pate, B. H.; Pratt, D. W., Next generation techniques in the high resolution spectroscopy of biologically relevant molecules. *Phys Chem Chem Phys* **2011,** *13* (16), 7253-62.
48. Nerz-Stormes, M. The Basics Nuclear Magnetic Resonance Spectroscopy. http://www.brynmawr.edu/chemistry/Chem/mnerzsto/The_Basics_Nuclear_Magnetic_Resonance%20_Spectroscopy_2.htm.
49. Sonstrom, R. E.; Neill, J. L.; Mikhonin, A. V.; Doetzer, R.; Pate, B. H., Chiral analysis of pantolactone with molecular rotational resonance spectroscopy. *Chirality* **2022,** *34* (1), 114-125.
50. Mayer, K. J. Chiral Analysis by Chiral Tag Rotational Spectroscopy. University of Virginia, Charlottesville, VA, 2022.
51. Wollenhaupt, M., Photoelectron circular dichroism in different ionization regimes. *New Journal of Physics* **2016,** *18* (12).
52. Patterson, D.; Schnell, M., New studies on molecular chirality in the gas phase: enantiomer differentiation and determination of enantiomeric excess. *Phys Chem Chem Phys* **2016,** *16* (23), 11114-23.
53. Studying Chirality with Vibrational Circular Dichroism. http://gaussian.com/vcd/.
54. Ma, Y.; Oleynikov, P.; Terasaki, O., Electron crystallography for determining the handedness of a chiral zeolite nanocrystal. *Nat Mater* **2017,** *16* (7), 755-759.
55. Bernath, P., *Spectra of Atoms and Molecules*. 3 ed.; Oxford University Press: 2016.
56. C.H. Townes, A. L. S., *Microwave Spectroscopy*. Dover Publications Inc.: 1975.
57. Plusquellic, D. F. *JB95 Spectral Fitting Program*, 2016.
58. Kisiel, Z., *Assignment and Analysis of Complex Rotational Spectra*. Ed. Kluwer Academic Publishers: 2001.
59. Kisiel, Z. P., L.; Medvedev, I.R.; Winnewisser, M.; De Lucia, F.C.; Herbst, E., Rotational spectrum of trans-trans diethyl ether in the ground and three excited vibrational states. *J. Mol. Spectrosc.* **2005,** *233*, 231-243.
60. Pickett, H. M., The fitting and prediction of vibration-rotation spectra with spin interactions. *J. Mol. Spec.* **1991,** *148*, 371-377.
61. Williams, C. a., *Phys. Rev.* **1934,** *45* (234).
62. Balle, T. J.; Flygare, W. H., Fabry–Perot cavity pulsed Fourier transform microwave spectrometer with a pulsed nozzle particle source. *Review of Scientific Instruments* **1981,** *52* (1), 33-45.

63. Campbell, E. J.; Buxton, L. W.; Balle, T. J.; Flygare, W. H., The theory of pulsed Fourier transform microwave spectroscopy carried out in a Fabry–Perot cavity: Static gas. *The Journal of Chemical Physics* **1981,** *74* (2), 813-828.
64. Park, G. B.; Field, R. W., Perspective: The first ten years of broadband chirped pulse Fourier transform microwave spectroscopy. *J Chem Phys* **2016,** *144* (20), 200901.
65. Brown, G. G.; Dian, B. C.; Douglass, K. O.; Geyer, S. M.; Pate, B. H., The rotational spectrum of epifluorohydrin measured by chirped-pulse Fourier transform microwave spectroscopy. *Journal of Molecular Spectroscopy* **2006,** *238* (2), 200-212.
66. Brown, G. G.; Dian, B. C.; Douglass, K. O.; Geyer, S. M.; Shipman, S. T.; Pate, B. H., A broadband Fourier transform microwave spectrometer based on chirped pulse excitation. *Rev Sci Instrum* **2008,** *79* (5), 053103.
67. Whitehead, N., Planets Form in Organic Soups With Different Ingredients. In *Series of New Images Reveals That Planets Form in Organic Soups—and No Two Soups Are Alike*, Center for Astrophysics | Harvard & Smithsonian.
68. Observatory, T. N. R. A. https://public.nrao.edu/.
69. Frisch, M. J. T., G. W.; Schlegel, H. B.; Scuseria, G. E.; Robb, M. A.; Cheeseman, J. R.; Scalmani, G.; Barone, V.; Petersson, G. A.; Nakatsuji, H.; Li, X.; Caricato, M.; Marenich, A. V.; Bloino, J.; Janesko, B. G.; Gomperts, R.; Mennucci, B.; Hratchian, H. P.; Ortiz, J. V.; Izmaylov, A. F.; Sonnenberg, J. L.; Williams-Young, D.; Ding, F.; Lipparini, F.; Egidi, F.; Goings, J.; Peng, B.; Petrone, A.; Henderson, T.; Ranasinghe, D.; Zakrzewski, V. G.; Gao, J.; Rega, N.; Zheng, G.; Liang, W.; Hada, M.; Ehara, M.; Toyota, K.; Fukuda, R.; Hasegawa, J.; Ishida, M.; Nakajima, T.; Honda, Y.; Kitao, O.; Nakai, H.; Vreven, T.; Throssell, K.; Montgomery, J. A., Jr.; Peralta, J. E.; Ogliaro, F.; Bearpark, M. J.; Heyd, J. J.; Brothers, E. N.; Kudin, K. N.; Staroverov, V. N.; Keith, T. A.; Kobayashi, R.; Normand, J.; Raghavachari, K.; Rendell, A. P.; Burant, J. C.; Iyengar, S. S.; Tomasi, J.; Cossi, M.; Millam, J. M.; Klene, M.; Adamo, C.; Cammi, R.; Ochterski, J. W.; Martin, R. L.; Morokuma, K.; Farkas, O.; Foresman, J. B.; Fox, D. J. *Gaussian 16*, Revision C.01; Gaussian, Inc, Wallingford CT, 2016.
70. Mata, R. A.; Suhm, M. A., Benchmarking Quantum Chemical Methods: Are We Heading in the Right Direction? *Angew Chem Int Ed Engl* **2017,** *56* (37), 11011-11018.
71. Grimme, S.; Steinmetz, M., Effects of London dispersion correction in density functional theory on the structures of organic molecules in the gas phase. *Phys Chem Chem Phys* **2013,** *15* (38), 16031-42.
72. Puzzarini, C., Rotational spectroscopy meets theory. *Phys Chem Chem Phys* **2013,** *15* (18), 6595-607.
73. Grimme, S.; Schreiner, P. R., Computational Chemistry: The Fate of Current Methods and Future Challenges. *Angew Chem Int Ed Engl* **2018,** *57* (16), 4170-4176.
74. Patterson, D.; Schnell, M.; Doyle, J. M., Enantiomer-specific detection of chiral molecules via microwave spectroscopy. *Nature* **2013,** *497* (7450), 475-7.
75. Patterson, D.; Doyle, J. M., Sensitive chiral analysis via microwave three-wave mixing. *Phys Rev Lett* **2013,** *111* (2), 023008.
76. Grabow, J. U., Fourier transform microwave spectroscopy: handedness caught by rotational coherence. *Angew Chem Int Ed Engl* **2013,** *52* (45), 11698-700.

Chapter 2: Introduction to Three-Wave Mixing (3WM) Rotational Spectroscopy

2.1: *Measurement Principle*

Three-wave mixing rotational spectroscopy (3WM) is an adaptation on rotational spectroscopy such that a chiral signature can be measured and used to distinguish a pair of enantiomers.[1-3] Traditional rotational spectroscopy cannot be used to spectroscopically resolve enantiomers since enantiomers produce the same rotational spectra due to having the same moments-of-inertia and magnitude of electric dipole moment vector components. However, a molecule's chirality can be exploited when placed in a chiral environment, so proposed analytical methods must incorporate the entire three-dimensional structure of a molecular species within some chiral environment to observe a distinguishing feature. Most spectroscopic techniques, such as IR and NMR spectroscopy, experience this same challenge. These techniques subject a sample to plane polarized light and the resulting emission or absorption is measured. Much like using a flashlight to cast a shadow of one's hand on a wall, the identity of the hand used to cast the shadow would be unknown if looking at the shadow by itself. However, in techniques like VCD, the interaction of circularly polarized light (the chiral environment) with the coupling of the electric and magnetic dipole moments (characteristic of a molecule's three-dimensional structure) of each enantiomer allows for a chiral signature to be observed.

A measurement can now be done within rotational spectroscopy to also produce a chiral signature. If one considers the enantiomeric pair as shown below in Fig 2.1a, the electric dipole moment components in the principal axis system will be composed of two components that mirror each other while the third components point in opposite directions. The sign of each

inertial axis that the electric dipole moment components are defined by are arbitrarily chosen, but once it is chosen for one enantiomer, the other enantiomer must follow suit and have one component opposite sign between the two. The scalar triple product ($(\mu_a \times \mu_b) \cdot \mu_c$), represents the combination of these three vectors and changes sign between enantiomers, as shown below. This sign change will become a measurement principle that can be used as a physical characteristic that will interact differently in a chiral system prepared using three orthogonal electric field polarizations of light.

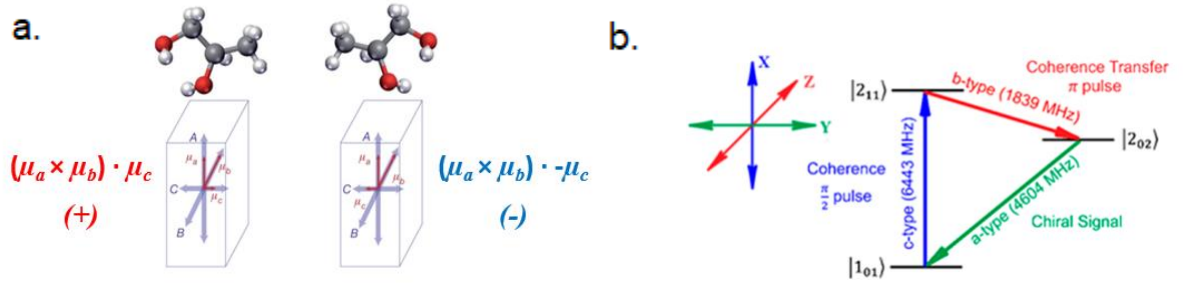

Figure 2.1: **(a)** The mirror-like electric dipole vector components of the chiral molecule 1,2-propanediol and the change of sign for the scalar triple product of those vector components. Figure adapted from Patterson *et al*. 2013.[1] **(b)** 3WM measurement cycle depicted from Lobsiger *et al*. 2015.[4] Three-wave mixing incorporates three transitions to invoke a chiral response from a chiral molecule. The cycle of transitions will consist of an a-, b-, and c-type transition, and each transition incorporates a different linear polarization of the electric field of light indicated by different colors.

Certain conditions in the measurement must be met to generate a chiral signal. In Fig 1.2b (from the work of Lobsiger *et al.*[4]), a cycle of rotational transitions is used to produce a chiral signal which will have the same frequency for each enantiomer but the sign change in $((\mu_a \times \mu_b) \cdot \mu_c)$ will invoke a change in sign in the signals' phase; the phase will be shifted by π radians (180°) for one enantiomer. This cycle consists of an a-, b-, and c-type transition which utilizes each of the electric dipole moment components, and each transition will utilize an orthogonal

polarization of the electric field of light. The specific details of these transitions, polarizations, and nomenclature will be described in the next section.

In the case where there is a mixture of enantiomers present, the measurement principle allows for the ratio of the two enantiomers to be quantified. The net signal is a combination of the two enantiomeric signals of opposite phase and therefore destructively interfere. In other words, the enantiomeric excess (EE) is directly proportional to the intensity of the net chiral signal. The relationship is given in Equation 2.1.

$$EE = \frac{N_L - N_R}{N_L + N_R} * 100\% = C * \frac{Chiral\ Signal}{Achiral\ Signal} * 100\% = C * R * 100\% \qquad (2.1)$$

N_L and N_R are the number densities of the two enantiomers such that their difference divided by their sum is proportional to the chiral signal divided by an achiral signal represented by the sum of the two enantiomers. *C* is a proportionality constant that included instrument response factors and *R* is used to represent the ratio of the chiral signal and achiral signal. The inclusion of the sum of the enantiomers is required to normalize the chiral signal that is susceptible to changes in the measurement like gas pressure, gas temperature, and electronics' noise temperature.

2.2: *Quantum Dynamics*

In order to describe the 3WM technique at the quantum level, one must consider how molecules interact with light and how a series of light fields with particular electric field polarization and wave propagation direction can yield chiral emission of a sample with an EE. An abbreviated description is provided here; however, if the reader's curiosity persists to know the details from first principles, the final chapter of the book *Frontiers and Advances in Molecular Spectroscopy*[5] and the supplemental materials of Lobsiger *et al*.[4] are suggested.

To start, an equation of motion is needed to describe the molecules (more generally, particles). The time-dependent Schrödinger Equation is used.

$$i\hbar \frac{\partial \Psi(x,t)}{\partial t} = \hat{H}\,\Psi(x,t) \tag{2.2}$$

Where *i* is the unit imaginary number, $\hbar$ is the reduced Planck's constant, t is time, $\hat{H}$ is the Hamiltonian operator and $\Psi(x,t)$ is the wave equation representing the particles position in space *x* at time *t*. $\widehat{H}$ can be rewritten as:

$$\hat{H} = \hat{T} + \hat{V} \tag{2.3}$$

Where $\hat{T}$ is the kinetic energy operator such that $\hat{T} = \frac{\hbar^2}{2m}\frac{\partial^2}{\partial x^2}$ where the new variable *m* is mass, and $\hat{V}$ is the potential energy operator that depends on the case to be studied. For the special case of a conservative system in which total energy is conserved, the forces acting upon the particles are not time dependent, i.e. $\vec{F} \neq f(t)$. The set of solutions one obtains from the time dependent Schrödinger Equation in this special case is known to be separable such that:

$$\Psi(x,t) = \phi(t) \cdot \theta(x) \tag{2.4}$$

Where $\phi(t) = e^{-i\frac{E}{\hbar}t}$ represents the phase description of the particle (with *E* being the total energy of the system) and where $\theta(x)$ is the spatial equation to describe the position of the particles. The above can be substituted back into the Schrödinger Equation:

$$\widehat{H}\,\theta(x) = E\,\theta(x) \tag{2.5}$$

One now needs to find the set of '*n*' wavefunctions, $\Psi_n(x)$, that fit into this equation such that applying the Hamiltonian on the wavefunction returns the original wavefunction and produces constants called the eigen values, E_n. In this case the eigenvalues are the allowed energies of the particle(s).

$$\{\Psi_n(x)\} \leftrightarrow \{E_n\} \tag{2.6}$$

Wavefunctions that describe the electronic motion that will retain their shape but provide eigenvalue constants consist of exponentials or sine/cosine functions. The solution to the equation of motion to describe the particles can be written as:

$$\Psi_n(x,t) = \theta_n(x)\, e^{-i\frac{E}{\hbar}t} \tag{2.7}$$

There are some special properties for the set of wavefunctions $\{\Psi_n(x)\}$ that satisfy the Schrödinger Equation. They must all be orthonormal to each other such that:

$$\int_{-\infty}^{\infty} \theta_n{}^*(x) \cdot \theta_m(x)\, dx = 0, if\ n \neq m \tag{2.8}$$

This set of eigenfunctions must also have completeness, meaning any function, *f*, that satisfies the conditions of a wavefunction can be rewritten as a linear combination of other functions, θ_n,

multiplied by a scalar value coefficient, c_n. The functions can be solved for in Equation 2.9 and are simplified in Equations 2.10 and 2.11. The set $\{c_n\}$ must exist and be unique.

$$f(x) = c_0\theta_0(x) + c_1\theta_1(x) + c_2\theta_2(x) + \cdots\ c_n\theta_n(x) \tag{2.9}$$

$$f(x) = \sum_{n=0}^{\infty} c_n\,\theta_n(x) \tag{2.10}$$

$$c_n = \int_{-\infty}^{\infty} \theta_n{}^*(x) \cdot f(x) \tag{2.11}$$

Using the conservative system assumption from Equation 2.4, one can consider this as a subset of the full solutions to the Schrödinger Equation where $\Psi_n(x,t) = \ \theta_n(x)\ e^{-i\frac{E}{\hbar}t}$. It must also be true that any linear combination of these wave functions, $\Phi(x,t)$, is also a solution to the Schrödinger equation:

$$\Phi(x,t) = c_0\, e^{-i\frac{E_0}{\hbar}t}\ \theta_0(x) + c_1\, e^{-i\frac{E_1}{\hbar}t}\ \theta_1(x) + \cdots + c_n\, e^{-i\frac{E_n}{\hbar}t}\ \theta_n(x) \tag{2.12}$$

This is known as a superposition of states, and this combination is no longer stationary and moves in time. The probability distribution will no longer cancel out the time terms from the complex conjugate.

If the system (a molecule in this case) now interacts with a resonant light wave for one of its allowed transitions, a calculation for the interaction between the electric field of the light wave with the molecule is needed using Rabi's solutions mentioned in Section 1.4. Initially, the molecule can be described using just Coulomb's forces in the Hamiltonian of the Schrödinger equation, $\widehat{H}_{molecule}\Psi_{molecule} = E\ \Psi_{molecule}$, and yields stationary state solutions. A pulse of light can then be applied with electric field strength, E_0, and frequency, ω_{Light}, from t=0 to the

pulse duration, t=t_{pulse}. After the light is turned off, the molecule will return to $\widehat{H}_{molecule}$ over time, but at t_{pulse}, the wavefunction will be in a superposition state described in Equation 2.13, where one can calculate the coefficient values that account for the population of the molecules within each state. In a simplified case using a two-level system (Figure 2.2), the system at t=0 is assumed to be in the ground state, E_0. Note that, in reality, multiple states will be occupied at a given bulk temperature.

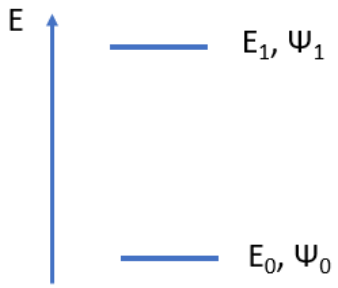

Figure 2.2: Simplistic two-level energy diagram with accompanying wavefunctions for describing the superposition state created in 3WM.

As light, $\frac{E_1-E_0}{\hbar} = \omega_{Light}$, resonant with the energy difference between the two states enters the system, the superposition state at the later time, t_{pulse}, can be described when the light is turned off.

$$\Phi(x, t_{pulse}) = c_0(t_{pulse})\,\Psi_0(x,t) + c_1(t_{pulse})\,\Psi_1(x,t) \qquad (2.13)$$

Through Rabi's equations, the average energy, $\langle H \rangle$, at time t is described by Equation 2.14 and the superposition state can be rewritten as Equation 2.15, knowing that the coefficients must be sinusoidal in nature, normalizing *via* $\cos^2(\theta) + \sin^2(\theta) = 1$, and using Euler's equations.

$$\langle H \rangle(t) = |c_0(t)|^2 E_0 + |c_1(t)|^2 E_1 \tag{2.14}$$

$$\Phi(x, t_{pulse}) = \cos\left(\frac{\Theta}{2}\right) \Psi_0 - i \sin\left(\frac{\Theta}{2}\right) \Psi_1 \tag{2.15}$$

Where $\Theta = \Theta_{Rabi}$ is called the Rabi flip angle and ω_{Rabi} is called the Rabi frequency, which is the rate at which energy is exchanged between the light and molecule. These are defined in Equations 2.16 and 2.17. ⟨μ⟩ is the transition dipole moment and is affected by the sign of the electric dipole moment vector component used in a transition. **E** is the electric field strength of the pulse of light interacting with the molecules.

$$\Theta = \omega_{Rabi} \; t_{pulse} \tag{2.16}$$

$$\omega_{Rabi} = \frac{\langle \mu \rangle \mathbf{E}}{\hbar} \tag{2.17}$$

Figure 2.3 shows a plot of Equation 2.17 which oscillates at the Rabi frequency as the light pulse interacts with the system and results in a smooth transition between states. As the light interacts with the system, the wave function can be described by the linear combination of the two state's wave functions. At certain points, it appears as if the light never interacted with the system, which is not intuitive in the classical sense.

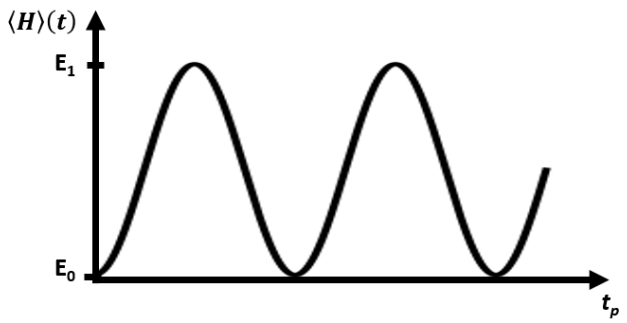

Figure 2.3: Energy of the superposition state as a function of light pulse duration follows a sinusoidal shape described by Rabi's equations where the contribution of each energy level's scalar coefficient will change smoothly. The system oscillates between the two energy levels of Figure 2.2 at the Rabi frequency.

Important points that can be used as tools for quantum manipulation can be defined along the curve seen in Figure 2.4. Note that in practice, these curves are not perfect and will also have dampening effects from dephasing due to collisions as the length of t_{pulse} is increased.

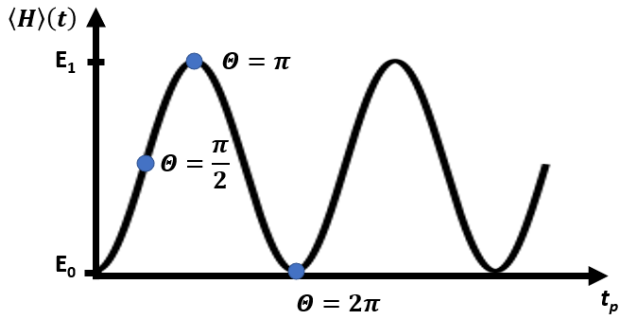

Figure 2.4: The important points along the Rabi cycle curve correspond to specific Rabi flip angles. As the length of a pulse of light is extended, a molecule will transition through the energy levels smoothly, being in a superposition state of the two.

When $\Theta = \pi$, the population in the first wave function (lower energy state) becomes zero, and the system is defined to exist only in the upper energy state. Equation 2.15 then becomes:

$$\Phi\left(x, t_{pulse} \rightarrow \text{"}\pi\text{"}\right) = \cos\left(\frac{\pi}{2}\right)\Psi_0 - i\,\sin\left(\frac{\pi}{2}\right)\,\Psi_1 \tag{2.18}$$

$$\Phi\left(x, t_{pulse} \rightarrow \text{"}\pi\text{"}\right) = -\Psi_1 \tag{2.19}$$

This is referred to as a 'π – pulse' and such a pulse completely transfers any population from the state to another state. This is also known as a 'system inversion'. In this way, no coherent emission is generated (the probability distribution following the treatment will be stationary). When $\Theta = 2\pi$, this is called a '2π – pulse' and the net result appears like the system absorbed no energy. This is also called 'self-induced transparency'. When $\Theta = \frac{\pi}{2}$, this is called a '$\frac{\pi}{2}$ – pulse' which leaves the system at a halfway point between the two energy states defined by a time-dependent superposition state of the two wavefunctions. To measure a signal using Fourier transform rotational spectroscopy, a pulse of light is applied at the proper pulse duration to achieve a $\frac{\pi}{2}$ – pulse to create this time-dependent solution. In turn, this will yield maximum signals strengths from the molecules by creating maximum coherence of the system and a time dependent solution. As this solution evolves in time as an oscillating electric dipole moment, the molecule will emit light yielding a free induction decay that can be collected.

To generate a chiral signature, these special Rabi conditions and the polarization of the electric field of light are used. The 3WM process using these conditions can be described with Bloch sphere diagrams similar to those shown in the works of Grabow,[3] Pate and Pratt[6] and an article in the *Annual Review of Physical Chemistry* by Domingos *et al*.[7] More detail is provided in the next section, but in short, the procedure of Lobsiger *et al*[4] is followed, which provides previous results from the Pate group and collaborators:

1. Apply a $\frac{\pi}{2}$ - pulse to generate coherence between an initial and second rotational energy state incorporating one electric dipole moment component and one mutually orthogonal electric field polarization.
2. Apply a π - pulse to transfer the generated coherence to now be between the initial state and a third state, incorporating a second electric dipole moment component and mutually orthogonal electric field polarization in an orthogonal propagation direction.
3. Detect the emission generated at the sum or difference frequency that is forced to incorporate the final electric dipole moment component, final electric field polarization, and detected along the same propagation direction as the $\frac{\pi}{2}$ - pulse (but emits radially).

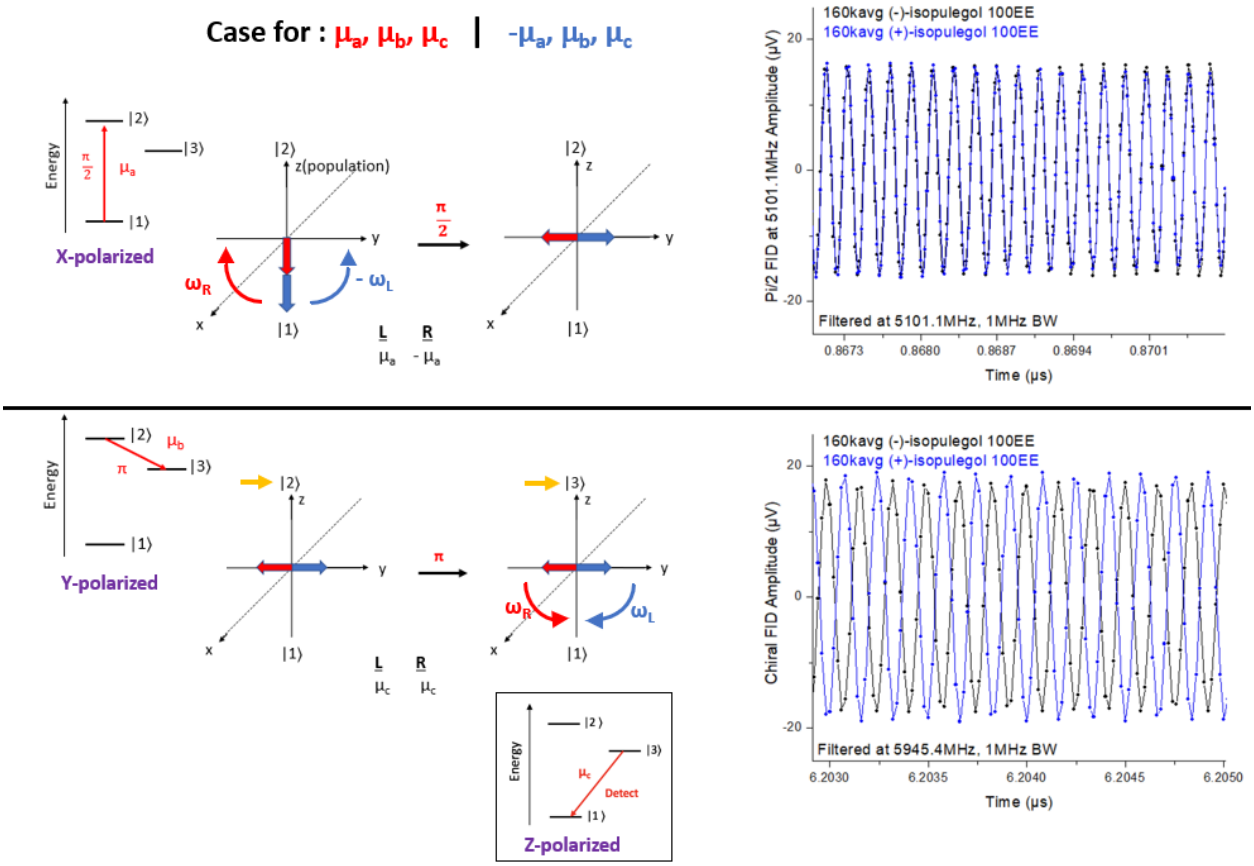

Figure 2.5: A pulse sequence of 1) $\frac{\pi}{2}$-pulse, X-polarization, a-type transition followed by 2) π-pulse, Y-polarization, b-type transition, and a third wave at the c-type transition frequency is generated with Z-polarization. The Bloch sphere diagrams, where the z-axis represents population difference shows the transition of the population between two energy states through the Rabi cycles. Population is initially in state $|1\rangle$ with population vectors in red and blue (stacked for clarity) to represent two enantiomers. Following the procedure and Rabi equations, a chiral signature seen as a change in phase of 180° is observed from the difference in one of the electric dipole moment vector components. Separately measured spectra for the two enantiomers are shown to illustrate a traditional rotational spectroscopy measurement versus using the 3WM technique to see a chiral signature.

In Figure 2.5, the z-axis of the Bloch sphere diagram represents the population difference between two energy states given in Dirac notation as $|1\rangle$ and $|2\rangle$. Initially, both enantiomers (shown in red and blue) have populations only in the ground state (vectors shown on top of one another for clarity). In reality, there would be many molecules present and there would be some

amount in both states for a given temperature. For this example, however, it is assumed that all population is in the ground state, $|1\rangle$. A $\frac{\pi}{2}$ - pulse polarizes the initial population and brings the populations into optimal coherence (Rabi flip angle of $\frac{\pi}{2}$ brings the population difference vector into the X-Y plane), in a superposition state between energy states $|1\rangle$ and $|2\rangle$ with approximately equal populations in each given in Equation 2.14. In this case, the differing electric dipole moment vector component is assumed to be μ_a, and the first transition is an a-type transitions such that the two population vectors rotate in opposite directions onto the X-Y plane by following Equations 2.16 and 2.17 where the Rabi flip angle (and Rabi frequency) would have opposite sign for this transition. An example of the experimentally measured free induction decay (FID) using traditional rotational spectroscopy of this initial excitation with (+)- and (-)-isopulegol yields the result that the two enantiomers emit in phase and cannot be distinguished. The opposite sign of the μ_a component negates the direction of rotation of the population vector on the Bloch sphere diagram yielding no net difference.

Directly after the $\frac{\pi}{2}$ - pulse, a π - pulse is applied for a b-type transition to transfer coherence from being between states $|1\rangle$ and $|2\rangle$ to be between states $|1\rangle$ and $|3\rangle$. The system, in a time-dependent superposition state, will now coherently emit light at the last transition connecting states $|1\rangle$ and $|3\rangle$. Here, the electric dipole moment component of the c-type transition, μ_c, has the same sign between the enantiomers, and the Rabi frequencies would therefore have the same sign. This causes the rotation to be in opposite directions so that it is no longer canceled out by the opposing sign of the electric dipole moment component. This final

change in sign is signified by the opposite phase of the FID of the system; the emission will have opposite phase and therefore give a chiral signature.

It is important to note that the electric field polarizations of the first two pulses must be orthogonal and the resulting chiral emission will have the last mutually orthogonal polarization that is forced upon the molecules by constraining the propagation direction of the two excitation pulses and their polarizations. The electric field polarization of the chiral emission is then set by the measurement geometry of two excitation pules. The emitted light wave is, by definition, a transverse wave, so by setting the electric field polarizations of the three waves, the direction that the emitted wave can travel is limited. The wave vector of light must have propagation direction, electric field polarization, and magnetic field polarization mutually orthogonal. Following the description provided in Figure 2.5 for the transition cycle and electric field polarizations, Figure 2.6 displays a typical measurement geometry and the produced wave vectors.

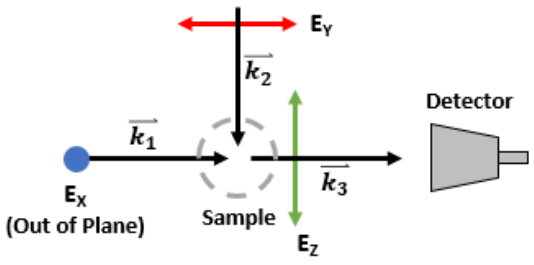

Figure 2.6: Measurement geometry and wave vectors, $\vec{k}$, of the three waves in the experiment including their electric field polarizations, $\mathbf{E}_X$, $\mathbf{E}_Y$, $\mathbf{E}_Z$. The emitted wave is forced in the direction of the initial drive pulse.

Accounting for the electric field polarization of the three waves being mutually orthogonal, the direction of the emitted wave is not the same as the direction of a typical 3WM phase-matched wave laser experiment. This leads to a phase mismatch vector that reduces the intensity of the emitted chiral emission, shown in Figure 2.8. However, this phase mismatch is related to the second wave and can be reduced by simply using a lower frequency coherence transfer pulse where the magnitude of a wave vector is proportional to the frequency of light, $|\vec{k}| \propto \nu_{light}$, summarized below in Figure 2.7.

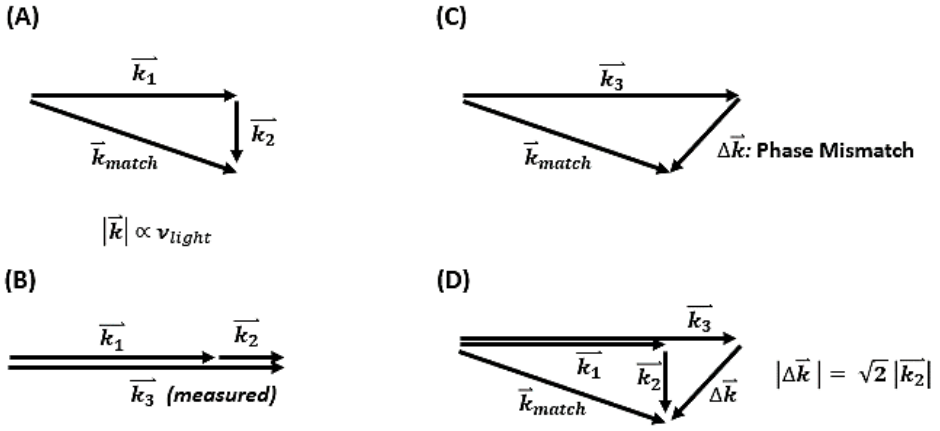

Figure 2.7: Phase matching restrictions on the 3WM measurements. (A) The two wave-vector excitation pulse set-up for 3WM and the phase matching vector where the signal would typically propagate in a sum frequency generation 3WM laser experiment. (B) Due to the constraints by electric field orthogonality of the experiment, the measured wave must propagate in the direction of $\overrightarrow{k_1}$. (C) The phase mismatch vector is the vector between the phase matching vector and the sum frequency vector. (D) the phase mismatch vector and $\overrightarrow{k_2}$ vector are related, and by reducing the frequency of $\overrightarrow{k_2}$, the phase mismatch will be reduced and allow for the generation of stronger 3WM signals.

In summary, by creating this time-dependent superposition of states and tailoring the excitation pulses to meet coherence creation, coherence transfer, and both of correct propagation direction and electric field polarization, it is now possible to distinguish the emission of an enantiomeric pair by rotational spectroscopy. This is made possible since the three-

dimensional structure of the molecule interacts with the three polarizations of the electric field of light and enantiomers in a chiral environment will act differently.

One challenge that looms over the technique is that while the absolute phase of each enantiomer can be theoretically calculated from these simple equations and knowing the electric dipole moment, it is difficult to measure the absolute phase experimentally. Electronics add frequency-dependent phase shifts and calibrating for all such effects or adding potential relative markers is difficult, in practice. To this point, it is not clear in the literature that any group has achieved this absolute phase calibration and therefore a reference sample of known absolute configuration is needed to determine which enantiomer is present in excess. If this problem were solved, 3WM rotational spectroscopy could provide a measurement of absolute configuration with no reference sample, revolutionizing the analytical bottleneck in areas like chiral drug design.

2.3: A *Literature Review of Three-Wave Mixing Rotational Spectroscopy*

The 3WM rotational spectroscopy technique is still relatively young, having first been done experimentally in 2013.[1, 2] As such, there is only a small collection of published literature on the technique, so a brief literature review up until present results is provided to aid in understanding the technique's progression. 3WM rotational spectroscopy is a gas phase technique that incorporates previous concepts of sum/difference frequency generation from much earlier work done in the IR and visible frequencies of the electromagnetic spectrum in liquid surfaces with an example by M. A. Belkin *et al* published in *Physical Review Letters* in 2000.[8]

However, as described broadly in the previous section, 3WM rotational spectroscopy has very tailored pulse propagation directions and electric field polarizations which that presents additional phase matching challenges.

In 2012, Eizi Hirota published a paper in the *Proceedings of the Japan Academy, Ser. B* that theoretically described a method in which a chiral signature could be detected using a three-level system of rotational energy levels in the microwave regime.[9] In 2013, this theory was tested experimentally and published in two papers by David Patterson, Melanie Schnell, and John Doyle in *Nature*[1] and by Patterson and Doyle in *Physical Review Letters*.[2] The second was really the first published paper using proper 3WM rotational spectroscopy. In the first, the authors used a DC field to achieve the rotational state mixing using the Stark effect and was not rotational state manipulation by resonant pulses via Rabi conditions. This first result detailed their measurement using the small chiral molecule, 1,2-propanediol. A cryogenic buffer gas cell was used to cool the sample. Large mirrors were used to couple light into the chamber and excite molecules through two spatial modes of the mirrors and allow for orthogonal polarization. Microwave light was sent into the aperture of one of the mirrors to apply the $\frac{\pi}{2}$ - pulse, and after, the mirrors had a rapidly changing voltage applied to them to generate a low-frequency electric field for the π - pulse. Their results are shown in Figure 2.8.

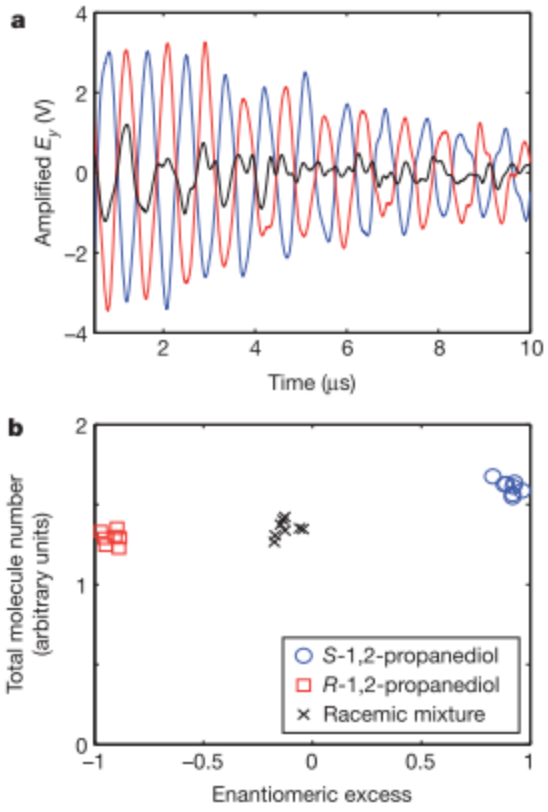

Figure 2.8: The final results from Patterson *et al.*[1] showed the enantiomers of propanediol could be distinguished via 3WM rotational spectroscopy as observed by the difference in phase of the chiral emission in the top figure (S-1,2-propanediol in blue, R-1,2-propanediol in red, racemic 1,2-propanediol in black). Measurement reproducibility is presented in the bottom plot.

Along with these results, Patterson and Doyle's paper provides additional descriptions of the measurement apparatus used in the experiments, including a microwave pulse and low-frequency pulse generated from electrodes. The absolute configuration differentiation for another molecule, 1,3-butanediol was also presented. The reproducibility in their measurements of a racemic mixture and 2% excess of the S-1,2-propanediol is provided below in Figure 2.9. Note that each data point represents the collection of 5 million FIDs and that no source of normalization through an achiral measurement was used to account for the influence of experimental conditions on the chiral emission intensity, which may suggest why the

reproducibility of their measurements looks poor. The data in this plot has a large scatter suggesting the measurement precision is an issue, which is not ideal for analytical chemistry.

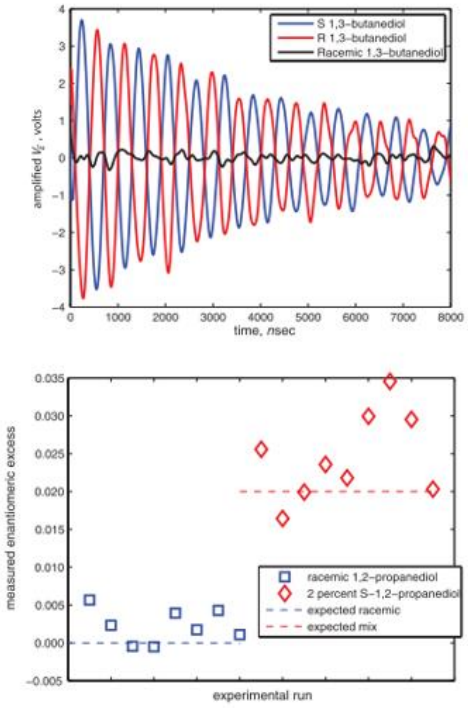

Figure 2.9: Results from Patterson *et al*.[2] Top: the chiral emission is shown to have opposite phase for each enantiomer of 1,3-butanediol while a racemic mixture produces no net emission. Bottom: Measurements on the enantiomeric excess were done to show reproducibility in the measurement and ability to measure small changes in EE by using a 2% excess of S-1,2-propanediol. Each data point is the average of 5 million FIDs and only 90 seconds of experimental time.

Jens Grabow followed up on these two papers in 2013 with more detail on the theoretical principles behind the technique and also used the nomenclature common in the NMR field, namely the π and $\frac{\pi}{2}$ - pulses and Bloch sphere diagrams.[3]

In 2014, these previous groups published a paper in Angewandte Communications[10] demonstrating they could perform the measurement introducing the sample with a supersonic expansion, a wave horn antenna to broadcast the coherence pulse, RF electrodes on the horn to

broadcast the coherence transfer pulse, and a second wave horn tilted at 45° to capture the chiral emission with the final polarization of electric fields. Additionally, they showed that the experiment could be done on multiple conformers of carvone in the pulsed jet without any issues arising from the double resonance nature of the experiment. Each of two conformers of carvone could be measured separately and were compared in their absolute configuration determinations and EEs. In the same year, Patterson and Schnell published a paper in PCCP Perspective[11] exploring some of the newer techniques in AC and EE determinations for chiral analysis. For 3WM they described their works using a cryogenic buffer gas cell and a supersonic expansion from a modification of their chirped-pulse FTMW spectrometer (both set-ups using electrodes to generate the low-frequency coherence transfer pulse.

In 2015, there were a few papers published. Shubert *et al* (Patterson, Schnell, and Doyle)[12] used the set-up with a supersonic expansion to claim they could calibrate their instrument to measure the absolute phase of each enantiomer and forego the need of a reference sample for an AC assignment by directly comparing their results to a theoretical prediction. Their work involved accounting for the timing of each excitation pulse and the chiral emission through the individual electronics and cables of the spectrometer. Dispersion effects from the various components altered how the final phase of the enantiomers was detected compared to what it should be after the completion of the coherence transfer pulse. These absolute phase measurements reported large errors due to the sum of the components' dispersion effects. It was noted that additional work is needed to ensure that the technique is generalized for other molecules and systems. This group published a second paper[13] later that year showcasing the AC and EE determination of one component of a complex mixture of essential oils (menthone in

peppermint oil), indicating this technique has an inherent strength over many techniques that require prior separation of mixtures.

The Pate group and collaborators in a paper by Lobsiger *et al.* in *The Journal of Physical Chemistry Letters*[4] provided an in-depth look at how one would optimize the 3WM measurements and examine the fundamental experimental quirks of the technique. They used two sets of wave horn antennae to better control the excitation pulses within the measurement and additionally used an arbitrary waveform generator to directly synthesize the excitation pulses for much higher phase stability and reproducibility within the measurements. A high sampling rate digitizer was used to directly record the chiral emission without any down sampling that had previously been done. The details for optimal pulse sequences to induce the largest population difference between the initial two states pumped were provided. The chiral emission was also detected on a transition using the largest electric dipole moment component to obtain stronger chiral emission. It was also noted that one would want the coherence transfer pulse to have low frequency to reduce the effects of phase mismatch in the experiments where pulse propagation direction and polarization restrictions cause spatial overlap problems when the frequency of the coherence transfer pulse is too high. Their experimental design is shown in Figure 2.10.

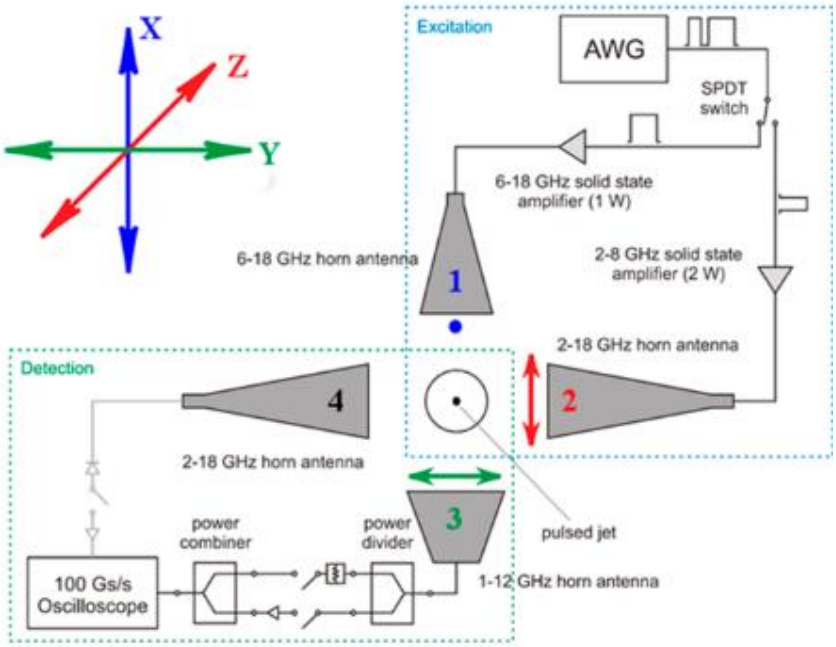

Figure 2.10: The Pate group and collaborators[4] use of a modified version of a chirped-pulse FTMW spectrometer to perform 3WM measurements with a supersonic jet expansion. Care was taken in the electric field polarization set-up, and high sampling/digitization rates of the arbitrary waveform generator and oscilloscope allow for direct synthetization and digitization of the pulses and emission.

In 2017, Sandra Eibenberger, Doyle, and Patterson published a paper in *Physical Review Letters*[14] with an intriguing look at 3WM by including an additional step. As before, the 3WM experiment was performed in a buffer gas cell but incorporated an additional transition that allowed for the effective population or depopulation of one enantiomer in a rotational state. In this way, that it is possible to induce an EE within a rotational energy state itself (they report a 0.6% induced excess) which could be used in the future to separate enantiomers (for purification, for example) in a quantum dynamical way. Pérez *et al.* followed this study by using a supersonic jet expansion to rotationally cool the populations into their lower rotational states and achieved a state-specific enantiomer excess on the order of 6%.[15] Their procedure is shown in Figure 2.11

where additional transitions are also used to probe the enantiomeric excess as they sweep through the phase of their transition to induce the EE.

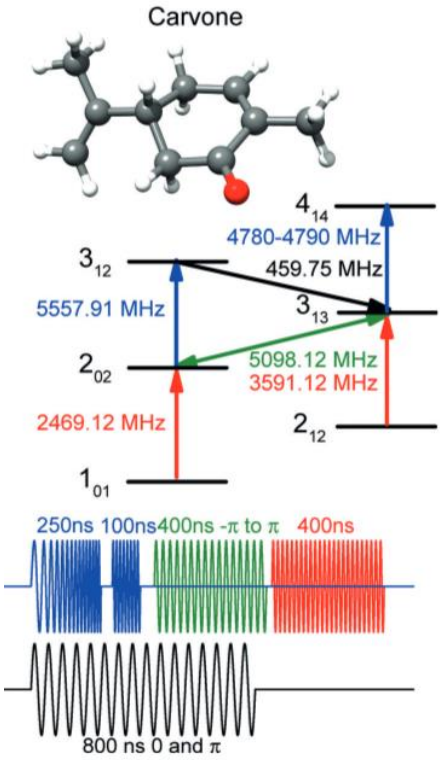

Figure 2.11: Figure depicted from Pérez *et al*.[15] Authors use additional phase/polarization controlled pulses to populate or depopulate a rotational energy state of one enantiomer (green transition). Transitions in red are used to probe the populations. Enantioenrichment of 6% in a rotational state is reported when using a supersonic jet expansion for rotationally cooling the molecules before the 3WM procedures.

David Pratt and Brooks Pate commented on these previous results with a *Highlights* paper.[6] They provided a figure adapted from Jens Grabow (provided as an adaptation in Figure 2.5) to describe the enrichment process with simplistic Bloch sphere diagrams. This is shown in Figure 2.12 where a final transition between states $|1\rangle$ and $|3\rangle$ is used to rotate the population vectors of each enantiomer in opposite directions.

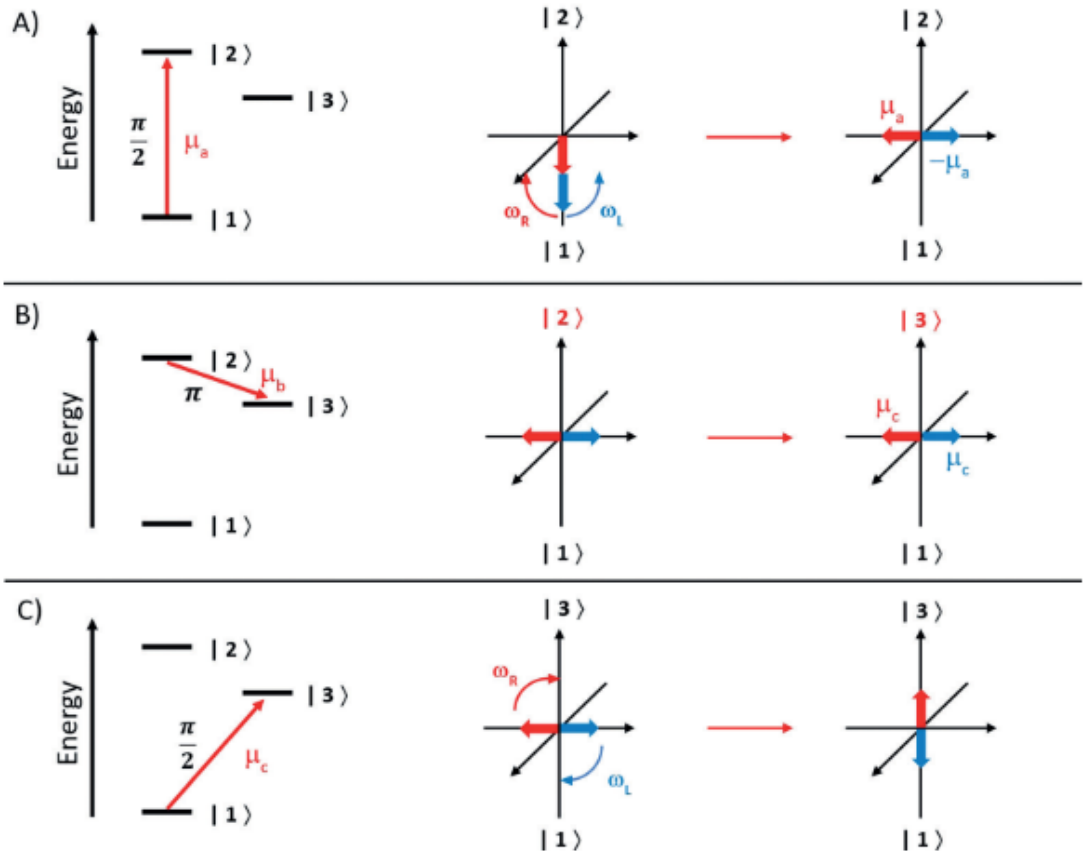

Figure 2.12: Figure from Pratt and Pate.[6] The 3WM process is described using Bloch sphere diagrams where the vectors represent the population difference between two energy states. After creating and then transferring coherence to generate a system that produces a chiral signature, the final transition is instead driven to continue rotating the population vectors to create single state enrichment of one enantiomer over another, which was demonstrated experimentally by Pérez *et al*.[15]

In 2018, Sérgio Domingos, Pérez, and Schnell published a review article in *Annual Review of Physical Chemistry*[7] to summarize the 3WM process and recent literature. They also note that a more robust method is needed to calibrate the absolute phase that was previously published and that for now, a reference sample is needed to determine AC. This paper provides a nice summary of the advancements made by the Patterson/Schnell/Doyle, and Pate research groups

towards the 3WM rotational spectroscopy technique. Later in 2018, Schnell and collaborators also did a measurement with an AC determination using the technique for pulegone, which was published in their paper titled *Structure Determination, Conformational Flexibility, Internal Dynamics, and Chiral Analysis of Pulegone and Its Complex with Water*.[16]

Kevin Lehmann provided theoretical insight into how spatial degeneracy influences 3WM and optimal ways to produce the strongest chiral signals in his paper published in *The Journal of Chemical Physics* in 2018.[17] He also provides an in-depth analysis of the theory of 3WM in a chapter within *Frontiers and Advances in Molecular Spectroscopy*.[5] In previous results, the degeneracy of M_J for measurements on molecules in the various rotational energy states was ignored. This degeneracy was calculated and shown to cause a reduction in the possible chiral emission signal. As the rotational energy level, *J*, increases, the population of molecules as a function of M_J is spread out over many states. Lehmann calculated that this will provide modest decreases in overall chiral signals where each state would have its own Rabi frequency such that optimizing for a $\frac{\pi}{2}$ - and π - pulse is done as a combination of all these states where each Rabi frequency would contribute to the overall experiment. In the high *J* limit, reductions of ~two thirds were predicted. Lehmann demonstrated that the optimal pulse sequence (using the P, Q, R notation [$\Delta J = -1$, $\Delta J = 0$, $\Delta J = +1$, respectively]) would likely not be a Q-Q-Q cycle where all three energy levels have the same value of J. The R-Q-P and P-Q-R cycles were predicted to work better for the 3WM technique as they consist of larger population differences, and these two cases provided similar results where the R-Q-P case yielded a slight favorability. Along with this, more discussion was provided for the phase mismatch that also reduces chiral signals. The phase mismatch comes about from using two excitation pulses over the molecular sample from

orthogonal directions with orthogonal electric field polarizations. This causes the chiral signal to prefer one direction (head to tail vector addition), yet the chiral emission is restricted by the wave vector having to point in another direction with the final orthogonal electric field polarization. By reducing the frequency of the coherence transfer pulse, the vectors, in the limit of this pulse going to DC frequency, would point in the same direction with reduced phase mismatch.

An additional paper on state-specific EE enrichment was also published from the Schnell group in 2018,[18] where they applied two 3WM cycles connected via a transition in the final state of the first cycle and initial state of the second cycle to place populations of one enantiomer into one rotational state and population of another enantiomer into another state. In the future enantiomers could then be separated by techniques like electrostatic deflectors or state-selective collision experiments following their initial procedure.

In 2019, the Schnell and Patterson groups showed that one could do 3WM techniques to measure the AC of a very subtle change in a molecules structure – that of chirality by isotopic substitution so long as a reference sample exists of known AC.[19] Their test molecule was (R/S)-benzyl-α-D_1 alcohol. A cryogenic buffer gas cell was used for the sample and most notable, a 3WM cycle with a 16 MHz coherence transfer pulse was used. This would suggest that the phase mismatch would be greatly optimized, but comparisons of the efficiency of the detection transition through single photon excitation versus 3WM was not reported.

Lastly, the most recent published work that includes 3WM is a minireview article in Chemical Science by Domingos, Pérez, Mark D. Marshall, Helen Leung, and Schnell.[20] Here, 3WM rotational spectroscopy was compared to the new chiral tag rotational spectroscopy technique[21]

that is currently under development by the Pate group. A 3WM set-up, shown in Figure 2.13, was used to determine AC with a reference sample and the EE measurement was achieved using a normalization scheme to measure an EE of 49.8 ± 5.1 EE. The authors compared this to their result from the chiral tagging measurement of 46.7 ± 0.2. The sample was prepared to be EE=47.2 ± 0.4, so the chiral tagging measurement was within experimental error. This paper highlighted two important points that will be discussed later. For one, the error involved in the 3WM experiment was much higher than the chiral tag experiment (or of typical errors in the most common technique – chiral chromatography). While this could be that they chose to measure their normalization signal on a separate gas injection, it was likely a case of signal fluctuation from the supersonic jet gas injection. Some statistical treatment to illustrate this effect is provided later in the next chapter. Secondly, the chiral signal shown in Figure 2.14 had an intensity that was only ~1% of what the direct transition used for normalization (same rotational transition) was measured to be. This is most likely a result of the phase mismatch problem mentioned previously where the coherence transfer pulse used had a frequency of 3057.15 MHz. This was much higher than frequencies used in the past literature. Typical efficiencies of the 3WM cycle are 20-30% (and in one case 50%) in measurements performed by the Pate lab group and will be discussed in the next chapter.

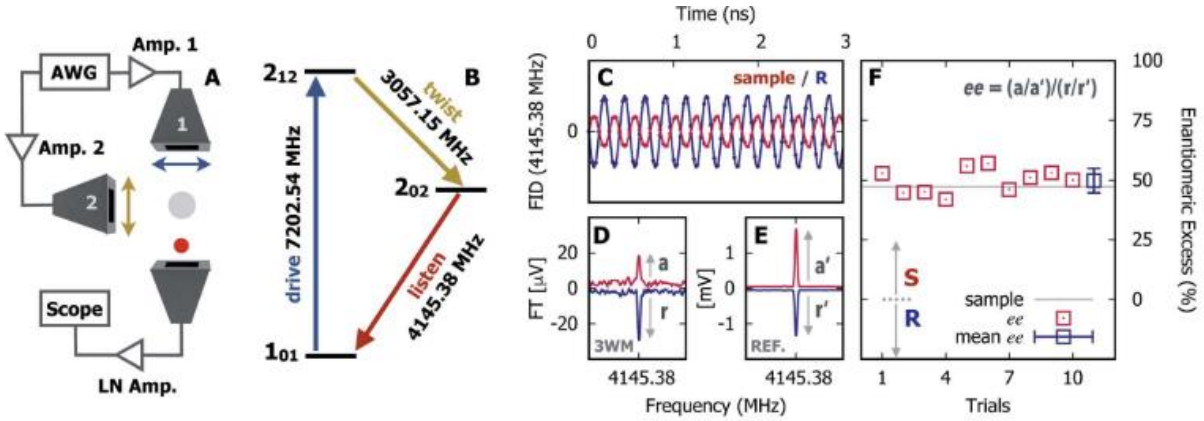

Figure 2.13: Figure depicted from Domingos *et al*.[20] The set-up on the left was used for 3WM measurements on the molecule styrene oxide with the measurement cycle shown in the middle. The AC was determined by comparison to a sample of known AC. EE was determined by using an achiral signal during the experiment for normalization. A resulting EE was measured to be 49.8 ± 5.1%.

Chapter 2 References:

1. Patterson, D.; Schnell, M.; Doyle, J. M., Enantiomer-specific detection of chiral molecules via microwave spectroscopy. *Nature* **2013,** *497* (7450), 475-7.
2. Patterson, D.; Doyle, J. M., Sensitive chiral analysis via microwave three-wave mixing. *Phys Rev Lett* **2013,** *111* (2), 023008.
3. Grabow, J. U., Fourier transform microwave spectroscopy: handedness caught by rotational coherence. *Angew Chem Int Ed Engl* **2013,** *52* (45), 11698-700.
4. Lobsiger, S.; Perez, C.; Evangelisti, L.; Lehmann, K. K.; Pate, B. H., Molecular Structure and Chirality Detection by Fourier Transform Microwave Spectroscopy. *J Phys Chem Lett* **2015,** *6* (1), 196-200.
5. *Frontiers and Advances in Molecular Spectroscopy*. Elsevier: 2018.
6. Pratt, D. W.; Pate, B. H., Chiral Imprinting in the Gas Phase. *Angew Chem Int Ed Engl* **2017,** *56* (51), 16122-16124.
7. Domingos, S. R.; Perez, C.; Schnell, M., Sensing Chirality with Rotational Spectroscopy. *Annu Rev Phys Chem* **2018**.
8. M. A. Belkin, T. A. K., K,-H. Ernst, L. Yan, and Y.R. Shen, Sum-Frequency Vibrational Spectroscopy on Chiral Liquids: A Novel Technique to Probe Molecular Chirality. *Physical Review Letters* **2000,** *85* (21).
9. Hirota, E., Triple resonance for a three-level system of a chiral molecule. *Proceedings of the Japan Academy, Series B* **2012,** *88* (3), 120-128.
10. Shubert, V. A.; Schmitz, D.; Patterson, D.; Doyle, J. M.; Schnell, M., Identifying enantiomers in mixtures of chiral molecules with broadband microwave spectroscopy. *Angew Chem Int Ed Engl* **2014,** *53* (4), 1152-5.
11. Patterson, D.; Schnell, M., New studies on molecular chirality in the gas phase: enantiomer differentiation and determination of enantiomeric excess. *Phys Chem Chem Phys* **2014,** *16* (23), 11114-23.
12. Shubert, V. A.; Schmitz, D.; Medcraft, C.; Krin, A.; Patterson, D.; Doyle, J. M.; Schnell, M., Rotational spectroscopy and three-wave mixing of 4-carvomenthenol: A technical guide to measuring chirality in the microwave regime. *J Chem Phys* **2015,** *142* (21), 214201.
13. Shubert, V. A.; Schmitz, D.; Perez, C.; Medcraft, C.; Krin, A.; Domingos, S. R.; Patterson, D.; Schnell, M., Chiral Analysis Using Broadband Rotational Spectroscopy. *J Phys Chem Lett* **2015,** *7* (2), 341-50.
14. Eibenberger, S.; Doyle, J.; Patterson, D., Enantiomer-Specific State Transfer of Chiral Molecules. *Phys Rev Lett* **2017,** *118* (12), 123002.
15. Perez, C.; Steber, A. L.; Domingos, S. R.; Krin, A.; Schmitz, D.; Schnell, M., Coherent Enantiomer-Selective Population Enrichment Using Tailored Microwave Fields. *Angew Chem Int Ed Engl* **2017,** *56* (41), 12512-12517.
16. Krin, A.; Perez, C.; Pinacho, P.; Quesada-Moreno, M. M.; Lopez-Gonzalez, J. J.; Aviles-Moreno, J. R.; Blanco, S.; Lopez, J. C.; Schnell, M., Structure Determination, Conformational Flexibility, Internal Dynamics, and Chiral Analysis of Pulegone and Its Complex with Water. *Chemistry* **2018,** *24* (3), 721-729.
17. Lehmann, K. K., Influence of spatial degeneracy on rotational spectroscopy: Three-wave mixing and enantiomeric state separation of chiral molecules. *J Chem Phys* **2018,** *149* (9), 094201.
18. Perez, C.; Steber, A. L.; Krin, A.; Schnell, M., State-Specific Enrichment of Chiral Conformers with Microwave Spectroscopy. *J Phys Chem Lett* **2018,** *9* (16), 4539-4543.
19. Satterthwaite, L.; Perez, C.; Steber, A. L.; Finestone, D.; Broadrup, R. L.; Patterson, D., Enantiomeric Analysis of Chiral Isotopomers via Microwave Three-Wave Mixing. *J Phys Chem A* **2019,** *123* (14), 3194-3198.

20. Domingos, S. R.; Perez, C.; Marshall, M. D.; Leung, H. O.; Schnell, M., Assessing the performance of rotational spectroscopy in chiral analysis. *Chem Sci* **2020,** *11* (40), 10863-10870.
21. Brooks H. Pate, L. E., Walther Caminati, Yunjie Xu, Javix Thomas, David Patterson, Cristobal Perez, Melanie Schnell, Quantitative Chiral Analysis by Molecular Rotational Spectroscopy. In *Chiral Analysis*, 2 ed.; 2018; pp 679-729.

Chapter 3: Quantitative Chiral Analysis by Microwave Three-Wave Mixing Rotational Spectroscopy

I'd like to acknowledge the work of Taylor Smart, a recent graduate from our group, and, Arthur Wu, a previous undergraduate student, as they took part in the building and optimizing the instrument as well as the weeks of data collection and analysis within this chapter.

3.1: *Introduction:*

Three-wave mixing rotational spectroscopy is a relatively new chiral spectroscopy with potential for absolute configuration (AC) and enantiomeric excess (EE) determinations and having minimum requirements on sample preparation and quantum chemistry calculations. While research has been done to show the capability of three-wave mixing rotational spectroscopy in addressing parts of chiral analysis, developing the technique into a universal, robust, analytical approach has lagged. The technique has the advantage of easily determining AC with a reference sample,[1-6] but the experimental uncertainties of determining EE is reported to be quite low on the order of ±5 EE or higher.[2, 3] This is not on par with that of chiral chromatography with uncertainties on the order of ≤ 2 EE, often with much lower uncertainty, on the order of ±0.1 EE, so long as eluted enantiomers can be completely separated.[7]

Additionally, the importance of normalizing the chiral signal by an achiral signal that represents the sum of enantiomer populations has not previously been shown in detail. Normalization is required due to the possibility of signal fluctuations over the course of measurements, primarily caused by fluctuations in the total amount of gas released in back-to-back pulsed jet sample introduction. The most recent 3WM result in the literature reported using direct excitation of the transition used to monitor the chiral signal on a separate sample injection in order to normalize for fluctuations every other data point.[8] However, the difference in each

sample introduction can cause this normalization to include significant amounts of error. The possibility of normalizing within the same sample injection is discussed herein with two methods.

In this work, calibration curves were measured, and the quantitative limits of precision and accuracy in EE determination by the technique were assessed. Stability of the calibration curve will be discussed, as will be its implications for EE determinations. The phase stability of the technique provides excellent confidence in AC determination with a reference sample, and this will be shown with many measurements along the calibration curves. However, as will be seen, due to current limitations on measurement precision, the practicality of the technique is heavily limited. Its inherent strength in handling complex mixtures without prior separation is the main advantage left to the technique. Measurements on commercial samples and complex essential oil mixtures with many components are used to show the capabilities of 3WM rotational spectroscopy.

3.2: *Methods*

3.2.1: *Sample Preparation and Gravimetric Determinations*

Isopulegol (2-isopropenyl-5-methylcyclohexanol) contains three chiral centers, and therefore eight possible stereoisomers, making it a more complex chiral molecule to investigate by standard instrumental approaches. It is commonly used in the commercial process of making menthol, a compound widely known in today's world.[9] (+) and (-) enantiomers were purchased from Sigma Aldrich and used without further purification. Samples of known enantiomeric excess with (-)-isopulegol in excess were prepared and quantified by gravimetric analysis: EE = 95.20,

89.90, 79.67, 54.06, 29.80, 9.84, 3.01. (+)-isopulegol was measured by chiral GC in the Certificate of Analysis (CoA) to have an enantiomeric ratio of 99.3%, (EE = 98.6). (-)-isopulegol was measured by chiral GC in the CoA to have an enantiomeric ratio of 100% (EE = 100).

Much the same, samples of menthone, a similar molecule with two chiral centers and with two low energy conformers present in high abundance, were prepared to construct a calibration curve for the two lowest energy conformers – Menthone A and Menthone B, with quantum chemistry on these conformers provided elsewhere.[10] (+)-Menthone, Analytical Standard, reported in the CoA as EE = 100 by chiral GC and (-)-Menthone, Analytical Standard, reported in the CoA as EE = 90 by chiral GC were purchased and used to prepare mixtures gravimetrically with EE = 75.25, 49.66, 24.33 with (-)-menthone in excess. These samples were purchased from Sigma Aldrich without further purification.

Various other samples were purchased and measured against the generated calibration curves to determine accuracy of the technique. Isopulegol was purchased from TCI America and measured to be EE = 74.7 with (-)-isopulegol in excess by in-house GC and chiral tag rotational spectroscopy methods. Isopulegol, Mixture of Isomers, 98% was purchased from Alfa Aesar and determined in-house to be EE ≈ 5 with (-)-isopulegol in excess. A commercial sample of Menthone, Mixture of Isomers, 98% was also used from Alfa Aesar and determined to be 98.04 EE by chiral tag rotational spectroscopy, in-house. All chemical mixtures and commercial samples are given in Table 3.1.

Leaf oil mixtures are used to show the power of 3WM rotational spectroscopy in determining AC and EE of individual components of a highly complex mixture of very similar

molecules without need of prior separation. Buchu leaf oil (distilled from the *Barosma betulina pillans* plant) is used as an ingredient in fragrances for its minty/fruity odor.[11] It is composed of compounds like the diastereomers menthone and isomenthone as well as other similar molecules like limonene, pulegone, buchu camphors, and numerous components of minor abundances including many thiol-containing compounds.[11] With this mixture, menthone could be measured directly in the commercial sample without doping. This oil has been analyzed by chiral GC and reported to have menthone (menthone and isomenthone making up ~40% of the mixture) with high enantiopurity (EE > 98), typical of naturally synthesized compounds, with the (+)-enantiomer in excess.[11] Sigma Aldrich (-)-isopulegol was also doped in Buchu Oil, Betulina to be 20% v/v as an additional test case. TCI Isopulegol was doped in a sage leaf oil (Dalmatian Sage FCC) mixture to be 20% v/v, and a gravimetrically determined to be EE= 71.6. Sage leaf oil is commonly used for food flavoring and contains an array of very similar monoterpene ketone compounds like thujone and camphor as well as many minor components, with well over twenty components in total.[12]

Table 3.1: *List of Chemical Samples Used in the Three-Wave Mixing Experiments*

Isopulegol (Sigma Aldrich), used to make calibration data points

- (+)-isopulegol, analytical standard, PN#: 59765, Lot#: BCBV5994; enantiomeric ratio = 99.3% by chiral GC
- (-)-isopulegol, analytical standard, PN#: 59770, Lot#: BCBV8724; enantiomeric ratio = 100% by chiral GC
- Buchu leaf oil, Betulina. PN#: W530345-Sample-K, Lot#: MKBQ2763V
    - (-)-isopulegol, 20% v/v doped in Buchu Oil, Betulina; gravimetrically determined to be 71.62 EE

Isopulegol (TCI America)

- Isopulegol, PN#M0320, Lot: G6Q2C-QD
- Sage Oil, Dalmatian FCC, 50% Thujone, PN#C:4119, Lot#: MD65852 (See *J. Agric. Food Chem.* 1999, 47, 5, 2048–2054)[12]
    - (-)-isopulegol, 20% v/v doped in sage oil; determined to be 74.7 EE by chiral tag rotational spectroscopy (in-house)

Menthone (Sigma-Aldrich), used to make calibration data points

- (+)-Menthone, analytical standard; PN#: 63675, Lot#: BCBV4512; enantiomeric ratio = 100% by chiral GC
- (-)-Menthone, analytical standard; PN#: 63677, Lot#: BCBR6463V; enantiomeric ratio = 95% by chiral GC

Menthone (Alfa Aesar)

- Menthone, Mixture of Isomers, 98%; determined to be 98.04 EE by chiral tag rotational spectroscopy (in-house)

Naturally Occurring Menthone in Buchu Leaf Oil (Sigma Aldrich)

- Buchu leaf oil, Betulina. PN#: W530345-Sample-K, Lot#: MKBQ2763V, Menthone EE > 98 (See *Phytochemical Analysis*, 1994, 5, 61-67)[11]

3.2.2: *Instrumental Components*

The microwave three-wave mixing spectrometer consists of commercial electronics and standard wave horn antennae. These electronics aid in the creation of two resonant excitation pulses of electromagnetic radiation with orthogonal electric field polarizations using ridged wave horn antennae. The pulses interact with molecules of interest in the gas phase that are produced by using a seeded molecular beam of neon (typically 0.1% mixtures of analyte in neon) with a supersonic jet expansion introduction source into vacuum. After exciting the molecules in the jet expansion with each of the tailored excitation pulses designed to create coherence and transfer that coherence to a third transition, there is subsequent detection of the free induction decay at a third frequency consisting of the last mutually orthogonal polarization. A schematic of the spectrometer used to perform this technique is shown in Figure 3.1. The theoretical details of the experiment have been described in detail within Chapter 2.

The spectrometer used an arbitrary waveform generator (AWG, Tektronix AWG70002A) with Python-generated pulse sequences of square-wave shaped pulses of single frequency light. An oscilloscope (Tektronix DPO72304DX) was triggered by the AWG and used to record and digitize the FID produced by the molecules present in the experiment directly at 50 GS/s without down-mixing.

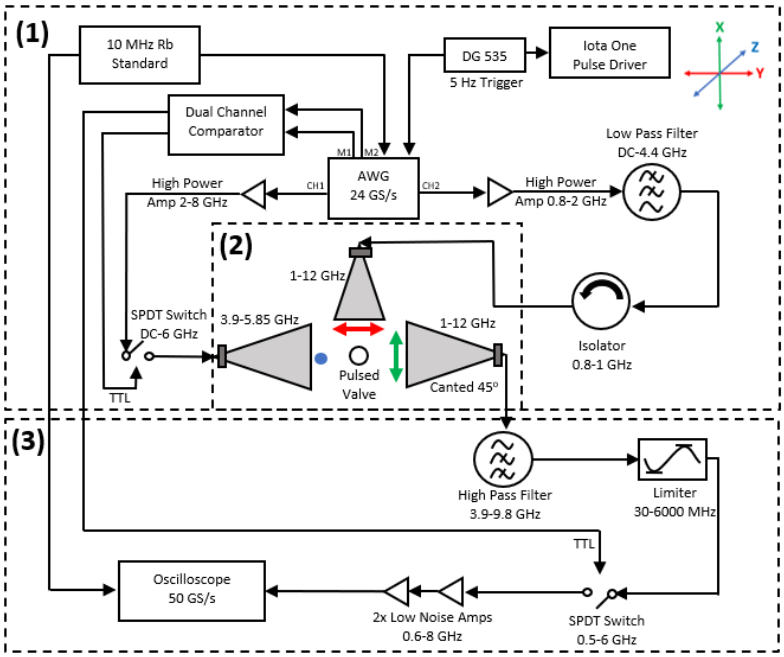

Figure 3.1: A top-view schematic for the microwave 3WM spectrometer is shown with the block diagram of the electrical components of the instrument. The spectrometer consists of **(1)** the microwave excitation generation, **(2)** the region of sample injection by seeded molecular beam pulsed jet expansion under vacuum plus molecular excitation/detection by wave horn antennae, and **(3)** the signal collection and digitization. The $\frac{\pi}{2}$ -, π -, and normalization transition pulses are generated by the AWG operating at 24 GS/s and each travel through a series of subsequent electronics to amplify the signal as well as reduce noise in the measurement. Switches are used to protect detection electronics from the high-power excitation pulses and reduce noise power from amplifiers. The free-induction decay was digitized by a 50 GS/s oscilloscope to capture signals directly without down mixing.

The AWG and oscilloscope are connected to a 10 MHz Rb frequency standard to allow for coherent signal averaging. A digital delay/pulse generator (DG535 Stanford Research Systems) is internally triggered for variable output pulses at a 5 Hz repetition rate and is used to first trigger an Iota One pulse valve driver (Parker-Hannifin) for sample injection into the vacuum chamber and secondly used to trigger the AWG 1.2 ms later to begin the measurement pulse sequence for interaction with the sample. The Iota One pulses a solenoid valve (Parker General Valve Series 9, 28 V), lifting an armature/poppet system for 700 μs and creating a supersonic jet expansion through a 1 mm hole orifice set in a sample holding baseplate. The baseplate functions as a

reservoir for liquid or solid samples and can be heated using an inserted cartridge heater to produce enough vapor pressure for optimal mixtures of analyte in neon.

3.2.3: *3WM Pulse Creation*

The $\frac{\pi}{2}$ - pulse is first generated by the AWG through Channel 1 at ~-7 dBm. This pulse travels through a high-power amplifier (Mini-Circuits, ZVE-3W-83+, 2-8 GHz) with a gain of +30-40 dB and then travels through a switch (RF Lambda RFSP2TRDC06G, DC-6 GHz). The switch is in place to allow the excitation pulse to pass and otherwise is blocked to attenuate additional amplified noise power during the detection window of the experiment. The pulse is then broadcast by a wave horn antenna (FXR, Inc Model H638A, 3.95-5.85 GHz) into the chamber; in this case, the pulse travels in the Y-direction with Z-polarization (seen in Figure 3.1).

The π - pulse travels through a separate circuit and is introduced by Channel 2 of the AWG. The pulse first travels through a 10 W high-power amplifier (Mini-Circuits, ZHL-10W-2G+, 0.8-2 GHz) with +40-49 dB gain. The pulse then travels through a low pass filter (Pasternack, PE87FL1014, DC-4.4 GHz) to protect the system from producing high power at higher frequencies that could damage the receiver. The inclusion of an isolator (DITOM Microwave Inc, D3I0810S) was deemed necessary to protect from amplified signals being able to travel back down the circuit from any reflections in the chamber, producing unwanted frequency components. The pulse is then broadcast from a wave horn antenna (Narda ATM, 1-12-440EM-NF, 1-12 GHz) traveling in the X-direction with Y-polarization.

3.2.4: *Molecular Interaction and Excitation Region*

The chamber must extend in three directions of the jet expansion region of space in a T-shape. This molecular excitation region is ~15 cm from each broadcasting face of the excitation horns as well as the receiver horn and is ~15 cm below the output of the pulsed nozzle sample introduction. The chamber is ~122 cm long and has ~53 cm diameter, which can be greatly reduced in size for more efficient measurements in the future since the region of interest is that where the two excitation pulses overlap. The chamber has one diffusion pump (Varian, VHS-10, 10" ASA) backed by a mechanical pump and booster combination (Edwards E2M40 and EH250).

The sample is produced in the gas phase by heating a sample holding reservoir baseplate at the end of the nozzle of a pulsed solenoid valve to generate sufficient vapor pressure. The sample is mixed with neon gas as a carrier with typical backing pressure of 15 psig. This mixture is delivered as an approximate 0.1% analyte in neon gas mixture. The chamber walls are covered in microwave absorbing foam (ECCOSORB AN-72 and ECCOSORB AN-75) backed with conductive sheet metal to reduce and prevent resonances and reflections from occurring in the chamber that could add unwanted frequency components to the measured signals.

3.2.5: *Free Induction Decay* (*FID) Detection*

The detection horn (Narda ATM, 1-12-440EM-NF, 1-12 GHz) is angled at 45^{o} to capture the polarization of the signals from the three-waving mixing chiral emission and the normalization transition emissions which have electric field polarizations that are orthogonal to one another. Having the wave horn angled results in a loss of power from the detected signals

(~factor of $\sqrt{2}$ in signal intensity). The signal passes through a high pass filter (Mini-circuits, VHF-3500+, 3.9-9.8 GHz). This protects the receiver, amplifiers, and the oscilloscope from low frequency pulses, namely the high power π-pulse. After the high pass filter, the signal travels through a limiter (VLM-63-2W+, 30-6000 MHz) to decrease any high amplitude waves, namely the $\frac{\pi}{2}$ - pulse, down to 5-10 dBm. This protects the next component. A SPDT switch (SPDTRF-ZFSWA2R-63DR+, 500-6000 MHz) follows and is used to heavily attenuate the transmission of the excitation pulses reaching the oscilloscope. This switch, as well as the previous switch on the $\frac{\pi}{2}$ – pulse transmission circuit, is controlled via a low voltage signal from the AWG passing through a TTL logic dual comparator box (Pulse Research Lab, PRL-350TTL-NIM). Marker channels on the AWG from Channels 1 and 2 are used to produce these signals. After the detection switch, a series of two low noise amplifiers (Mini-circuits, ZX60-83LN-S+, 0.5-8 GHz) each boosts the molecular signals by approximately +21 dB to raise the measured signals to detectable levels.

The frequency range of the experiment was limited to being used in the 800-2000 MHz range for the π-pulse and the ~3.95-5.85 GHz range for the $\frac{\pi}{2}$ - and direct normalization transitions. While this is the current limitation, electronics and wave horn antenna can easily be changed to fit another frequency range. To obtain the normalization and three-wave mixing signals, the time domain data obtained from the oscilloscope is processed and cut into sections based on the locations of the signals and exclude the excitation pulses. The FID of the 3WM signal and the direct normalization transition are selected after the excitation pulses and after the detection switch had opened. 1.5 μs of FID for the $\frac{\pi}{2}$ – pulse signal and 13 μs each for the chiral

and direct excitation FIDs are used. The $\frac{\pi}{2}$ – pulse FID is much less due to the requirement that the $\frac{\pi}{2}$ - and π-pulses must be relatively close together in time for optimal chiral signals.

3.3: *System Optimization*

3.3.1: *3WM Cycle Optimization*

In each of the three species measured, the same 3WM cycle of rotational transitions could be used, and each cycle is presented in Figure 3.2. For isopulegol, measured rotational constants were determined from broadband MRR spectra taken by a CP-FTMW instrument in-house. Measured rotational constants and theoretical electric dipole components for menthone are used from Schmitz et al.[10] Quantum chemistry calculated electric dipole moment vector components are presented in Table 3.2.

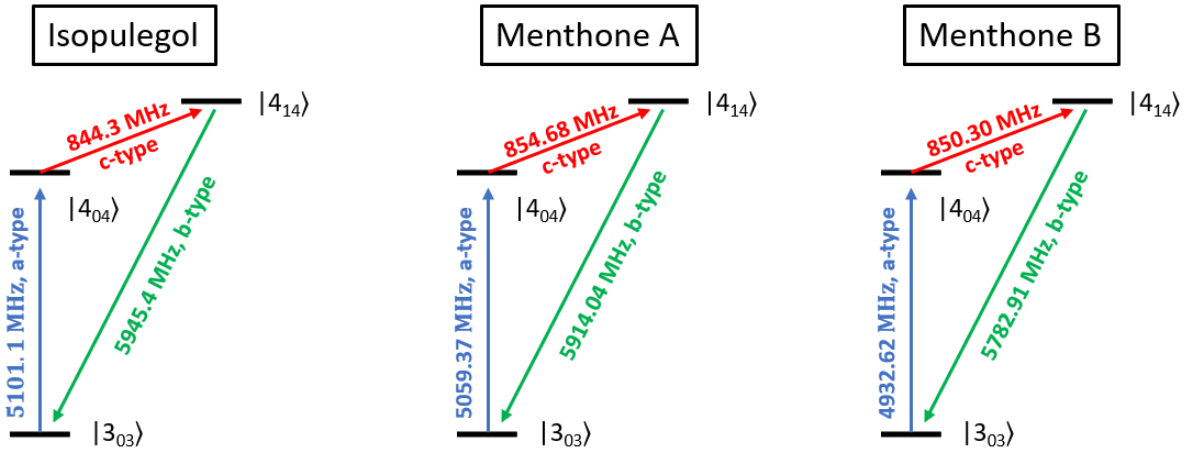

Figure 3.2: 3WM cycle energy diagrams. The same cycle of rotational energy levels was used for the three species of these experiments to limit any additional complications caused by M_J degeneracy in the transitions. The a-, b-, and c-type refer to the electric dipole moment allowed transition type.

Table 3.2: *Electric Dipole Moment Vector Components of Analytes*

Species	$\lvert\mu_a\rvert$ (D)*	$\lvert\mu_b\rvert$) (D)	$\lvert\mu_c\rvert$ (D)
Isopulegol	0.5	2.0	0.5
Menthone A	1.3	2.7	0.5
Menthone B	1.3	2.5	1.2

*Electric dipole moment calculated at B3LYP/6-311++G(d,p) level of theory[10]

Table 3.3: *Measurement Pulse Durations*

	$\frac{\pi}{2}$ - Pulse Duration (ns)	$\frac{\pi}{2}$ - Normalization Pulse (ns)	π-Pulse Duration (ns)
Species	a-type	b-type	c-type
Isopulegol	900	900	2000
Menthone A	800	500	1600
Menthone B	650	600	600

Each of the transitions for each species needed to be optimized for its respective $\frac{\pi}{2}$ - and π - pulse conditions within the experiment. The approach taken by Lobsiger *et al*. is also used in these experiments.[4] The pulse duration of the $\frac{\pi}{2}$ – pulse was varied and the intensity of the resulting FID was recorded as a function of the pulse duration. Nutation curves were then constructed to find the ideal pulse duration for a $\frac{\pi}{2}$ – pulse condition for the first excitation pulse, as is described using Rabi's equations in Chapter 2. The π - pulse durations were found by fixing the duration of the $\frac{\pi}{2}$ – pulse and varying the duration of the π - pulse while monitoring the intensity of the created chiral signal. The maximum intensity of the chiral signal signified optimization of the π - pulse. The optimized pulse durations used are given in Table 3.3. The nutation results for each transition are depicted in Figure 3.3.

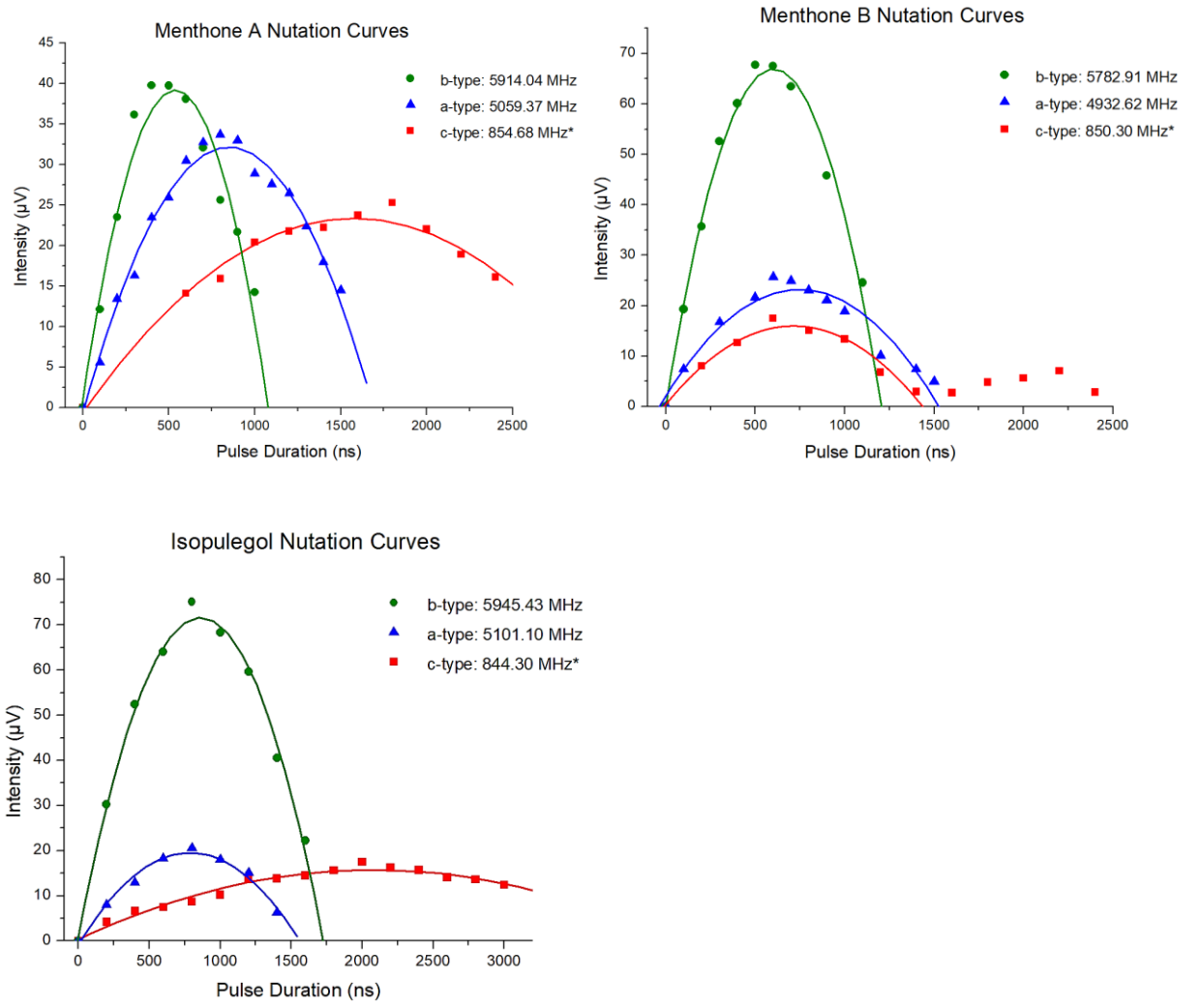

Figure 3.3: Nutation curves for the three test samples showing the optimization process for the two excitation pulses and additional normalization pulse used 3WM. The second excitation pulse is optimized indirectly by holding the first excitation pulse at its optimal pulse length, varying the second pulse length, and tracking the chiral signal intensity. The maximum intensity of the chiral signal being generated determines the second excitation pulse's optimal pulse length.

There is a general agreement in the comparison the optimized pulse durations and electric dipole moment vector components between the molecules with respect to Rabi's equations in Chapter 2. Longer pulse durations are needed for weaker dipole moment components to reach the optimal condition. However, the a-type, $\frac{\pi}{2}$ – pulse duration for

isopulegol relative to the menthone conformers appears to be an outlier, where one would expect the pulse duration for a 0.5 Debye dipole moment to require at least twice the duration as the 1.3 Debye dipole moments for Menthone A and B. One reason for this discrepancy could be caused by large amplitude motion in the hydroxyl, -OH torsion within isopulegol. A 2-D potential energy surface at B3LYPD3BJ/6-311G++(d,p) level of theory is depicted in Figure 3.4. The lowest minima used in these experiments is not well-defined and could lead to large amplitude motion of the hydroxyl torsion angle such that the wave function extends beyond the region near the equilibrium geometry. The hydroxyl group is the most polar in the molecule and this movement could lead to a change in the dipole moment direction such that the electric dipole moment vector components are less accurate.

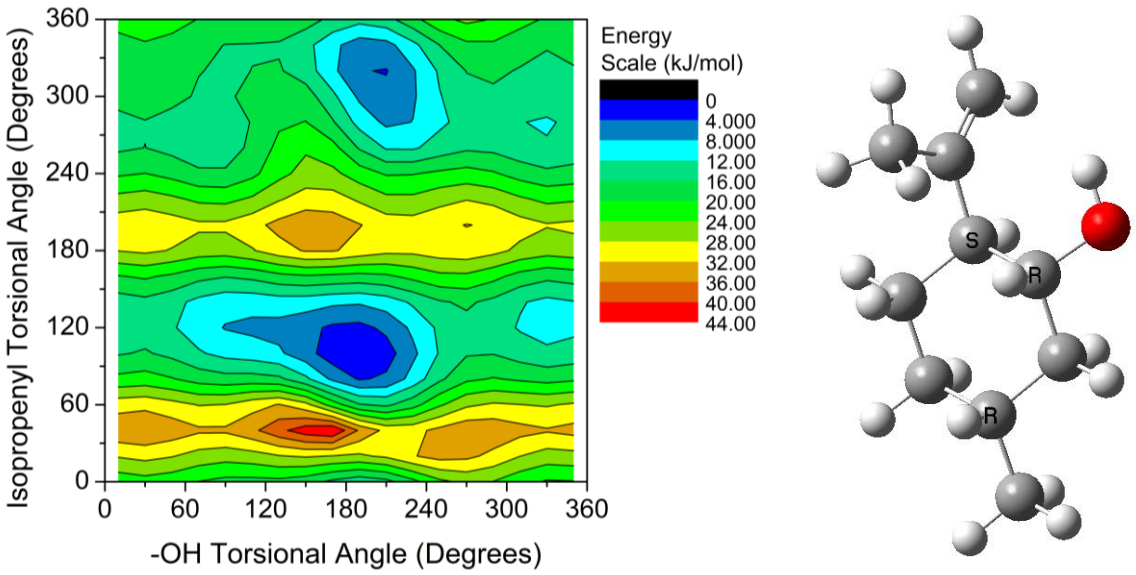

Figure 3.4: 2-D potential energy surface for isopulegol for rotation of hydroxyl and isopropenyl groups. The lowest energy minima used in these experiments does not have a well-defined minimum which could lead to large amplitude motion in the OH torsion that can change the dipole moment direction. Calculated at the B3LYPD3BJ/6-311G++(d,p) level of theory.

3.3.2: *Normalization of the Chiral Signal*

As was alluded to in Chapter 2, a signal representing the sum of the number densities of both enantiomers is needed for EE measurements. Normalization is also required in these experiments to account for fluctuations in the chiral signal; for instance, changes in the electric field throughout signal averaging can cause issues when comparing one chiral signal of a particular EE with another. Changes in backing gas pressure or the sample injection could also cause discrepancy among other fluctuations in back-to-back measurements with a pulsed jet nozzle. However, by normalizing the chiral signal by an achiral signal recorded during the same sample injection window, the possible changes over time can be ratioed out. This possible issue is demonstrated in Figure 3.5 using two different backing gas pressures in which the changes in

experimental conditions are correlated over time for each of the two signals. Figure 3.6 shows the results of a long series of measurements to assess the ability for normalization to lessen any fluctuations in the chiral signal and to determine how long the calibrations may be upheld. Measuring the same sample over two sample loadings and over multiple days, where the instrument was completely powered down, shows that the ratio still holds up remarkably well as is demonstrated by the flatness in Figure 3.6 and reduction of the coefficient of variation (CoV, standard deviation / mean * 100%) which is used to measure the spread in the measurements.

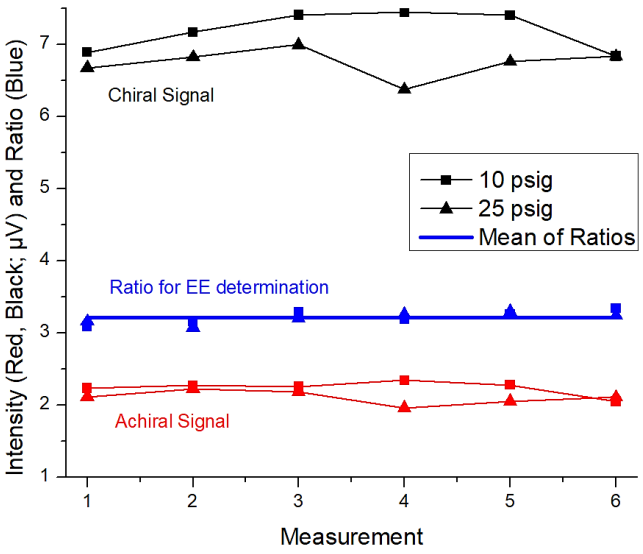

Figure 3.5: Individual chiral signals (black) each representing averaging 40,000 FIDs during the experiment are subject to changes in the supersonic jet expansion, backing gas pressure (as shown in this figure), electric field strength, etc.; however, normalizing the chiral signal by an achiral signal (red) measured during the same measurement effectively removes these changes per recorded measurement as seen in the ratio of the two signals (blue) after taking multiple measurements.

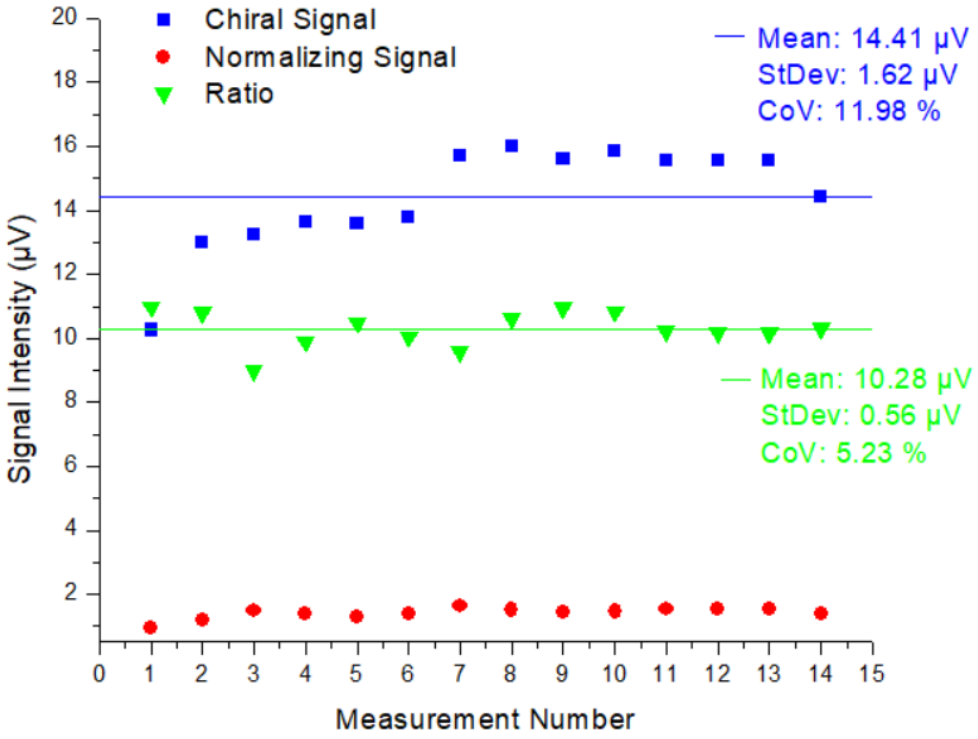

Figure 3.6: (-)-isopulegol measurement using Scheme 1 (data in appendix, Section 3.6). A 1.5 µs cut was used after the pi/2 pulse to use the FID from the 5101 MHz transition as normalization to the chiral signal. Each measurement was the resulting average of 40,000 FIDs and took ~2.2 Hr per measurement. Two sample loadings were used to collect this data. Measurements 1-6 on sample loading 1, and measurements 7-14 on sample loading 2. This took five days to complete, and measurements were completed during the following days: Day 1: 1-4; Day 2: 5-6; Day 3: 7-8; Day 4: 9-11; Day 5: 12-14. Even over two sampling loadings, electronics being warmed up and cooled down, the ratio takes out many of the possible issues as well as the slow drift noticed in the chiral signal.

There are options one can take for what achiral signal to use for the normalization to account for the possibility of other influences on the chiral signal. One option for a normalization scheme is to monitor the FID of the initial transition used to generate coherence in the system. In this way, one can separate the $\frac{\pi}{2}$ - pulse and π - pulse to allow for a short collection period for a signal to use for normalization. In Lobsiger *et al*., the authors show that for optimizing the 3WM experiment, one should use the strongest electric dipole moment component for the detection

transition for passive signal gain.[4] Additionally, since population difference is proportional to the frequency of the transition, it is best to use a higher frequency transition for the initial excitation pulse to generate a larger coherence that will be transferred to coherence detected in the final transition. Generally, the choice for these two excitation transitions can use weak electric dipole moment components because these are being manipulated with the ability to increase power being put into the quantum system with amplifiers. However, with these caveats, it is likely that the signal used in this normalization scheme would be weak. The benefit, though, for this scheme is that the signal used for normalization would be using the same molecules that eventually produce the chiral signal such that possible fluctuations caused by number density fluctuations in the pulsed jet would be effectively removed. With these fluctuations removed, one would expect amplifier noise to be the dominant contributor for fluctuations in the measured ratio of chiral to normalization signals.

Another logical choice for a normalization scheme would be to measure the transition used to monitor the chiral signal with a direct, single frequency measurement after the 3WM measurement but within the same gas pulse. Since this transition is using the strongest electric dipole moment component, these signals will be stronger than the chiral signal and any source of frequency dependent power fluctuations would be removed from the measured ratio. The measurement then consists of the 3WM process followed by a monitoring period for the chiral signal and then a second period for providing the achiral normalization measurement all within the same gas pulse. This does, however, sample different populations of molecules in the pulsed jet and may have fluctuations in the measured ratio caused by number density or temperature differences.

Two normalization schemes were tested to normalize the chiral signal by an achiral signal occurring during the experiments. Depicted In Figure 3.7, in the first scheme, excitation pulses are broadcast into the chamber with a delay of 3 μs between. This allows for the FID of the $\frac{\pi}{2}$ - transition to be collected (1.5 μs in length) and used as a normalization signal. After the π - pulse, there is a 40 μs long detection window for the chiral signal's FID to be recorded and 13 μs of this recording is Fourier transformed and used.

In the other measurement scheme, the 3 μs delay is removed to maximize the chiral signal and a direct, achiral transition at the chiral signal frequency is applied after the 40 μs recording but within the same gas injection. The FID of this 'normal' transition is also recorded for 40 μs and 13 μs of the recording is Fourier transformed to be used as a normalization signal. The results of each scheme will be discussed in the next section.

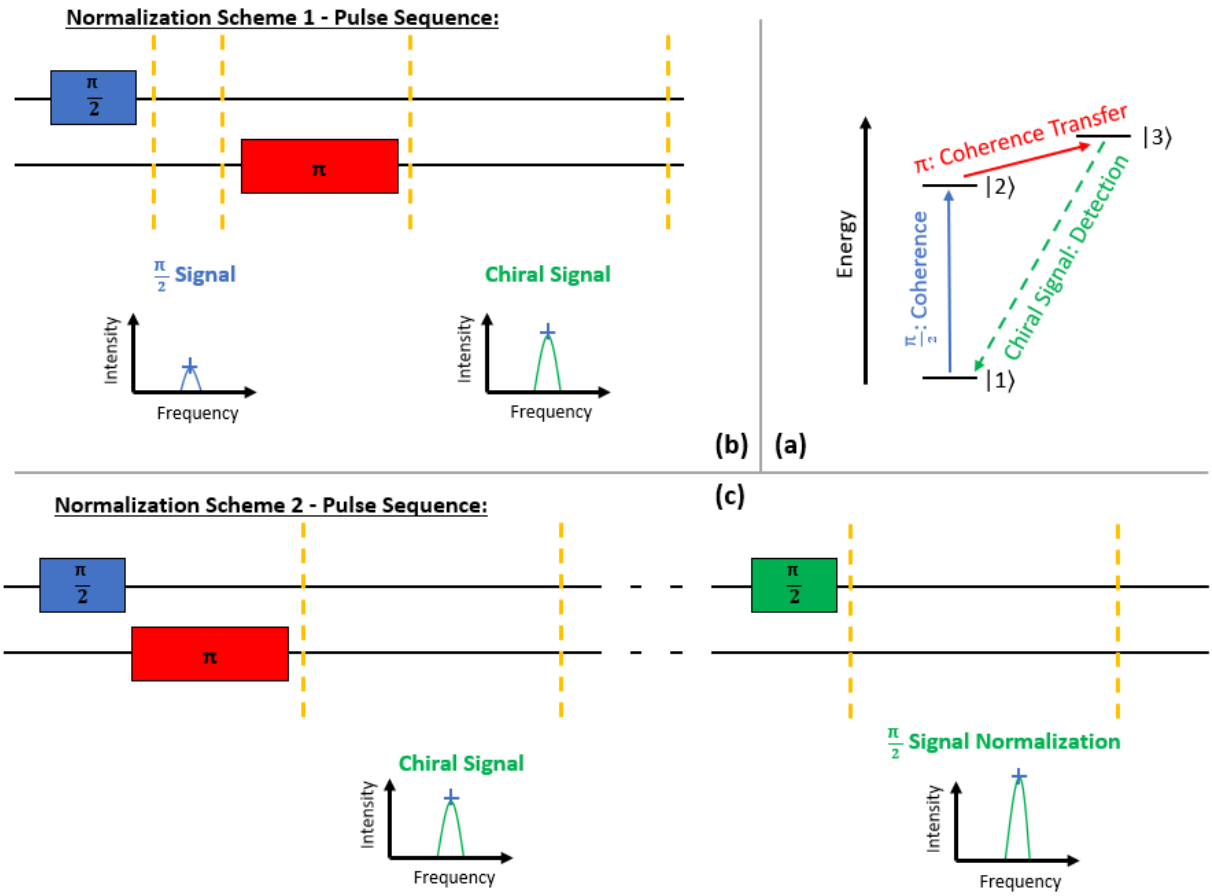

Figure 3.7: (1) The generic three level system for three-wave mixing demonstrating the initial two excitation transitions with pulse durations to meet the $\frac{\pi}{2}$ - and π - conditions followed by the detection of the chiral signal. **(2)** This normalization scheme uses the $\frac{\pi}{2}$ - FID to normalize the chiral signal by Fourier transforming a 1.5 µs section after this pulse. **(3)** The second normalization scheme uses a separate 'normal' rotational transition signal during the same sample injection to normalize the chiral signal, recorded for 13 µs. This transition utilizes the strongest dipole component leading to a higher SNR for normalization.

3.4: *Results and Discussion*

3.4.1: 3WM Cycle Efficiency

Within the measurements, one can determine the efficiency of creating the chiral signal at the sum or difference frequency through manipulating the quantum system with optimal coherence creation and coherence transfer pulses. This is observed by comparison of the chiral signal to the signal generated at the same frequency but by direct, single frequency excitation. In a perfect experiment, the efficiency would be very high, where we assume the initial population difference is the same in each of these two cases. However, there are reasons for the efficiency of the 3WM process to never reach 100%. Rotational spectroscopy uses transitions between rotational energy levels where there can be many different degenerate quantum states with different M_J values in each rotational level. This M_J - dependance of the transition dipole moment results in each of these states having its own, different Rabi frequency. Applying the light pulse duration over these degenerate states leads to M_J averaging such that there is no one perfect pulse duration for the transition. From the literature, it is expected that the effect of M_J averaging with respect to the pulse duration over these degenerate levels can reduce the possible chiral signal on the order of a factor of one-third to one-half.[13, 14]

One of the other possible reasons for lower efficiencies is phase matching conditions. This effect is described in detail within Chapter 2 and reasons that the lower the coherence transfer pulse frequency, the higher this efficiency would be. In the literature, other groups have used frequencies as high as ~3 GHz for the coherence transfer pulse.[8] The ratio of the chiral signal observed to that of direct, single wave excitation at the frequency is reported to be on the order

of 1-2% in such a case.[8] This directly limits how useful the technique can be if proper care isn't taken to optimize the efficiency to maximize sensitivity in the chiral signal. The effects of lower signal-to-noise on these transitions affecting overall precision in EE determinations will be discussed in a later section. It is not clear how much the phase matching conditions will affect the efficiency of the 3WM measurement, and the effect might become partially irrelevant as the wavelength of the excitation pulses is on the order of the cross section of the gas pulse, which is approximately 10-12 cm). This effect might be irrelevant when the excitation pulse wavelength is long enough to pass over the gas pulse in only half of a wavelength (one sign of the wave), which would occur at approximately ≤ 1.5 GHz. More care on this topic is a subject for further research.

In our measurements, coherence transfer pulses below 1 GHz are used, and measured efficiencies are ~20-60%. This is depicted in Figures 3.9-3.11 through the comparison of the chiral signal and achiral (directly excited) signal for each of the three species measured in these experiments. Each spectra represents the average of 160,000 FIDs. Some caveats must be mentioned. All three cycles pertain to the same rotational transitions and the coherence transfer pulses only differ in frequency minimally, so based on phase matching restrictions, the efficiencies should be relatively the same.

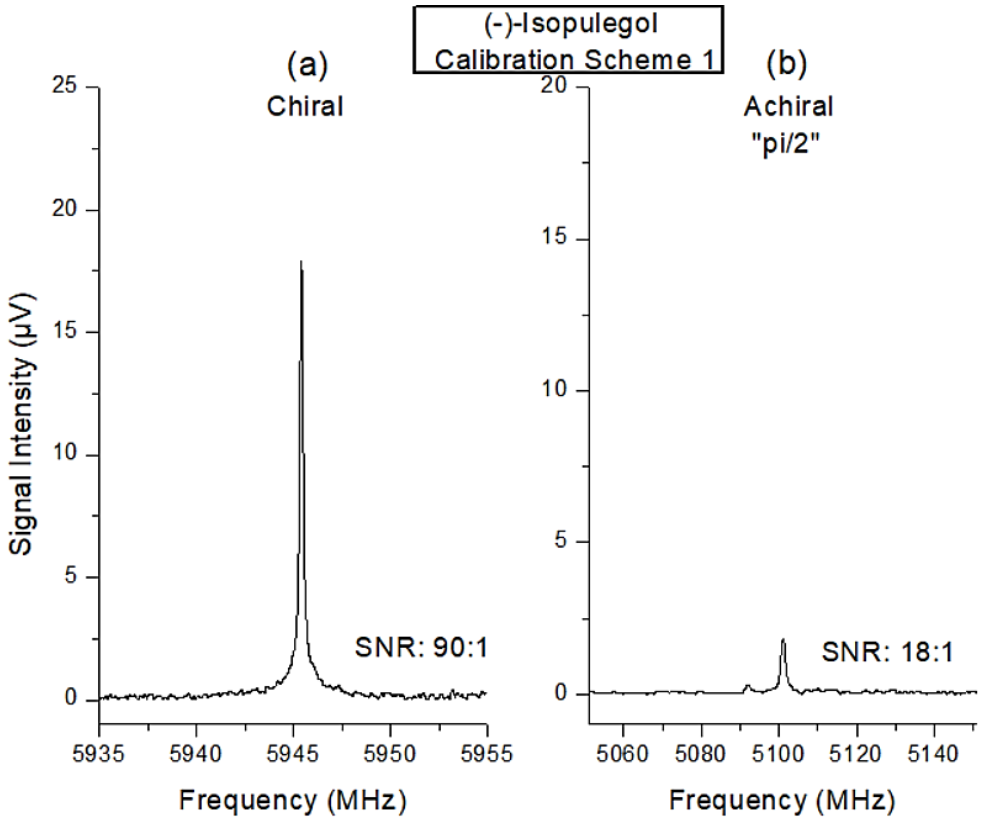

Figure 3.8: Normalization Scheme 1 signal-to-noise ratio comparison on the chiral and normalization signals. Each of the two displayed signals is the coadd of four measurements and total average of 160,000 FIDs. In this scheme, a 1.5 µs portion of the FID between the two excitation pulses is recorded to acquire the achiral signal from the $\frac{\pi}{2}$ – pulse. The chiral signal is recorded for 13 µs.

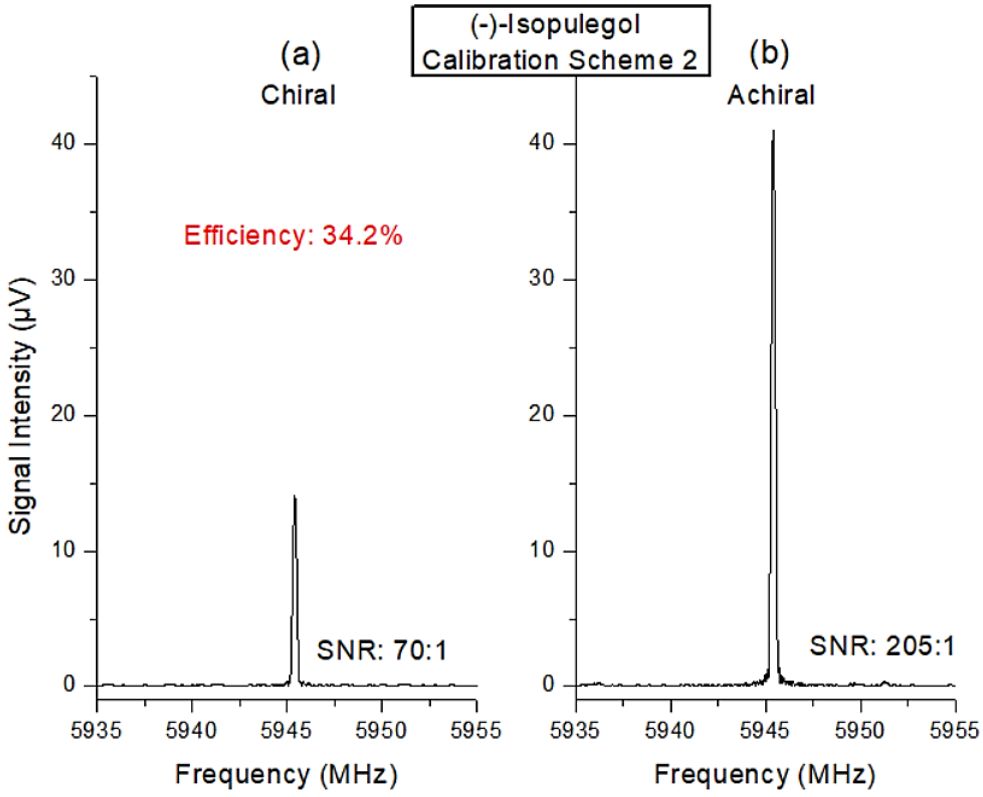

Figure 3.9: Normalization Scheme 2 signal-to-noise ratio comparison of the chiral and achiral, normalization signal. Efficiency of the 3WM cycle for isopulegol is determined by comparing the signal intensity of the 3WM chiral signal to that of a directly excited transition at the same frequency. Each of the two displayed signals is the coadd of four measurements and total average of 160,000 FIDs. Each signal is recorded for 13 μs.

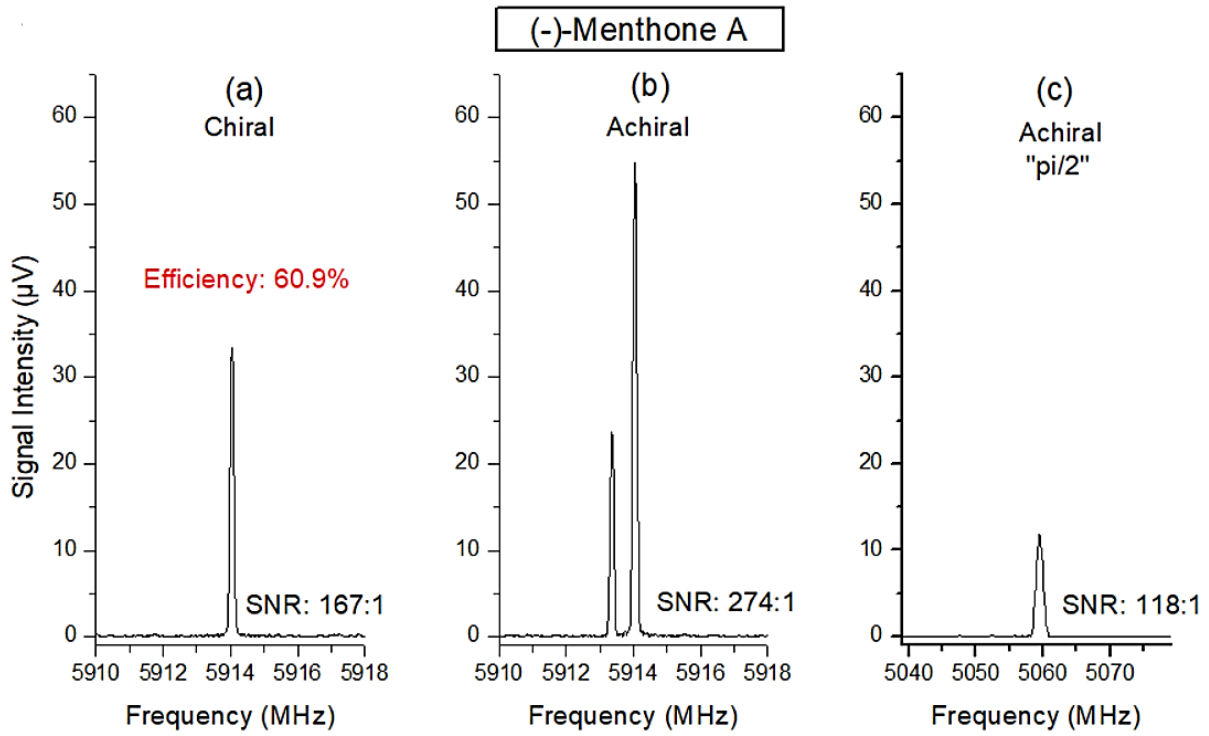

Figure 3.10: Combination of Normalization Scheme 1 and 2 used for Menthone A. Efficiency of the 3WM cycle for determined by comparing the signal intensity of the 3WM chiral signal to that of a directly excited transition at the same frequency. Each of the displayed signals is the coadd of four measurements and total average of 160,000 FIDs. An advantage of 3WM rotational spectroscopy is that the chiral signal is only observed for doubly resonant pulse excitation. Whereas, an additional, nearby transition is excited during the direct excitation depicted in panel (b).

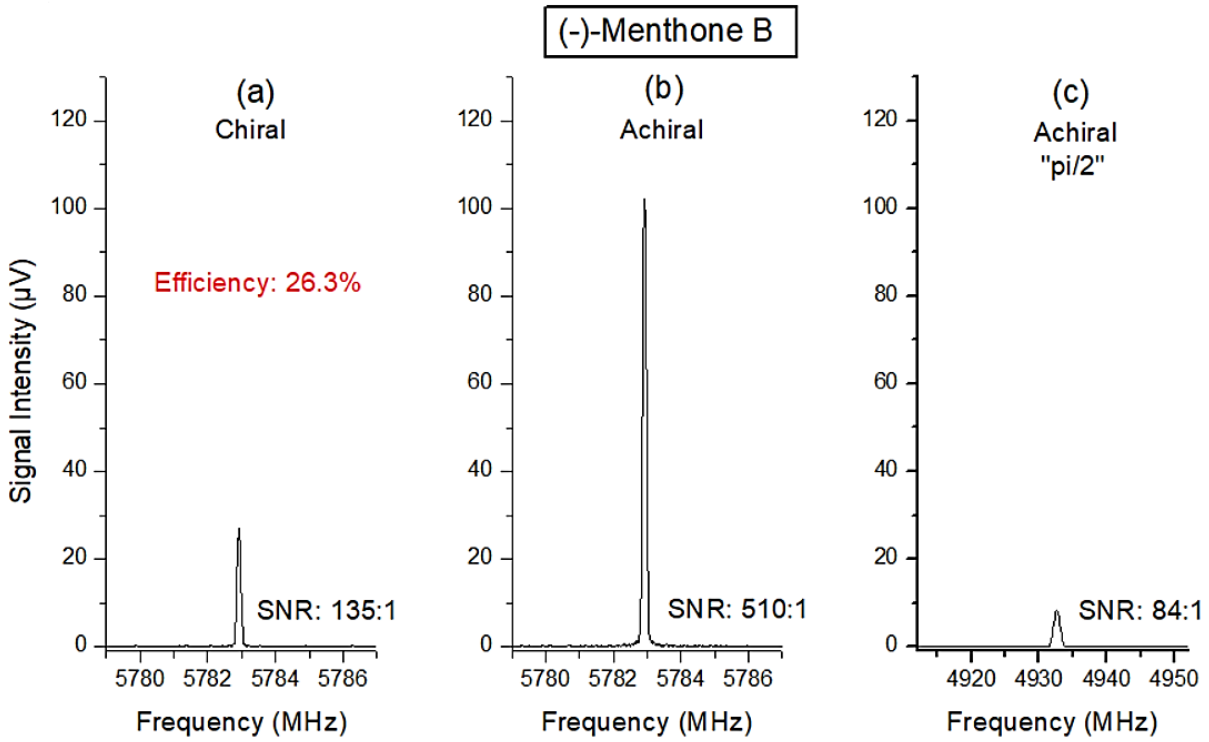

Figure 3.11: Combination of Normalization Scheme 1 and 2 used for Menthone B. Efficiency of the 3WM cycle for determined by comparing the signal intensity of the 3WM chiral signal to that of a directly excited transition at the same frequency. Each of the two displayed signals is the coadd of four measurements and total average of 160,000 FIDs.

3.4.2: *Absolute Configuration and Phase Measurements*

The phase of the chiral signal obtained by 3WM rotational spectroscopy corresponds to the AC of the enantiomer in excess within a measured sample. Because of the importance of measuring the phase within each measurement, the instrument needs to be referenced to a stable frequency standard for reproducibility in back-to-back measurements and over long periods of time. Over the course of the measurements to obtain calibration curves, many hours and even days were taken to construct a curve's worth of data points. The phase reproducibility of the instrumentation is excellent, allowing for coherent signal averaging even if the sampling conditions changed over time or after samples were exchanged between experiments. Figure 3.12 depicts an example of four FIDs at different EE's which required thorough cleaning of the sample reservoirs, powering down of the electronics, and breaking vacuum. The phase of the detected chiral signal is consistent over the course of these measurements even though approximately one day was taken between each EE sample.

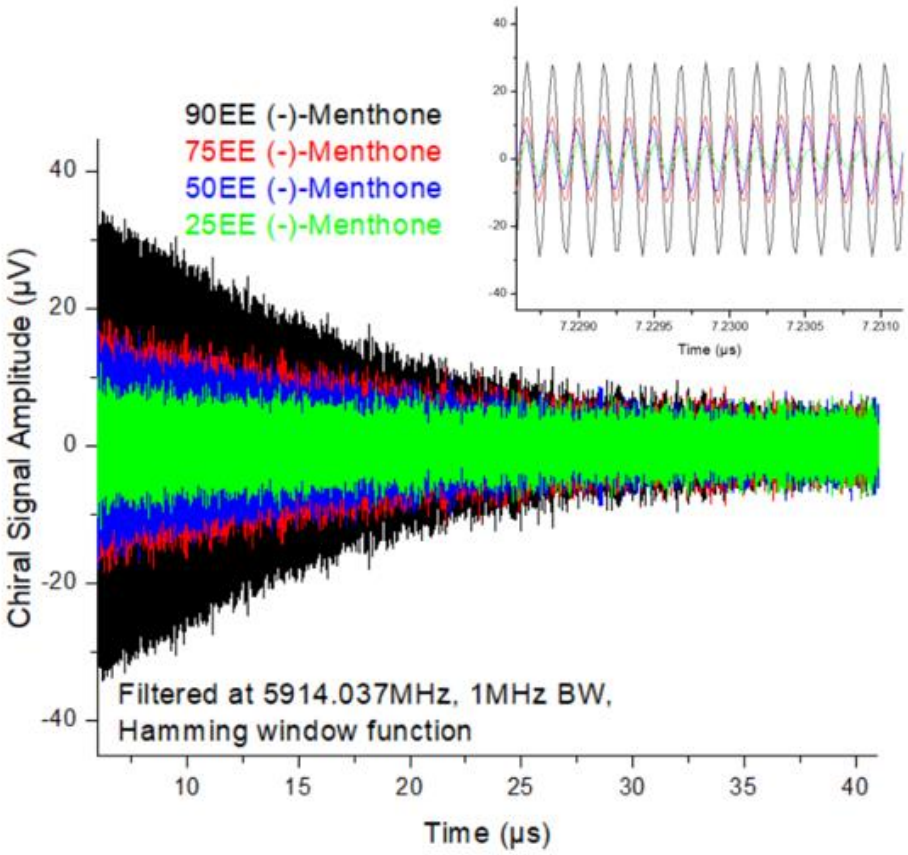

Figure 3.12: Phase stability within the measurements and at various EEs. FIDs from measuring the calibration curve of menthone are shown. FIDs show excellent phase reproducibility over the measurements lasting ~2 hours per data point where each displayed FID is the average of 4 measurements at each EE along the calibration curve. Phase reproducibility is expected to last on the order of many days to weeks at a time, even with significant alteration to the sample introduction when changing samples and cleaning sample holding reservoirs.

Again, the phase of the detected chiral signal will be exactly out of phase for each enantiomer, so referencing the chiral signal of an unknown AC sample with that of a known AC is straightforward. Figures 3.13 and 3.14 depict the measured chiral signal of separately measured enantiomeric reference samples of isopulegol and the two conformers of menthone. With the high phase stability and phase reproducibility in the measurements, so long as a reference sample of known EE exists, fast determinations of AC are possible.

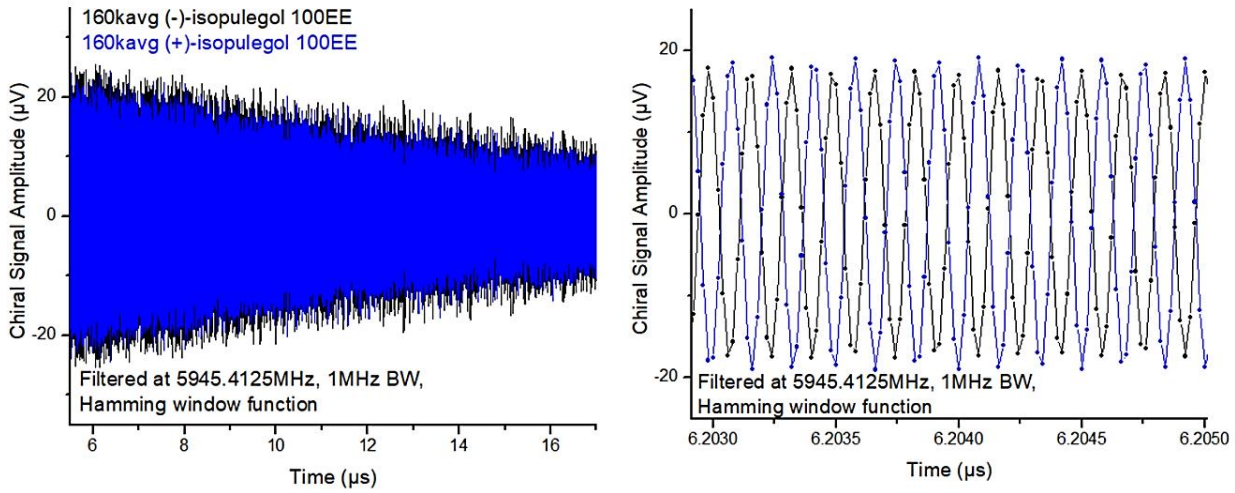

Figure 3.13: Measurements of reference samples of each enantiomer of isopulegol. Exact opposite phase in the chiral signal was observed and depicted in the zoom-in on the right. Circles represent the data points directly recorded from the oscilloscope (50 GS/s). Signals are digitally filtered to remove any unwanted electrical spurs in the measurement.

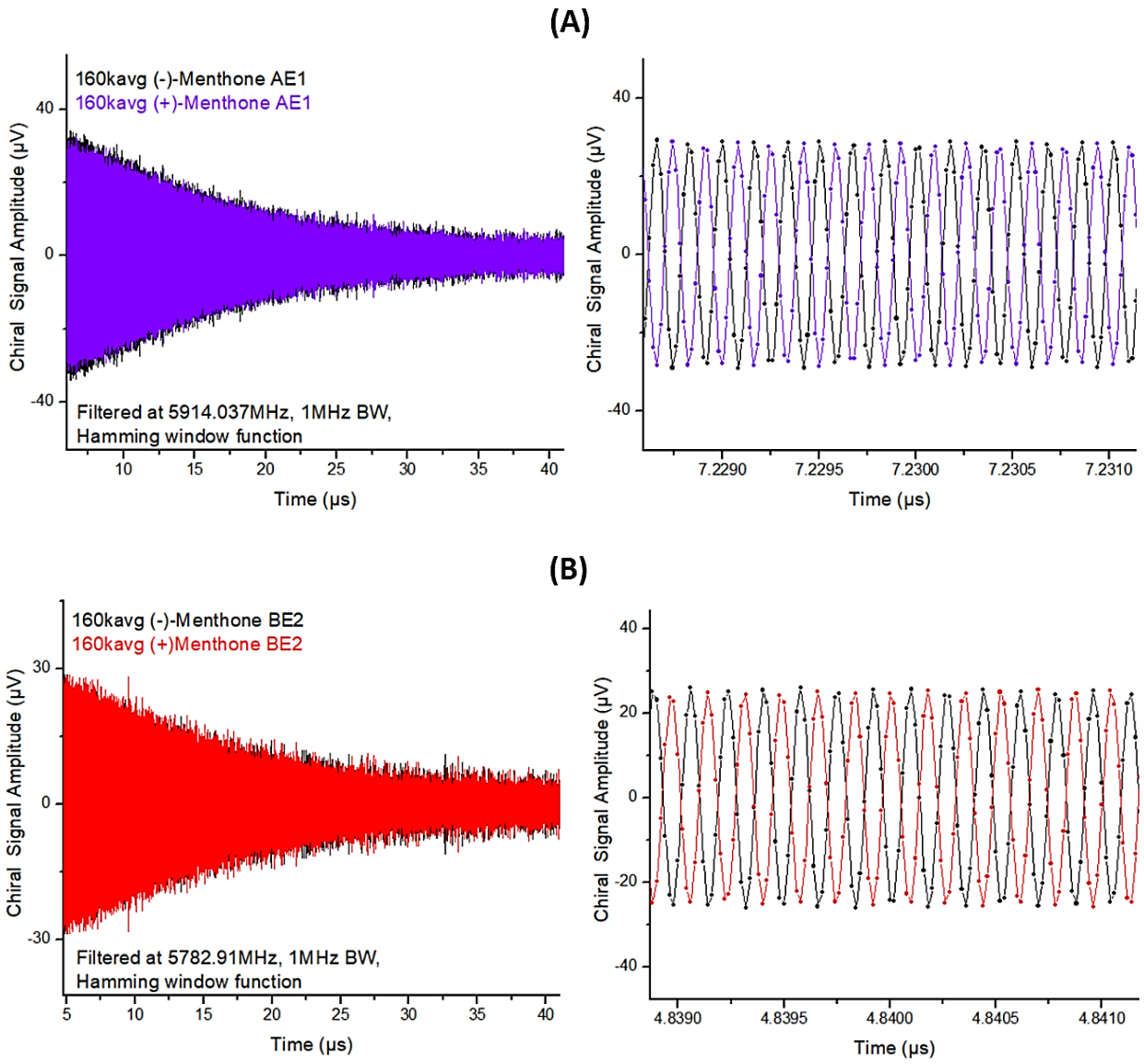

Figure 3.14: Measurements of reference samples of each enantiomer of menthone for the two conformers of menthone: **(A)** Menthone A and **(B)** Menthone B. Exact opposite phase in the chiral signal was observed and depicted in the zoom-in for each FID. Circles represent the data points directly recorded from the oscilloscope (50 GS/s). Signals are digitally filtered to remove any unwanted electrical spurs in the measurement.

Commercial samples of isopulegol and menthone were used to illustrate AC determination by 3WM rotational spectroscopy. Figure 3.15 shows the FID of the chiral signal for a reference (-)-isopulegol vs that of a sample labeled “Mixture of Isomers” purchased from TCI America. The right panel of this figure shows a zoom in of the digitally filtered FID in which the phase of the commercial sample matches that of the reference leading to an AC determination of (-)-isopulegol, which is confirmed by the CoA. A measurement on a commercial sample of menthone from Alfa Aesar is depicted in Figure 3.16 in which the sample can be determined to be (-)-menthone in excess by its exact match in phase of the chiral signal to the reference sample. In each of these examples, however, the commercial sample’s FID is at reduced amplitude suggesting that the EE, which is proportional to the chiral signal amplitude, must be lower. The quantitation of these EE’s is discussed in the next section. Additionally, a complex oil sample of Buchu leaf oil was measured to determine the EE and AC of naturally occurring menthone, which is one of its major components. Figure 3.17 shows the phase comparison for the two conformers of menthone in this sample which is opposite to that of the (-)-menthone reference sample thus providing an AC determination of (+)-menthone in excess for this sample.

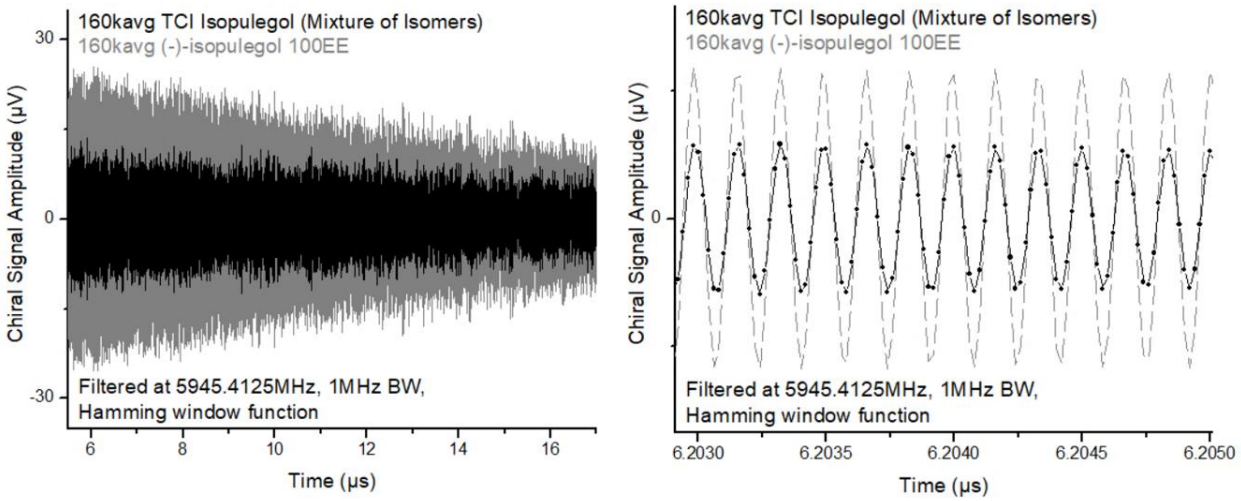

Figure 3.15: Measurement of a commercial sample of isopulegol shows that the chiral signal phase is a match to the reference sample that determines the absolute configuration of the sample to be (-)-isopulegol.

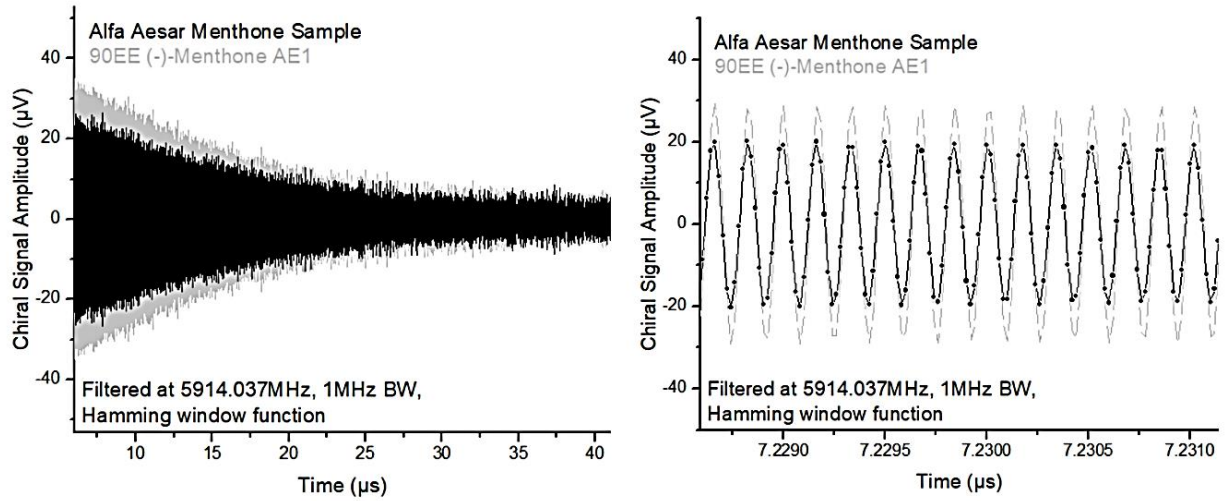

Figure 3.16: Measurement of a commercial sample of menthone shows that the chiral signal yields a match in phase to the reference sample thus determining the absolute configuration of the sample to be (-)-menthone.

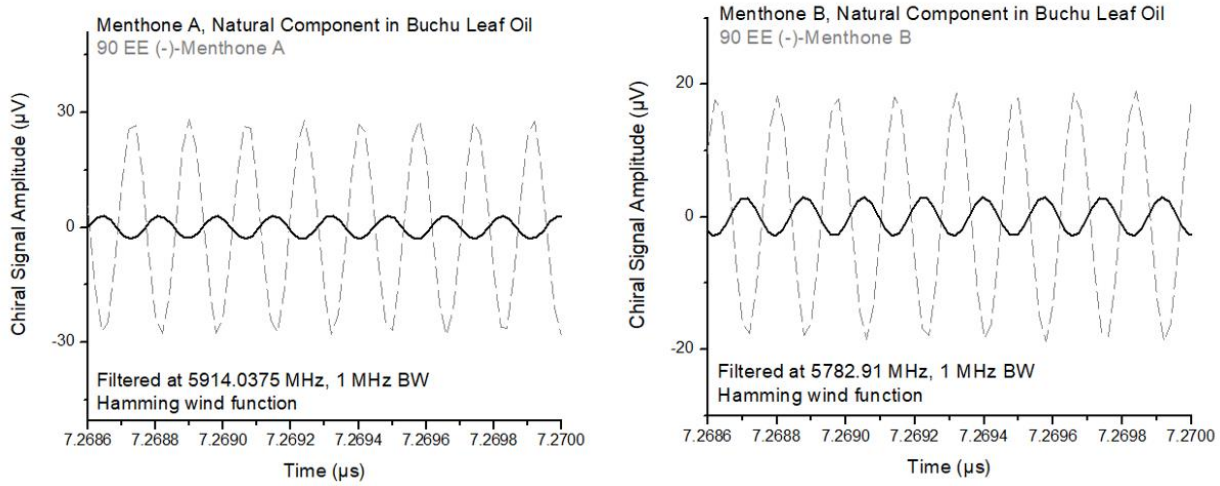

Figure 3.17: Measurement of Buchu Oil, Betulina with naturally occurring menthone shows that the chiral signal from either conformer of menthone yields a phase opposite to the reference sample thus determining the absolute configuration of the sample to be (+)-menthone in excess.

3.4.3: *Calibration Curves and Potential for Quantitative EE Determination*

Calibration curves were measured and are depicted in Figures 3.18-3.23 as gravimetrically determined EE *vs* the determined ratio (*R*) of the chiral signal normalized by an achiral signal coming from Normalization Scheme 1 or 2 (shown previously in Figure 3.7). These confirm linearity of the measurement. Each data point represents 40,000 FIDs averaged together, and at least four data points were taken at each EE to determine measurement precision. The raw data is shown in the appendix, Section 3.6.

Care was taken in the design of the sequence of measurements constructing the calibration curves such that the accuracy and reliability of the curves could be assessed. Generally, this sequence involved going in the order of **[1]** (-)-enantiomer, **[2]** (+)-enantiomer, **[3]** calibration curve data points, **[4]** a repeat of the initial (-)-enantiomer, **[5]** and then commercial samples and mixtures. Between each sampling loading, the vacuum chamber was opened, the sample reservoirs within the vacuum chamber were removed and these reservoirs were cleaned thoroughly before the next sample was loaded. The removal and reinstallation of these sample reservoirs changes the instrument response function due to alterations in the pulsed jet nozzles.

As the instrument was limited to 5 Hz repetition rate, each data point took 2.2 hours. This time can be greatly reduced to measurements only lasting seconds or minutes in the future by using a faster vacuum pump on a smaller vacuum chamber to allow for higher frequency of gas injections. Additionally, measuring multiple FIDs per gas injection can increase speeds by factors of five or more. However, this great length of time and the number of data points in each calibration curve alludes to the longevity of the measured calibration and the phase stability,

which was discussed in the previous section. The calibration curve for isopulegol, which measured multiple calibration points and many additional replicates at the EE=100 sample, took roughly three weeks to acquire all of the data.

The average of the data points at each EE are plotted in a separate calibration curve depicted in the right panels within each of Figures 3.18-3.23. Commercial samples were measured to determine accuracy of the technique. Additionally, measurements in complex mixtures without prior separation were done and plotted on the calibration curves below. 95% confidence intervals are used to display precision in the measurements and to provide discussion on the accuracy of the measured commercial samples and complex oil mixtures. Measured EE values are extracted from the calibration curve data by dividing the measured ratio *R* of each sample by the slope of the calibration curve, *C* (from Equation 2.1, Chapter 2 and reworked in Equations 3.1 and 3.2). The known EE values from the CoAs or in-house chiral GC / chiral tag rotational spectroscopy measurements, determined EE's, percent errors, and the lower and upper confidence interval values are reported in Table 3.4.

$$R_{Measured} = C * EE_{Gravimetric} \tag{3.1}$$

$$EE_{Determination} = \frac{R_{Measured}}{C} \tag{3.2}$$

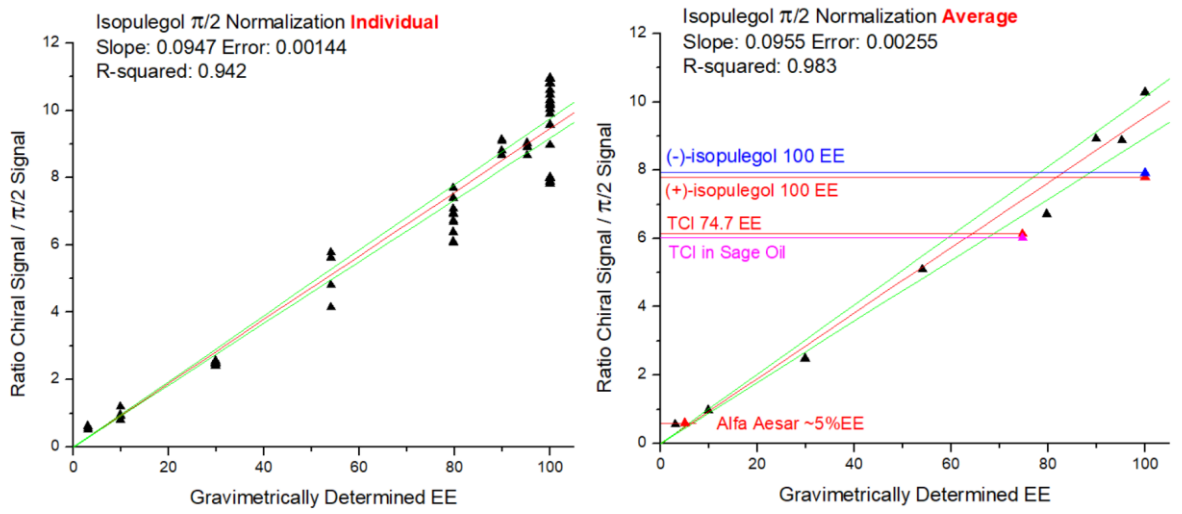

Figure 3.18: Isopulegol calibration curve using Normalization Scheme 1 – normalizing by using the π/2 FID between excitation pulses. **Left**: Individual measurements taken at each gravimetrically determined EE sample with the average in red and a 95% confidence window in green. **Right**: Average values of the individual measurements at each gravimetrically determined EE. Commercial samples and a measurement of isopulegol doped in a complex sage leaf oil mixture are plotted in this calibration curve.

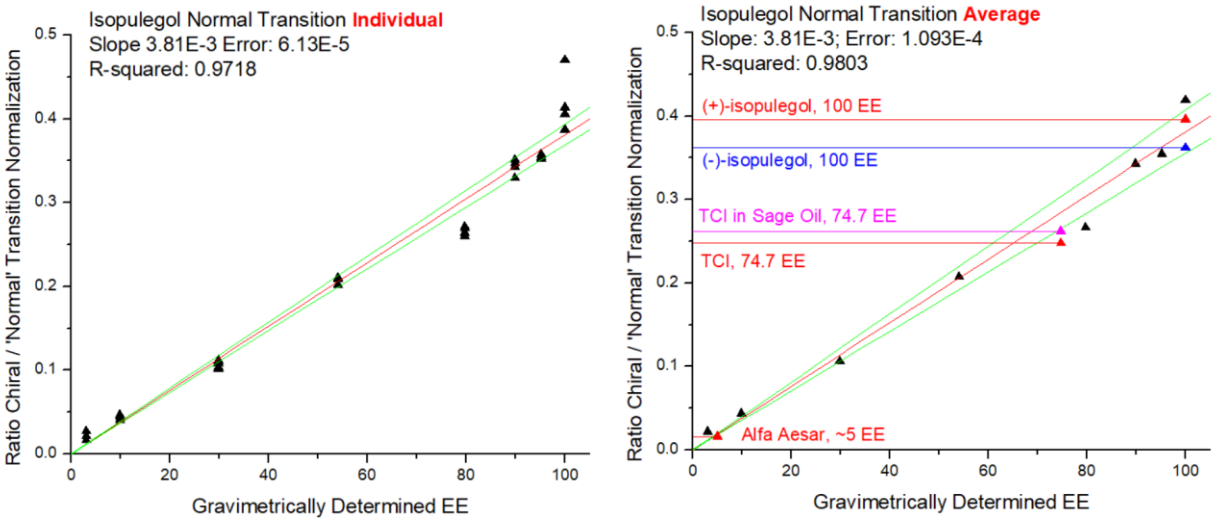

Figure 3.19: Isopulegol calibration curve using Normalization Scheme 2 – normalizing by a separate, direct transition at the same frequency. **Left**: Individual measurements taken at each gravimetrically determined EE sample with the average in red and a 95% confidence window in green. **Right**: Average values of the individual measurements at each gravimetrically determined EE. Commercial samples and a measurement of isopulegol doped in a complex sage leaf oil mixture are plotted in this calibration curve.

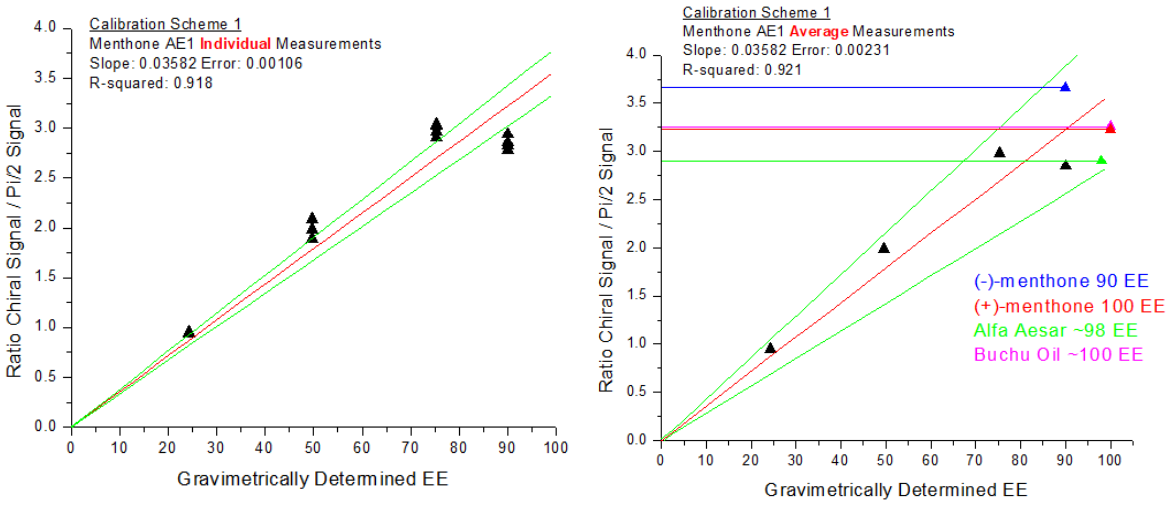

Figure 3.20: Menthone A calibration curve using Normalization Scheme 1 – normalizing by using the π/2 FID between excitation pulses. **Left**: Individual measurements taken at each gravimetrically determined EE sample and a 95% confidence window in green. **Right**: Average values of the individual measurements at each gravimetrically determined EE. Commercial samples and a measurement of menthone naturally occurring in a complex Buchu leaf oil mixture are plotted in this calibration curve.

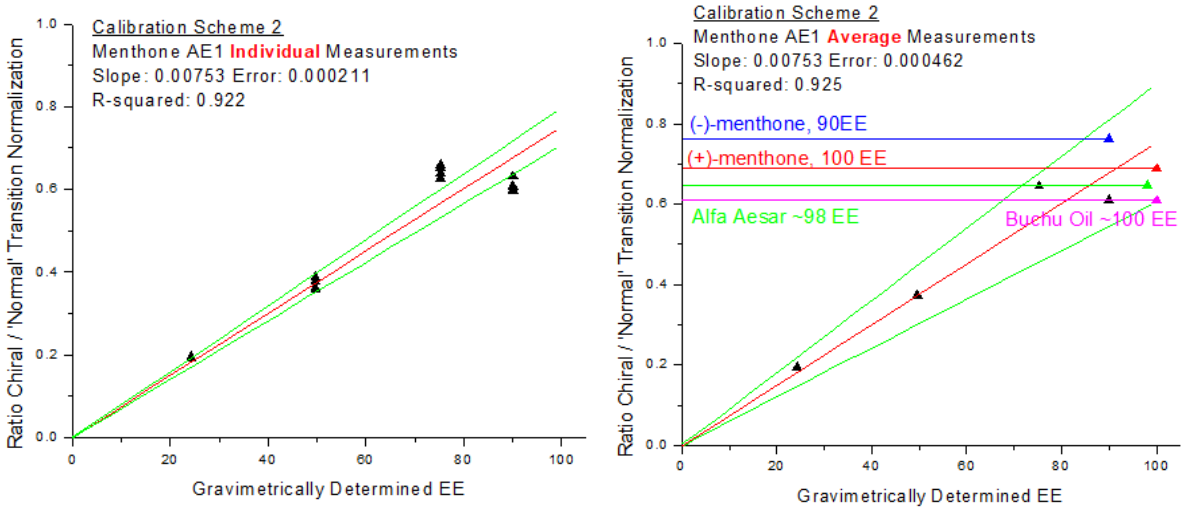

Figure 3.21: Menthone A calibration curve using Normalization Scheme 2 – normalizing by a separate, direct transition at the same frequency. **Left**: Individual measurements taken at each gravimetrically determined EE sample and a 95% confidence window in green. **Right**: Average values of the individual measurements at each gravimetrically determined EE. Commercial samples and a measurement of menthone naturally occurring in a complex Buchu leaf oil mixture are plotted in this calibration curve.

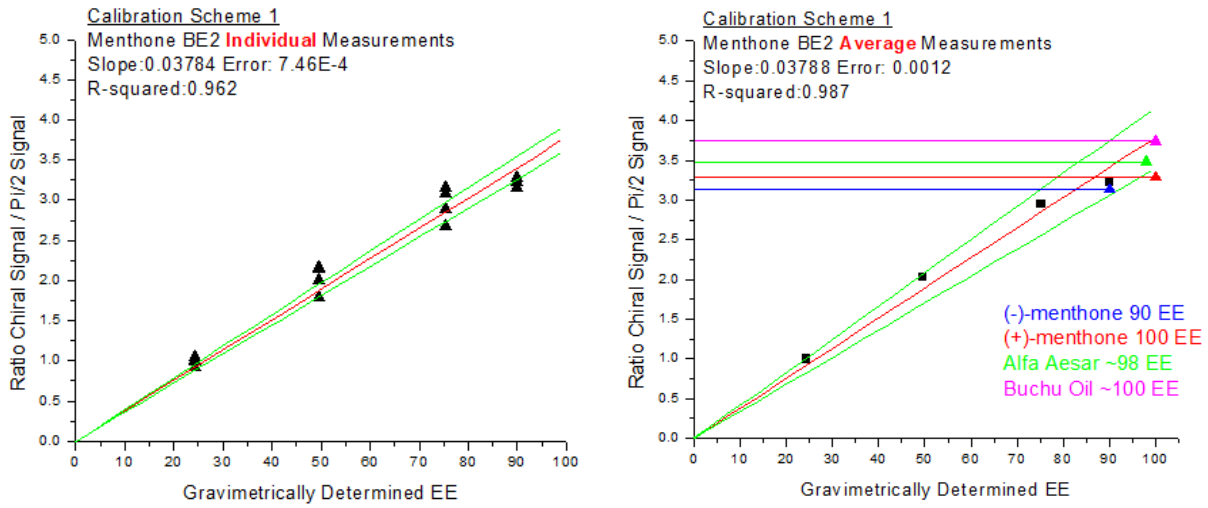

Figure 3.22: Menthone B calibration curve using Normalization Scheme 1 – normalizing by using the π/2 FID between excitation pulses. **Left**: Individual measurements taken at each gravimetrically determined EE sample and a 95% confidence window in green. **Right**: Average values of the individual measurements at each gravimetrically determined EE. Commercial samples and a measurement of menthone naturally occurring in a Buchu leaf oil mixture are plotted in this calibration curve.

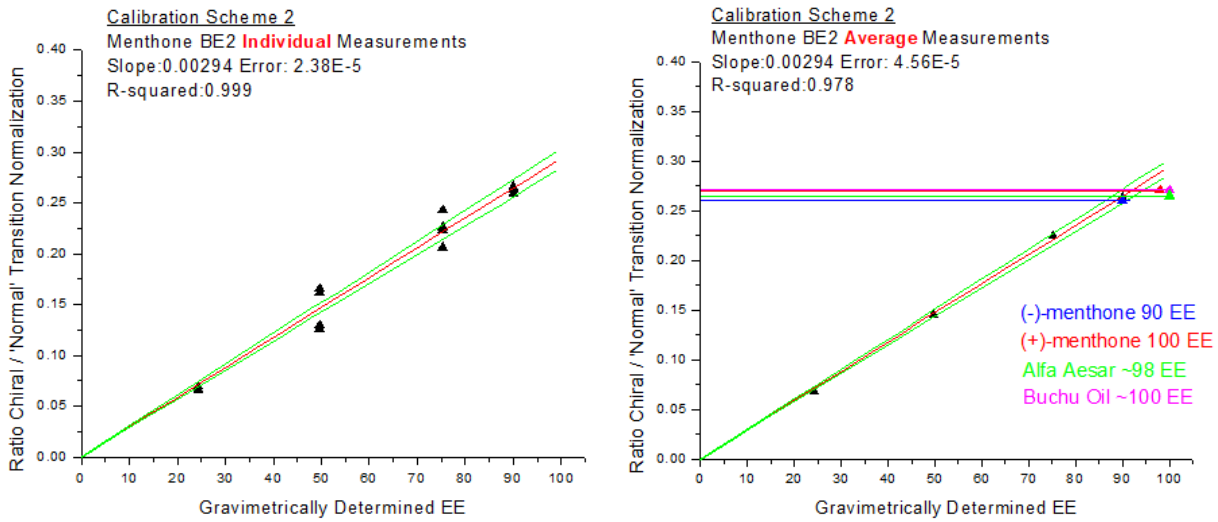

Figure 3.23: Menthone B calibration curve using Normalization Scheme 2 – normalizing by a separate, direct transition at the same frequency. **Left**: Individual measurements taken at each gravimetrically determined EE sample and a 95% confidence window in green. **Right**: Average values of the individual measurements at each gravimetrically determined EE. Commercial samples and a measurement of menthone naturally occurring in a Buchu leaf oil mixture are plotted in this calibration curve.

Table 3.4: EE Determinations of Commercial Samples for Isopulegol and Menthone by 3WM Rotational Spectroscopy Measurements

Sample Name (Normalization Scheme 1)	Known Sample EE	EE Determination	$\|\%\ Error\|$	95% LCI*	95% UCI*
100 EE (-)-isopulegol	100.0	83.0	17.0	78.1	88.6
100 EE (+)-isopulegol	98.6	81.5	17.3	76.7	87.0
Isopulegol, TCI America	74.7	64.3	13.9	60.5	68.6
Isopulegol, Alfa Aesar	5.0	6.2	24.0	5.8	6.6

Sample Name (Normalization Scheme 2)	Known Sample EE	EE Determination	$\|\%\ Error\|$	95% LCI	95% UCI
100 EE (-)-isopulegol	100.0	95.1	4.9	89.0	101.9
100 EE (+)-isopulegol	98.6	103.9	5.4	97.3	111.4
Isopulegol, TCI America	74.7	65.1	12.9	60.9	69.8
Isopulegol, Alfa Aesar	5.0	4.1	18.0	3.9	4.4
Isopulegol in Sage Oil	74.7	68.8	7.9	66.5	71.0

Sample Name (Normalization Scheme 1)	Known Sample EE	EE Determination	$\|\%\ Error\|$	95% LCI	95% UCI
(-)-Menthone A	90.0	102.3	13.7	84.9	128.6
(+)-Menthone A	100.0	90.1	9.9	74.8	113.4
Menthone A, Alfa Aesar	98.0	81.0	17.3	67.2	101.9
Menthone A, Buchu Oil	>98.0	91.0	7.1	75.5	114.4

Sample Name (Normalization Scheme 2)	Known Sample EE	EE Determination	$\|\%\ Error\|$	95% LCI	95% UCI
(-)-Menthone A	90.0	101.4	12.7	84.4	126.2
(+)-Menthone A	100.0	91.4	8.6	76.5	113.6
Menthone A, Alfa Aesar	98.0	85.7	12.6	71.6	106.7
Menthone A, Buchu Oil	>98.0	80.8	17.6	76.3	86.0

Sample Name (Normalization Scheme 1)	Known Sample EE	EE Determination	$\|\%\ Error\|$	95% LCI	95% UCI
(-)-Menthone B	90.0	82.7	8.1	75.1	91.9
(+)-Menthone B	100.0	86.8	13.2	78.8	96.5
Menthone B, Alfa Aesar	98.0	91.9	6.2	83.5	102.1
Menthone B, Buchu Oil	>98.0	98.7	0.7	89.7	109.8

Sample Name (Normalization Scheme 2)	Known Sample EE	EE Determination	$\|\%\ Error\|$	95% LCI	95% UCI
(-)-Menthone B	90.0	88.7	1.4	86.4	91.0
(+)-Menthone B	100.0	90.1	9.9	87.8	92.4
Menthone B, Alfa Aesar	98.0	91.9	6.2	89.6	94.3
Menthone B, Buchu Oil	>98.0	92.1	6.0	89.1	95.4

*LCI and UCI refer to the lower and upper confidence band intervals

Within these calibration curves and commercial sample measurements, the measurement error was observed to be large compared to other techniques like chiral GC and chiral tag rotational spectroscopy. In the individual data point calibration curves (left panel of Figures 3.18-3.23), one can notice the trend that at higher EE, the data becomes much more spread where the achiral signal and chiral signal are both large. At lower EE, where the achiral signal is large, but the chiral signal is small and against an effective zero background at the noise floor, the data is less spread out. The coefficient of variation (CoV: standard deviation at each EE divided by its mean, (σ_I/I)) is used to assess the precision of the measurements and yields values averaging around 5-7% in the measured ratio values (reported in tables within the appendix of Section 3.6). This 5-7% value appears to come from signal intensity fluctuation likely caused by the fluctuation in the pulsed jet expansion. This provides an approximate ± 7% error in the measured EE value following Equations 3.3-3.7 if the assumption is used that the fluctuation in intensity values, σ_I/I = 0.05. The signal intensities from the averaged FIDs for the two measured transitions are denoted as I_{chiral} and $I_{normalization}$, σ_{EE} is the standard deviation of the data points for the respective EE sample, and σ_{chiral} and $\sigma_{normalization}$ are the standard deviations of each transitions data sets at each EE.

$$EE = \frac{I_{chiral}}{I_{normalization}} \cdot \frac{1}{C} \tag{3.3}$$

$$\frac{\sigma_{EE}}{EE} = \sqrt{\left(\frac{\sigma_{chiral}}{I_{chiral}}\right)^2 + \left(\frac{\sigma_{normalization}}{I_{normalization}}\right)^2} \tag{3.4}$$

$$\sigma_{EE} = EE * \sqrt{\left(\frac{\sigma_{chiral}}{I_{chiral}}\right)^2 + \left(\frac{\sigma_{normalization}}{I_{normalization}}\right)^2} \tag{3.5}$$

$$\sigma_{EE} = EE * \sqrt{(0.05)^2 + (0.05)^2} \quad (3.6)$$

$$\frac{\sigma_{EE}}{EE} \cong 0.07 \quad (3.7)$$

The root cause of this high fractional error, $\frac{\sigma_{EE}}{EE}$, is likely to be signal intensity fluctuations during the experiment caused by fluctuations of number density fluctuation in back-to-back pulsed jet expansions. Over many three-wave mixing experiments and chiral tag rotational spectroscopy measurements within our group, this ~5-7% value appears to hold true. Using the assumed 5% intensity fluctuation, the error in each EE measurement *vs* the gravimetrically determined EE shows a larger spread at larger EE values. This is shown in Figure 3.24 and 3.25. In Figure 3.26, the measurement error per EE (fractional error) value is plotted against the gravimetrically determined EE values for all three-wave mixing measurements reported in this chapter.

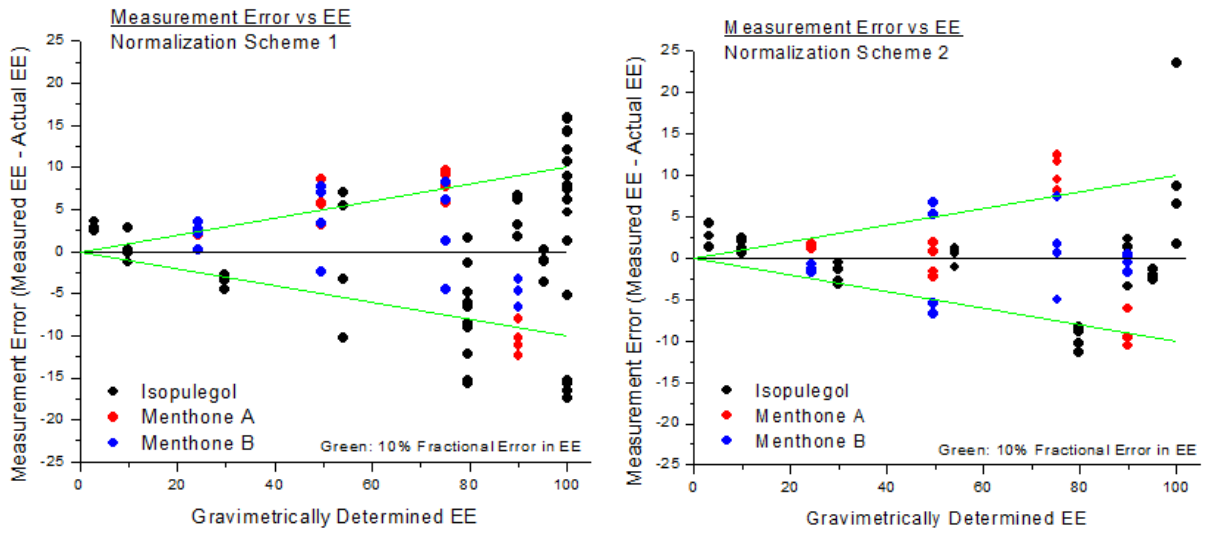

Figure 3.24: Measurement error (Measured EE – Actual EE) as a function of EE in each of the EE determinations made during all of the 3WM experiments in this thesis. The left panel shows the data set taken using Normalization Scheme 1 and the right panel shows the data set taken for Normalization Scheme 2 (See Figure 3.7). Measurement error increases as a function of EE, likely due to a constant found intensity fluctuation in the pulsed supersonic jet sample introduction. This fluctuation makes EE measurements at high EE more challenging for this technique as the fractional error as each EE can be as high as 10%. Both normalization schemes have approximately the same level of error.

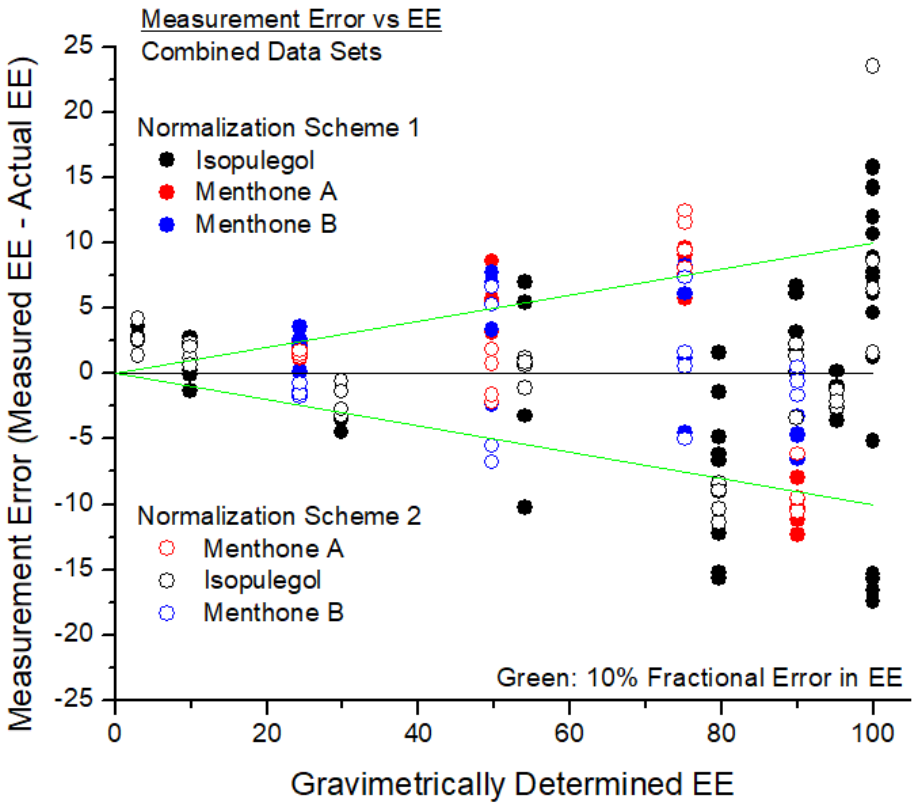

Figure 3.25: Combination of the datasets from Normalization Scheme 1 and 2 (See Figure 3.7) showing the measurement error (Measured EE – Actual EE) as a function of EE. The green line shows a 10% fractional measurement error in EE to give a sense of the fractional error in these measurements.

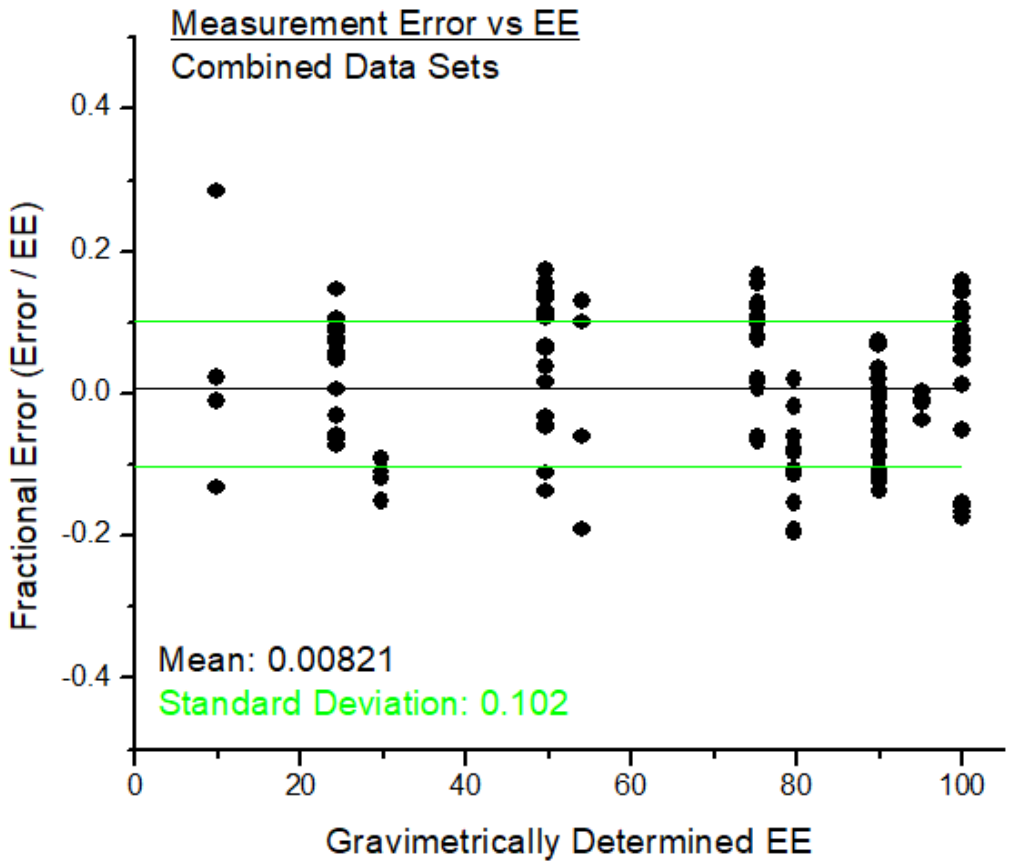

Figure 3.26: Fractional error (measurement error per EE) as a function of EE for all three-wave mixing measurements used in the calibration curves of this chapter. The mean error is close to zero with a standard deviation showing a fractional error of approximately 10%, depicted in green.

3.4.4: Assessment of Normalization Schemes

An assessment can be made on which of the normalization methods is preferred. As was mentioned in Section 3.3.2, the two logical choices for normalization each have a potential drawback. Normalizing by the FID of the $\frac{\pi}{2}$ – pulse transition in Normalization Scheme 1 is expected to have a weak signal for normalization whereas choosing a separate transition later in the gas injection may add additional fluctuation effects. The fluctuation in the measured ratio, $\frac{\sigma_R}{\mathrm{R}}$, is described in Equation 3.8.

$$(\frac{\sigma_R}{R})^2 = (\frac{\sigma_{Chiral}}{\mathrm{I}_{chiral}})^2 + (\frac{\sigma_{Norm}}{I_{Norm}})^2 \quad (3.8)$$

In the case of Normalization Scheme 1, where the same molecules in the pulsed jet are being monitored for the normalization signal and then for the chiral signal, strong reduction in number density fluctuation is expected. If this were perfect, the fluctuation in the measured intensity value (σ_I) would just be equal to the signal-to-noise ratio (SNR) where the noise level would be limited by the amplifiers, σ_I = SNR. Equation 3.8 would thus become:

$$(\frac{\sigma_R}{R})^2 = (\frac{1}{SNR_{chiral}})^2 + (\frac{1}{SNR_{Norm}})^2 \quad (3.9)$$

Since SNR_{Norm} can be low in this normalization scheme, the fluctuation in the measured ratio is dominated by the signal-to-noise ratio of this normalization, shown in Equation 3.11. This can limit the precision on the measurement if the given molecule has a weak transition for this normalization signal. Isopulegol for example, with a SNR = 18 depicted previously in Figure 3.8 would limit this uncertainty to ~5% in the measured ratio.

$$(\frac{\sigma_R}{R})^2 \approx (\frac{1}{SNR_{Norm}})^2 \quad (3.10)$$

$$\sigma_R \approx \left(\frac{1}{SNR_{Norm}}\right) \cdot R \quad (3.11)$$

However, for Normalization Scheme 2, where the signal-to-noise ratio on the normalization signal is high relative to the chiral signal and the signals are taken at different parts of the gas pulse, it is not as clear how the fluctuations should behave. In several other measurements with pulsed jets done in our lab group, the fluctuation appears to be constant, $(\frac{\sigma_R}{R})^2 = constant$, typically seen as 10% or less. While the assessment of measurement errors

in Normalization Scheme 1 and Normalization Scheme 2 in Figure 3.24 shows similar results, it may be more practical to use Normalization Scheme 2 in general due to the possibility of the normalization signal used in Scheme 1 to be weak with low signal-to-noise.

3.5: *Conclusions*

We report an in-depth quantitative approach to determining the accuracy and precision of the recently developing 3WM rotational spectroscopy technique. By creating a series of gravimetrically determined EE samples of isopulegol and menthone, a wider spread in measurement error at larger EE's can be seen while a much smaller spread is seen in smaller EEs. For most cases, this is unfortunately unappealing to chemists and the drug industry where drugs or starting materials tend to be designed to be close to enantiopure and the quantitative determination of the amount of the small enantiomer impurity is wanted. However, the technique has the unique strength of determining AC and EE of various multi-stereocentered chiral molecules in complex mixtures without any prior separation as was shown by doping known EE samples into essential oils or determining natural AC and EE of components within essential oils. This also has an advantage of much room for improvement in speed of the measurement. Not having to separate mixtures (in this case having twenty or more components in the leaf oil mixtures) can save chemists a lot of time and headache during synthetic procedures and allow one to obtain the AC and EE of multiple species during multiple synthetic steps from raw sample mixtures. This feature of 3WM rotational spectroscopy can be very advantageous for samples with challenging separation protocols or of small amount so long as a reference sample

is available, but admittedly, this can also be a weakness for the technique if a reference sample is not available.

In the future, a closer look at the fluctuations caused by the pulsed jet expansion could aid in increasing precision of the technique or by using different sampling techniques like that of a buffer gas cell used in the literature.[6, 15] Additionally, there is a simple theoretical way of determining AC without a reference sample by calibrating the absolute phase of the chiral signal; however, this approach proves to be challenging in practice and has not yet had a robust solution to address the issues within. If this problem is solved, chemists could have a quick way of determining the AC of the enantiomer in excess of a wide variety of molecules in seconds without need of another approach to verify the AC first.

3.6: *Appendix*

Table 3.5: Calibration Curve 1 - Isopulegol

*The calibration curve data consists of normalization using a 1 μs pause between the two excitation pulses to collect the undisturbed π/2 signal (5101.1 MHz) within three-wave mixing measurement. All intensities are measured in μV, and each trial is an average of 40,000 FIDs measured at a repetition rate of 5 Hz. The coefficient of variation (CoV) is measured in % (standard deviation / mean * 100%) and used to measure the fluctuation in measured data.*

100 EE (-)-Isopulegol

Parameter	Trial A / μV	Trial B / μV	Trial C / μV	Trial D / μV	Trial E / μV	Trial F / μV
3WM Signal	10.2637	12.9803	13.2588	13.6197	13.5721	13.7798
π/2 Signal	0.9358	1.2013	1.4771	1.3749	1.2952	1.3712
Ratio	10.9678	10.8049	8.9763	9.9058	10.4788	10.0497
	Trial G / μV	Trial H / μV	Trial I / μV	Trial J / μV	Trial K / μV	Trial L / μV
3WM Signal	15.7076	16.0025	15.6292	15.8495	15.5352	15.5789
π/2 Signal	1.6396	1.5095	1.4268	1.4649	1.5225	1.5337
Ratio	9.5803	10.6015	10.9537	10.8193	10.2037	10.1578
	Trial M / μV	Trial N / μV	Average / μV	CoV / %		
3WM Signal	15.5504	14.4076	14.4097	10.8143		
π/2 Signal	1.5291	1.3978	1.4057	11.9761		
Ratio	10.1697	10.3074	10.2841	5.2313		

100 EE (+)-Isopulegol

Parameter	Trial A / μV	Trial B / μV	Trial C / μV	Trial D / μV	Average / μV	CoV / %
3WM Signal	17.6861	17.3164	18.9877	18.0506	18.0102	3.4492
π/2 Signal	2.1620	2.2954	2.4992	2.3078	2.3161	5.1881
Ratio	8.1803	7.5439	7.5975	7.8216	7.7859	3.2165

95 EE (-)-Isopulegol

Parameter	Trial A / μV	Trial B / μV	Trial C / μV	Trial D / μV	Average / μV	CoV / %
3WM Signal	18.5980	17.9223	17.8549	16.7061	17.7703	3.8249
π/2 Signal	2.0897	2.0675	2.0012	1.8503	2.0022	4.6719
Ratio	8.9000	8.6684	8.9222	9.0289	8.8799	1.4805

90 EE (-)-Isopulegol

Parameter	Trial A / μV	Trial B / μV	Trial C / μV	Trial D / μV	Average / μV	CoV / %
3WM Signal	14.1439	13.1540	11.4401	10.7910	12.3823	10.7740
π/2 Signal	1.5567	1.4927	1.2513	1.2430	1.3859	10.1484
Ratio	9.0860	8.8121	9.1429	8.6815	8.9307	2.1342

80 EE (-)-Isopulegol

Parameter	Trial A / μV	Trial B / μV	Trial C / μV	Trial D / μV	Average / μV	CoV / %
3WM Signal	10.6114	10.7936	11.6531	11.8384	11.2241	4.7188
π/2 Signal	1.7401	1.7810	1.7302	1.8545	1.7765	2.7547
Ratio	6.0981	6.0603	6.7351	6.3835	6.3192	4.2826

80 EE (-)-Isopulegol Repeat

Parameter / μV	Trial A / μV	Trial B / μV	Trial C / μV	Trial D / μV	Trial E / μV	Trial F / μV
3WM Signal	12.6818	12.2165	11.8018	11.5505	12.9438	13.0492
π/2 Signal	1.8974	1.7673	1.5341	1.5596	1.8604	1.8423
Ratio	6.6837	6.9126	7.6929	7.4062	6.9576	7.0829

Parameter	Average / μV	CoV / %
3WM Signal	12.3739	4.5544
π/2 Signal	1.7435	8.2903
Ratio	7.1226	4.6957

55 EE (-)-Isopulegol

Parameter	Trial A / µV	Trial B / µV	Trial C / µV	Trial D / µV	Average / µV	CoV / %
3WM Signal	5.5205	9.2146	8.1469	6.5160	7.3495	19.4270
π/2 Signal	0.9550	1.6366	1.6934	1.5714	1.4641	20.2916
Ratio	5.7806	5.6304	4.8109	4.1465	5.0921	12.9416

30 EE (-)-Isopulegol

Parameter	Trial A / µV	Trial B / µV	Trial C / µV	Trial D / µV	Average / µV	CoV / %
3WM Signal	3.9720	4.0268	4.0212	4.1593	4.0448	1.7174
π/2 Signal	1.5983	1.6804	1.5687	1.6576	1.6263	2.7501
Ratio	2.4851	2.3963	2.5633	2.5093	2.4885	2.4227

10 EE (-)-Isopulegol

Parameter	Trial A / µV	Trial B / µV	Trial C / µV	Trial D / µV	Average / µV	CoV / %
3WM Signal	1.4758	1.0183	1.0178	1.0758	1.1469	16.6834
π/2 Signal	1.5489	1.2591	1.1041	0.8985	1.2026	19.7335
Ratio	0.9529	0.8088	0.9218	1.1973	0.9702	14.6026

5 EE (-)-Isopulegol

Parameter	Trial A / µV	Trial B / µV	Trial C / µV	Trial D / µV	Average / µV	CoV / %
3WM Signal	0.6375	0.6302	0.5156	0.6746	0.6145	9.6833
π/2 Signal	1.0198	1.1369	0.9946	1.2110	1.0906	8.0562
Ratio	0.6251	0.5543	0.5185	0.5571	0.5637	6.8383

100 EE (-)-Isopulegol Recheck

Parameter	Trial A / µV	Trial B / µV	Trial C / µV	Trial D / µV	Average / µV	CoV / %
3WM Signal	19.2857	20.5027	19.7206	21.0880	20.1492	3.4525
π/2 Signal	2.4074	2.6231	2.4985	2.6427	2.5429	3.7681
Ratio	8.0110	7.8161	7.8930	7.9797	7.9250	0.9623

Table 3.6: Calibration Curve 2 - Isopulegol

*The calibration curve data consists of normalization using a separate, normal rotational transition (5945.425 MHz) within the same sample injection 40 μs after the three-wave mixing cycle measurement. All intensities are measured in μV, and each trial is an average of 40,000 FIDs measured at a repetition rate of 5 Hz. The coefficient of variation (CoV) is measured in % (standard deviation / average * 100) and used to measure the spread of the data.*

100 EE (-)-Isopulegol

Parameter	Trial A / μV	Trial B / μV	Trial C / μV	Trial D / μV	Average / μV	CoV / %
3WM Signal	29.4199	29.2633	28.5069	-	29.0634	1.3717
5945 MHz Normalization	71.0860	72.1171	73.6299	-	72.2777	1.4454
Ratio	0.4139	0.4058	0.3872	-	0.4023	2.7788

100 EE (+)-Isopulegol

Parameter	Trial A / μV	Trial B / μV	Trial C / μV	Trial D / μV	Average / μV	CoV / %
3WM Signal	21.4117	23.1514	23.7099	23.6676	22.9851	4.0664
5945 MHz Normalization	54.0904	57.5982	60.1874	60.2935	58.0424	4.3487
Ratio	0.3958	0.4019	0.3939	0.3925	0.3961	0.9068

95 EE (-)-Isopulegol

Parameter	Trial A / μV	Trial B / μV	Trial C / μV	Trial D / μV	Average / μV	CoV / %
3WM Signal	20.2241	20.9549	21.0825	21.2357	20.8743	1.8602
5945 MHz Normalization	57.3782	59.3819	58.9360	59.8847	58.8952	1.5925
Ratio	0.3525	0.3529	0.3577	0.3546	0.3544	0.5830

90 EE (-)-Isopulegol

Parameter	Trial A / μV	Trial B / μV	Trial C / μV	Trial D / μV	Average / μV	CoV / %
3WM Signal	14.7900	17.3630	18.0204	17.8833	17.0142	7.6838
5945 MHz Normalization	44.8873	49.9597	51.3100	52.1483	49.5763	5.6833
Ratio	0.3295	0.3475	0.3512	0.3429	0.3428	2.3979

80 EE (-)-Isopulegol

Parameter	Trial A / µV	Trial B / µV	Trial C / µV	Trial D / µV	Average / µV	CoV / %
3WM Signal	18.8502	19.5048	19.4524	18.2539	19.0153	2.6785
5945 MHz Normalization	69.4268	72.3790	74.7844	69.1139	71.4260	3.2481
Ratio	0.2715	0.2695	0.2601	0.2641	0.2663	1.6828

55 EE (-)-Isopulegol

Parameter	Trial A / µV	Trial B / µV	Trial C / µV	Trial D / µV	Average / µV	CoV / %
3WM Signal	13.5889	14.0919	14.3272	14.3930	14.1003	2.2393
5945 MHz Normalization	67.3389	67.6294	68.0997	68.8060	67.9685	0.8159
Ratio	0.2018	0.2084	0.2104	0.2092	0.2074	1.6062

30 EE (-)-Isopulegol

Parameter	Trial A / µV	Trial B / µV	Trial C / µV	Trial D / µV	Average / µV	CoV / %
3WM Signal	5.5113	7.5362	6.5268	5.9802	6.3886	11.7982
5945 MHz Normalization	54.4927	67.6810	63.2251	55.1782	60.1442	9.2161
Ratio	0.1011	0.1113	0.1032	0.1084	0.1060	3.8187

10 EE (-)-Isopulegol

Parameter	Trial A / µV	Trial B / µV	Trial C / µV	Trial D / µV	Average / µV	CoV / %
3WM Signal	1.9379	1.6773	1.7977	1.5289	1.7354	8.6859
5945 MHz Normalization	41.6414	40.0072	39.5930	38.3066	39.8871	2.9866
Ratio	0.0465	0.0419	0.0454	0.0399	0.0434	6.1109

5 EE (-)-Isopulegol

Parameter	Trial A / µV	Trial B / µV	Trial C / µV	-	Average / µV	CoV / %
3WM Signal	1.3507	1.0542	0.5321	-	0.9790	34.5658
5945 MHz Normalization	62.7432	38.5639	32.0336	-	44.4469	29.7191
Ratio	0.0215	0.0273	0.0166	-	0.0218	20.0901

100 EE (-)-Isopulegol Repeat After Calibration Curve

Parameter	Trial A / µV	Trial B / µV	Trial C / µV	Trial D / µV	Average / µV	CoV / %
3WM Signal	21.6709	21.1043	21.4332	15.5384	19.9367	12.7770
5945 MHz Normalization	61.6595	61.0884	57.7791	40.7516	55.3196	15.4382
Ratio	0.3515	0.3455	0.3710	0.3813	0.3623	3.9913

Table 3.7: Isopulegol Commercial Samples and Mixtures

*The calibration curve data consists of normalization using both normalization schemes. All intensities are measured in μV, and each trial is an average of 40,000 FIDs measured at a repetition rate of 5 Hz. Samples are measured by chiral GC and chiral tagging rotational spectroscopy for comparison of EE. The coefficient of variation (CoV) is measured in % (standard deviation / average * 100) and used to measure the spread of the data.*

TCI America Sample: 3WM and 5945 MHz Normalization (Normalization Scheme 1)

Parameter	Trial A / μV	Trial B / μV	Trial C / μV	Trial D / μV	Average / μV	CoV / %
3WM Signal	10.9147	10.6838	10.3001	11.0779	10.7441	2.7189
5945 MHz Normalization	44.4236	43.2969	42.7631	42.9205	43.3511	1.4969
Ratio	0.2457	0.2468	0.2409	0.2581	0.2479	2.5498

TCI America Sample: 3WM and *π*/2 Normalization (Normalization Scheme 2)

Parameter	Trial A / μV	Trial B / μV	Trial C / μV	Trial D / μV	Average / μV	CoV / %
3WM Signal	7.9083	8.6563	8.2261	8.4455	8.3090	3.3324
π/2 Signal	1.3206	1.4079	1.4331	1.2627	1.3561	5.0279
Ratio	5.9885	6.1482	5.7402	6.6884	6.1413	5.6615

TCI Sample Doped in Sage Oil: 3WM and 5945 MHz Normalization (Normalization Scheme 1)

Parameter	Trial A / μV	Trial B / μV	Trial C / μV	Trial D / μV	Average / μV	CoV / %
3WM Signal	0.9300	1.4435	2.0230	1.8958	1.5731	27.2845
5945 MHz Normalization	3.1385	5.7672	7.7583	7.8812	6.1363	31.3451
Ratio	0.2963	0.2503	0.2607	0.2405	0.2620	8.0439

TCI Sample Doped in Sage Oil: 3WM and *π*/2 Normalization (Normalization Scheme 2)

Parameter	Trial A / μV	Trial B / μV	Trial C / μV	Trial D / μV	Average / μV	CoV / %
3WM Signal	2.2307	2.4583	2.4583	2.7163	2.4867	7.0242
π/2 Signal	0.3866	0.3923	0.4229	0.4191	0.4052	3.9435
Ratio	5.7706	6.2666	6.0099	6.4805	6.0186	4.4356

Alfa Aesar Sample: 3WM and 5945 MHz Normalization (Normalization Scheme 2)

Parameter	*Trial A-D Coadd (120kavg) / μV
3WM Signal	0.4798
5945 MHz Normalization	35.5223
Ratio	0.0135

**Signal-to-noise ratio was low for individual 40kavg FIDs, so only the coadd of four measurements is shown*

Alfa Aesar Sample: 3WM and *π*/2 Normalization (Normalization Scheme 1)

Parameter	*Trial A-D Coadd (160kavg) / μV
3WM Signal	0.6008
π/2 Signal	1.0836
Ratio	0.5544

**Signal-to-noise ratio was low for individual 40kavg FIDs, so only the coadd of four measurements is shown*

Table 3.8: Calibration Curve - Menthone A (Combined Normalization Schemes 1 and 2)

*The calibration curve data consists of normalization using both normalization schemes within each measurement. Each trial is an average of 40,000 FIDs. Calibration point EE's are confirmed gravimetrically. The same sample is used for Menthone A and Menthone B during the same sample loading. The coefficient of variation (CoV) is measured in % (standard deviation / average * 100) and used to measure the spread of the data.*

90 EE (-)-Menthone A (From Sigma Aldrich)

Parameter	Trial A / µV	Trial B / µV	Trial C / µV	Trial D / µV	Average / µV	CoV / %
3WM Signal	34.8653	35.0799	33.5131	31.0540	33.6281	4.7667
π/2 Signal	12.5285	12.2862	11.8665	10.5669	11.8120	6.4078
5914 MHz Normalization	57.5830	58.6531	55.2928	49.1760	55.1762	6.6527
Ratio 3WM to *π/2*	2.7829	2.8552	2.8242	2.9388	2.8503	2.0067
Ratio 3WM to 5914 MHz	0.6055	0.5981	0.6061	0.6315	0.6103	2.0706

100 EE (+)-Menthone A (From Sigma Aldrich)

Parameter	Trial A / µV	Trial B / µV	Trial C / µV	Trial D / µV	Average / µV	CoV / %
3WM Signal	30.7185	33.7825	31.8077	32.6451	32.2384	3.4837
π/2 Signal	9.6836	10.3579	9.8475	10.0439	9.9832	2.5154
5914 MHz Normalization	43.3389	47.4550	45.2339	46.3650	45.5982	3.3391
Ratio 3WM to *π/2*	3.1722	3.2615	3.2300	3.2503	3.2285	1.0656
Ratio 3WM to 5914 MHz	0.7088	0.7119	0.7032	0.7041	0.7070	0.5007

75 EE (-)-Menthone A

Parameter	Trial A / µV	Trial B / µV	Trial C / µV	Trial D / µV	Average / µV	CoV / %
3WM Signal	14.2070	15.7181	16.1082	17.2404	15.8184	6.8620
π/2 Signal	4.8958	5.2046	5.4264	5.6717	5.2996	5.3917
5914 MHz Normalization	22.6444	24.0370	25.2553	26.1044	24.5103	5.3202
Ratio 3WM to *π/2*	2.9019	3.0200	2.9685	3.0397	2.9825	1.7885
Ratio 3WM to 5914 MHz	0.6274	0.6539	0.6378	0.6604	0.6449	2.0208

50 EE (-)-Menthone A

Parameter	Trial A / µV	Trial B / µV	Trial C / µV	Trial D / µV	Average / µV	CoV / %
3WM Signal	20.8137	14.7505	9.4345	7.1041	13.0257	40.5490
π/2 Signal	11.0075	7.0666	4.7724	3.5787	6.6063	42.8890
5914 MHz Normalization	58.2605	38.8319	26.0807	18.3088	35.3705	42.7213
Ratio 3WM to *π/2*	1.8909	2.0873	1.9769	1.9851	1.9851	3.5085
Ratio 3WM to 5914 MHz	0.3573	0.3799	0.3617	0.3880	0.3717	3.4045

25 EE (-)-Menthone A

Parameter	Trial A / µV	Trial B / µV	Trial C / µV	Trial D / µV	Average / µV	CoV / %
3WM Signal	7.6853	6.0612	5.0320	4.4728	5.8128	21.0221
π/2 Signal	8.1734	6.4481	5.2827	4.7032	6.1518	21.5472
5914 MHz Normalization	40.0046	31.4580	25.9338	22.7626	30.0397	21.7735
Ratio 3WM to *π/2*	0.9403	0.9400	0.9526	0.9510	0.9460	0.6184
Ratio 3WM to 5914 MHz	0.1921	0.1927	0.1940	0.1965	0.1938	0.8730

90 EE (-)-Menthone A Repeat After Calibration Curve

Parameter	Trial A / μV	Trial B / μV	Trial C / μV	Trial D / μV	Average / μV	CoV / %
3WM Signal	21.9039	19.9479	18.4386	18.8778	19.7920	6.7559
π/2 Signal	6.1345	5.6447	4.9274	4.9566	5.4158	9.3162
5914 MHz Normalization	28.5295	26.7843	23.5565	23.0465	25.4792	8.9116
Ratio 3WM to *π/2*	3.5706	3.5339	3.7421	3.8086	3.6638	3.1313
Ratio 3WM to 5914 MHz	0.7678	0.7448	0.7827	0.8191	0.7786	3.4711

Alfa Aesar Commercial Sample): (-)-Menthone A (~98 EE by Chiral Tagging)

Parameter	Trial A / μV	Trial B / μV	Trial C / μV	Trial D / μV	Average / μV	CoV / %
3WM Signal	19.1337	23.9135	28.7175	24.7585	24.1308	14.1219
π/2 Signal	7.3909	8.6389	9.4486	7.7207	8.2998	9.7067
5914 MHz Normalization	32.5357	37.2793	42.9571	36.2013	37.2434	10.0372
Ratio 3WM to *π/2*	2.5888	2.7681	3.0393	3.2068	2.9008	8.2263
Ratio 3WM to 5914 MHz	0.5881	0.6415	0.6685	0.6839	0.6455	5.6488

Buchu Leaf Oil Sample Containing Natural (+)-Menthone (~Enantiopure)

Parameter	Trial A / μV	Trial B / μV	Trial C / μV	Trial D / μV	Average / μV	CoV / %
3WM Signal	2.8673	3.8231	3.6474	4.6477	3.7464	16.8862
π/2 Signal	0.8792	1.1156	1.2496	1.3558	1.1500	15.4807
5914 MHz Normalization	4.6359	6.0144	6.6116	7.3926	6.1636	16.3602
Ratio 3WM to *π/2*	3.2613	3.4270	2.9189	3.4281	3.2588	6.3726
Ratio 3WM to 5914 MHz	0.6185	0.6357	0.5517	0.6287	0.6086	5.4963

Table 3.9: Calibration Curve - Menthone B (Combined Normalization Schemes 1 and 2)

*The calibration curve data consists of normalization using both normalization schemes within each measurement. Each trial is an average of 40,000 FIDs. Calibration point EE's are confirmed gravimetrically. The same sample is used for menthone A and menthone B during the same sample loading. The coefficient of variation (CoV) is measured in % (standard deviation / average * 100) and used to measure the spread of the data.*

90 EE (-)-Menthone B (From Sigma Aldrich)

Parameter	Trial A / µV	Trial B / µV	Trial C / µV	Trial D / µV	Average / µV	CoV / %
3WM Signal	26.6003	27.5368	27.4019	26.0466	26.8964	2.2580
π/2 Signal	8.4267	8.5255	8.3550	8.0743	8.3454	2.0108
5783 MHz Normalization	100.3622	103.4860	104.2129	100.3126	102.0934	1.7384
Ratio 3WM to *π/2*	3.1567	3.2299	3.2797	3.2259	3.2230	1.3589
Ratio 3WM to 5914 MHz	0.2650	0.2661	0.2629	0.2597	0.2634	0.9334

100 EE (+)-Menthone B (From Sigma Aldrich)

Parameter	Trial A / µV	Trial B / µV	Trial C / µV	Trial D / µV	Average / µV	CoV / %
3WM Signal	30.4258	29.4699	28.6591	28.1683	29.1808	2.9335
π/2 Signal	9.3741	8.9171	8.7467	8.4897	8.8819	3.6294
5783 MHz Normalization	118.1436	113.5307	110.7396	107.8985	112.5781	3.3579
Ratio 3WM to *π/2*	3.2457	3.3049	3.2766	3.3180	3.2863	0.8457
Ratio 3WM to 5914 MHz	0.2572	0.2596	0.2588	0.2611	0.2592	0.5333

75 EE (-)-Menthone B

Parameter	Trial A / μV	Trial B / μV	Trial C / μV	Trial D / μV	Average / μV	CoV / %
3WM Signal	26.0803	15.3297	11.2620	12.9344	16.4016	35.1917
π/2 Signal	9.7480	5.3008	3.5645	4.2016	5.7037	42.3609
5783 MHz Normalization	126.3091	68.7876	46.3636	57.2267	74.6718	41.3132
Ratio 3WM to *π/2*	2.6755	2.8919	3.1595	3.0785	2.9513	6.3191
Ratio 3WM to 5914 MHz	0.2065	0.2229	0.2429	0.2260	0.2246	5.7567

50 EE (-)-Menthone B

Parameter	Trial A / μV	Trial B / μV	Trial C / μV	Trial D / μV	Average / μV	CoV / %
3WM Signal	3.8197	3.6136	5.7533	5.7903	4.7442	21.7157
π/2 Signal	2.1346	1.8003	2.6828	2.6653	2.3207	16.0542
5783 MHz Normalization	30.2961	27.8627	35.6238	34.9862	32.1922	10.0563
Ratio 3WM to *π/2*	1.7894	2.0072	2.1445	2.1725	2.0284	7.4693
Ratio 3WM to 5914 MHz	0.1261	0.1297	0.1615	0.1655	0.1457	12.2928

25 EE (-)-Menthone B

Parameter	Trial A / μV	Trial B / μV	Trial C / μV	Trial D / μV	Average / μV	CoV / %
3WM Signal	8.9563	9.1003	8.1324	7.3191	8.3770	8.5200
π/2 Signal	9.6680	9.0980	7.9826	6.9365	8.4213	12.4678
5783 MHz Normalization	135.1788	134.9346	121.3602	105.5726	124.2616	9.7803
Ratio 3WM to *π/2*	0.9264	1.0003	1.0188	1.0552	1.0001	4.6939
Ratio 3WM to 5914 MHz	0.0663	0.0674	0.0670	0.0693	0.0675	1.6782

90 EE (-)-Menthone B Repeat After Calibration Curve

Parameter	Trial A / μV	Trial B / μV	Trial C / μV	Trial D / μV	Average / μV	CoV / %
3WM Signal	31.6565	37.2173	32.2067	24.9528	31.5083	13.8411
π/2 Signal	11.5692	12.6082	9.7391	7.0570	10.2434	20.5689
5783 MHz Normalization	127.5914	148.2899	116.5385	86.5362	119.7390	18.6253
Ratio 3WM to *π/2*	2.7363	2.9518	3.3069	3.5359	3.1327	9.8746
Ratio 3WM to 5914 MHz	0.2481	0.2510	0.2764	0.2884	0.2659	6.3831

Alfa Aesar Commercial Sample): (-)-Menthone B (~98 EE by Chiral Tagging)

Parameter	Trial A / μV	Trial B / μV	Trial C / μV	Trial D / μV	Average / μV	CoV / %
3WM Signal	20.3958	18.0531	16.7604	14.9227	17.5330	11.3631
π/2 Signal	5.9047	5.1390	4.9475	4.1852	5.0441	12.1275
5783MHz Normalization	75.3491	65.6555	64.2001	54.3321	64.8842	11.4798
Ratio 3WM to *π/2*	3.4541	3.5129	3.3877	3.5656	3.4801	1.9066
Ratio 3WM to 5914 MHz	0.2707	0.2750	0.2611	0.2747	0.2703	2.0777

Buchu Leaf Oil Sample Containing Natural (+)-Menthone (~Enantiopure)

Parameter	Trial A / μV	Trial B / μV	Trial C / μV	Trial D / μV	Average / μV	CoV / %
3WM Signal	4.3883	4.8383	3.7071	3.7598	4.1734	11.2178
π/2 Signal	1.2258	1.2599	0.9913	0.9890	1.1165	11.3698
5783 MHz Normalization	16.8177	17.8319	14.2861	12.8743	15.4525	12.7526
Ratio 3WM to *π/2*	3.5800	3.8401	3.7398	3.8015	3.7404	2.6533
Ratio 3WM to 5914 MHz	0.2609	0.2713	0.2595	0.2920	0.2709	4.7996

Chapter 3 References:

1. Patterson, D.; Doyle, J. M., Sensitive chiral analysis via microwave three-wave mixing. *Phys Rev Lett* **2013,** *111* (2), 023008.
2. Shubert, V. A.; Schmitz, D.; Patterson, D.; Doyle, J. M.; Schnell, M., Identifying enantiomers in mixtures of chiral molecules with broadband microwave spectroscopy. *Angew Chem Int Ed Engl* **2014,** *53* (4), 1152-5.
3. Shubert, V. A.; Schmitz, D.; Medcraft, C.; Krin, A.; Patterson, D.; Doyle, J. M.; Schnell, M., Rotational spectroscopy and three-wave mixing of 4-carvomenthenol: A technical guide to measuring chirality in the microwave regime. *J Chem Phys* **2015,** *142* (21), 214201.
4. Lobsiger, S.; Perez, C.; Evangelisti, L.; Lehmann, K. K.; Pate, B. H., Molecular Structure and Chirality Detection by Fourier Transform Microwave Spectroscopy. *J Phys Chem Lett* **2015,** *6* (1), 196-200.
5. Krin, A.; Perez, C.; Pinacho, P.; Quesada-Moreno, M. M.; Lopez-Gonzalez, J. J.; Aviles-Moreno, J. R.; Blanco, S.; Lopez, J. C.; Schnell, M., Structure Determination, Conformational Flexibility, Internal Dynamics, and Chiral Analysis of Pulegone and Its Complex with Water. *Chemistry* **2018,** *24* (3), 721-729.
6. Satterthwaite, L.; Perez, C.; Steber, A. L.; Finestone, D.; Broadrup, R. L.; Patterson, D., Enantiomeric Analysis of Chiral Isotopomers via Microwave Three-Wave Mixing. *J Phys Chem A* **2019,** *123* (14), 3194-3198.
7. Payne, C.; Kass, S. R., How Reliable Are Enantiomeric Excess Measurements Obtained By Chiral HPLC? *ChemistrySelect* **2020,** *5* (6), 1810-1817.
8. Domingos, S. R.; Perez, C.; Marshall, M. D.; Leung, H. O.; Schnell, M., Assessing the performance of rotational spectroscopy in chiral analysis. *Chem Sci* **2020,** *11* (40), 10863-10870.
9. Azkaar, M.; Mäki-Arvela, P.; Vajglová, Z.; Fedorov, V.; Kumar, N.; Hupa, L.; Hemming, J.; Peurla, M.; Aho, A.; Murzin, D. Y., Synthesis of menthol from citronellal over supported Ru- and Pt-catalysts in continuous flow. *Reaction Chemistry & Engineering* **2019,** *4* (12), 2156-2169.
10. Schmitz, D.; Shubert, V. A.; Betz, T.; Schnell, M., Exploring the conformational landscape of menthol, menthone, and isomenthone: a microwave study. *Front Chem* **2015,** *3*, 15.
11. Thomas Kopke, A. D., and Armin Mosandl, Chiral Compounds of Essential Oils XIV: Simultaneous Stereoanalysis of Buchu Leaf Oil Compounds. *Phytochemical Analysis* **1994,** *5*, 61-67.
12. Nigel B. Perry, R. E. A., Nerida J. Brennan, Malcolm H. Douglas, Anna J. Heaney, Jennifer A. McGimpsey, and Bruce M. Smallfield, Essential Oils from Dalmatian Sage (Salvia officinalis L.): Variations among Individuals, Plant Parts, Seasons, and Sites. *J. Agric. Food Chem.* **1999,** *47*, 2048-2054.
13. *Frontiers and Advances in Molecular Spectroscopy*. Elsevier: 2018.
14. Lehmann, K. K., Influence of spatial degeneracy on rotational spectroscopy: Three-wave mixing and enantiomeric state separation of chiral molecules. *J Chem Phys* **2018,** *149* (9), 094201.
15. Porterfield, J. P.; Satterthwaite, L.; Eibenberger, S.; Patterson, D.; McCarthy, M. C., High sensitivity microwave spectroscopy in a cryogenic buffer gas cell. *Rev Sci Instrum* **2019,** *90* (5), 053104.

Chapter 4: ChiralSpec: A Millimeter-Wave Three-Wave Mixing Instrument with Astrochemical Applications

This chapter is composed of a collaboration with Dr. Shanshan Yu and Dr. Deacon Nemchick at NASA's Jet Propulsion Laboratory, California Institute of Technology (NASA). Kevin Mayer, a recent graduate our group, was also a key member in the construction and testing of the ChiralSpec prototype instrument throughout this collaboration, and I want to thank him for his part in the project.

4.1: *Introduction to Astrochemical Applications*

Since its discovery by Louis Pasteur, chirality has been shown to play a fundamental role in living organisms. The amino acids and sugars that make up proteins and nucleotides, respectively, throughout all forms of life are chiral, and more importantly they only appear as one enantiomeric form – a predominance of all life on Earth termed homochirality.[1] Homochirality is therefore an important biosignature in the search for life in our solar system in places such as Enceladus, Europa, Titan, and Mars.[2, 3] The 2013 Planetary Science Decadal Survey recommends "a detailed characterization of organics to search for signatures of biological origin, such as molecules with preferred chirality or unusual patterns of molecular weights" as one of the key future investigations in the hunt for past or present life beyond Earth. Generally, the primary tool of choice for the detection and identification of simple organics for planetary and astrobiology investigations are mass spectrometers;[4, 5] however, mass spectrometry (MS) alone cannot address the challenge of successfully deconvolving mixtures of structurally complex organic molecules with approximately the same molecular weight. MS lacks the detection capability required for chiral analysis without the use of additional derivatizing schemes and by including chromatography. Spectroscopic methods, like vibrational circular dichroism (VCD), used to distinguish between enantiomers have been limited by the reliance on the interference

of the electric and magnetic dipole moments to produce an enantiomer-specific signal, which is typically four to five orders of magnitude weaker than achiral signals for these techniques.[6, 7] The three-wave mixing (3WM) rotational spectroscopy technique described theoretically in Chapter 2 has been shown to produce strong chiral signals in Chapter 3, comparable to single photon excitation; however, this technique has been limited to the microwave regime from 300 MHz – 15 GHz, where high amounts of power are required to perform measurements that are not in compliance with extraterrestrial missions. These high powers are necessary where an electric field strength sufficient to achieve excitation faster than dephasing is required. In the microwave regime, the long wavelengths lead to large spot size requiring high peak power to produce suitable electric fields. However, if one could instead move to the millimeter wave regime, the shorter wavelengths improve the ability to focus the power to a smaller spot size so that a sufficient electric field for excitation faster than dephasing is possible while using less overall power.

The first use of millimeter-wave (mm-wave) radiation in 3WM rotational spectroscopy to produce an enantiomer specific signal will be described in this chapter. mm-wave radiation allows for the reduction of size, weight, and power consumption of components in the instrumentation, which are qualities needed for extraterrestrial missions to measure key biosignatures. Propylene oxide is used as a test case molecule due to its high volatility and compatible electric dipole components ($|\mu_a|$=0.94, $|\mu_b|$=1.68, $|\mu_c|$=0.48, $|\mu_{total}|$=1.98; obtained using B3LYPD3BJ / def2TZVP level of theory).

4.2: *Experimental Design*

The mm-wave 3WM instrument, coined as ChiralSpec, was designed to operate in two modes important to biomarker recognition:

(1) Survey mode, performing as a traditional mm-wave spectrometer to characterize and quantify multicomponent mixtures

(2) Chirality detection mode, utilizing the 3WM technology to distinguish enantiomers of key chiral molecules within a mixture to determine AC and quantify EE

3WM requires that a sample be readily brought into the gas phase (by either heating or laser ablation) and that the molecule of interest must have at least one non-zero electric dipole component for the survey mode and three non-zero electric dipole components for the chirality detection mode.

A design was originally attempted to use three mm-wave transitions for the 3WM cycles. However, for the test case molecule used in these studies, chiral emission could not be detected under these conditions. This was likely due to phase matching conditions discussed thoroughly in Chapter 2 and will be discussed in a later section. Instead, a combination of mm-wave and cm-wave instrumentation was used and generated a chiral signal in these measurements. We note that the addition of a cm-wave in this instrumentation adds much more power requirements to the overall instrument, and this effect is an area for future research.

A schematic of the spectrometer for the mm-wave/cm-wave three-wave mixing spectrometer is shown in Figures 4.1 and 4.2. mm-wave radiation was produced by passing lower

frequency microwave light from an Agilent E8267D analog signal synthesizer through a x6 active Millitech multiplier chain. Continuous wave radiation was pulsed by applying voltage to a switch for a set pulse duration controlled by an SRS DG645 Pulse Generator. This pulsed mm-wave was then amplified to ~100 mW through a series of JPL in-house amplifiers and broadcast by a wave horn antenna to an off-axis parabolic mirror. The mirror focuses the radiation through a Teflon window and into the vacuum chamber containing the gaseous sample.

Centimeter-wave (cm-wave) radiation was produced directly from a Valon 5015 signal generator and similarly pulsed using a switch. The cm-wave was amplified to 3 W and broadcast via a microwave wave horn antenna that was placed in the middle of the vacuum chamber, 7 cm away from the path of the excitation signal. Metal-backed microwave absorber foam was placed opposite this horn to limit reflections off the metal vacuum chamber.

The resulting chiral signal from the 3WM process was collected from an off-axis parabolic mirror rotated 90° in relation to the mirror of the driving $\frac{\pi}{2}$ - pulse. Detection of the chiral signal required mixing the emission with a signal generated from another Agilent E8267D analog signal generator that is passed through another x6 active multiplier chain to the Millitech mixer. All chiral signals were mixed down to 120 MHz and amplified before passing through a low pass filter and a high pass filter and then digitized by a Tektronix oscilloscope at 1 GS/s.

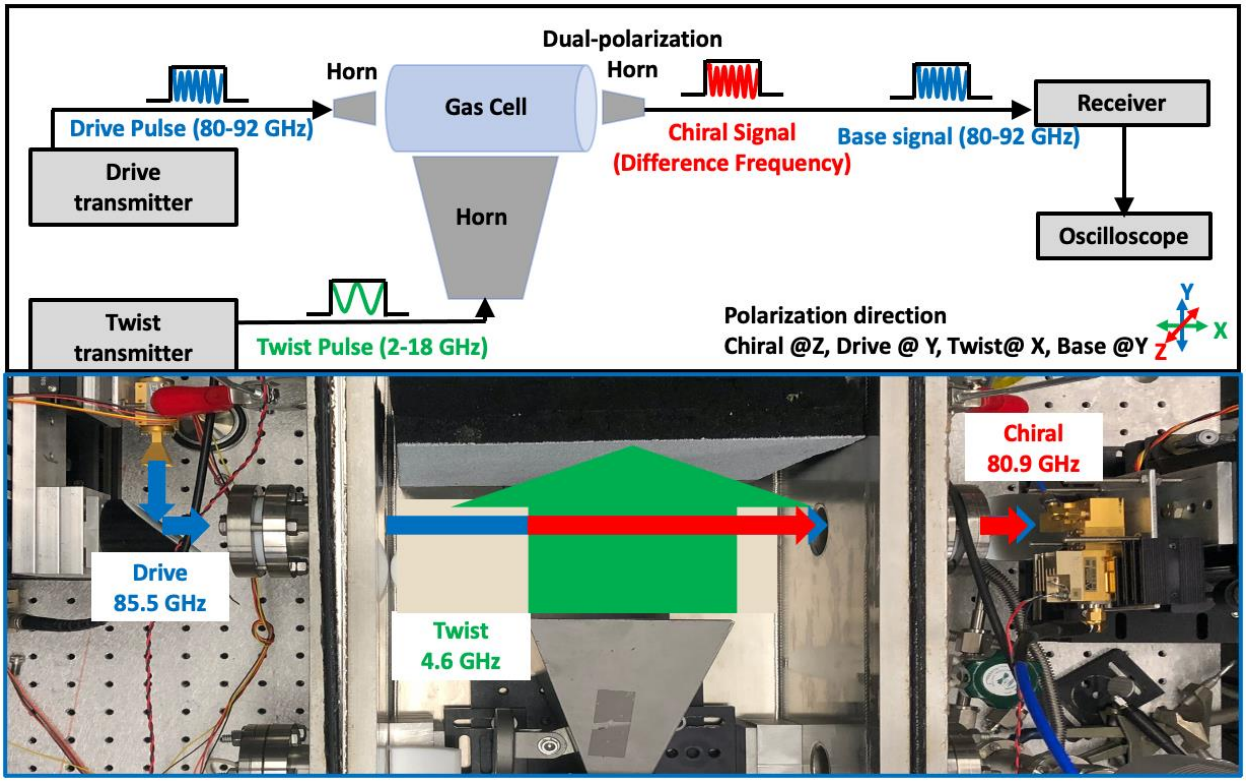

Figure 4.1: ChiralSpec block diagram (top) and experimental setup (bottom) for obtaining the chiral signals. The coherence generation pulse (Drive wave) propagates on the X-axis with Y-polarization. The coherence transfer pulse (Twist wave) propagates on the Y-axis with X-polarization. The chiral signal propagates on the X-axis with Z-polarization. ChiralSpec is in base spectroscopy mode if the receiver horn is rotated 90°.

Propylene oxide is used as a test case molecule due to its high volatility and compatible electric dipole components. This molecule is also the only chiral molecule to have been detected in the interstellar medium by radio astronomy detection.[8] R-, RS-, and S-propylene oxide were purchased from Sigma-Aldrich without further purification. Sample was introduced by opening a valve to a sample vial containing propylene oxide and allowing the vapor pressure to pressurize the chamber. A gate valve-controlled diffusion pump allowed for control over the pressure inside the chamber. All experiments were held at 3-5 mTorr to reduce pressure broadening.

Transition frequencies with their respective quantum numbers were obtained from the CDMS molecular database[9] and private communications with Holger Muller. 3WM cycles of a-, b-, and c-type transitions were chosen based upon transition dipole moment strength and calculated intensities at room temperature.

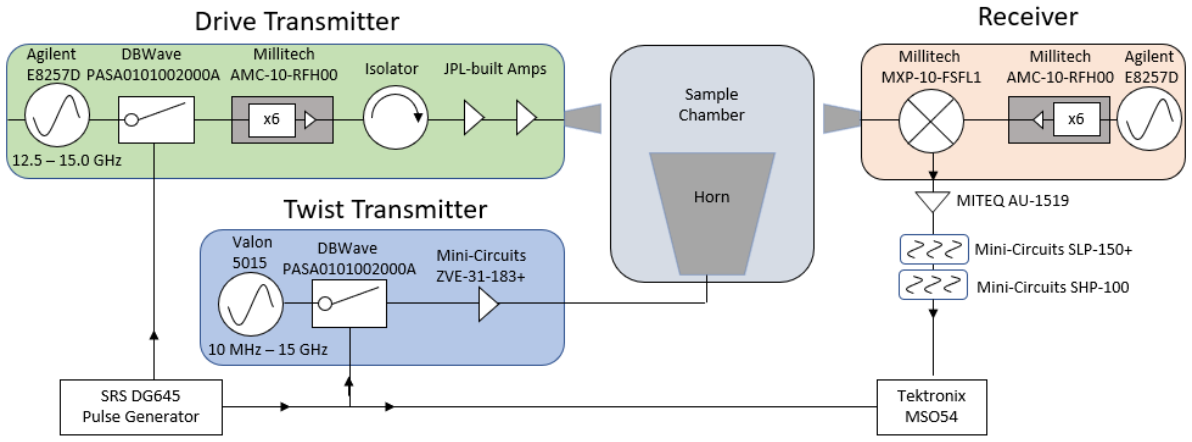

Figure 4.2: Schematic of the ChiralSpec Instrument. SPDT switches are used to produce square waves of various lengths from frequency synthesizers for optimal $\frac{\pi}{2}$ - and π - pulses to generate chiral emission of a static gas sample of ~3-5 mTorr.

4.3: *Results*

Multiple cycles were attempted using mm-wave and cm-wave radiation and the results are provided in Table 4.1. The 80866-4616-85482 MHz cycle was the only cycle of those tested to produce a detectable chiral signal. Cycles containing only Q-branch transitions are predicted to produce significantly weaker chiral signatures than for other cycles, and without a low frequency transition being incorporated in the cycle, the phase matching requirements are predicted to significantly reduce the chiral signature.[10]

Table 4.1: *3WM Cycles for Propylene Oxide Used in the ChiralSpec Experiments*

Pulse	Frequency (MHz)	J*	K_a*	K_c*	J	K_a	K_c	Log(I)[a]
π/2	80867.8138	7	0	7	6	1	6	-4.8
π	4616.345	7	1	7	7	0	7	-7.9
chiral	85484.1588	7	1	7	6	1	6	-5.1
π/2	83173.272	20	2	18	20	2	19	-6.5
π	12295.8013	20	3	18	20	2	18	-7.0
chiral	95469.0733	20	3	18	20	2	19	-4.6
π/2	80530.7695	6	1	6	5	0	5	-4.8
π	15261.4468	6	1	5	6	1	6	-7.9
chiral	95792.2163	6	1	5	5	0	5	-5.8
π/2	79714.7317	31	6	26	31	5	26	-5.8
π	12564.3821	31	6	25	31	6	26	-7.8
chiral	92279.1138	31	6	25	31	5	26	-4.4
π/2	81725.6294	6	4	3	6	3	3	-6.1
π	7052.9975	7	3	4	6	4	3	-7.9
chiral	88778.6269	7	3	4	6	3	3	-5.1

[a] Intensities were obtained from simulations of the spectrum at room temperature

The optimal pulse lengths for all W-band (75-110 GHz) transitions were measured by operating the spectrometer as a traditional rotational spectrometer. The excitation pulse duration was varied by opening a switch for different durations to find the maximum intensity of emitted radiation that follows a nutation curve for a given transition. The maxima of these curves determine the pulse length yielding optimal coherence between the two rotational states of the transition to determine the $\frac{\pi}{2}$ - pulse condition for that frequency. For example, in Figure 4.3, the 85482 MHz nutation curve yielded maximum intensity with a pulse duration of 440 ns.

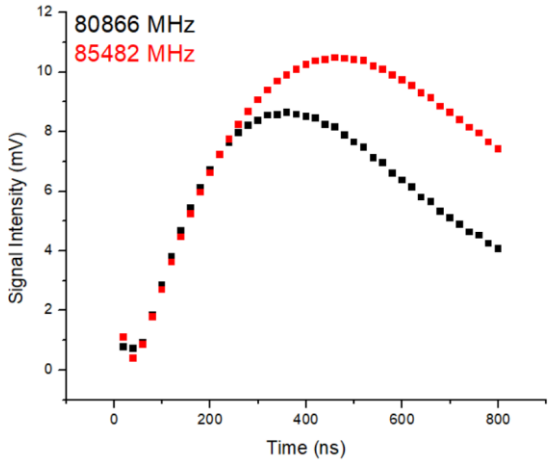

Figure 4.3: Nutation curves for the two W-band transitions within the 80866-4616-85482 MHz 3WM cycle by varying pulse duration. In general, these nutation curves are used to produce the greatest chiral emission intensity by finding the optimal pulse durations to meet the $\frac{\pi}{2}$ - and π – pulse conditions of the experiment.[11]

Following this procedure, the π - pulse duration was optimized by keeping the $\frac{\pi}{2}$ - pulse constant and monitoring the signal intensity of the chiral emission to obtain an additional nutation curve. The maximum chiral signal intensity produced determines the optimal π - pulse duration. Optimal position for the start of the π - pulse was investigated as well. Starting the π - pulse at the same time as the $\frac{\pi}{2}$ - pulse yielded the greatest chiral signal intensity with a 1.5 μs long pulse duration. This is most likely due to the fast decay (on the order of 2 μs) of the chiral emission at these frequencies. The described measurement scheme and 3WM cycle are depicted in Figure 4.4.

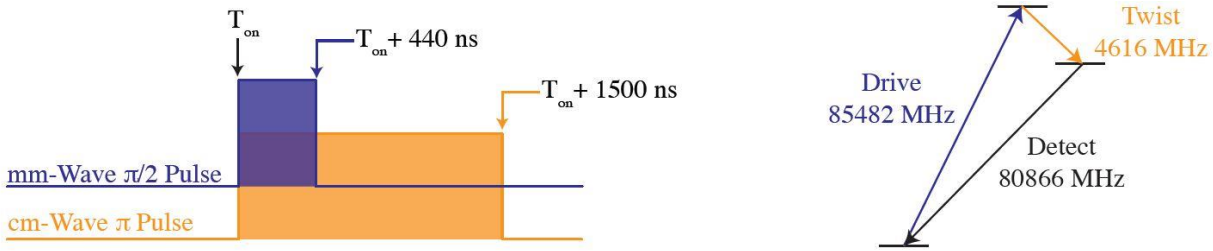

Figure 4.4: (Left) Measurement schematic for the two excitation pulses for the 80866-4616-85482 MHz 3WM cycle, including the relative timing of the pulses. These pulses were overlapped for optimal chiral signals. (Right) The 3WM cycle used for propylene oxide showing the Drive (coherence) and Twist (coherence transfer) transitions followed by the chiral emission closing the cycle.

The chiral emission was recorded in the time domain using a Tektronix oscilloscope at 1 GS/s and post-processed on a local computer. The W-band emission was mixed down to 120 MHz to require less processing speed during digitization. Due to the weak chiral emission, the time domain was digitally filtered to remove influence of electrical spurs and to clearly see the phase shift of 180° of the two enantiomers measured separately and no net signal for a racemic mixture. Figure 4.5 shows the results for each enantiomer and the racemic mixture measured separately. Collisional dephasing in these static gas cell experiments causes the coherence of the chiral and achiral emission to be much shorter, lasting ~2 μs compared to ~40 μs in the pulsed jet experiments in the literature.[11]

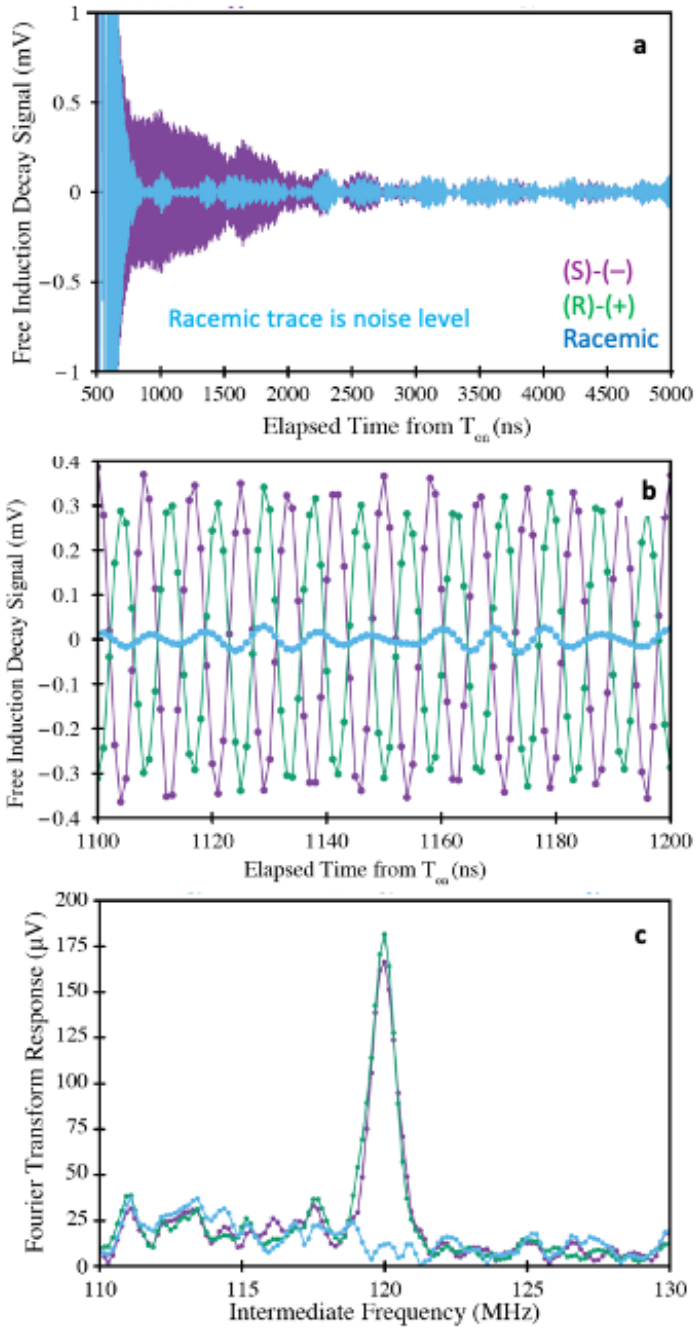

Figure 4.5: Achieved mm-wave chirality detection: (a) Raw time-domain signal showing signal duration of ~2.5 μs; (b) zoomed time-domain signal showing 180° phase difference between enantiomers; and (c) Fourier transform of the full 4.5 μs of emission collected. The received signal at 80866 MHz was mixed down to 120 MHz for digitization at 1 GS/s. The circles represent the digitization data points. A 180° phase shift is seen between the enantiomers (purple and green) and the racemic sample (blue) yields no observable signal above the noise. The emission is filtered to remove spurious signals and show the phase shift between enantiomers clearly.

4.4: *Discussion*

3WM rotational spectroscopy can provide a powerful insight into potential biomarkers. Homochirality detection or, more generally, the enantiomeric excess of key molecules like amino acids and sugars can aid in giving additional detail to complicated samples obtained in interesting locations within our solar system. ChiralSpec could also serve as a compliment to mass spectrometry for molecular identification through its survey mode.

ChiralSpec, when used as a traditional mm-wave spectrometer, can yield signals with high sensitivity for molecules with rotational transitions within its bandwidth. Rotational spectroscopy is also advantageous in the case of isomers or molecules of similar mass that mass spectrometry has challenges with. Detection is essentially background-free with minor caveats that the excitation and detection frequencies be separated far enough that the power distribution of the excitation does not overlap with the detection transition.

As a 3WM rotational spectrometer, the probability of a cycle producing chiral emission for another molecule is incredibly low; however, in these rare cases, there are often many cycles within the instrument's bandwidth that can be used in the experiment. Analytes with more than one low energy conformer will also have distinct rotational spectra and therefore distinct 3WM cycles. This is also advantageous if the lowest energy conformer has weaker electric dipole components or has transitions outside of the instrument's bandwidth. In the literature, 3WM has been demonstrated on molecules with multiple chiral centers, in complex mixtures of differing volatilities without prior separation, and on larger molecules with molecular weights around 150 g/mol.[11-17] Many smaller molecules considered as prebiotic or biotic such as sugars and amino

acids fall within this current limit and contain electric dipole components that are compatible with the 3WM technique.

Another important factor in the background-free detection is that the chiral emission is generated at a polarization that is orthogonal to the excitation polarizations. This allows one to build the instrument to further reduce size, weight, and power of the components and allows for more certainty in the measurement detection. The physical size of the instrument can be drastically reduced as the overlap of the injected sample by the two excitation beams, on the order of a few cm^3, is the region of greatest importance. Reduction in size and power of the electronics is also possible, and there have been impressive rotational spectrometers designed on chips demonstrating possible future designs.[18-21]

The 80866-4616-85482 MHz measurement cycle that generated the chiral signature for propylene oxide used a much lower frequency of light for the coherence transfer pulse than the initial coherence pulse and the chiral emission; the cycles involving three high frequency transitions yielded no net chiral signature. The chiral emission also produced a weaker chiral signal compared to signals obtained through single wave excitation. The literature and experiments performed at the University of Virginia suggest an efficiency of ~20-30% for the signal detected via the 3WM cycle compared to the signal generated from a single transition at that frequency. These experiments only had an efficiency of ~1%. The weakness of the chiral signature is likely due to the phase matching restrictions mentioned previously in Chapter 2 and will be explored in future work by using cycles with a lower π – pulse frequency.

Demonstration of AC differentiation was achieved in these experiments as shown previously in Figure 4.5. Absolute phase calibration of the chiral emission could determine the enantiomer in excess directly from the phase of the chiral emission compared to theory without a reference sample of known AC, but this calibration still requires additional research and a solution is not clear yet. However, with a reference sample of known EE, a calibration curve can be constructed incorporating the known EE and 0 EE (racemic mixture) occurring at the origin to determine an unknown EE.

The limit of detection (LOD) of $1x10^{-3}$ Torr ($3x10^{13}$ molecules/cm^3) and $3x10^{-5}$ Torr (10^{12} molecules/cm^3) was achieved for propylene oxide's chirality and base spectroscopy abundance measurements, respectively. Figure 4.6 shows the linear regression of peak height versus pressure to determine the LOD. The recording time for each spectral trace is 1 second. The three waves for chirality measurements are at 85.482 GHz (Drive), 4.616 GHz (Twist) and 80.866 GHz (Listen). The base spectroscopy is at 85.484 GHz and is performed by rotating the receiver horn 90° to change the polarization, as seen previously in Figure 4.1. The chiral signal intensity depends on how strongly the molecule can interact with light at the three frequencies involved in the 3WM as well as on phase matching restrictions. As mentioned in Chapters 2 and 3, literature results also suggest that it is essential to have a low frequency for the π – pulse in this instrument geometry. For example, Domingos *et al.* measure only ~1% efficiency of their chiral signal with a π – pulse of 3057 MHz.[12]

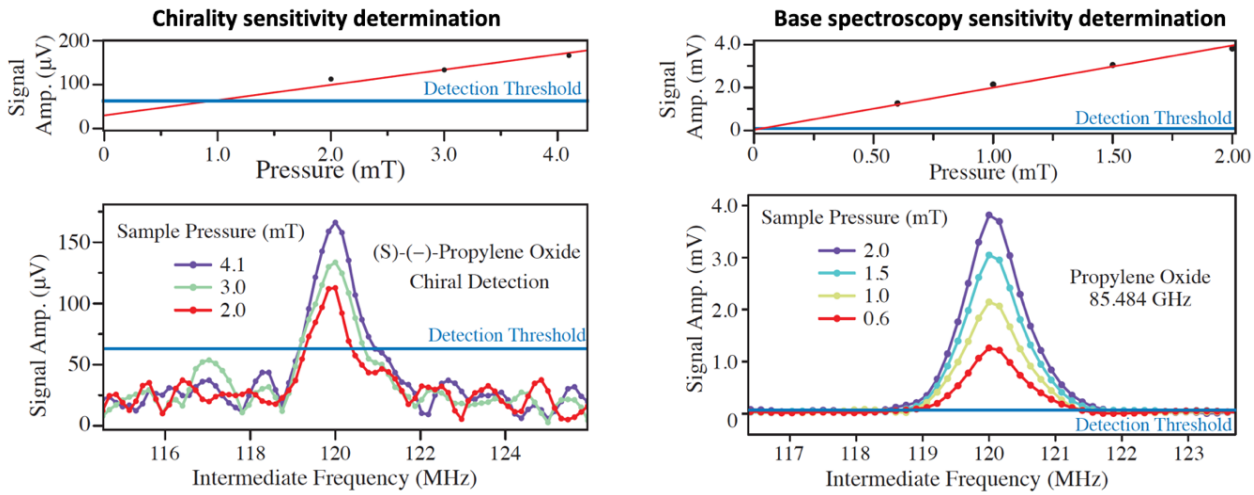

Figure 4.6. Propylene oxide chiral signals (left bottom) and single transition signals (right bottom) observed with ChiralSpec at various sample pressures. Linear regressions of peak height in μV versus pressure is shown on the top panels. Horizontal blue lines indicate the 5σ detection threshold which was obtained by multiplying the mean of noise signals between 115-116 MHz by 5. The cross point of the blue lines and linear regress indicates the limit of detection.

The detection sensitivity of ChiralSpec depends on the input pulse power, detector noise, and gas cell length. ChiralSpec's LOD for propylene oxide can be improved by two orders of magnitude to 10^{-5} Torr (3×10^{11} molecules/cm^3) for chirality and 3×10^{-7} Torr (10^{10} molecules/cm^3) for abundance quantification. The sensitivity improvement can be achieved by

(1) 100 times faster data acquisition by replacing the oscilloscope with a faster digitizer

(2) 100 times longer data acquisition time (100 seconds versus 1 second).

Each of the improvements increases the sensitivity by $\sqrt{100} = 10$. We have confirmed these two sensitivity improvements are feasible by performing Allen deviation measurements, where the Allen time is how long one instrument can integrate to increase the signal-to-noise ratio. The Allen time with the implementation of the two improvements is 26 minutes. Once the Allen time is surpassed, the signal-to-noise ratio doesn't increase with further integration. Therefore,

increasing the integration time by two orders of magnitude to 100 seconds will increase the signal-to-noise ratio by 10.

4.5: *Conclusions*

The novel approach of using mm-wave radiation in 3WM rotational spectroscopy to produce chiral emission of the enantiomers of propylene oxide was demonstrated in this work. The use of mm-wave technology significantly reduced the power requirements of excitation and detection chains for the experiment as well as reducing the physical size and weight for future instrument models to comply with the stringent requirements of extraterrestrial missions. The ChiralSpec instrument aims to operate in two modes: one to search for molecular signals from many molecules within the instruments bandwidth and the second to operate in the chiral signature detection mode that uses 3WM rotational spectroscopy. Future studies will involve improving the efficiency of the 3WM chiral signal compared to the signal of single photon excitation as well as studying larger and more complex molecules, such as the amino acid alanine, that are more relevant as biomarkers. These larger molecules are often challenging to bring into the gas phase without thermal dissociation, so this will be explored. Possible complications could include molecules with atoms that produce hyperfine splitting of rotational transitions like that of nitrogen. Furthermore, different instrument geometry schemes will be examined, including applying orthogonally polarized excitation pulses in the same direction and the detection of the chiral signature in the perpendicular direction.

Chapter 4 References:

1. Blackmond, D. G., The origin of biological homochirality. *Philos Trans R Soc Lond B Biol Sci* **2011,** *366* (1580), 2878-84.
2. Visions and Voyages for Planetary Science in the Decade 2013-2022. http://solarsystem.nasa.gov/2013decadal/.
3. Russell, M. J.; Murray, A. E.; Hand, K. P., The Possible Emergence of Life and Differentiation of a Shallow Biosphere on Irradiated Icy Worlds: The Example of Europa. *Astrobiology* **2017,** *17* (12), 1265-1273.
4. al., G. e., Organic compounds on comet 67P/Churyumov-Gerasimenko revealed by COSAC mass spectrometry. *Science* **2015,** *349* (6247).
5. Goesmann, F.; Brinckerhoff, W. B.; Raulin, F.; Goetz, W.; Danell, R. M.; Getty, S. A.; Siljeström, S.; Mißbach, H.; Steininger, H.; Arevalo, R. D.; Buch, A.; Freissinet, C.; Grubisic, A.; Meierhenrich, U. J.; Pinnick, V. T.; Stalport, F.; Szopa, C.; Vago, J. L.; Lindner, R.; Schulte, M. D.; Brucato, J. R.; Glavin, D. P.; Grand, N.; Li, X.; van Amerom, F. H. W.; the, M. S. T., The Mars Organic Molecule Analyzer (MOMA) Instrument: Characterization of Organic Material in Martian Sediments. *Astrobiology* **2017,** *17* (6-7), 655-685.
6. Stephens, P. J., Theory of Vibrational Circular Dichroism. *J. Phys. Chem.* **1985,** *89* (5), 748-752.
7. He, Y.; Wang, B.; Dukor, R. K.; Nafie, L. A., Determination of absolute configuration of chiral molecules using vibrational optical activity: a review. *Appl Spectrosc* **2011,** *65* (7), 699-723.
8. Brett A. McGuire, P. B. C., Ryan A. Loomis, Ian A. Finneran, Philip R. Jewell, Anthony J. Remijan, Geoffrey A. Blake, Discovery of the interstellar chiral molecule propylene oxide (CH3CHCH2O). *Science* **2016,** *352* (6292), 1449-1452.
9. Müller, H. S. P.; Thorwirth, S.; Roth, D. A.; Winnewisser, G., The Cologne Database for Molecular Spectroscopy, CDMS. *Astronomy & Astrophysics* **2001,** *370* (3), L49-L52.
10. Lehmann, K. K., Influence of spatial degeneracy on rotational spectroscopy: Three-wave mixing and enantiomeric state separation of chiral molecules. *J Chem Phys* **2018,** *149* (9), 094201.
11. Lobsiger, S.; Perez, C.; Evangelisti, L.; Lehmann, K. K.; Pate, B. H., Molecular Structure and Chirality Detection by Fourier Transform Microwave Spectroscopy. *J Phys Chem Lett* **2015,** *6* (1), 196-200.
12. Domingos, S. R.; Perez, C.; Marshall, M. D.; Leung, H. O.; Schnell, M., Assessing the performance of rotational spectroscopy in chiral analysis. *Chem Sci* **2020,** *11* (40), 10863-10870.
13. Patterson, D.; Schnell, M., New studies on molecular chirality in the gas phase: enantiomer differentiation and determination of enantiomeric excess. *Phys Chem Chem Phys* **2014,** *16* (23), 11114-23.
14. Shubert, V. A.; Schmitz, D.; Patterson, D.; Doyle, J. M.; Schnell, M., Identifying enantiomers in mixtures of chiral molecules with broadband microwave spectroscopy. *Angew Chem Int Ed Engl* **2014,** *53* (4), 1152-5.
15. Shubert, V. A.; Schmitz, D.; Medcraft, C.; Krin, A.; Patterson, D.; Doyle, J. M.; Schnell, M., Rotational spectroscopy and three-wave mixing of 4-carvomenthenol: A technical guide to measuring chirality in the microwave regime. *J Chem Phys* **2015,** *142* (21), 214201.
16. Krin, A.; Perez, C.; Pinacho, P.; Quesada-Moreno, M. M.; Lopez-Gonzalez, J. J.; Aviles-Moreno, J. R.; Blanco, S.; Lopez, J. C.; Schnell, M., Structure Determination, Conformational Flexibility, Internal Dynamics, and Chiral Analysis of Pulegone and Its Complex with Water. *Chemistry* **2018,** *24* (3), 721-729.
17. Domingos, S. R.; Perez, C.; Schnell, M., Sensing Chirality with Rotational Spectroscopy. *Annu Rev Phys Chem* **2018**.

18. Drouin, B. J.; Tang, A.; Schlecht, E.; Brageot, E.; Gu, Q. J.; Ye, Y.; Shu, R.; Frank Chang, M. C.; Kim, Y., A CMOS millimeter-wave transceiver embedded in a semi-confocal Fabry-Perot cavity for molecular spectroscopy. *J Chem Phys* **2016,** *145* (7), 074201.
19. Nemchick, D. J.; Drouin, B. J.; Cich, M. J.; Crawford, T.; Tang, A. J.; Kim, Y.; Reck, T. J.; Schlecht, E. T.; Chang, M. F.; Virbila, G., A 90-102 GHz CMOS based pulsed Fourier transform spectrometer: New approaches for in situ chemical detection and millimeter-wave cavity-based molecular spectroscopy. *Rev Sci Instrum* **2018,** *89* (7), 073109.
20. Nemchick, D. J.; Drouin, B. J.; Tang, A. J.; Kim, Y.; Chang, M.-C. F., Sub-Doppler Spectroscopy With a CMOS Transmitter. *IEEE Transactions on Terahertz Science and Technology* **2018,** *8* (1), 121-126.
21. Tang, A.; Drouin, B.; Kim, Y.; Virbila, G.; Chang, M.-C. F., 95–105 GHz 352 mW All-Silicon Cavity-Coupled Pulsed Echo Rotational Spectroscopy System in 65 nm CMOS. *IEEE Transactions on Terahertz Science and Technology* **2017,** *7* (3), 244-249.

Chapter 5: Copper-Catalyzed Transfer Hydrodeuteration of Aryl Alkenes with Quantitative Isotopomer Purity Analysis by Molecular Rotational Resonance Spectroscopy

The following chapter is primarily reproduced from Vang, Z. P.; Reyes, A.; Sonstrom, R. E.; Holdren, M. S.; Sloane, S. E.; Alansari, I. Y.; Neill, J. L.; Pate, B. H.; Clark, J. R., Copper-Catalyzed Transfer Hydrodeuteration of Aryl Alkenes with Quantitative Isotopomer Purity Analysis by Molecular Rotational Resonance Spectroscopy. J Am Chem Soc ***2021,*** *143 (20), 7707-7718. The Supplementary Information, which contains much more detail on the synthetic chemistry, NMR results, and quantum chemistry calculations outside of the scope of this dissertation, can be found here: https://doi.org/10.1021/jacs.1c00884*

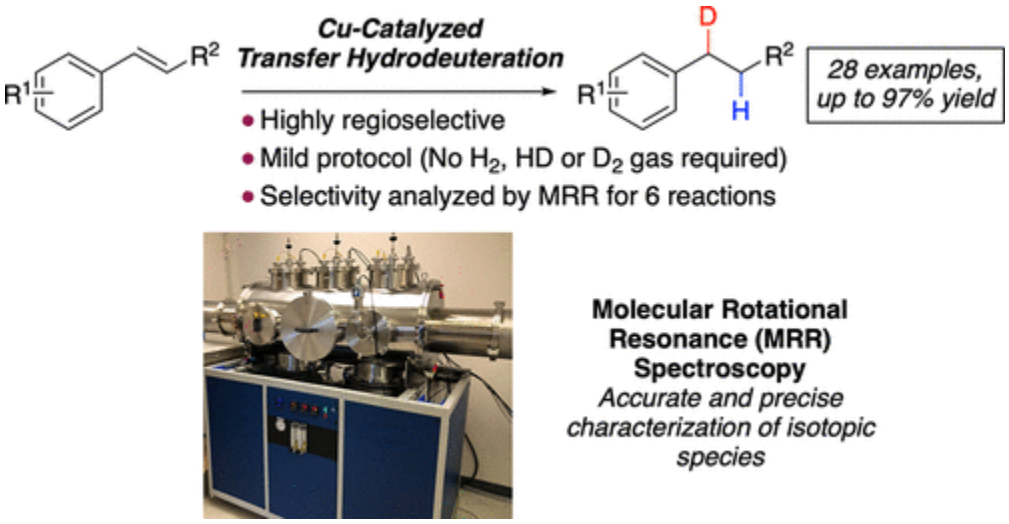

5.1: *Abstract*

A copper-catalyzed alkene transfer hydrodeuteration reaction that selectively incorporates one hydrogen and one deuterium atom across an aryl alkene is described. The transfer hydrodeuteration protocol is selective across a variety of internal and terminal alkenes and is also demonstrated on an alkene-containing complex natural product analog. Beyond using ^{1}H, ^{2}H, and ^{13}C NMR analysis to measure reaction selectivity, six transfer hydrodeuteration products were analyzed by molecular rotational resonance (MRR) spectroscopy. The application of MRR spectroscopy to the analysis of isotopic impurities in deuteration chemistry is further explored through a measurement methodology that is compatible with high-throughput sample

analysis. In the first step, the MRR spectroscopy signatures of all isotopic variants accessible in the reaction chemistry are analyzed using a broadband chirped-pulse Fourier transform microwave spectrometer. With the signatures in hand, measurement scripts are created to quantitatively analyze the sample composition using a commercial cavity enhanced MRR spectrometer. The sample consumption is below 10 mg with analysis times on the order of 10 min using this instrument—both representing order-of-magnitude reduction compared to broadband MRR spectroscopy. To date, these measurements represent the most precise spectroscopic determination of selectivity in a transfer hydrodeuteration reaction and confirm that product regioselectivity ratios of >140:1 are achievable under this mild protocol.

5.2: *Introduction*

Reactions that incorporate deuterium into molecular scaffolds are of topical relevance to scientists across several disciplines. Among many applications, deuterated small molecules are used as standards for high-resolution mass spectrometry[1–3] and can serve as probes to study reaction mechanisms,[4,5] perform kinetic isotope effect experiments,[6,7] determine the stereochemical course of microbiological or enzymatic reactions, and elucidate biosynthetic pathways.[8–17] Importantly, deuterated small molecules are also deployed to alter absorption, distribution, metabolism, and excretion (ADME) properties of drug molecules.[18,19] Consequently, designing deuterated bioisosteres to modify the metabolic "soft spots" of small molecule drugs holds much potential for the development of safer therapeutics.[20–24]

Transition metal catalyzed reactions are commonly used to selectively install oxygen, nitrogen, or carbon functionality into small molecules.[25,26] Mild protocols and modular catalytic

frameworks are often exploited in these reactions to optimize both reactivity and selectivity. However, highly selective transition metal catalyzed methods for deuterium incorporation remain underdeveloped. For example, transition metal catalyzed hydrogen isotope exchange (HIE) reactions efficiently incorporate deuterium into small molecules, but significant challenges exist to control the quantity and precise placement of deuterium in a given molecule.[27,28] Specific to making small molecules with one deuterium atom installed at a benzylic carbon, a general technique to access small molecules with a benzylic C(sp^2)–D bond was recently reported.[29] However, to make a small molecule with exactly one benzylic C(sp^3)–D bond, chemists typically use reactions involving stoichiometric organometallic intermediates.[30]

The similar physical properties of deuterium relative to hydrogen further complicate unselective deuteration reactions. Isotopic mixtures are not only inseparable using common purification techniques, but common spectroscopic techniques used to characterize organic compounds are insufficient at measuring the precise location and quantity of deuterium in isotopic product mixtures. This can have major implications in drug discovery, and guidance to address deuterated active pharmaceutical ingredients (APIs) is being developed for these spectroscopic and synthetic challenges.[31] Ultimately, synthetic access to deuterated compounds free of isotopic impurities and analytical methods to identify all isotopic species in a product mixture will be crucial for developing novel deuterated APIs.

Catalytic transfer hydrogenations represent powerful and mild methods for the reduction of alkene functionality.[32–35] We believe that mechanistically similar catalytic transfer hydrodeuteration reactions hold much promise for making selectively deuterated small molecules. Until recently, selective catalytic hydrodeuteration reactions were rare and usually

employed as mechanistic probes for alkyne semireductions.[36–38] A major challenge in catalytic transfer hydrodeuteration is discriminating between hydrogen (H) and deuterium (D) for selective incorporation into alkene functionality.[39,40] Catalytic alkene transfer hydrodeuteration reactions are now possible on a variety of alkenes.[41–45] Transition metal catalyzed transfer hydrodeuteration typically occurs in a regioselective manner for unactivated terminal alkenes, but selectivity is generally lower for terminal aryl alkene substrates (Scheme 5.1a).[41–43] Alternatively, using a boron catalyst, highly selective installation of deuterium into activated 1,1-diarylalkenes is possible, but with a limited alkene scope (Scheme 5.1b).[44,45]

Scheme 5.1. *Transfer Hydrodeuteration of Alkenes*

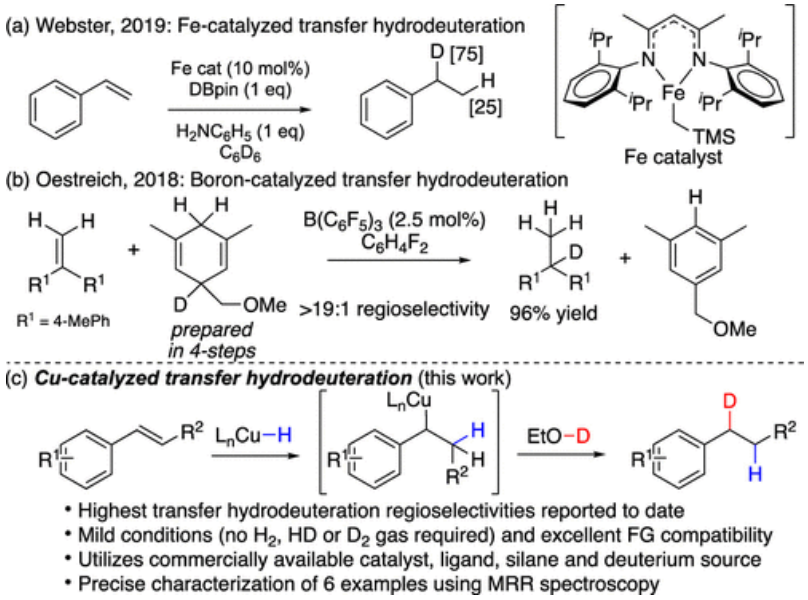

5.3: *Reaction Optimization and Scope*

Based on insight gleaned from our recently published Cu-catalyzed regioselective aryl alkyne transfer hydrodeuteration studies, we hypothesized that a highly regioselective aryl alkene transfer hydrodeuteration may be possible (Scheme 5.1c).[46] Cu-catalyzed aryl alkene hydroamination reactions are also regioselective, and we envisioned the transfer hydrodeuteration occurring with excellent regioselectivity because of the thermodynamic favorability of the benzylic copper intermediate depicted in Scheme 5.1c.[47–51] Under transfer hydrodeuteration conditions, we reasoned that the H-donor and D-donor would operate at distinct points during the reaction and therefore allow for precise insertion of each atom at the desired location within the aryl alkene.

Accordingly, *tert*-butyldimethylsilyl-protected (TBS) cinnamyl alcohol *trans*-**1** was chosen as the aryl alkene for reaction optimization. In the presence of catalytic $Cu(OAc)_2$, dimethoxymethylsilane (DMMS was chosen for the optimization studies because it can be easily removed under vacuum during product purification), and EtOD, we found that bidentate bisphosphine ligands such as DPPE, DPPF, *rac*-BINAP, and DPPBz were not efficient at supporting the desired transformation (Table 5.1, entries 1–4). Switching to the more sterically crowded DTB-DPPBz ligand dramatically affected reactivity, and deuterated aryl alkane **2** was isolated in 85% yield (entry 5). Importantly, evaluation of the product by ^{1}H, ^{2}H, and ^{13}C NMR revealed that one deuterium atom was incorporated exclusively at the benzylic position (>20:1 regioselective ratio). Varying the deuterium source revealed that using CH_3OD led to a slight decrease in yield (entry 6), while D_2O only led to partial conversion to product **2** (entry 7). Employing 2-propanol-d_8 permitted the catalyst loading to be lowered and was similarly efficient as EtOD (entry 8).

Ultimately, returning to the reaction conditions from entry 5 and decreasing the catalyst loading to 1 mol % was found to be optimal (entry 9).

Table 5.1. *Reaction Optimization*[a]

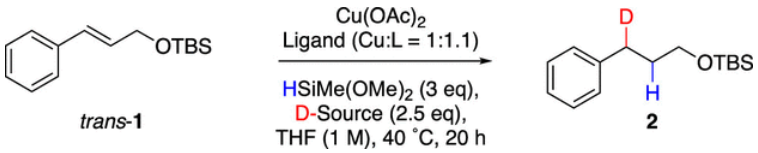

Entry	$Cu(OAc)_2$	Ligand	D-Source	**1** (%)	**2**(%)
1	2 mol%	L1	EtOD	69[b]	--
2	2 mol%	L2	EtOD	70[b]	--
3	2 mol%	L3	EtOD	89[b]	--
4	2 mol%	L4	EtOD	47[b]	--
5	2 mol%	L5	EtOD	--	85[c]
6	2 mol%	L5	MeOD	8[c]	69[c]
7	2 mol%	L5	D_2O	59[c]	21[c]
8	1 mol%	L5	IPA-d_8	--	85[c]
9	1 mol%	L5	EtOD	--	90[c]

[a]Reactions conducted using 0.2 mmol of substrate. $Cu(OAc)_2$ was used as a 0.2 M solution in THF.
[b]Yield was determined by ^1H NMR analysis of the crude reaction mixture, using mesitylene as an internal standard.
[c]Denotes isolated product yield.

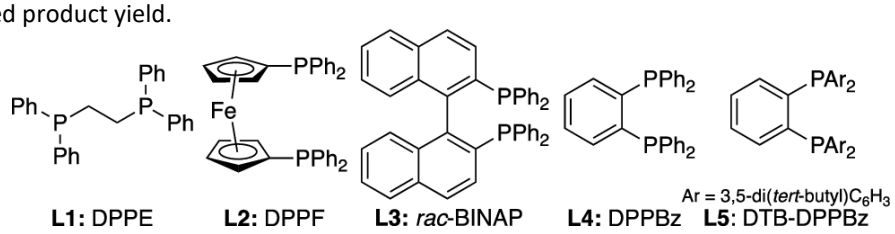

With the optimal reaction conditions in hand, we evaluated the substrate scope of the reaction (Scheme 5.2). Electron-rich monosubstituted alkenyl arenes containing oxygen functionality performed well in the reaction, and excellent yields of the desired deuterated products were obtained (Scheme 5.2a, **4a**–**4d**, 73–97% yield). Alternatively, an alkenyl arene substituted with an electron-withdrawing nitro group also underwent transfer hydrodeuteration

to provide the deuterated aryl alkane, albeit in moderate yield (**4e**, 47% yield). Nitrogen substitution is permitted on the alkenyl arene substrate (**4f**–**4g**, 57–97% yield). Importantly, we demonstrated that polymethylhydrosiloxane could be used instead of DMMS in the synthesis of **4g**. We also found that (4-vinylphenyl)boronic acid pinacol ester can undergo Cu-catalyzed transfer hydrodeuteration (**4h**, 67% yield).

Scheme 5.2. *Aryl Alkene Transfer Hydrodeuteration Substrate Scope*

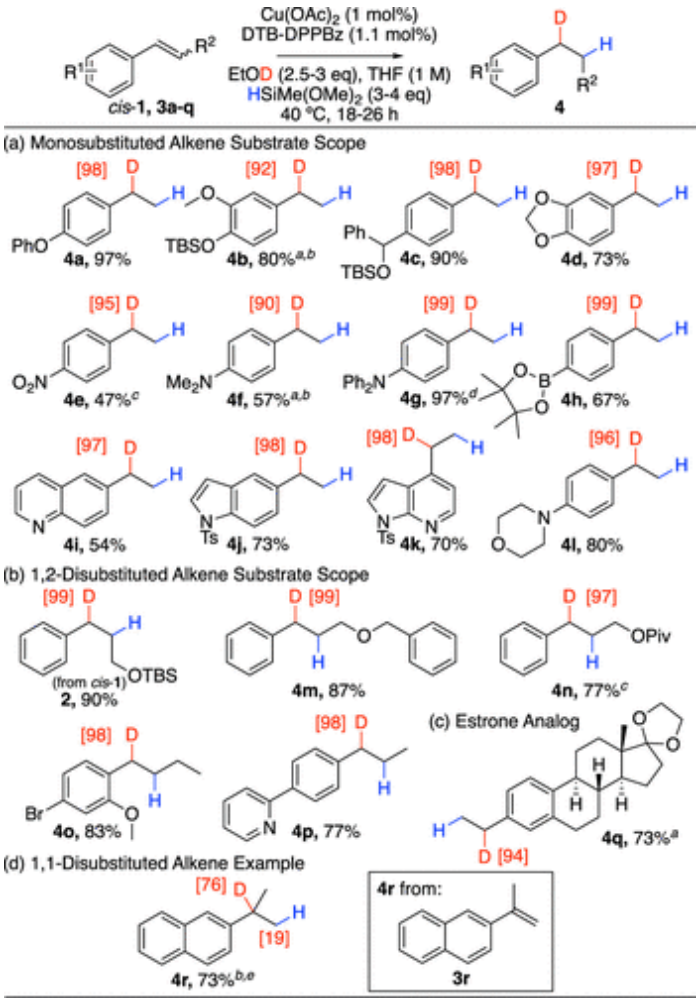

[a]2 mol % $Cu(OAc)_2$ and 2.2 mol % DTB-DPPBz used.
[b]IPA-d_8 (3 equiv) used instead of EtOD.
[c]Reaction conducted at 5 °C.
[d]Polymethylhydrosiloxane (3 equiv) used instead of $HSiMe(OMe)_2$.
[e]3 mol % $Cu(OAc)_2$, 3.3 mol % DTB-DPPBz, and $HSiMe(OMe)_2$ (4 equiv) used at 60 °C.

Due to their prevalence in bioactive molecules, nitrogen- and oxygen-containing heterocycles were examined under the transfer hydrodeuteration protocol.[52,53] We found that quinoline, indole, and azaindole substituted alkenes perform well in the transfer hydrodeuteration reaction (**4i**–**4k**, 54–73% yield). Alternatively, an alkenyl arene substituted with a morpholine ring is efficiently converted to the deuterated aryl alkane product (**4l**, 80% yield). Internal alkene substrates are also viable candidates for transfer hydrodeuteration. Cinnamyl alcohol derivatives were evaluated when the alcohol was protected with a TBS, benzyl (Bn), or pivaloyl (Piv) group (Scheme 5.2b). All three derivatives were deuterated in high yield (**2**, **4m**–**4n**, 77–90% yield). Notably, product **2** was synthesized from the *cis*-alkene starting material, whereas in Table 5.1 it was synthesized from the *trans*-alkene starting material. Substitution on the arene is also possible for internal alkene substrates. A bromine substituted alkenyl arene and pyridine substituted alkenyl arene underwent transfer hydrodeuteration in high yield (**4o**–**4p**, 77–83% yield). Notably, no dehalogenation product was observed in the synthesis of **4o**. We also explored the capacity for the Cu-catalyzed transfer hydrodeuteration to proceed in a complex small molecule setting (Scheme 5.2c). Accordingly, a vinyl substituted estrone analog was deuterated in good yield (**4q**, 73% yield). Lastly, we evaluated the transfer hydrodeuteration reaction selectivity for a 1,1-disubstituted aryl alkene (Scheme 5.2d). The reaction of **3r** was only moderately selective with deuterium incorporation favoring the benzylic position (4:1 benzylic:methyl selectivity). We attribute the moderate selectivity to the demanding steric environment of this 1,1-disubstituted alkene inhibiting the Cu-catalyst from approaching the benzylic site.

The alkenyl arene transfer hydrodeuteration scope was extended, and the resulting isotopic products were analyzed using molecular rotational resonance (MRR) spectroscopy (Scheme 5.3; see below for analysis details). In addition to a vinyl biphenyl substrate, polyaromatic compounds such as 2-vinylnaphthalene and 2-methoxy-6-vinylnaphthalene were readily converted to their corresponding deuterated products (**6a**–**c**, 83–91% yield). Heterocycle-containing aryl alkenes and an internal alkene were also evaluated under the transfer hydrodeuteration protocol (**6d**–**6f**, 76–86% yield). In all six examples, the major products (**6a**–**f**) were formed in high yield in a highly regioselective manner. In addition to providing higher sensitivity measurements for isotopic product analysis, using MRR to analyze the reaction products depicted in Scheme 5.3 further validates our claims that this reaction is highly regioselective. It removes any ambiguity when analyzing isotopic product mixtures consisting of isotopologues and isotopomers that share deuterium substitution at the same atom, such that several isotopic species contribute to the same $^{1}H/^{2}H$ resonance in an NMR spectrum. It also precisely quantifies each regioisomer, even when the d_0-species is present in the product mixture.

Scheme 5.3. *Substrate Scope Analyzed by Molecular Rotational Resonance*

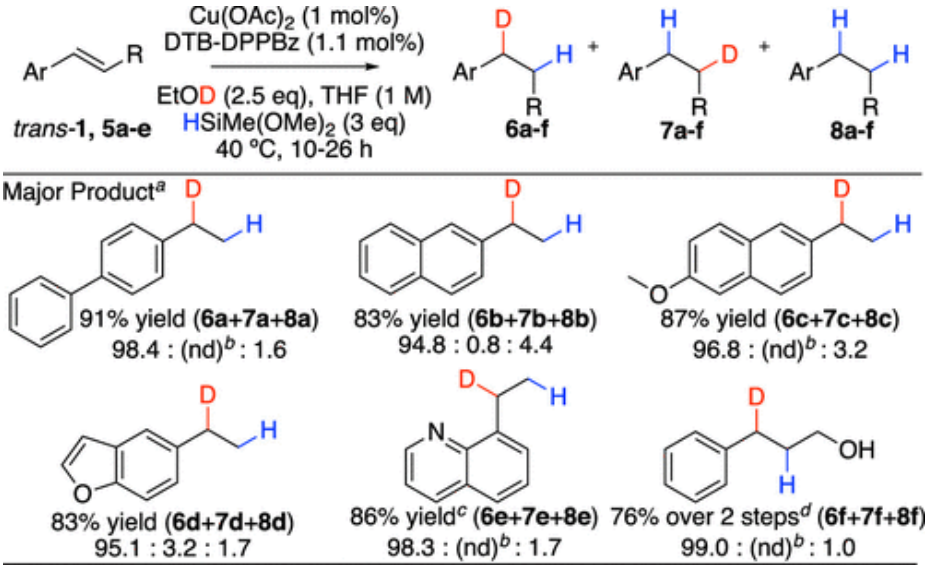

[a]The major products were **6a**–**f**, the product distribution was determined by MRR, and the ratio represents the ratio of all products in the product mixture (**6a**–**f**:**7a**–**f**:**8a**–**f**) after purification.
[b]Compound not detected (nd) by ^{2}H NMR or MRR. See Supporting Information (SI) for detection limits.
[c]2 mol % $Cu(OAc)_2$ and 2.2 mol % DTB-DPPBz were used.
[d]Transfer hydrodeuteration product was purified then subjected to TBS deprotection.

To demonstrate the versatility of the reaction, we hypothesized that flipping the regioselectivity of the reaction would be possible by simply replacing the Si–H and EtOD with Si–D and EtOH. This was examined with vinyl biphenyl substrate **5a** (Scheme 5.4a) and resulted in an 80% yield of desired product **7a**. An increase of the "underdeuterated" transfer hydrogenation side product **8a** was observed in this reaction likely because of the reduced deuterium content in the Si–D reagent.

Scheme 5.4. *Reaction Studies*

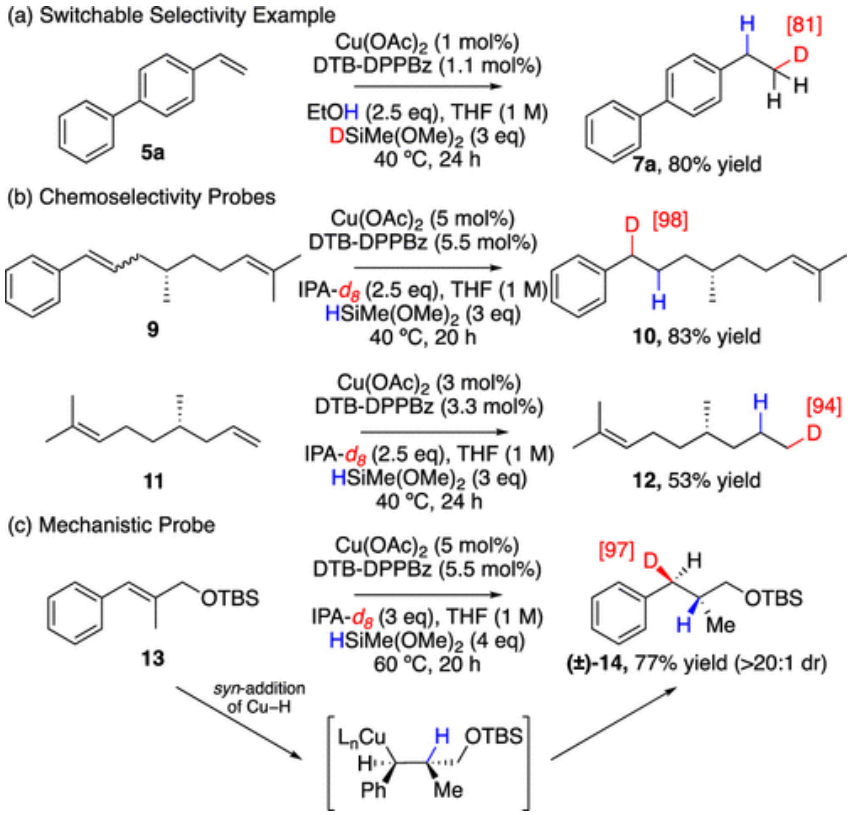

To probe the chemoselectivity of the reaction, we performed the transfer hydrodeuteration on a substrate containing both a 1,2-disubstituted styrenyl alkene and 1,1,2-trisubstituted alkene (Scheme 5.4b, substrate **9**). We were pleased to find the reaction was not only highly selective for incorporation of deuterium at the benzylic site of **10** but also chemoselective, as no reduction of the 1,1,2-trisubstituted alkene was observed. Another chemoselectivity probe was carried out using substrate **11**. In this case, the chemoselective reaction of an unactivated terminal alkene was evaluated in the presence of a more sterically hindered internal alkene. Furthermore, substrate **11** evaluated the potential for an unactivated alkene to undergo regioselective Cu-catalyzed transfer hydrodeuteration using the DTB-DPPBz ligand. Isolation of deuterated product **12** revealed that the reaction was highly selective for

copper inserting into the less sterically hindered terminal position of the terminal alkene, as no reduction of the trisubstituted alkene was observed. Ongoing studies in our research group are underway to explore the scope of the Cu-catalyzed alkene transfer hydrodeuteration for unactivated alkenes. Lastly, we probed whether the selectivity of the Cu–H insertion into the alkene occurred with *syn*- or *anti*-addition using 1,2,2-trisubstituted alkene **13**. We isolated product **(±)-14** in 77% yield (>20:1 dr) which suggests that *syn*-addition of the Cu–H across the alkene is operative (Scheme 5.4c). Furthermore, this example also indicates that trisubstituted alkenes are viable substrates for regioselective transfer hydrodeuteration.

5.4: *Spectroscopic Analysis of Products*: *Quantitative Sample Analysis by Molecular Rotational Resonance Spectroscopy – A New Tool for Deuteration Chemistry*

The isotopic composition of the reaction products depicted in Scheme 5.3 was analyzed by molecular rotational resonance (MRR) spectroscopy. The measurements provide high resolution and specificity for the analysis of isotopic species and represent the first quantitative assessment of the MRR spectroscopy technique for deuterated impurity analysis. In MRR spectroscopy, the rotational spectrum arises through electric-dipole transitions between the quantized rotational kinetic energy levels of the molecule.[54] In the rigid rotor approximation, the energy levels can be calculated from the three rotational constants (*A*, *B*, *C*) derived from the moments-of-inertia for rotation about the three principal rotational axes (I_A, I_B, I_C),

$$A = \frac{\hbar^2}{2 * I_A} \tag{5.1}$$

where the moment-of-inertia is calculated from the nuclear masses and the shortest distance of each nucleus to the rotation axis.

$$I_A = \sum m_i r_{A_i}^2 \tag{5.2}$$

The intensities for the rotational transitions are governed by the electric dipole moment, and the molecule must be polar to have a rotational spectrum.

MRR spectroscopy provides measurement solutions for several of the challenges that have been highlighted for the analysis of deuterated molecules.[31] The important feature of rotational spectroscopy in this application is that each isotopic variant has its own unique spectral signature. In particular, isotopomers have distinct MRR spectra and can be separately analyzed within a complex mixture.[55] By comparison, mass spectrometry can only analyze the isotopologue composition. NMR spectroscopy also has limitations and cannot perform the composition analysis when isoptologues and isotopomers in the mixture share deuterium substitution at the same atom such that several isotopic species contribute to the same $^{1}H/^{2}H$ resonance. MRR spectroscopy has two additional advantages in this application. First, MRR spectroscopy has exceptionally high spectral resolution so that spectral overlap is not an issue even for complex mixtures. Second, the rotational spectrum for any isotopic variant can be predicted to high accuracy using the equilibrium geometry obtained from quantum chemistry so that high-confidence identification of isotopic species is possible without the need for reference samples.[55–57]

For the products depicted in Scheme 5.3, the rotational spectrum was measured using a broadband chirped-pulse Fourier transform microwave (CP-FTMW) spectrometer operating in

the 2–8 GHz frequency range.[58–60] The broadband spectral coverage makes it possible to capture enough of the rotational spectrum to obtain a highly characteristic spectral pattern for each isotopic variant of the analyte present in the sample. The adiabatic expansion of a dilute mixture of the analyte in neon (0.1% mixture) into the spectrometer vacuum chamber produces a cold gas with a rotational temperature of about 1 K. The cooling of the gas increases the measurement sensitivity through reduction of the partition function. The reduced Doppler broadening of the pulsed jet expansion produces a high-resolution spectrum (line width of about 70 kHz fwhm). This feature is crucial in isotopologue/isotopomer analysis because it is not possible to separate the different species by chromatography to simplify the analysis.[61] CP-FTMW instruments have a large linear dynamic range so that quantitative analysis can be performed using the spectral transition intensities even for trace impurities.[58]

In the Cu-catalyzed transfer hydrodeuteration reaction, a possible impurity is the "misdeuterated" reaction product that results from deuterium inserting at the homobenzylic position and hydrogen at the benzylic position (minor product **7** in Scheme 5.3). The reaction is also expected to produce "underdeuterated" reaction product where there is no deuterium incorporation (minor product **8** in Scheme 5.3). This reaction product is expected from the hydrogen impurities in the alcohol-OD or trace H_2O in the alkenyl arene substrate, silane, and alcohol-OD. An overview of the MRR analysis for two of the reaction products is shown in Figure 5.1. The top panel of images shows narrow regions of the measured spectrum where the strongest transition in the rotational spectrum of different isotopic variants of 5-ethylbenzofuran (**6d**, **7d**, **8d**) are expected. The dominant isotopic species in the sample is the desired reaction product **6d** as indicated by the strong observed transition in the rotational spectrum assigned to

this isotopomer. The attribution of the observed spectrum to the specific isotopomer is based on the agreement between experimental and theoretical rotational constants. For the transfer hydrodeuteration of 5-vinylbenzofuran, the underdeuterated impurity **8d** is also observed.

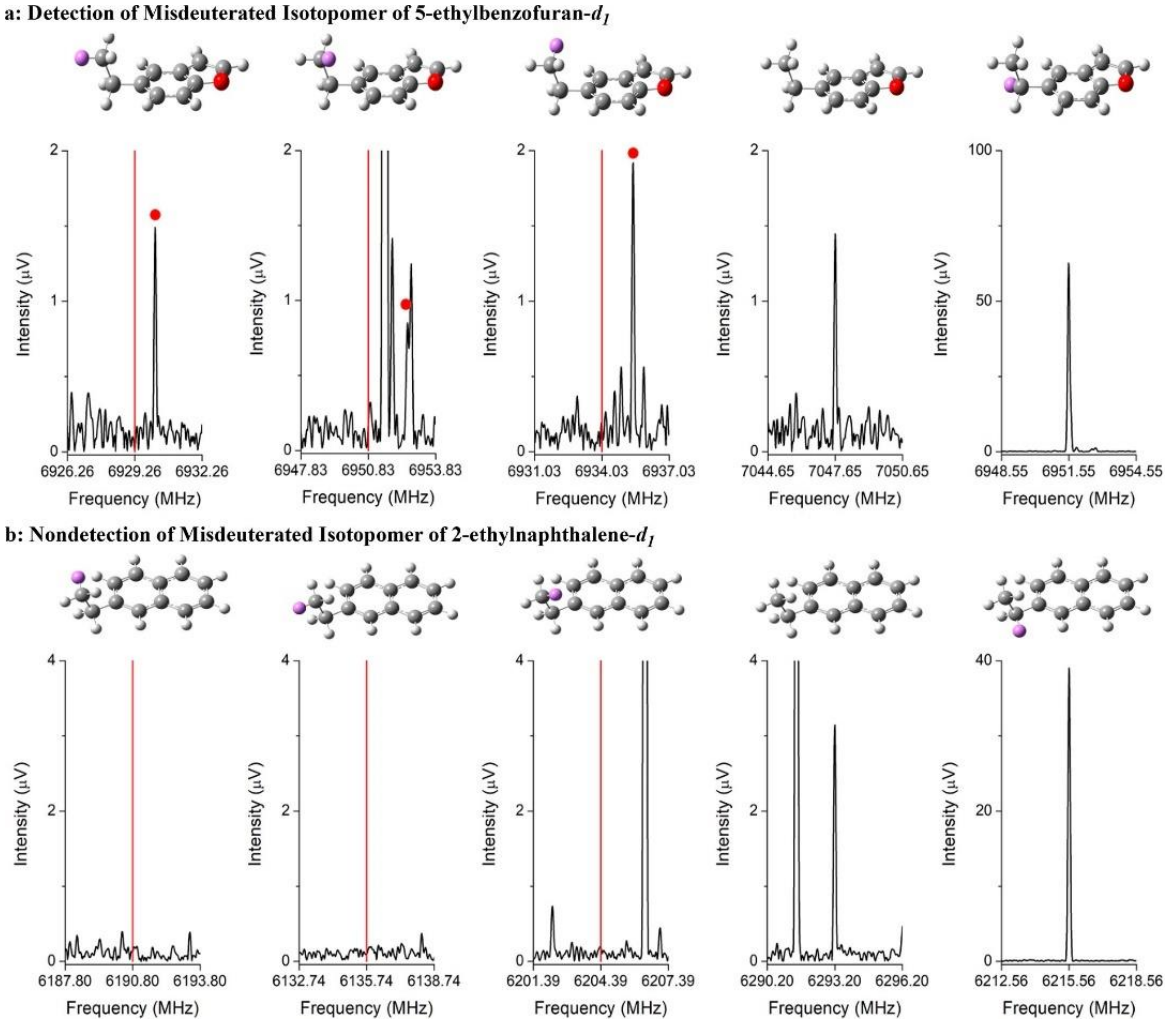

Figure 5.1: The isotopologue and isotopomer analysis of two of the reaction products is illustrated. Part (a) shows the analysis of the 5-ethylbenzofuran-d_1 sample (**6d**, **7d**, **8d**). The first three panels show a 6 MHz window of the rotational spectrum centered on the predicted transition frequency for the strongest transition in the spectrum (also marked by the vertical red line). The conformers of the d_1-methyl isotopomer give different spectra and the deuteration position for each transition is denoted by the purple-colored atom in the structure above the spectral region. A transition assigned to each isotopomer rotational spectrum is observed and marked by the red dot. The fourth panel is centered on the observed frequency of the underdeuterated isotopologue. The fifth panel shows the rotational transition for one of the two conformers of the desired isotopomer of 5-ethylbenzofuran-d_1 (note the change in the intensity axis scale). Part (b) shows the same analysis using the strongest rotational transition of 2-ethylnaphthalene-d_1 (**7b**). In this case, no transitions in the prediction window for the misdeuterated isotopomer can be assigned to rotational spectra. The lack of detection of any rotational transitions is used to derive the upper limit to misdeuterated 2-ethylnaphthalene-d_1 reported in the SI.

In the case of the misdeuterated reaction product **7d**, three equal intensity rotational spectra are expected from the conformational isomers of this isotopomer. The first three spectral regions shown in Figure 5.1a are 6 MHz frequency bandwidth windows centered on the predicted transition frequency obtained using the quantum chemistry equilibrium geometry calculated using the B3LYP density functional theory with Grimme's D3 dispersion correction including Becke–Johnson damping and the 6-311++G(d,p) basis set model chemistry in Gaussian16.[62] The transitions marked by the red dot are assigned to the rotational spectra of the three conformers of the d_1-methyl isotopomer. The conformational geometry associated with the spectral transition is indicated by the purple atom in the molecular structure shown above the section of the spectrum. The ^{2}H NMR spectrum of the ethylbenzofuran sample is shown in the Supporting Information (SI), and the resonance for the methyl group is barely detectable. The MRR measurement has about an order-of-magnitude higher sensitivity than the ^{2}H NMR measurement. Figure 5.1b illustrates the analysis of the transfer hydrodeuteration of 2-vinylnaphthalene (**6b**, **7b**, **8b**), where no misdeuteration reaction product is identified at the measurement sensitivity using the broadband MRR instrument.

After the initial analyses of the six reaction products depicted in Scheme 5.3 (these results are tabulated in the SI), a modified MRR analysis approach was developed to address some weaknesses in the application of MRR to the development of synthetic methodologies for selective deuteration chemistry. One issue with the CP-FTMW analysis is the possibility that the spectral signature of an isotopic impurity is missed because the quantum chemistry predictions of the rotational spectrum make it difficult to identify the spectrum when it is near the detection limit. The sample consumption for the analysis is also a potential limitation. The broadband MRR

analysis initially performed for the products depicted in Scheme 5.3 consumed 60–100 mg to reach a detection limit of about 1% on the expected isotopic impurities. Finally, the measurement time is approximately 3 h. Shorter measurement times are needed to facilitate screening of reaction conditions to optimize the deuteration selectivity.

The new measurement approach combines broadband MRR spectroscopy to obtain the spectral signatures of all possible isotopic species accessible from the transfer hydrodeuteration chemistry, with high-throughput sample analysis performed on an IsoMRR instrument.[63] The IsoMRR instrument uses the tunable cavity-enhanced FTMW design introduced by Balle and Flygare.[64] The instrument employs coaxial injection of the sample through a solenoid valve mounted in the resonator mirror as introduced by Grabow, Stahl, and Dreizler to increase the measurement sensitivity.[65] The compact instrument design is based off the mini-FTMW instrument design from NIST.[66] The IsoMRR spectrometer has approximately an order-of-magnitude greater sensitivity than the broadband spectrometer for equal sample consumption. The instrument is also capable of performing high-throughput sample screening.[67] The trade-off of using a cavity-enhanced FTMW spectrometer is that the cavity resonator limits the measurement bandwidth to about 1 MHz. Due to the small bandwidth window, efficient use of the instrument relies on the availability of the transition frequencies of each isotopic species to be studied and these are supplied from the broadband analysis.

The sample analyzed by broadband MRR is prepared by performing the reaction with a 1:1 mixture of H and D reagents so that a “cocktail” of all possible reaction products is produced (Scheme 5.5). Once this sample is analyzed, the spectral signatures are used to set up a high-speed measurement script using a cavity-enhanced Fourier transform microwave (FTMW)

spectrometer. This measurement methodology was tested on the isolated products from the Cu-catalyzed "cocktail" reactions performed with **5a**, **5b**, and **5d** shown in Scheme 5.5 below:

Scheme 5.5. *Cu-catalyzed "Cocktail" Reaction*

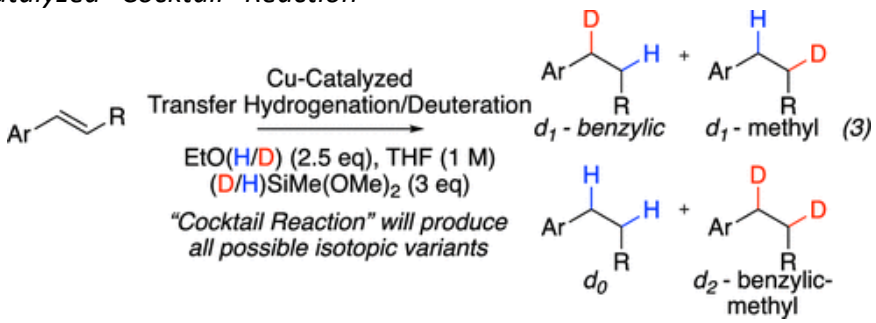

The analysis of the reaction mixture using the broadband CP-FTMW spectrometer is illustrated in Figure 5.2 for the Cu-catalyzed "cocktail" reaction of 2-vinylnaphthalene **5b**. Panels A and B show the spectrum for a commercial sample of ethylnaphthalene-d_0 for simplicity (this species is also the dominant species in the cocktail reaction mixture). Panel A shows the MRR spectrum in a small frequency range of the full 2–8 GHz measured spectrum. The rotational spectrum prediction from the equilibrium geometry and dipole moments obtained from the quantum chemistry geometry optimization is shown in blue and is a close match to the observed pattern. Panel B shows an expanded frequency region for two of the transitions in ethylnaphthalene-d_0. The assignment listed above each transition uses the usual notation in rotational spectroscopy that labels the energy levels $J_{Ka\,Kc}$.[54] The blue spectrum simulation is from quantum chemistry. The red simulation uses the experimental fit rotational constants which are given in the Supplementary Information.

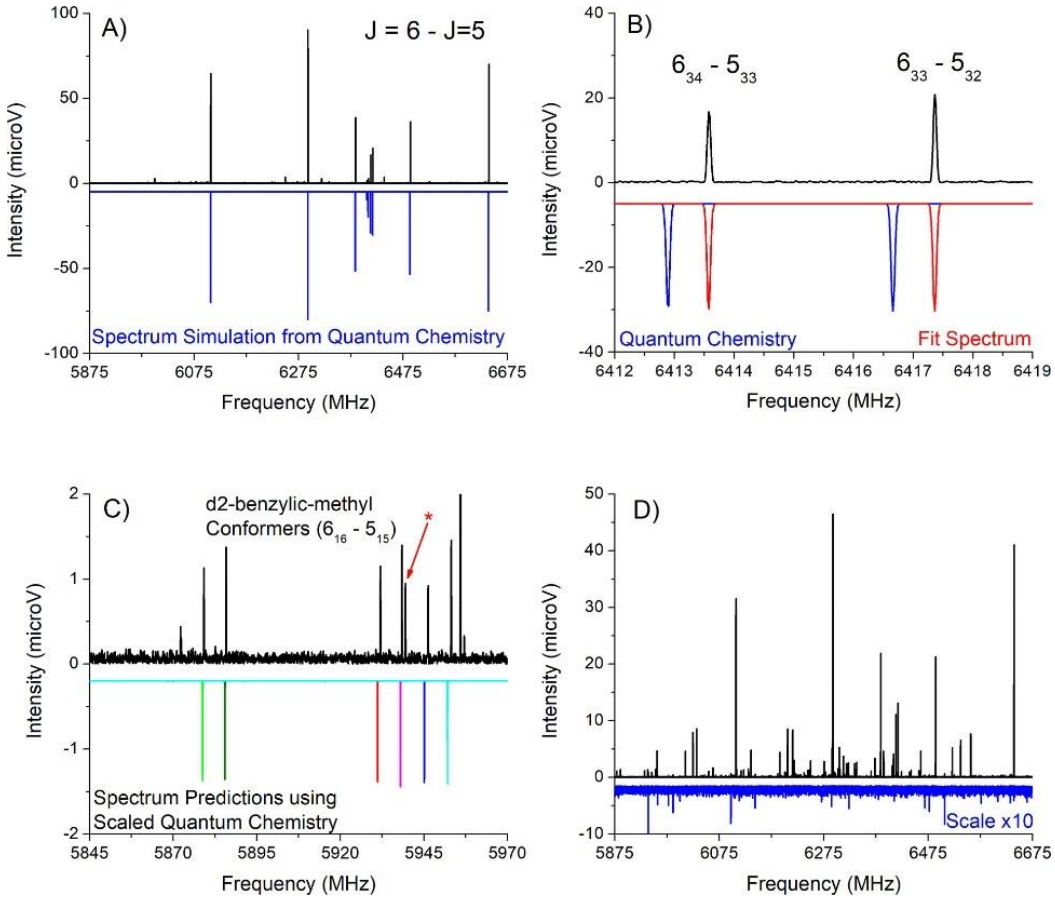

Figure 5.2: Portrayed above is the predicted and experimental analysis of the 2-ethylnaphthalene product mixture from the cocktail reaction and the method for analyzing the reaction product mixture when a near 1:1 mixture of H and D-reagents is used in the Cu-catalyzed transfer hydrogenation/deuteration reaction. Panels A and B show the basic MRR analysis process for a commercial sample of 2-ethylnaphthalene-d_0. The simulation of the spectrum from quantum chemistry (blue) is used to guide an experimental fit of the rotational constants (Panel B, red) of the spectrum. The results from this initial fit are used to make scaled predictions for the rotational constants for other isotopic species. The predicted transitions for the six conformers of the d_2-benzylic-methyl isotopomer are shown in Panel C. The transition marked with a red asterisk is unassigned. All strong transitions are assigned to four chemical species (d_0, d_1-benzylic, d_1-methyl, d_2-benzylic-methyl), and no further species could be identified in the residuals of the reaction product mixture spectrum shown in Panel D (blue, with the intensity multiplied by a factor of 10).

The spectral signatures of each deuterated 2-ethylnaphthalene species can be predicted to high accuracy using the theoretical equilibrium geometry and scale factors obtained from the theoretical and fit constants of ethylnaphthalene-d_0. This process is described in the Supporting Information and is a common analysis tool in rotational spectroscopy where it is used to identify ^{13}C (and other) isotopomers in natural abundance in structure determination.[68] The accuracy of

this analysis is illustrated in Panel C where the predicted transitions of the $6_{16} - 5_{15}$ rotational transitions of the six conformers of the d_2-benzylic-methyl isotopomer are compared to the measured spectrum. The Supporting Information gives the comparison between the scaled rotational constant predictions and the experimental fit rotational constants for the 11 isotopic species identified in the spectrum. Agreement is on the order of 0.01%. Panel D shows the $J = 6 - J = 5$ spectral region of the reaction product mixture and the residual spectrum (blue) after all isotopic species (including the rotational spectra for the 12 singly substituted ^{13}C isotopomers of the dominant ethylnaphthalene-d_0 species) are cut from the spectrum. The only isotopomers identified in the spectrum are d_0, d_1-benzylic, d_1-methyl, and d_2-benzylic-methyl, and this is consistent with the proposed reaction products.

The broadband spectrum can be used to perform quantitative analysis of the reaction product mixture. To average fluctuations from the frequency-dependent electric field of the chirped excitation pulse, the total intensity of a set of rotational transitions is used. The analysis needs to include the spectral intensity from all conformers of a given isotopomer. The result using eight transitions in the 2-ethylnaphthalene spectrum is shown in Table 5.2. Analysis of the results for the 5-ethylbenzofuran and ethylbiphenyl product mixtures are included in the Supporting Information.

Table 5.2. *Isotopic Composition of the 2-Ethylnaphthalene Mixture Giving the Total Intensity for Eight Transitions of Each Conformer for the Four Chemically Distinct Isotopic Variants Observed in the Spectrum*

d_0		d_1-benzylic		d_1-methyl		d_2-benzylic-methyl	
	280 μV	D19[a]	57.0 μV	D22	38.0 μV	D19 D22	8.17 μV
		D20	55.4 μV	D23	36.3 μV	D19 D23	8.72 μV
				D24	41.9 μV	D19 D24	7.82 μV
						D20 D22	9.25 μV
						D20 D23	9.38 μV
						D20 D24	10.6 μV
Total	280 μV		112.4 μV		116.2 μV		53.9 μV
%	49.8		20.0		20.7		9.6
d_1-methyl conformers:				Mean: 38.7 μV		σ = 2.84 μV	
d_2-benzylic-methyl conformers:				Mean: 8.99 μV		σ = 0.98 μV	

[a]The isotope labels, like D19, refer to the atom labeling from the quantum chemistry geometry optimization as shown in the Supporting Information.

There are two important spectroscopy details in the analysis. First, the analysis assumes that the dipole moment is the same for all isotopic variants so that the total spectral intensity is directly proportional to the isotopic composition. The dipole moment differs for the different species through two effects. Deuterium substitution reorients the principal axis system for molecular rotation and changes the components of the dipole moment vector in this axis system. This effect can be calculated from the equilibrium geometry and is negligible in the samples analyzed in this work. For example, the value of μ_a^2—the square of the component of the electric dipole moment along the a-principal axis which governs the intensities of the transitions used in the analysis—varies by just 0.1% for the 12 rotationally distinct structures analyzed for ethylnaphthalene. The dipole moment also changes magnitude upon deuteration from changes

in the zero-point motion of the C–H bond. These effects have been measured, and the bond dipole changes are on the order of 0.01 D which is small compared to the dipole moments of the molecules in this study (>0.4 D).[69] The second spectroscopy issue that can affect the quantitative analysis is the presence of nuclear quadrupole hyperfine splitting in the spectrum from the deuterium nucleus (I = 1). The quantitative analysis uses only a-type rotational transitions where the hyperfine structure is small compared to the line width and can, therefore, be neglected.

The accuracy of the sample composition analysis by broadband MRR spectroscopy has been validated by comparison to integration of specific resonances in the ^{1}H and ^{2}H NMR spectra of the reaction mixture. It is important to note that NMR spectroscopy cannot analyze the composition of this reaction mixture. The resonances used in the NMR analysis are assigned to the benzylic and methyl protons. However, the reaction mixture contains three isotopic species (d_1-benzylic, d_1-methyl, and d_2-benzylic-methyl) that contribute to the two resonances making it impossible to analyze the sample composition by NMR. This simple example illustrates the limitations of NMR spectroscopy for reaction product analysis in deuteration chemistry. MRR can perform the analysis because all isotopic variants have a unique spectral signature.

The accuracy of the MRR composition is assessed by calculating the expected NMR integration for the sample using the MRR results reported in Table 5.2 (2-ethylnaphthalene) and the Supporting Information (5-ethylbenzofuran and ethylbiphenyl). For example, the integration of the methyl proton resonance using the fractional composition of the sample is:

$$^{1}H \text{ Methyl} = (f_{d0}) * 3 + \left(f_{d1-benzylic}\right) * 3 + \left(f_{d1-methyl}\right) * 2 + \left(f_{d2-benzylic-methyl}\right) * 2 \quad (5.3)$$

The quantitative comparison between MRR and NMR resonance integrations is presented in Table 5.3 for four reaction mixtures that were analyzed in this work (this includes a second ethylbiphenyl (D-enhanced) mixture where the ratio of H/D reagents was 1:2 to increase the contribution from the deuterated species). The mean absolute percent difference between the results is 1% for the ^{1}H integration.

Table 5.3. *Comparison Between Calculated NMR Integration Using MRR Sample Composition and Measured NMR Integration*

	Ethylbenzofuran		**Ethylnaphthalene**		**Ethylbiphenyl**		**Ethylbiphenyl (D-enhanced)**	
NMR Resonance	**MRR[a]**	**NMR**	**MRR**	**NMR**	**MRR**	**NMR**	**MRR**	**NMR**
Methyl ^{1}H	2.72(1)	2.69	2.70(2)	2.71	2.69(2)	2.73	2.46(2)	2.46
Benzylic ^{1}H	1.45(2)	1.43	1.70(2)	1.71	1.66(2)	1.69	1.31(2)	1.29
Methyl ^{2}H	0.28(1)	0.31	0.30(2)	0.29	0.31(2)	0.27	0.54(2)	0.52
Benzylic ^{2}H	0.55(2)	0.57	0.30(2)	0.28	0.34(2)	0.30	0.69(2)	0.71
Mean Absolute Percent Difference (^{1}H Only):					1.0%			
Mean Absolute Percent Difference (All):					4.0%			

[a]The MRR integrations give the 1σ uncertainty derived from the composition uncertainty.

The reaction product mixtures prepared using a 1:1 ratio of H/D reagents were subsequently analyzed using the IsoMRR instrument. A measurement script was designed to permit detection of the four chemically distinct isotopic species at the 1% level for each of the three analytes. These scripts are described in the Supporting Information. The measurement script does not need to make measurements for all conformers of a given isotopomer. As shown in Table 5.2, equal amounts of the conformers are observed in the spectrum (within a 10% intensity uncertainty) so that the measurement can use just one and then apply the statistical

factor to get the total sample composition for the isotopomer. The sample composition from the IsoMRR measurements is compared to the CP-FTMW analysis in Table 5.4.

Table 5.4. *Comparison of Sample Composition Analysis by Broadband and Cavity-Enhanced MRR Spectroscopy*

Ethylbenzofuran	**Run 1**	**Run 2**	**Run 3**	**IsoMRR[a]**	**CP-FTMW[b]**	**|Difference|**
d_0	29.4%	30.3%	30.0%	29.9(0.45)	34(2.4)	4.1%
d_1-benzylic	33.7%	31.9%	31.8%	32.6(1.1)	38(2.1)	5.4%
d_1-methyl	13.4%	14.3%	15.1%	14.3(0.85)	11.4(0.8)	2.9%
d_2-methyl-benzylic	23.5%	23.5%	23.1%	23.4(0.23)	16.8(0.9)	6.6%
Ethylnaphthalene	**Run 1**	**Run 2**	**Run 3**	**IsoMRR[a]**	**CP-FTMW[b]**	**|Difference|**
d_0	55.2%	54.3%	54.2%	54.6(0.55)	50(2.7)	4.6%
d_1-benzylic	14.9%	15.1%	14.8%	14.9(0.15)	20(1.6)	5.1%
d_1-methyl	21.0%	21.5%	21.4%	21.3(0.26)	21(1.4)	0.3%
d_2-methyl-benzylic	9.0%	9.2%	9.6%	9.3(0.31)	9.6(0.6)	0.3%
Ethylbiphenyl	**Run 1**	**Run 2**		**IsoMRR[a]**	**CP-FTMW[b]**	**|Difference|**
d_0	49.7%	51.7%		50.7(1.4)	46(2.7)	4.9%
d_1-benzylic	18.7%	18.0%		18.4(0.49)	23(1.7)	4.7%
d_1-methyl	20.8%	20.3%		20.6(0.35)	21(1.4)	0.4%
d_2-methyl-benzylic	10.8%	9.9%		10.4(0.64)	10.6(0.7)	0.2%

[a]The IsoMRR results are the mean value of the replicate measurements with a 1σ sample standard deviation reported in parentheses.

[b]The measurement uncertainty reported for the CP-FTMW broadband measurements is a 1σ standard deviation determined by assuming that there is a 10% relative uncertainty in the intensity measurement ($(\sigma_I/I) = 0.1$) for each rotationally distinct species in the sample mixture.

The composition analysis from the two MRR instruments are in good agreement with a percentage variation of about 5%. However, the 5% accuracy has little practical importance in

applications of high-throughput screening where the measurement precision (better than 1%) is needed to determine which samples have higher purity. The lower accuracy of the IsoMRR measurements results from the instrument design which uses a cavity-resonator with high quality factor (*Q*) to enhance the measurement sensitivity. There has been no attempt to correct for frequency-dependent variation in the cavity *Q* in these measurements (although transitions in a narrow frequency range are used to minimize variations in the cavity *Q*). In practice, the IsoMRR measurements can achieve both high precision and accuracy by calibrating the instrument response using a reference sample that has been analyzed by broadband rotational spectroscopy where the quantitative accuracy is demonstrated in Table 5.3.

The more important feature of the IsoMRR measurements is the repeatability in back-to-back analysis runs which is about 1%. This measurement precision shows that the technique would be able to reliably detect changes in the sample composition for high-throughput screening of reaction conditions. The IsoMRR measurement for 2-ethylnaphthalene and 5-ethylbenzofuran uses 2.5 mg of sample (for ethylbiphenyl where the spectrum is weaker, the sample consumption is 5 mg). The measurement time is approximately 10 min (20 min for ethylbiphenyl). Both performance metrics are order-of-magnitude improvements over sample analysis by broadband MRR using the CP-FTMW spectrometer.

The IsoMRR instrument was also used to analyze the reaction products depicted in Scheme 5.3. These measurements detected the presence of the d_1-methyl isotopomer in ethylnaphthalene that was not observable in the broadband analysis (Figure 5.1b): (94.8% d_1-benzylic (**6b**), 4.4% d_0 (**8b**), 0.8% d_1-methyl (**7b**), <0.6% d_2 (nd)). For ethylbenzofuran, the IsoMRR analysis agrees with the broadband analysis within the performance comparison limits of Table

5.4: (95.1% d_1-benzylic (**6d**), 1.7% d_0 (**8d**), 3.2% d_1-methyl (**7d**), <0.7% d_2 (nd)). For ethylbiphenyl, only the underdeuterated isotopic impurity was detected: (98.4% d_1-benzylic (**6a**), 1.6% d_0 (**8a**), <0.7% d_1-methyl (**7a**) (nd), <1.3% d_2 (nd)). In addition, three separate preparations of ethylbiphenyl using the optimized chemistry were analyzed. The only two species detected were the desired d_1-benzylic and the underdeuterated d_0 isotopologue. The amount of d_0 (**8a**) impurity in the three samples was 1.6%, 2.3%, and 1.8%.

5.5: *Conclusions*

In summary, a highly regioselective alkene transfer hydrodeuteration for the synthesis of deuterated small molecules where deuterium is incorporated at the benzylic position is reported. The Cu-catalyzed reaction is able to incorporate both an H and a D across an alkene with high levels of precision. This mild protocol can be carried out across a broad range of aryl alkene substrates, including those containing heterocycles and reduceable functionality. A detailed characterization of six reaction product mixtures was performed using molecular rotational resonance spectroscopy. MRR provides a general method to perform isotopomer composition analysis of deuteration reactions. The following advantages of MRR spectroscopy for characterization of isotopic products were outlined during the characterization of six isotopic product mixtures from the alkene transfer hydrodeuteration reaction. (1) Isotopomers have distinct MRR spectra that can be predicted to high accuracy from the theoretical equilibrium geometry from quantum chemistry. This feature makes it possible to identify the isotopomers with high confidence without the need for reference samples. (2) Instruments for MRR provide

high spectral resolution so that isotopologue and isotopomer mixtures can be quantitatively analyzed without issues arising from signal overlap. (3) High-throughput analysis is possible using cavity-enhanced FTMW spectrometers making it possible to screen a wide range of reaction conditions for isotopic reactions. These capabilities were especially important for analyzing the reaction products from the reported Cu-catalyzed alkene transfer hydrodeuteration reaction. Reaction mixtures may contain three isotopic species (d_1-benzylic, d_1-methyl, and d_2-benzylic-methyl), and these contribute to two NMR resonances. This scenario made it challenging to analyze the sample composition by NMR. In addition to the enhanced sensitivity of MRR, the identification of the d_1-methyl isotopomer **7b** (the minor regioisomer from the transfer hydrodeuteration of 2-ethylnaphthalene) was possible. This species was not detected by NMR. Ultimately, using MRR spectroscopy to analyze the isotopic products formed from the reported highly regioselective Cu-catalyzed alkene transfer hydrodeuteration reaction led to the highest regioselectivities ever reported for this reaction. We anticipate that the advances reported for the selective hydrodeuteration chemistry and MRR spectroscopy will facilitate new reaction discovery in selective deuteration chemistry and expand the utility of deuterium-labeled organic compounds in applications that require the molecule has high deuterium content at precisely the desired site.

Chapter 5 References:

1. Atzrodt, J.; Derdau, V. Pd- and Pt-catalyzed H/D exchange methods and their application for internal MS standard preparation from a Sanofi-Aventis perspective. *J. Labelled Compd. Radiopharm.* **2010**, *53*, 674– 685, DOI: 10.1002/jlcr.1818

2. Qin, M.; Qiao, H.-q.; Yuan, Y.-j.; Shao, Q. A quantitative LC-MS/MS method for simultaneous determination of deuvortioxetine, vortioxetine and their carboxylic acid metabolite in rat plasma, and its application to a toxicokinetic study. *Anal. Methods* **2018**, *10*, 1023– 1031, DOI: 10.1039/C7AY02642K

3. Iglesias, J.; Sleno, L.; Volmer, D. A. Isotopic Labeling of Metabolites in Drug Discovery Applications. *Curr. Drug Metab.* **2012**, *13*, 1213– 1225, DOI: 10.2174/138920012803341357

4. Meek, S. J.; Pitman, C. L.; Miller, A. J. M. Deducing Reaction Mechanism: A Guide for Students, Researchers, and Instructors. *J. Chem. Educ.* **2016**, *93*, 275– 286, DOI: 10.1021/acs.jchemed.5b00160

5. Anslyn, E. V.; Dougherty, D. A. *Modern physical organic chemistry*; University Science Books: 2006; pp 424– 441.

6. Simmons, E. M.; Hartwig, J. F. On the Interpretation of Deuterium Kinetic Isotope Effects in C-H Bond Functionalizations by Transition-Metal Complexes. *Angew. Chem., Int. Ed.* **2012**, *51*, 3066– 3072, DOI: 10.1002/anie.201107334

7. Giagou, T.; Meyer, M. P. Kinetic Isotope Effects in Asymmetric Reactions. *Chem. - Eur. J.* **2010**, *16*, 10616– 10628, DOI: 10.1002/chem.201001018

8. Atzrodt, J.; Derdau, V.; Kerr, W. J.; Reid, M. Deuterium- and Tritium-Labelled Compounds: Applications in the Life Sciences. *Angew. Chem., Int. Ed.* **2018**, *57*, 1758– 1784, DOI: 10.1002/anie.201704146

9. Jarling, R.; Sadeghi, M.; Drozdowska, M.; Lahme, S.; Buckel, W.; Rabus, R.; Widdel, F.; Golding, B. T.; Wilkes, H. Stereochemical Investigations Reveal the Mechanism of the Bacterial Activation of n-Alkanes without Oxygen. *Angew. Chem., Int. Ed.* **2012**, *51*, 1334– 1338, DOI: 10.1002/anie.201106055

10. Klinman, J. P. A new model for the origin of kinetic hydrogen isotope effects. *J. Phys. Org. Chem.* **2010**, *23*, 606– 612, DOI: 10.1002/poc.1661

11. Schwab, J. M. Stereochemistry of an enzymic Baeyer-Villiger reaction. Application of deuterium NMR. *J. Am. Chem. Soc.* **1981**, *103*, 1876– 1878, DOI: 10.1021/ja00397a066

12. Battersby, A. R.; Gutman, A. L.; Fookes, C. J. R.; Günther, H.; Simon, H. Stereochemistry of formation of methyl and ethyl groups in bacteriochlorophyll a. *J. Chem. Soc., Chem. Commun.* **1981**, 645– 647, DOI: 10.1039/C39810000645

13. Leinberger, R.; Rétey, A.; Hull, W. E.; Simon, H. Steric Course of the NIH Shift in the Enzymic Formation of Homogentisic Acid. *Eur. J. Biochem.* **1981**, *117*, 311– 318, DOI: 10.1111/j.1432-1033.1981.tb06338.x

14. Lüthy, J.; Rétey, J.; Arigoni, D. Asymmetric Methyl Groups: Preparation and Detection of Chiral Methyl Groups. *Nature* **1969**, *221*, 1213– 1215, DOI: 10.1038/2211213a0

15. White, R. E.; Miller, J. P.; Favreau, L. V.; Bhattacharyya, A. Stereochemical dynamics of aliphatic hydroxylation by cytochrome P-450. *J. Am. Chem. Soc.* **1986**, *108*, 6024– 6031, DOI: 10.1021/ja00279a059

16. Shapiro, S.; Piper, J. U.; Caspi, E. Steric course of hydroxylation at primary carbon atoms. Biosynthesis of 1-octanol from (1R)- and (1S)-[1–3H,2H,1H; 1–14C]octane by rat liver microsomes. *J. Am. Chem. Soc.* **1982**, *104*, 2301– 2305, DOI: 10.1021/ja00372a031

17. Nelson, S. D.; Trager, W. F. The Use of Deuterium Isotope Effects to Probe the active site properties, Mechanism of Cytochrom P450-Catalyzed Reactions, and Mechanisms of Metabolically Dependent Toxicity. *Drug Metab. Dispos.* **2003**, *31*, 1481– 1497, DOI: 10.1124/dmd.31.12.1481

18. Pirali, T.; Serafini, M.; Cargnin, S.; Genazzani, A. A. Applications of Deuterium in Medicinal Chemistry. *J. Med. Chem.* **2019**, *62*, 5276– 5297, DOI: 10.1021/acs.jmedchem.8b01808

19. Gant, T. G. Using Deuterium in Drug Discovery: Leaving the Label in the Drug. *J. Med. Chem.* **2014**, *57*, 3595– 3611, DOI: 10.1021/jm4007998

20. Meanwell, N. A. Synopsis of Some Recent Tactical Application of Bioisosteres in Drug Design. *J. Med. Chem.* **2011**, *54*, 2529– 2591, DOI: 10.1021/jm1013693

21. Stepan, A. F.; Mascitti, V.; Beaumont, K.; Kalgutkar, A. S. Metabolism-guided drug design. *MedChemComm* **2013**, *4*, 631– 652, DOI: 10.1039/c2md20317k

22. Belleau, B.; Burba, J.; Pindell, M.; Reiffenstein, J. Effect of Deuterium Substitution in Sympathomimetic Amines on Adrenergic Responses. *Science* **1961**, *133*, 102– 104, DOI: 10.1126/science.133.3446.102

23. Harbeson, S. L.; Tung, R. D. Deuterium Medicinal Chemistry: A New Approach to Drug Discovery and Development. *Medchem News* **2014**, *24*, 8– 22

24. Schmidt, C. First deuterated drug approved. *Nat. Biotechnol.* **2017**, *35*, 493– 494, DOI: 10.1038/nbt0617-493

25. Ludwig, J. R.; Schindler, C. S. Catalyst: Sustainable Catalysis. *Chem.* **2017**, *2*, 313– 316, DOI: 10.1016/j.chempr.2017.02.014

26. Zhou, Q.-L. Transition-Metal Catalysis and Organocatalysis: Where Can Progress Be Expected?. *Angew. Chem., Int. Ed.* **2016**, *55*, 5352– 5353, DOI: 10.1002/anie.201509164

27. Atzrodt, J.; Derdau, V.; Fey, T.; Zimmermann, J. The Renaissance of H/D Exchange. *Angew. Chem., Int. Ed.* **2007**, *46*, 7744– 7765, DOI: 10.1002/anie.200700039

28. Atzrodt, J.; Derdau, V.; Kerr, W. J.; Reid, M. C–H Functionalisation for Hydrogen Isotope Exchange. *Angew. Chem., Int. Ed.* **2018**, *57*, 3022– 3047, DOI: 10.1002/anie.201708903

29. Puleo, T. R.; Strong, A. J.; Bandar, J. S. Catalytic α-Selective Deuteration of Styrene Derivatives. *J. Am. Chem. Soc.* **2019**, *141*, 1467– 1472, DOI: 10.1021/jacs.8b12874

30. Karlsson, S.; Hallberg, A.; Gronowitz, S. Hydrozirconation of (E)-3-methoxy-1-phenyl-1-propene and (E)-3-phenyl-2-propenol. *J. Organomet. Chem.* **1991**, *403*, 133– 144, DOI: 10.1016/0022-328X(91)83094-K

31. Czeskis, B.; Elmore, C. S.; Haight, A.; Hesk, D.; Maxwell, B. D.; Miller, S. A.; Raglione, T.; Schildknegt, K.; Traverse, J. F.; Wang, P. Deuterated Active Pharmaceutical Ingredients: A Science-Based Proposal for Synthesis, Analysis, and Control. Part 1: Framing the Problem. *J. Labelled Compd. Radiopharm.* **2019**, *62*, 690– 694, DOI: 10.1002/jlcr.3743

32. Wang, D.; Astruc, D. The Golden Age of Transfer Hydrogenation. *Chem. Rev.* **2015**, *115*, 6621– 6686, DOI: 10.1021/acs.chemrev.5b00203

33. Korytiaková, E.; Thiel, N. O.; Pape, F.; Teichert, J. F. Copper(i)-Catalysed Transfer Hydrogenations with Ammonia Borane. *Chem. Commun.* **2017**, *53*, 732– 735, DOI: 10.1039/C6CC09067B

34. Chatterjee, I.; Oestreich, M. Brønsted Acid-Catalyzed Transfer Hydrogenation of Imines and Alkenes Using Cyclohexa-1,4-dienes as Dihydrogen Surrogates. *Org. Lett.* **2016**, *18*, 2463– 2466, DOI: 10.1021/acs.orglett.6b01016

35. Lau, S.; Gasperini, D.; Webster, R. L., Amine-Boranes as Transfer Hydrogenation and Hydrogenation Reagents: A Mechanistic Perspective. *Angew. Chem., Int. Ed.* **2021**, DOI: 10.1002/anie.202010835

36. Semba, K.; Fujihara, T.; Xu, T.; Terao, J.; Tsuji, Y. Copper-Catalyzed Highly Selective Semihydrogenation of Non-Polar Carbon-Carbon Multiple Bonds using a Silane and an Alcohol. *Adv. Synth. Catal.* **2012**, *354*, 1542– 1550, DOI: 10.1002/adsc.201200200

37. Whittaker, A. M.; Lalic, G. Monophasic Catalytic System for the Selective Semireduction of Alkynes. *Org. Lett.* **2013**, *15*, 1112– 1115, DOI: 10.1021/ol4001679

38. Kaicharla, T.; Zimmermann, B. M.; Oestreich, M.; Teichert, J. F. Using Alcohols as Simple H_2-Equivalents for Copper-Catalysed Transfer Semihydrogenations of Alkynes. *Chem. Commun.* **2019**, *55*, 13410– 13413, DOI: 10.1039/C9CC06637C

39. Okuhara, T.; Tanaka, K.-I. Orientation in the Addition of HD to Butadiene on MoS_2. *J. Chem. Soc., Chem. Commun.* **1976**, 199– 200, DOI: 10.1039/c39760000199

40. Okuhara, T.; Kondo, T.; Tanaka, K. Oriented Adsorption of Hydrogen Deuteride on Zinc Oxide and Addition to Butadiene. *J. Phys. Chem.* **1977**, *81*, 808– 809, DOI: 10.1021/j100523a026

41. Espinal-Viguri, M.; Neale, S. E.; Coles, N. T.; Macgregor, S. A.; Webster, R. L. Room Temperature Iron-Catalyzed Transfer Hydrogenation and Regioselective Deuteration of Carbon–Carbon Double Bonds. *J. Am. Chem. Soc.* **2019**, *141*, 572– 582, DOI: 10.1021/jacs.8b11553

42. Wang, Y.; Cao, X.; Zhao, L.; Pi, C.; Ji, J.; Cui, X.; Wu, Y. Generalized Chemoselective Transfer Hydrogenation/Hydrodeuteration. *Adv. Synth. Catal.* **2020**, *362*, 4119– 4129, DOI: 10.1002/adsc.202000759

43. Linford-Wood, T. G.; Coles, N. T.; Webster, R. L. Room temperature iron catalyzed transfer hydrogenation using *n*-butanol and poly(methylhydrosiloxane). *Green Chem.* **2021**, *23*, 2703– 2709, DOI: 10.1039/D0GC04175K

44. Walker, J. C. L.; Oestreich, M. Regioselective Transfer Hydrodeuteration of Alkenes with a Hydrogen Deuteride Surrogate Using $B(C_6F_5)_3$ Catalysis. *Org. Lett.* **2018**, *20*, 6411– 6414, DOI: 10.1021/acs.orglett.8b02718

45. Li, L.; Hilt, G. Regiodivergent DH or HD Addition to Alkenes: Deuterohydrogenation versus Hydrodeuterogenation. *Org. Lett.* **2020**, *22*, 1628– 1632, DOI: 10.1021/acs.orglett.0c00213

46. Sloane, S. E.; Reyes, A.; Vang, Z. P.; Li, L.; Behlow, K. T.; Clark, J. R. Copper-Catalyzed Formal Transfer Hydrogenation/Deuteration of Aryl Alkynes. *Org. Lett.* **2020**, *22*, 9139– 9144, DOI: 10.1021/acs.orglett.0c03632

47. Liu, R. Y.; Buchwald, S. L. CuH-Catalyzed Olefin Functionalization: From Hydroamination to Carbonyl Addition. *Acc. Chem. Res.* **2020**, *53*, 1229– 1243, DOI: 10.1021/acs.accounts.0c00164

48. Zhu, S.; Niljianskul, N.; Buchwald, S. L. Enantio- and Regioselective CuH-Catalyzed Hydroamination of Alkenes. *J. Am. Chem. Soc.* **2013**, *135*, 15746– 15749, DOI: 10.1021/ja4092819

49. Miki, Y.; Hirano, K.; Satoh, T.; Miura, M. Copper-Catalyzed Intermolecular Regioselective Hydroamination of Styrenes with Polymethylhydrosiloxane and Hydroxylamines. *Angew. Chem., Int. Ed.* **2013**, *52*, 10830– 10834, DOI: 10.1002/anie.201304365

50. Sorádová, Z.; Šebesta, R. Enantioselective Cu-Catalyzed Functionalizations of Unactivated Alkenes. *ChemCatChem* **2016**, *8*, 2581– 2588, DOI: 10.1002/cctc.201600252

51. Mohr, J.; Oestreich, M. Balancing C = C Functionalization and C = O Reduction in Cu-H Catalysis. *Angew. Chem., Int. Ed.* **2016**, *55*, 12148– 12149, DOI: 10.1002/anie.201606701

52. Vitaku, E.; Smith, D. T.; Njardarson, J. T. Analysis of the Structural Diversity, Substitution Patterns, and Frequency of Nitrogen Heterocycles among U.S. FDA Approved Pharmaceuticals. *J. Med. Chem.* **2014**, *57*, 10257– 10274, DOI: 10.1021/jm501100b

53. Taylor, R. D.; MacCoss, M.; Lawson, A. D. G. Rings in Drugs. *J. Med. Chem.* **2014**, *57*, 5845– 5859, DOI: 10.1021/jm4017625

54. W. Gordy, R. L. C. *Microwave Molecular Spectra*, 3rd ed.; Knovel, 1984; Chapter VII, pp 227– 296

55. Smith, J. A.; Wilson, K. B.; Sonstrom, R. E.; Kelleher, P. J.; Welch, K. D.; Pert, E. K.; Westendorff, K. S.; Dickie, D. A.; Wang, X.; Pate, B. H.; Harman, W. D. Preparation of cyclohexene isotopologues and stereoisotopomers from benzene. *Nature* **2020**, *581*, 288– 293, DOI: 10.1038/s41586-020-2268-y

56. Grimme, S.; Steinmetz, M. Effects of London dispersion correction in density functional theory on the structures of organic molecules in the gas phase. *Phys. Chem. Chem. Phys.* **2013**, *15*, 16031– 16042, DOI: 10.1039/c3cp52293h

57. Lee, K. L. K.; McCarthy, M. Bayesian Analysis of Theoretical Rotational Constants from Low-Cost Electronic Structure Methods. *J. Phys. Chem. A* **2020**, *124*, 898– 910, DOI: 10.1021/acs.jpca.9b09982

58. Brown, G. G.; Dian, B. C.; Douglass, K. O.; Geyer, S. M.; Shipman, S. T.; Pate, B. H. A broadband Fourier transform microwave spectrometer based on chirped pulse excitation. *Rev. Sci. Instrum.* **2008**, *79*, 053103 DOI: 10.1063/1.2919120

59. Neill, J. L.; Shipman, S. T.; Alvarez-Valtierra, L.; Lesarri, A.; Kisiel, Z.; Pate, B. H. Rotational spectroscopy of iodobenzene and iodobenzene–neon with a direct digital 2–8 GHz chirped-pulse Fourier transform microwave spectrometer. *J. Mol. Spectrosc.* **2011**, *269*, 21– 29, DOI: 10.1016/j.jms.2011.04.016

60. Pérez, C.; Lobsiger, S.; Seifert, N. A.; Zaleski, D. P.; Temelso, B.; Shields, G. C.; Kisiel, Z.; Pate, B. H. Broadband Fourier transform rotational spectroscopy for structure determination: The water heptamer. *Chem. Phys. Lett.* **2013**, *571*, 1– 15, DOI: 10.1016/j.cplett.2013.04.014

61. Armstrong, D. W.; Talebi, M.; Thakur, N.; Wahab, M. F.; Mikhonin, A. V.; Muckle, M. T.; Neill, J. L. A Gas Chromatography-Molecular Rotational Resonance Spectroscopy Based System of Singular Specificity. *Angew. Chem., Int. Ed.* **2020**, *59*, 192– 196, DOI: 10.1002/anie.201910507

62. Frisch, M. J.; Trucks, G. W.; Schlegel, H. B.; Scuseria, G. E.; Robb, M. A.; Cheeseman, J. R.; Scalmani, G.; Barone, V.; Petersson, G. A.; Nakatsuji, H.; Li, X.; Caricato, M.; Marenich, A. V.; Bloino, J.; Janesko, B. G.; Gomperts, R.; Mennucci, B.; Hratchian, H. P.; Ortiz, J. V.; Izmaylov, A. F.; Sonneberg, J. L.; Williams-Young, D.; Ding, F.; Lipparini, F.; Egidi, F.; Goings, J.; Peng, B.; Petrone, A.; Henderson, T.; Ranasinghe, D.; Zakrzewski, V. G.; Gao, J.; Rega, N.; Zheng, G.; Liang, W.; Hada, M.; Ehara, M.; Toyota, K.; Fukuda, R.; Hasegawa, J.; Ishida, M.; Nakajima, T.; Honda, Y.; Kitao, O.; Nakai, H.; Vreven, T.; Throssell, K.; Montgomery, J. A., Jr.; Peralta, J. E.; Ogliaro, F.; Bearpark, M. J.; Heyd, J. J.; Brothers, E. N.; Kudin, K. N.; Staroverov, V. N.; Keith, T. A.; Kobayashi, R.; Normand, J.; Raghavachari, K.; Rendell, A. P.; Burat, J. C.; Iyengar, S. S.; Tomasi, J.; Cossi, M.; Millam, J. M.; Klene, M.; Adamo, C.; Cammi, R.; Ochterski, J. W.; Martin, R. L.; Morokuma, K.; Farkas, O.; Foresman, J. B.; Fox, D. J. *Gaussian 16*, rev. C.01; Gaussian Inc.: Wallingford, CT, 2016.

63. The IsoMRR instrument is available from BrightSpec Inc.

64. Balle, T. J.; Flygare, W. H. Fabry–Perot cavity pulsed Fourier transform microwave spectrometer with a pulsed nozzle particle source. *Rev. Sci. Instrum.* **1981**, *52*, 33– 45, DOI: 10.1063/1.1136443

65. Grabow, J.; Stahl, W.; Dreizler, H. A multioctave coaxially oriented beam-resonator arrangement Fourier-transform microwave spectrometer. *Rev. Sci. Instrum.* **1996**, *67*, 4072– 4084, DOI: 10.1063/1.1147553

66. Suenram, R. D.; Grabow, J. U.; Zuban, A.; Leonov, I. A portable, pulsed-molecular-beam, Fourier-transform microwave spectrometer designed for chemical analysis. *Rev. Sci. Instrum.* **1999**, *70*, 2127–2135, DOI: 10.1063/1.1149725

67. Neill, J. L.; Mikhonin, A. V.; Chen, T.; Sonstrom, R. E.; Pate, B. H. Rapid Quantitation of Isomeric and Dehalogenated Impurities in Pharmaceutical Raw Materials Using MRR Spectroscopy. *J. Pharm. Biomed. Anal.* **2020**, *189*, 113474, DOI: 10.1016/j.jpba.2020.113474

68. Gordy, R. L. C. W. *Microwave Molecular Spectra*, 3rd ed.; Knovel, 1984; Chapter XIII, pp 647–724.

69. Fliege, E.; Dreizler, H. Investigation of the Stark Shift of the Benzene-d_1 l_{01} - 0_{00} Rotational Transition by Microwave Fourier Transform Spectroscopy. *Z. Naturforsch., A: Phys. Sci.* **1987**, *42a*, 72–78, DOI: 10.1515/zna-1987-0112

Chapter 6: A New Sampling System for Selective Deuteration Impurity Analysis by Rotational Spectroscopy

*The following chapter comprises a collaboration with the Harman group at the University of Virginia. The initial work can be found in Smith, J. A.; Wilson, K. B.; Sonstrom, R. E.; Kelleher, P. J.; Welch, K. D.; Pert, E. K.; Westendorff, K. S.; Dickie, D. A.; Wang, X.; Pate, B. H.; Harman, W. D., Preparation of cyclohexene isotopologues and stereoisotopomers from benzene. Nature **2020,** 581 (7808), 288-293. Sarah Brewster is aknowledged in the work within this chapter as she also took part in this collaboration during her undergraduate research studies. Additionally, much thanks is given to Dean Harman for the use of his figures and helpful discussion and to Justin Weatherford-Pratt of the Harman group for his role in the synthesis of all analytes in this chapter.*

6.1: *Introduction*:

Incorporating deuterium into Active Pharmaceutical Ingredients (APIs) in medicinal drugs has flourished in recent years. This is due to the benefits that the deuterium kinetic isotope effect (DKIE) can bring. The zero-point vibrational energy of a C-D bond is lower than that of a C-H bond such that the energy required to break the C-D bond will be higher than the C-H bond ($\Delta E_D > \Delta E_H$).[1, 2] This is summarized in Figure 6.1. As deuterium (D) is twice as heavy as hydrogen (H), and with this difference in activation energy, substituting deuterium in place of hydrogen at key locations of the drug's molecular geometry can affect rate-limiting steps of metabolic processes substantially.[1, 3-5] As an added benefit, this subtle change will often not affect other characteristics of the drug like its ability to bind to its target or change the overall shape of the drug, where the typical strategy is to substitute with fluorine or a methyl group.[1-3]

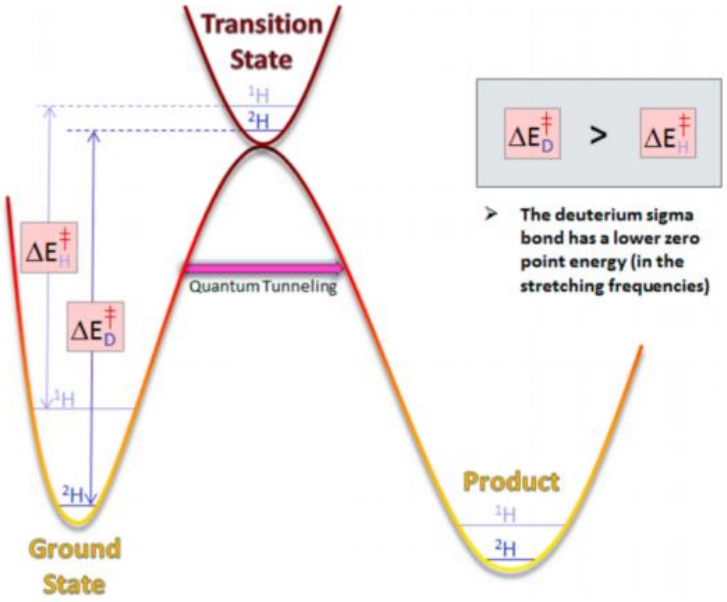

Figure 6.1: The standard model of the deuterium kinetic isotope effect depicted by Thomas G. Gant (dx.doi.org/10.1021/jm4007998 | J. Med. Chem. 2014, 57, 3595−3611).[2] The lower ground state zero-point energy of the C-D bond over the C-H bond leads to stability that can affect metabolic reaction rates in the body and reduce unsafe oxidated byproducts if deuterium is located at key parts of the molecule.

If a drug works at least in part by the breakage or formation of one of these C-D bonds, this isotopic substitution can increase the half-life of the drug and reduce dosage needed because the bond can better withstand metabolizing enzymes in the body.[1, 3, 4] The more stable C-D bond can also reduce chances of oxidation reactions taking place that can cause toxic byproducts so selectively incorporating deuterium can have major benefits to observed side effects from drugs caused by these byproducts.[1] Many deuterated drugs and deuterated APIs are now under development, and some have already been granted approval by the FDA.[1, 2, 5, 6] It was only recently that incorporating deuterium into a drug was FDA approved. Deutetrabenazine became the first FDA approved deuterated drug in 2017, which helped people with Huntington's disease by reducing the frequency of taking the medication and preventing withdrawal symptoms from the quick metabolism of the nondeuterated version of the drug.[3, 4]

Even though these drugs may not seems very different from their nondeuterated forms, the deuterated forms are considered “new chemical entities” and may be separately patented.[3, 5] The challenge lies in selectively incorporating the isotopic substitution and providing a full analysis to prove the chemical structure of the new drug and its efficacy and benefits.[3, 5] In regards to chemical structure, deuterium incorporation can unintentionally lead to various isomers classified as isotopomers (same amount of deuterium but in various locations on the molecule) and isotopologues (differing in the amount of deuterium atoms). These additional species are known as isotopic impurities, and each could have their own pharmacokinetic profile. Importantly and alarmingly, there is no clear guidance on the analytical approaches to take in identifying and quantifying all isotopic species being created in these syntheses, and industry standards for isotopic purity in APIs are just beginning to be developed. In fact, identifying and quantifying these species is quite difficult and separating them is even on the edge of impossibility because the substitution of a deuterium in place of a hydrogen is a very subtle change (more generally, any isotopic substitution). Therefore, an analytical technique is needed that can perform well in highly complex mixtures of molecules with very small differences to quantify levels of all the various isotopic impurities being produced by a synthetic procedure such that the analysis can guide synthetic chemists as to how to reduce these impurities. Mass spectrometry, while having its uses in the identification of isotopologues, would have great difficulty in the analysis of isotopomers, especially if fragmentation patterns are complex and difficult to interpret. NMR has been another technique used for these analyses; however, it has its restrictions when the deuterium incorporation is not in a unique location of the molecule and is convoluted by many overlapping features from the hydrocarbon species.

Recently, Molecular Rotational Resonance (MRR) spectroscopy has provided an analytical approach to identify and quantify the isotopic impurities produced in a synthetic pathway through a "cocktail" reaction, which generates all possibly isotopic isomers of a given reaction (discussed in Chapter 5).[7] This reaction allows for a library of possibly impurities to be made that can be referenced during the selective isotopic incorporation reactions. With known rotational transitions to be monitored, the analysis time can then become much faster by moving to a cavity instrument.[8] The motivation for the work in this chapter stems from another example of the analytical approach taken by MRR for isotopic impurities which was published in *Nature* in 2020: *Preparation of cyclohexene isotopologues and stereoisotopomers from benzene*.[9] This paper was the work of an ongoing collaboration between the Harman and Pate research groups at the University of Virginia. The Harman group uses a tungsten dearomatization agent in which a wide range of aromatic molecules can be bound to allow for stepwise additions of hydrogen or deuterium that can be used in a building block strategy.[9] The tungsten metal complex ($WTp(NO)(PMe_3)$) helps by mediating the additions in a regio- and stereo-specific way when a reducing agent like $NaBD_4$ is used in solution to incorporate deuterium onto an aromatic molecule, in this case converting benzene to various isotopologues of cyclohexene.[9] Scheme 6.1 shows an example of this stepwise addition of H/D (depicted as ^{x}H, where x = 1 or 2) onto benzene bound to the tungsten complex. Once the additions are complete, the cyclohexene can then be removed from the metal through heating or oxidative processes.

Scheme 6.1: *Stereoselective addition of deuterium to benzene bound to a WTp(NO)(PMe$_3$) complex. (With permission from W. D. Harman)*

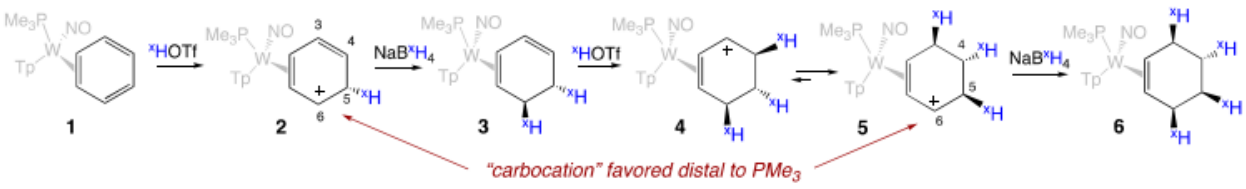

MRR spectroscopy is uniquely well-suited for the analytical challenges in isotopic impurity identification and quantification that can be summarized by four characteristic strengths of the technique:[10-13]

1) Each chemically distinct isotopic isomer has a unique spectral signature arising from the change in mass distribution when deuterium replaces hydrogen and, more generally, when any isotopic substitution takes place (^{13}C, ^{15}N, ^{18}O, ^{34}S, *etc.*)[14]
2) The signature for each of all possible isotopic isomers can be calculated to high accuracy from a single theoretical equilibrium geometry of the parent isotopic species from quantum chemistry calculations even if there is no existing reference sample for the isotopic isomers following Kraitchman's Equations[9, 15]
3) The CP-FTMW instrument has exceptionally high spectral resolution allowing identification of spectral fingerprints with effectively zero spectral overlap from very complex mixtures without prior chemical separation[10, 11]
4) When an isotopic impurity is measured and fit in a rotational spectrum, the species can easily be identified and quantified in any MRR spectrometer by its measured transition frequencies that are instrument-independent[10, 14]

The previous paper illustrates these strengths in detail.[9] In what on surface level seems like a simple molecule, the cyclohexene synthesized and shown in Scheme 6.1 and labeled in Figure 6.2 has 282 possible chemically distinct deuterated isomers exacerbated by the presence of ring-pucker conformations leading to 528 rotationally distinct deuterated isomers. Any small change in the mass distribution of the molecule will change the molecule's principal moments-of-inertia and produce a new, unique rotational spectrum for that molecular geometry. Calculating what the rotational spectrum of any of these many distinct isomers is straight forward, though. The spectrum can be determined through knowing the rotational constants (A, B, and C) from solving Schrödinger Equation with the rigid-rotor Hamiltonian operator for rotational kinetic energy as well as calculating the electric dipole moment vector in the principal axis system. One only needs to perform quantum chemistry calculations for the parent isotopologue species as, under the Born-Oppenheimer approximation, each isotopic isomer has the same equilibrium geometry. One can invoke zero-point vibrational energy calculation changes into this argument, but these effects are expected to be small and therefore these additional calculations are typically left out. The small change of mass at any point in the molecule will change the principal moments-of-inertia which can be quickly recalculated without performing quantum chemistry calculations on every isotopic substitution. Once additional isotopic isomers are identified and their rotational constants are known, scaling factors can then be used to update predictions to make isotopic isomer identification even easier and with higher confidence. The newly calculated rotational constants of the molecular geometry by substituting deuterium in the place of hydrogen will determine the quantized energy levels, and the electric dipole moment of the equilibrium geometry will determine the transition intensities. We note

that the change in mass on isotopic substitution will cause a change in the electric dipole moment vector, but these changes are expected to be very small (however this is an area for future research). With advances in quantum chemistry, like that of dispersion-corrected density functional theory,[16] the accuracy of the predicted rotational spectrum is very high, even with such small changes as exchanging hydrogen for deuterium.

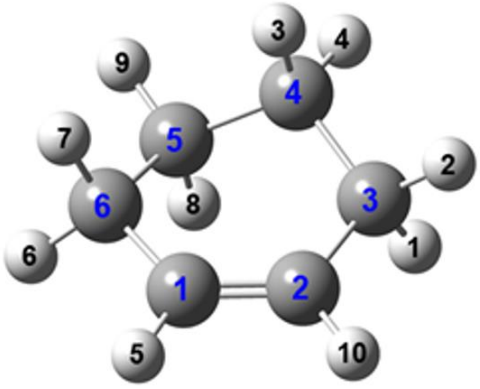

Figure 6.2: Labeling convention for cyclohexene's equilibrium geometry, performed at B3LYP D3BJ/6-311++G(d,p) level of theory.

The power that MRR spectroscopy has in structure identification to identify both isotopologues and isotopomers is depicted in Figure 6.3, called an isotope grid. Because cyclohexene is mostly planar with mass along the c-principal axis being essentially zero, a simplification can be made to show that effectively the sum of the rotational constants, (A+B), can give information on which isotopologue is present, while the difference of those constants, (A-B), can give information on where in the system the isotopic substitution is taking place, or rather, which isotopomer is present. Using just one structure from previously fit experimental result with refinement done by measuring ^{13}C-subsituted isotopomers in natural abundance to

get the rotational constants, the remaining 527 rotationally distinct structures are plotted in this grid. The isotope grid shows rows of points, where each point consists of an isotopic isomer, and where each row consists of the various isotopomers across (A-B) for the given isotopologue. Increasing in the amount of deuterium substitution along (A+B) shows very clear breaks for rows.

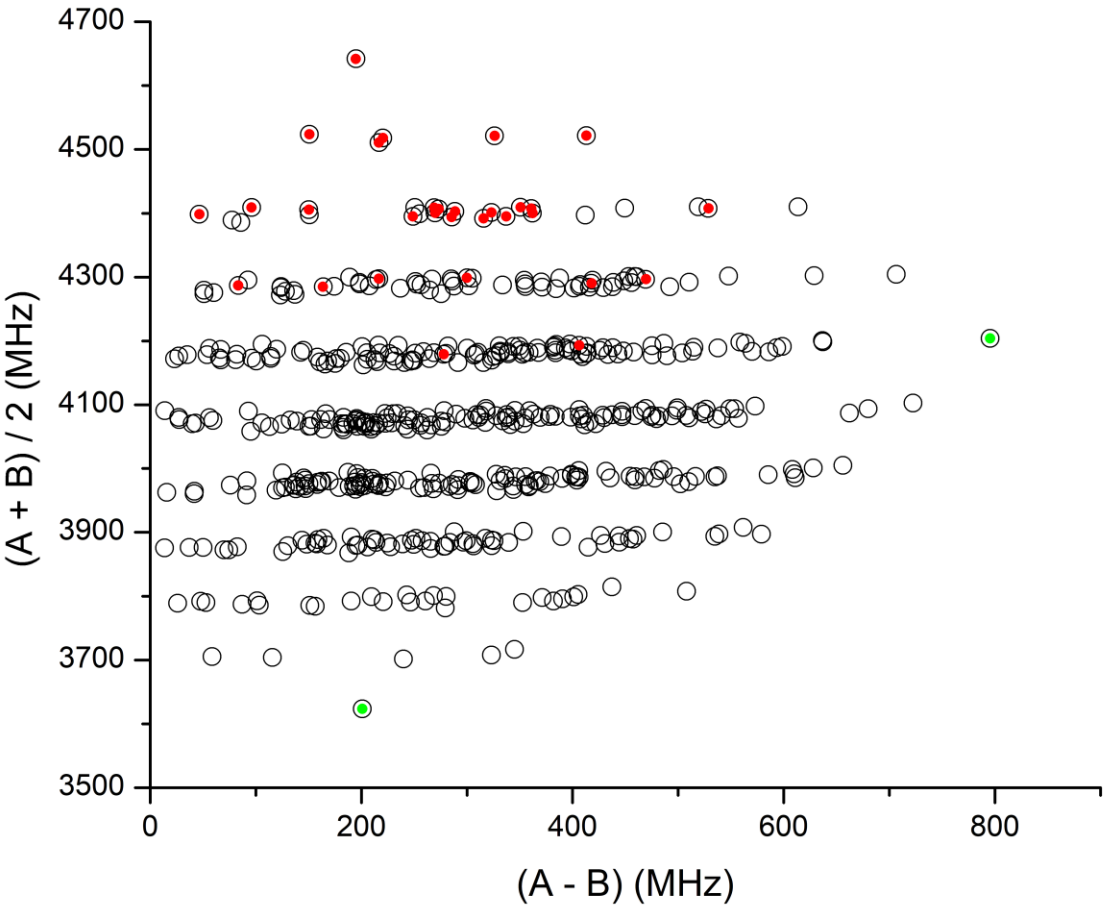

Figure 6.3: Isotope grid for cyclohexene. Black circles represent the predictions of all 528 rotationally distinct isotopic isomers while red circles represent experimentally fit species observed in the Harman collaboration project. Clear breaks in rows show the amount of deuteration in cyclohexene from the parent d0 to the last row for fully deuterated cyclohexene. Each row consists of the various isotopomers for the given isotopologue.

The grid is expanded in Figure 6.4 to show that within these isotopologue rows, every isotopomer is discernable from the other isotopomers. This is because every unique distribution of mass will have unique moments of inertia and thus unique rotational constants and thereby produce unique rotational spectra. This is unlike other techniques like mass spectrometry which may struggle to distinguish isotopomers in particular is fragmentation patterns are not clear or for NMR if many spectral features overlap or many impurities cause spectral complexity.

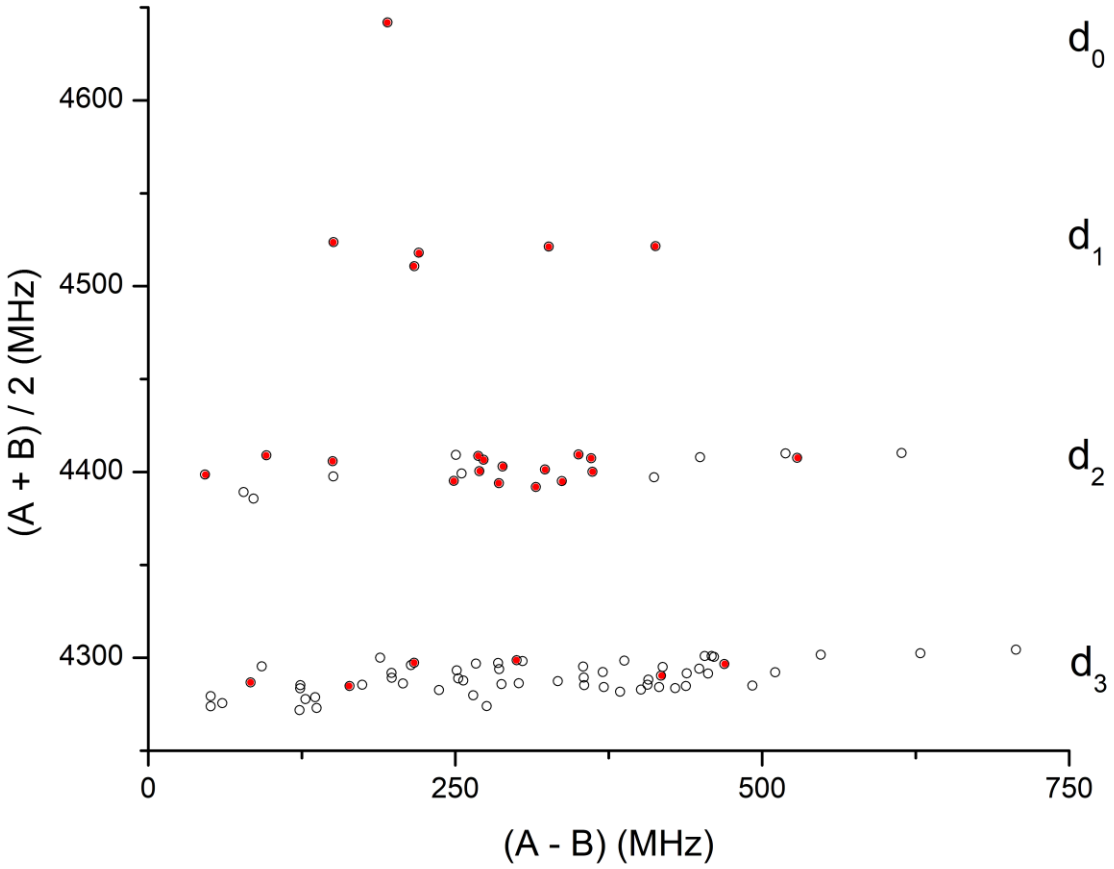

Figure 6.4: A zoom-in of the first four rows of the isotope grid in Figure 6.3. Each row pertains to the isotopologue on the right of the figure. Each data point is unique from the other isotopic isomers.

Even though 528 rotationally distinct isomers exist for cyclohexene, all these isomers were calculated to be resolvable in an MRR spectrum with little spectral overlap without need for chemical separation. Even with potential overlap of spectral features, there are often several transitions in the instruments bandwidth and at least in the case of cyclohexene, there are often patterns that help distinguish species like the presence of ring-pucker isomers, quadrupole nuclear hyperfine splitting, or other isotopic patterns. Of course, not all isomers are expected to be present in the reaction chemistry due to the governance of the tungsten metal complex that benzene is bound to when reductions to cyclohexene are made.[9] Identification of these many species is done through comparison of calculated rotational constants to experimentally fit rotational constants of observed spectra with accuracy on the order of <<1 MHz (much less than 1% error) in each constant.[16, 17] Comparison of all possible cyclohexene isotopic isomers to each experimental fit yielded clear best fits for the RMS percent error observed for high confidence in impurity identification.[9] The quantification of fractional abundances of all observed species were obtained through the comparison of each species spectral signature's intensity and will be discussed in detail in the next section.

In the previous work,[9] one common discrepancy between MRR and NMR analysis was that MRR measured higher abundances of isotopic isomer impurities. Evidence suggested that these impurities could be generated in the heating process used to liberate the cyclohexene product into the gas phase from the solid tungsten metal complex for analysis.[9] Sample was loaded into a small reservoir located within the vacuum chamber and heated where the walls of the reservoir were also heated. Long heating cycles on the order of 1-2 hours were required to acquire an appreciable abundance of cyclohexene gas since the heating was limited to

approximately 200°C by the pulsed nozzle sample injection system (o-rings and solenoid temperature limits). This temperature limit produces a slow release of cyclohexene from the metal, which it is believed could have led to deuterium/hydrogen scrambling in the cyclohexene. Additionally, in order to study new synthetic samples, the instrument needed to be broken down between every measured sample by breaking vacuum, cleaning sample-holding reservoirs, and warming up diffusion vacuum pumps that account for many hours between samples or limit the analysis to one day per sample. Therefore, the use of the technique in developing synthesis methodologies was limited, where reaction conditions may need to be screened, generating many samples for analysis.

In this chapter, a new sample cell was designed and implemented to allow for external sample heating (up to 250°C) for rapid release of analytes from the metal complex being used in the Harman research group as a follow up to the previous publication on this work. The new sample cell offers improvements to sampling efficiency and was used to provide further explanations to results of the previous work. The sample cell design and performance will be discussed herein, and additionally, two applications of the set-up will be shown:

1) Efficiency in the sampling and heating of the cell allowed MRR analysis to be able to inform and guide the synthesis to reduce isotopic impurities by connecting identified impurities to the reaction chemistry
2) The kinetic effects caused by changes in the ligand structure of the metal complex were studied in how they affected the activation energy of release of the analyte upon heating

6.2: *Sample Cell Design and Performance*:

A stainless-steel cell was designed such that a stainless-steel, sample-holding crucible within the cell was thermally isolated from the rest of the cell using a Vespel support post. This material was chosen as it has very low thermal conductivity and a higher temperature limit than the reservoir system used in previous experiments so that the walls of the system were not also being heated and also has low outgassing of volatiles that could interfere with the experiement.[9] A heating cartridge and thermocouple were attached to the sample-holding crucible for heating of samples with an Omega temperature controller. A dry scroll vacuum pump was used to pull vacuum on the cell and gas injection lines for purging, rapid sample mixture preparation, and quick turnaround of measurements. The sample cell is effectively a miniature gas cylinder that can be controlled much easier for creating constituent gas mixtures. A major advantage of the set-up is that sample can be heated at a lower temperature (~100°C) and vacuum/purged to remove any volatile impurities like remaining solvent and water, reducing the complexity of the analysis during the increased heating cycles to release the analyte from the metal complex.

The sample cell is pictured below in Figure 6.5. The sample cell volume with the added volume of the T-connector containing the electrical temperature control wires and connections is approximately 450 cm^3. An inlet allowed for gaseous samples and neon (used to make dilute mixtures) to be added. A dry scroll pump could be used to evacuate the cell between measurements. A pressure gauge was used to provide backing pressure control into the spectrometer. An additional liquid sample inlet for syringe sample injections was added for testing cell performance.

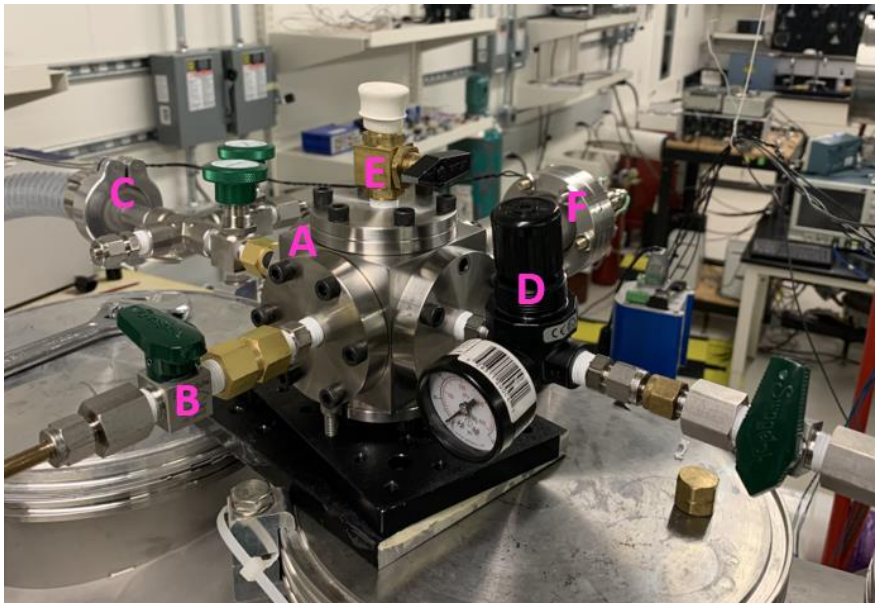

Figure 6.5: (A) The external sample cell with total volume ~450 cm^3. **(B)** The inlet for adding gaseous samples and backing gas, neon. **(C)** Outlet to dry scroll vacuum pump. **(D)** Pressure gauge to control backing pressure going into the instrument. **(E)** Liquid sample injection port. **(F)** Additional volume under vacuum where electrical connections for the heating cartridge and thermocouple wires are stored.

A general procedure for a measurement consists of the following. Liquid or solid sample is placed in the external cell's sample-holding crucible followed by removal of atmospheric pressure using the dry scroll vacuum pump. While not done in these experiments, the sample cell is small enough and transportable to allow for loading in nitrogen-filled gloveboxes for samples that might be air-sensitive. If samples were heated, they were heated under 1 atm neon gas for a desired duration. Following heating, additional neon is added to bring the analyte to a desired percent mixture in neon and the crucible's temperature is reduced to stop any additional processes from the higher heating (discussed in the next section). The sample in neon is then flowed through an output gas regulator at 15 psig and into three separate nozzle sources in a line. Solenoid valves (held open for 700 µs) pulse the gas mixture through a 1 mm orifice at a

repetition rate of 3 Hz into the vacuum chamber of the instrument to create a supersonic jet expansion for rotationally cooling the analyte. A CP-FTMW spectrometer is used for the analysis of each measurement within this chapter. Details of the rotational spectrometer are discussed elsewhere,[11, 18] but the important features used in these experiments will be described throughout this section. Microwave light in frequency ranges from 5.5-7.5 GHz, 2-8 GHz, or 6-18 GHz (dependent on the system being studied and available electronics) for varied chirp duration dependent on the electric dipole moment of the analyte is propagated through the three jet expansions to polarize the sample with a sequence of eight excitation/detection sequences per sample injection. This gives an effective measurement repetition rate of 24 Hz. Typical gas injections are on the order of 10 nmol in amount of analyte used per injection.

To test the performance of making analyte mixtures in the cell, a proxy to the cyclohexene measurements in the previous work was designed. First, a 0.1% mixture of cyclohexene gas in neon was made in a large gas cylinder and attached directly to the instrument without use of the sampling cell. Spectra were recorded to compare to the new sample cell performance as it is essentially a miniature version of the larger tanks typically used in these experiments. To approximate how much cyclohexene would be liberated from a typical amount of crystalline metal complex from the Harman group synthesis, an assumption was made of complete release of cyclohexene from 100 mg of metal complex sample during the heating. The molecular weight of the metal complex plus cyclohexene is 584 g/mol, so 100 mg of total sample equates to 0.00017 moles. Therefore, 0.00017 moles of cyclohexene were assumed to be released from heating with a molecular weight of 82 g/mol such that 14 mg cyclohexene total would be released from heating the 100 mg of metal complex. The density of cyclohexene is 0.811 g/mL, so this

equates to 17 µL of cyclohexene. Under ideal conditions and the approximate volume of the sample cell being 0.450 L, 17 µL of cyclohexene yields 0.00945 atm total partial pressure which equates to 7.18 Torr cyclohexene.

Generally, a 0.1% mixture of analyte in neon gas is made for analysis using a pulsed jet expansion sample introduction. However, for a smaller and less polar molecule, higher concentrations might perform better. Through trials *via* injection of the liquid cyclohexene and dilution with neon gas in the sample cell, 0.1%, 0.2%, 0.3%, and 0.4% mixtures were made and compared. It was observed that a 0.2% mixture performed best in the current system. For a 0.2% mixture in the new sample cell, where 7.18 Torr of cyclohexene is expected from full release of 100 mg of the metal complex sample, 3590 Torr of neon is needed. This equates to ~55 psi neon added to the sample cell; however, the sample was heated under 1 atm (0 psig / 15 psi) neon for a desired duration, and then the remaining ~40 psig neon was added as the sample cooled to stop any additional release of cyclohexene. In terms of heating, the sample was heated for ten minutes at 250 °C for complete release of cyclohexene and then allowed to cool to 140 °C. 12,000 FIDs were collected and averaged from the spectrometer in each measurement before the sample mixture began to run out from the sample cell.

The liquid injection proxy test was compared to a measurement with synthesized 3-d1-cyclohexene released from the Harman group's metal complex and found to be of similar intensity suggesting the assumption of complete release of cyclohexene from the metal complex to be reasonable. This was further confirmed by a series of measurements in which the metal complex sample was heated to 250 °C for three minutes, cooled to 140 °C, injected, and recorded followed by a vacuum purge and repeat until there was no longer any evidence of remaining

cyclohexene. The sum of intensity values for the dominate cyclohexene transition was compared to the intensity value of each heating cycle to acquire a percentage of cyclohexene released at each measurement. Heating for three minutes released ~90% of the cyclohexene present, so ten minutes of heating at 250 °C was decided upon for approximately full release of cyclohexene to be used in future experiments. The experiment was repeated using 210 °C for three-minute heating cycles to compare relative impurity levels in the measurement as the sample was heated. The constant relative abundance of each species is different to that observed in the previously used sampling heating set-up where impurity levels fluctuated over long heating times and impurities were measured to be much more pronounced (shown in three different measurements in Figure 6.7).[9] The constant relative abundance of each species over several measurements is shown in Figure 6.6. Note that there is a ring pucker isomerization within cyclohexene such that two spectra are observed for some chemically distinct species of cyclohexene. To elaborate, 3-cyclohexene-d1 (labeled by carbon position in Figure 6.2) is composed of 1-d1 and 2-d1 (labeled by deuterium position in Figure 6.2), 4-cyclohexene-d1 is composed of 3-d1 and 4-d1, 1-cyclohexene-d1 is only 5-d1, and the parent isotopologue is labeled as d0.

To determine relative abundances, the intensities of transitions measured in the desired frequency range can be compared for each species. For cyclohexene, only one dominate transition ($1_{1,1} \rightarrow 0_{0,0}$) is observed for each rotationally distinct species in the 5.5-7.5 GHz frequency range. To obtain levels of each chemically distinct species, the transition intensity of ring-pucker isomers are added together and compared to the other species transition intensities. Note that the electric dipole moment components are slightly different for each species. These

effects can be applied to the calculation of relative abundances but account for ~10% or less of the determined abundance. For instance, the ring-pucker isomers 1-d1 and 2-d1 in Figure 6.6 (deuterium label from Figure 6.2) which account for the total amount of 3-d1-cyclohexene (carbon position label) is expected to be of equal transition intensity but differ in their observed intensities by about 10% from these electric dipole effects. Additionally, in some cases, the nuclear quadrupole hyperfine structure caused by the non-spherical deuterium nucleus coupling with the overall rotation of the molecule can be resolved in the measured spectra. In these cases, the sum of the hyperfine components is used to represent the transition intensity used in the relative abundance calculations.

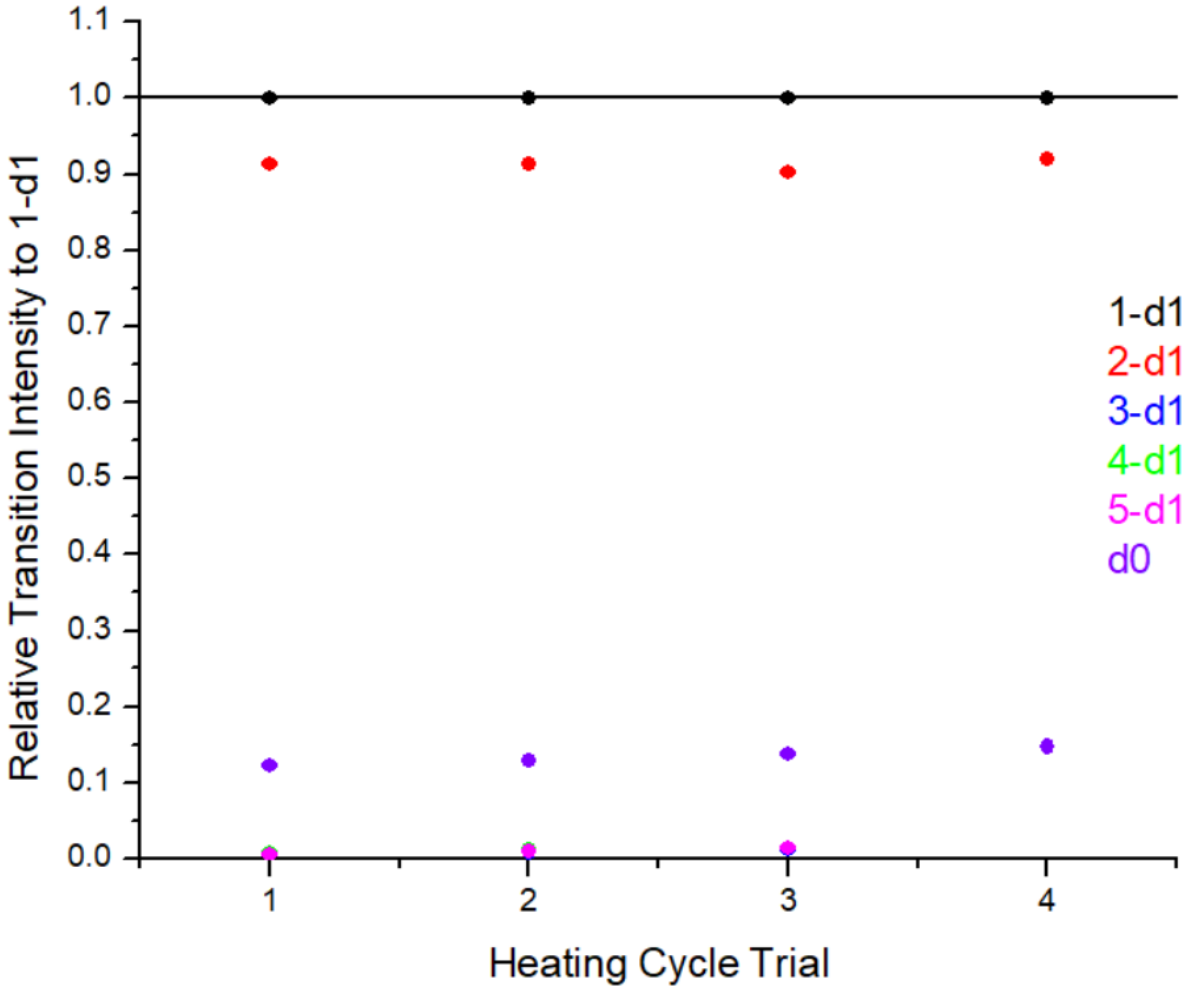

Figure 6.6: 3-d1-cyclohexene measured at multiple heating cycles of 210 °C for three minutes to liberate cyclohexene from the metal complex. Each rotationally distinct isotopomer observed, labeled by their deuterium position, is compared at each heating cycle showing constant relative impurities over multiple heating cycles.

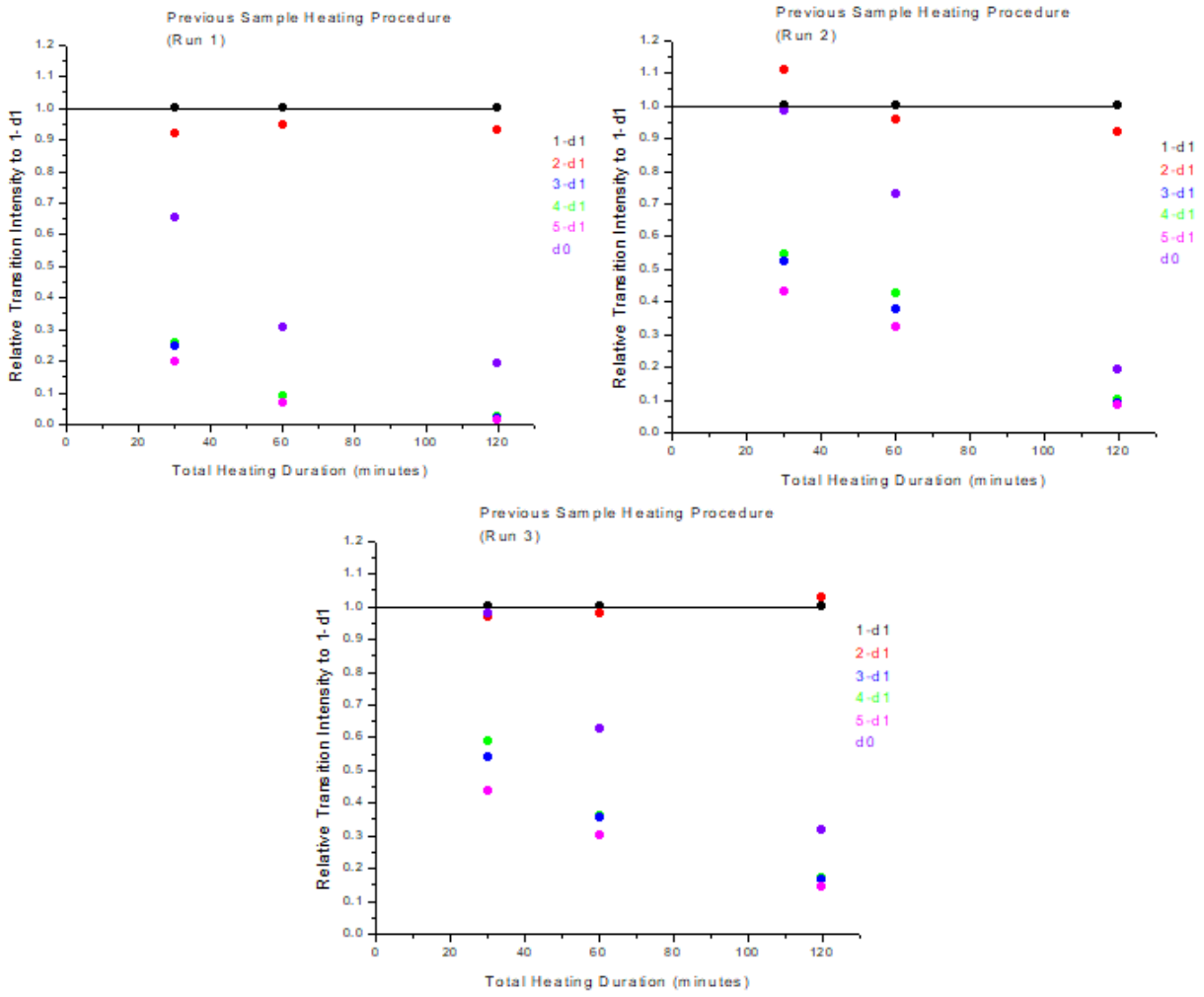

Figure 6.7: The previous sample heating procedure required much longer heating durations to release 3-d1-cyclohexene from the metal complex. Three heating cycles of 200 °C for various durations of time on three separate sampling loadings were done. Measured spectra show much more variance in the relative abundance of each impurity. This is likely due induced hydrogen/deuterium scrambling effects from much longer heating cycles and having every surface of the sample holding reservoir heated.

A primary difference in the new sample heating set-up to that of the old set-up is that only the heating crucible that holds the sample is heated. This crucible is separated by the piece of insulating Vespel support post so that once the cyclohexene is thermally released from the metal complex, it will no longer be further heated. In the previous set-up where the heating

reservoirs are placed under vacuum in the instrument's vacuum chamber, the walls of the small reservoir, sample introduction mechanisms are all being heated. With this new sampling method, the impurity levels are much more constant over the course of multiple heating cycles and consistent with the expected synthetic mechanisms allowing for more reliable quantitation.

6.3: *Applications*

6.3.1: *Guiding Synthesis with Isotopic Impurity Identification*

The new sampling system allows for quick measurements and quick turnaround between samples. In this way, the analytical method can better help synthetic chemists by giving real-time analyses of their reaction products. Once the library of possibly impurity species is known, relative abundances of each observed species can be measured quickly for subsequent samples. If a synthetic route produces high levels of a particular impurity, the synthetic chemists can alter their chemistry to attempt to reduce the production of that side product. One example of this is shown below in Table 6.1 and Figure 6.9, where the product, syn-3,4-d2-cyclohexene (depicted in Figure 6.8 for clarity) was the target molecule to be synthesized. Various levels of impurities were observed and are shown relative to that of the target species. The Harman group was able to take these impurity results and modify their synthetic procedure to reduce the amount of underdeuterated products observed in Trial 1 (highlighted in red). However, in the synthesis alteration, high levels of over deuterated products were made and can be seen in Trial 2 (highlighted in blue). Learning from these results, the final changes to the synthetic route led to Trial 3 where lower levels of impurities were observed in all cases.

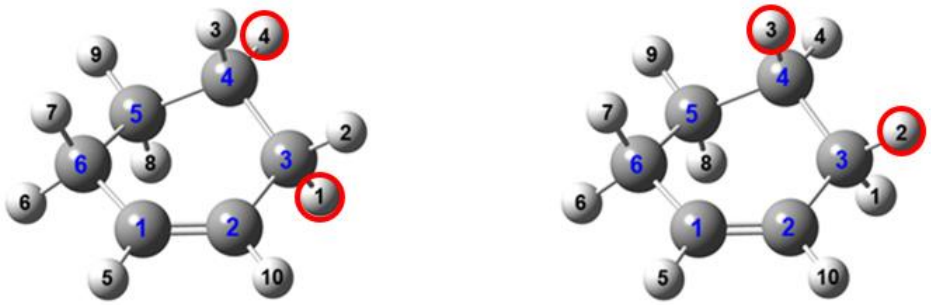

Figure 6.8: Syn-3,4-d2-cyclohexene has two rotationally distinct isomers with deuterium positions highlighted in red.

Table 6.1: *Syn-3,4-d2-Cyclohexene Impurity Analysis*

Species	Normalized Ratio to Desired Product (Syn-3,4-d2)		
(Carbon Position Label)	Trial 1*	Trial 2	Trial 3
Syn-3,4-d2	1	1	1
Anti-3,4-d2	0	0.0044	0
Syn-4,5-d2	0.0062	0.0061	0.0053
Syn-3,6-d2	0.0582	0.0218	0.0821
1,3-d2	0	0	0
2,3-d2	0.0066	0.0072	0.0030
3-d1	0.3219	0.0451	0.0520
4-d1	0.0393	0.0295	0.0258
1-d1	0.0028	0.0128	0
d0	0.0280	0.0097	0.0055
Syn-3,4-anti-5-d3	0	0.4594	0
Anti-3,4-anti-6-d3	0	0.0934	0

*Trials use different synthesis conditions described in text

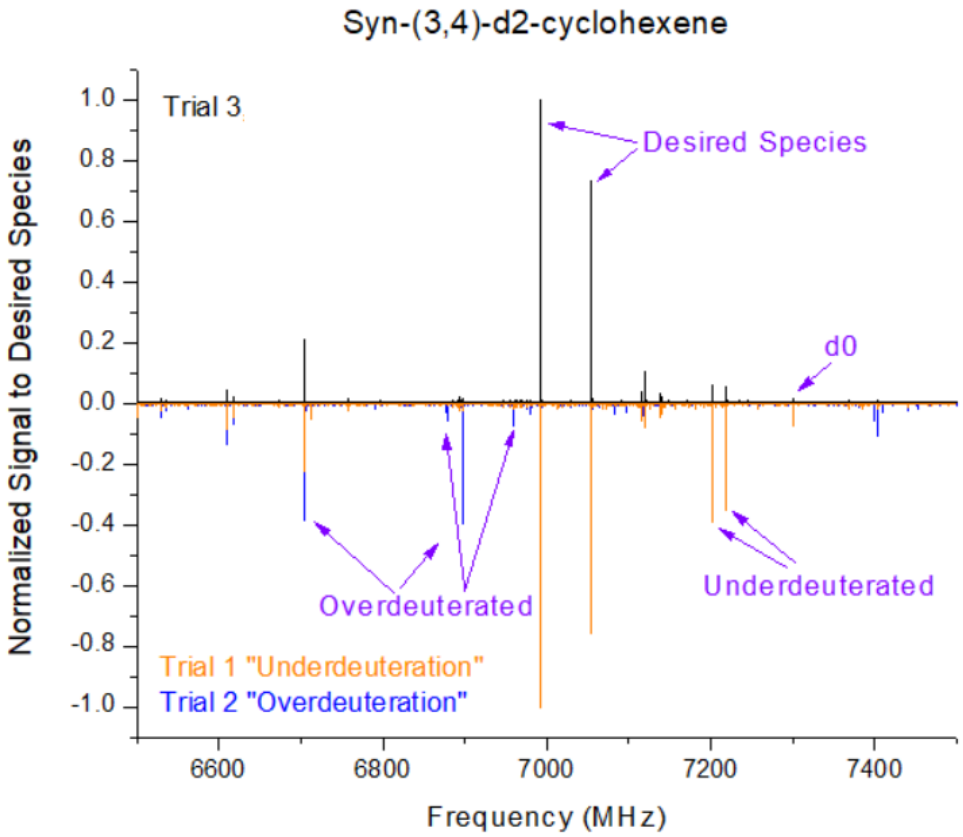

Figure 6.9: Spectroscopic signatures for the target synthetic product, syn-3,4-d2-cyclohexene and various isotopic impurities found during the synthesis trials. Trials 1 and 2 are plotted in the negative direction to show the spectrum in Trial 3 more clearly, where impurity levels are much lower. Note that the signature at ~6700 MHz for labeled for overdeuteration is not the same signature as that in black. The signature in black is at a different frequency belonging to the target molecule.

The general synthetic route to making deuterated cyclohexene on the metal complex is through reductions of benzene is shown in Scheme 6.2, where the locations of hydrogen or deuterium being added to the original benzene are denoted in a series of reaction stages. The final addition of hydride can actually take place at two sites due to the allyl shift nature of the molecule bound to the tungsten metal.[9] This shift leads to a branching ratio of possible products

that has a preference towards the target structure in each case but does allow for the reaction to take place in making an isotopic impurity.

Syn-3,4-d2-cyclohexene is synthesized following Scheme 6.3. However, in Trial 1 of the synthesis, high levels of underdeuteration in 3-d1-cyclohexene and d0-cyclohexene were observed. Scheme 3.5 depicts how the underdeuterated 3-d1-cyclohexene is likely to be produced because of the protium source in the reducing agent, $NaBD_3H$, used in Stage 2. The presence of a misdeuterated species, syn-3,6-d2-cyclohexene has a logical path as well coming from the branching ratio of the allyl shift mentioned previously (Scheme 3.6) where position 6 is deuterated in the final stage.

With this information, the changes were made to the synthesis by including CH_3OD in Stage 1 to correct for underdeuteration. However, as was found in the analysis during Trial 2 (Table 6.1), a large amount of overdeuterated products were observed. These also have a logical path to being produced as shown in Scheme 3.7 where the inclusion of CH_3OD leads to an unintentional exchange to take place adding the additional deuterium labeled in red. The increased abundance of syn,anti-3,4,5-d3-cyclohexene over anti,anti-3,4,6-d3-cyclohexene also supports these routes due to the effects of the branching ratio in the allyl shift structures depicted.

Finally, with new knowledge of the exchange taking place due to the CH_3OD, a cosolvent was added with steps using CH_3OD to act in mitigating this exchange. d3-acetonitrile was chosen as it cannot participate the exchange taking place. However, it could not be used alone due to solubility issues and was instead used as a cosolvent. Providing this compound removed the

accessibility of deuterium exchange in the early steps of the synthesis, and no spectral features for overdeuteration were observed in Trial 3.

Scheme 6.2: *General synthetic route for deuterated cyclohexene on tungsten metal complex (With permission from W. D. Harman)*

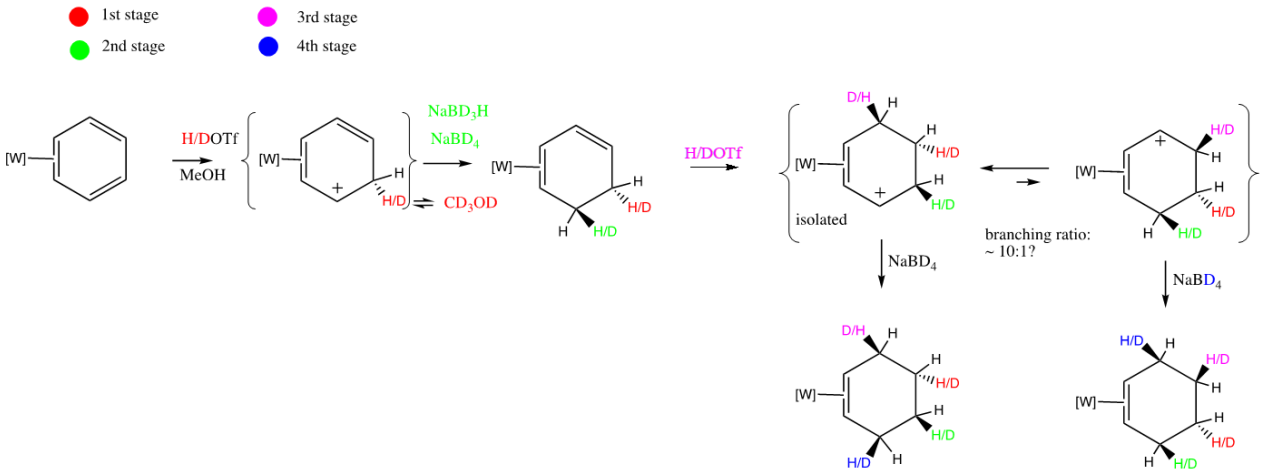

Scheme 6.3: *Synthetic route to target molecule syn-3,4-d2-cyclohexene (With permission from W. D. Harman)*

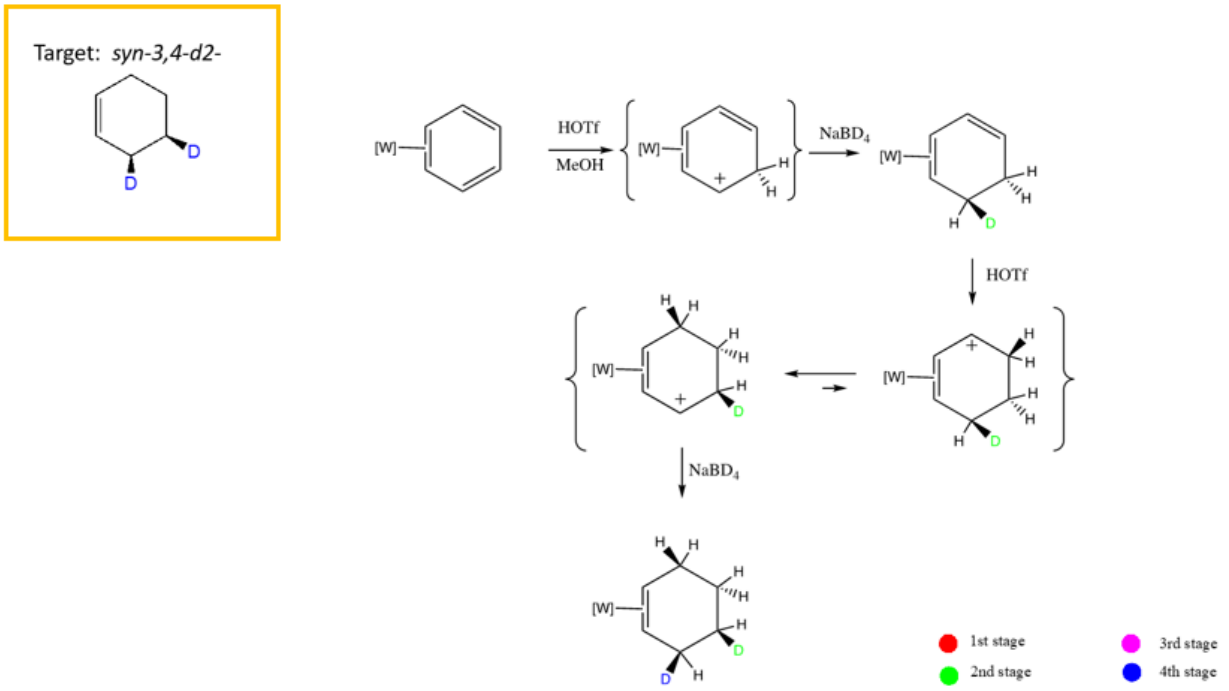

Scheme 6.4: *Underdeuteration synthetic route for observed 3-d1-cyclohexene impurity (With permission from W. D. Harman)*

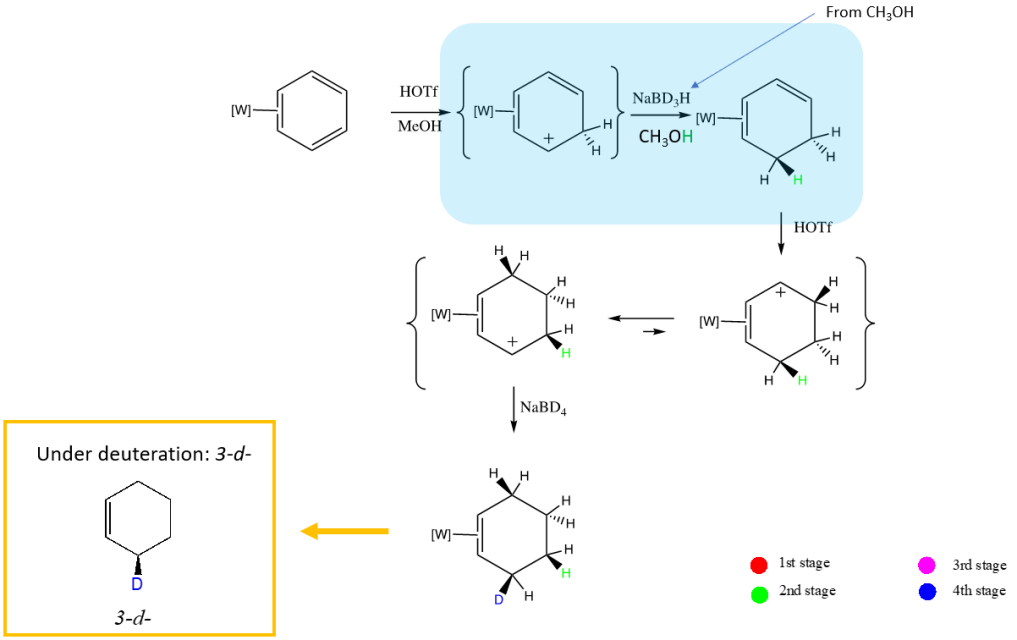

Scheme 6.5: *Misdeuteration synthetic route for observed syn-3,6-d2-cyclohexene (With permission from W. D. Harman)*

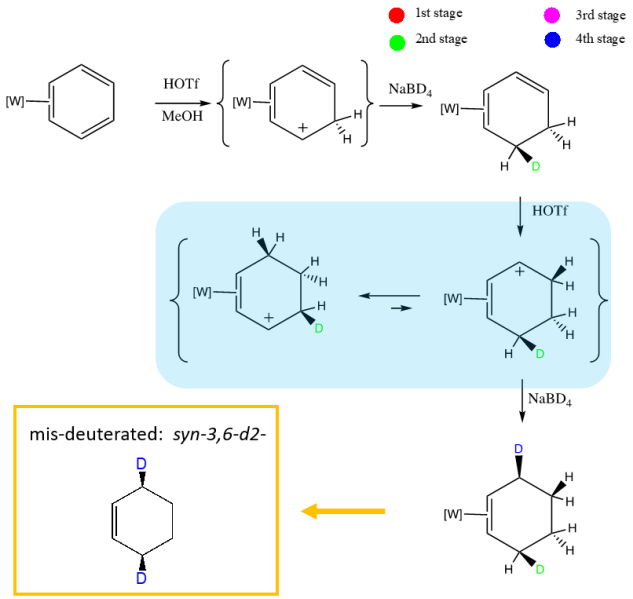

Scheme 6.6: *Overdeuteration synthetic route for observed anti,anti-3,4,6-d3-cyclohexene and syn,anti-3,4,5-d3-cyclohexene impurities (With permission from W. D. Harman)*

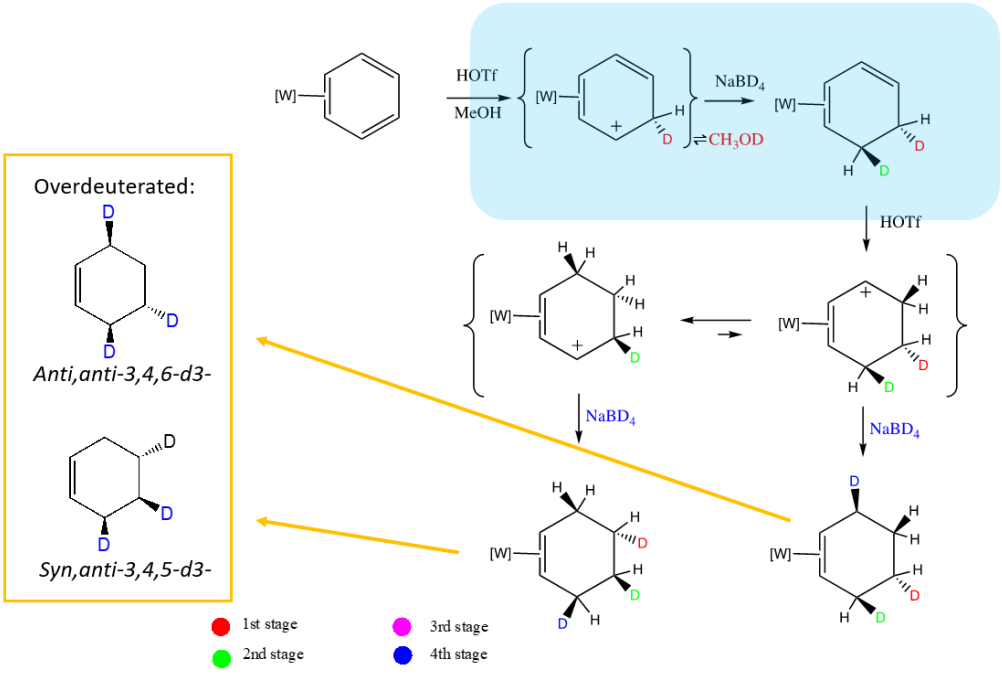

6.3.2: *Thermal Release Kinetics Study*

Due to the nature of the metal complex used in these experiments, one can use the sample cell to make measurements on the thermal release kinetics of ligands on the metal complex. By heating the metal complex, a species may be released once the activation energy of breaking the ligand bond is reached. In this collaboration, cyclohexene is being released by heating and can be monitored. For a simple heating model where a sample is heated at a fixed temperature for a fixed amount of time, the rate constant for that release is a constant. The release is expected to follow a typical Arrhenius treatment where the concentration of cyclohexene as a function of time, $[C](t)$, follows an exponential decay with more longer heating as:

$$[C](t) = [C]_0 \cdot e^{-k \cdot t} \tag{6.1}$$

Where $[C]_0$ is the initial concentration of cyclohexene on the metal complex, k is the rate constant, and t is time. To know how much cyclohexene total there is for the given sample, a measurement was done at high temperature for a long period of time to effectively release all the cyclohexene in the sample. After trialing a few temperatures and durations, we observed that heating the sample for ten minutes at 250°C removed >98% of the cyclohexene (limited by the noise level in additional heating cycles). We can then run the experiment with a shorter heating cycle first to release a fraction of the cyclohexene followed by a second measurement to release the remaining cyclohexene to get a total amount of cyclohexene present in the same. The fraction of cyclohexene released at a given temperature for a three-minute heating cycle is used to get the fraction released, f.

As shown in Equation 6.2, the fraction of cyclohexene, f, at a desired temperature heating cycle held for three minutes, t_{final}, is related to the rate constant. Taking the natural log of each side of the equation yields Equation 6.3, and this is then rearranged in Equation 6.4

$$\frac{[C](t = t_{final})}{[C]_0} = 1 - f = e^{-k \cdot t_{final}} \quad (6.2)$$

$$\ln(1 - f) = -k\ (3) \quad (6.3)$$

$$k = \frac{-\ln\ (1 - f)}{3} \quad (6.4)$$

The rate constant is related to the activation energy through Equation 6.5:

$$k = \frac{-\ln\ (1 - f)}{3} = A\ e^{\frac{-E_a}{R \cdot T}} \quad (6.5)$$

Where A is the pre-exponential factor, E_a is the activation energy, R is the universal gas constant, and T is temperature in Kelvin. Taking the natural log of both sides of Equation 6.5 yields a linear form, Equation 6.6:

$$\ln(k) = \ln(A) - (\frac{E_a}{R}) \cdot \frac{1}{T} \quad (6.6)$$

To probe the release kinetics of cyclohexene from the metal upon heating, a sample of synthesized 3-d1-cyclohexene was split into many measurements. Only a very small amount is needed for analysis, well below the 100 mg samples used above. A 3-5 mg portion of the sample was loaded into the sample cell and the ambient air was removed by the dry scroll vacuum pump and replaced by 1 atm of neon gas. The sample was heated to a desired temperature and held at that temperature for three minutes. We note that there is a non-negligible amount of time taken to reach the desired temperature (and to cool from this temperature). The sample is then allowed cooled to at least 140°C (413 K) to drastically slow the rate of cyclohexene release. To speed this

cooling process and to prepare the sample to be approximately 0.1% analyte in neon gas, 40 psig neon is added to the sample cell. The gas mixture is then delivered into the instrument at 15 psig for the measurement and signal averaged until the gas mixture runs out. Vacuum is pulled on the sample to remove any remaining analyte, and then the process is repeated on the same sample but held at 250°C for ten minutes to release the remaining cyclohexene. The ratio of the signal obtained during the first heating cycle to that of the second therefore represents the fraction of available cyclohexene released from the metal complex during the three-minute heating cycle. This is then repeated at several temperatures and plotted using Equation 6.6, above, to determine the activation energy from the slope of the curve and the pre-exponential factor from the y-intercept. The three lowest temperature data points were used to fit the data as the higher temperature data is subject to more error from being closer to the noise floor and subject to any carry-over effects. From the fit values obtained, the data from the measurements at multiple temperatures for the first fraction can be plot as shown in Figure 6.10 in blue. In this case, Equation 6.2 is rearranged to the following, where k(T) can be determined using Equation 6.5.

$$f(T) = 1 - e^{-k(T)\cdot t_{final}} \tag{6.7}$$

This process was repeated for a sample made when the ligand system of the metal complex was changed such that one ligand, trimethylphosphine, was exchanged for tributylphosphine. The reason for this change was because the tributylphosphine is cheaper, more readily available, and also that it is expected that the sterics involved in the larger hydrocarbon chains on tributylphosphine should allow cyclohexene to release at a lower temperature. The benefit of reducing the activation energy required to release cyclohexene is that at a low enough temperature, the analyte bound to the metal complex can be removed

simply by heating rather than by oxidative chemical processes making isolating the analyte much easier.

The two heating cycles to acquire the fraction released from the metal are repeated at multiple temperatures for the analyte made with the tributylphosphine ligand and the results of these two samples are displayed in Figure 6.10, where the circles represent the actual data points collected, the solid curve is the curve for the designated *A* constant and activation energy, E_a, and the dotted blue curves are upper and lower bounds of +/- 0.5 kcal/mol to give an idea for uncertainty. These measurements allow us to give a measurement on the activation energy difference of the cyclohexene bound to the metal when the ligand structure of the tungsten metal complex is changed. A reduction in activation energy of approximately 4 kcal/mol (and efficient cyclohexene release at ΔT = 50°C lower) is measured when trimethylphosphine is replaced with tributylphosphine in the ligand structure.

Measuring the activation energies and change in activation energy by other methods is difficult. The activation energy of the cyclohexene bound to the metal complex can be inferred from studies done on similar structures and situations. The calculated free energy (Δ*G*) for the bond dissociation of cyclohexene bound to MoTp(NO)(DMAP) is calculated to be ~26 kcal/mol and predicted to be 28 kcal/mol experimentally in an acetone solution.[19] In another study, for the switch between using PMe_3 and PBu_3 in the complexes WTp(NO)(PMe_3)(benzene) or WTp(NO)(PBu_3)(benzene), it is indicated that there is a free energy of activation difference of about 1.6 kcal/mol for benzene bound to these systems being displaced by acetone in solution at 298 K.[20] This free energy of activation observed in the benzene complex can be used as a lower limit for the change in activation energy for the release of cyclohexene from these complexes

using PMe_3 or PBu_3 as one of the ligands. Cyclohexene, with its ring pucker geometry, would be more susceptible to the sterics on the phosphine ligand, suggesting that the change might be greater. With these observations, calculations, and limitations (specifically that there aren't any calculations for a similar complex with PBu_3 and cyclohexene present), the measurements made using MRR spectroscopy (in the gas phase without solvent interactions) can be considered reasonable.

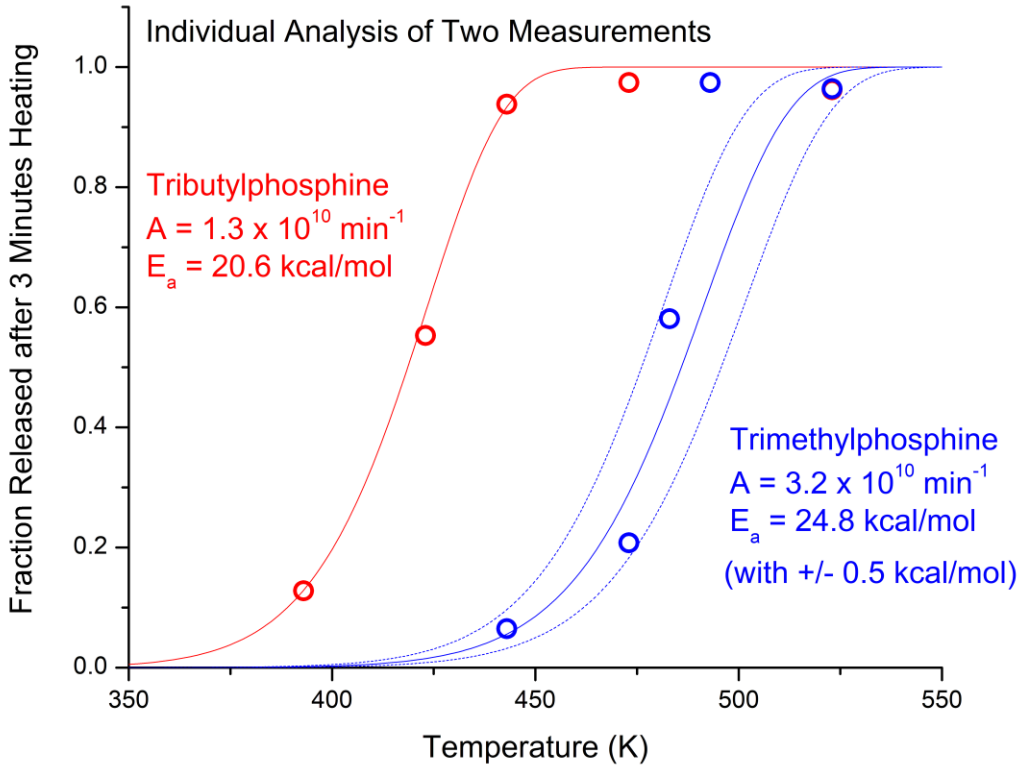

Figure 6.10: Synthesized 3-d1-cyclohexene was heated at a desired temperature for three minutes, allowed to cool to 140°C and then measured. The signal intensity of this fraction of cyclohexene released under these conditions is compared to the total amount of cyclohexene present via a second heating at 250°C for ten minutes to liberate any remaining cyclohexene from the metal complex. The observed fraction is plotted above in blue when using a metal complex that has a trimethylphosphine ligand during the synthesis vs when that ligand is replaced with tributylphosphine plotted in red. Replacing the ligand with tributylphosphine significantly lowers the temperature required to thermally release cyclohexene from the metal complex.

Additionally, a low intensity and dense spectrum was observed in the measurements using trimethylphosphine in the ligand structure that were believed to be coming from the analyte complexing through weakly-bound noncovalent interactions with trimethylphosphine. To prove that trimethylphosphine was also being released from the metal complex, we needed to move to our instrumental set-up for 6-18 GHz where trimethylphosphine has a strong transition. In this frequency range, both the analyte and trimethylphosphine could be monitored, so the experiments done on the fraction released for cyclohexene at various temperature was done again, and trimethylphosphine was monitored at the same time. The results for this series of measurements are shown in Figure 6.11 where the previous data set remains in blue. New data points for 3-d1-cyclohexene released are shown in cyan and agree quite well with the previous data set. Trimethylphosphine data points are shown in green and appear to match those of cyclohexene. This suggests two possible situations. One being that cyclohexene and trimethylphosphine have very similar activation energies and therefore release around the same time as the sample is heated. The other situation could be that cyclohexene is the first to be released from the metal but then the metal complex breaks apart releasing its other ligands and reducing to elemental tungsten. This second situation may be supported due to the remainder of sample after heating appearing black/metallic like tungsten metal whereas the original complex is light tan in color. Further analysis on the remainder after heating and analysis of other ligands are areas for future studies.

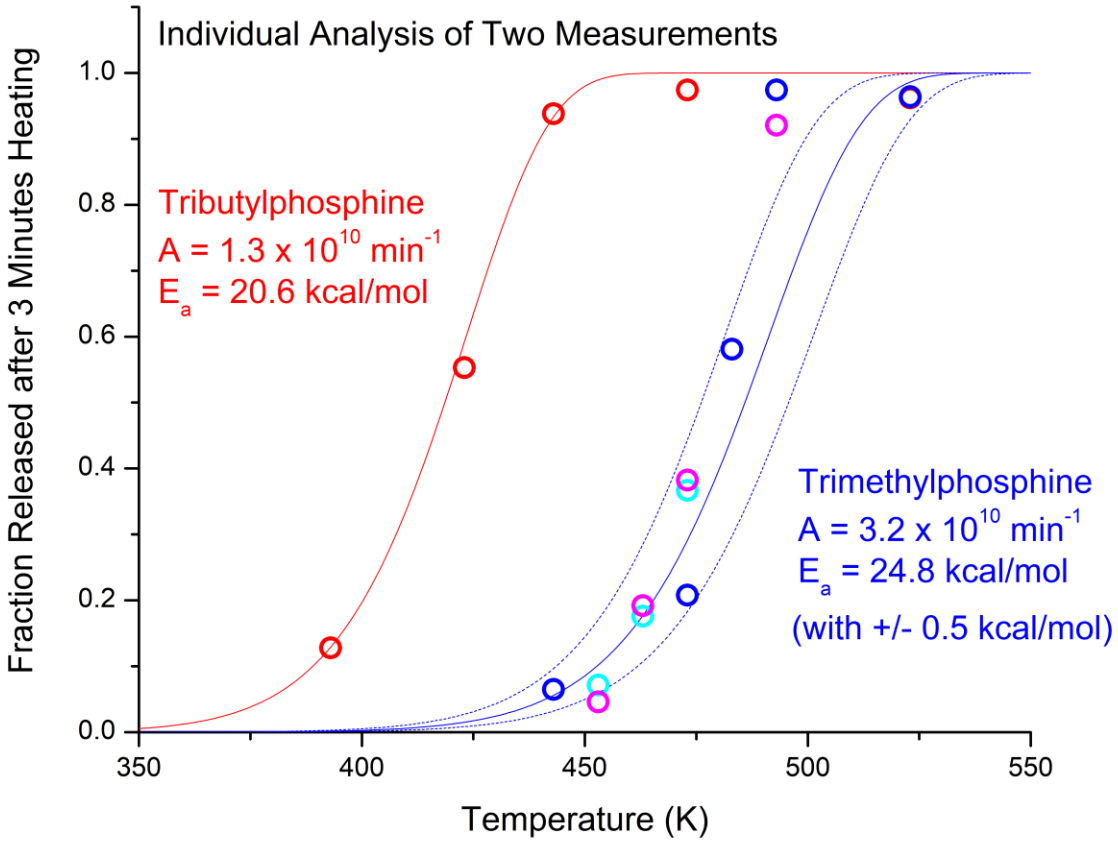

Figure 6.11: The same procedure as described in Figure 6.6 was used to measure the 3-d1-cyclohexene sample at various temperatures in the 6-18 GHz region in order to also record a transition and fraction released of the trimethylphosphine ligand (data points in magenta). The fraction released for trimethylphosphine, appears to track that of 3-d1-cyclohexene, shown in cyan, suggesting that either the two species release at very similar temperatures or that once cyclohexene is released, the remaining ligands are released from the metal.

6.4: *Conclusions*

A new sample cell was designed for preparing chemical mixtures for analysis by rotational spectroscopy in the gas phase. The sample cell provides an increased temperature range above previous studies which allows for much faster analyte release from a metal complex system used to selectively deuterate aromatic species. The sample cell was used to determine the fractional

abundance of minor isotopic impurities and allowed for very quick turn around in measurements. This increased speed, along with the much higher level of consistency in the measurements, allowed us to help guide the synthesis chemists involved in the project to alter their reactions to produce less impurities. Additionally, the thermal release of an analyte from the metal complex used could be studied through a series of measurements at various temperatures. This allowed us to compare how the activation energy of releasing the analyte changed when a different ligand structure was used in the synthesis.

This new system can effectively aid synthetic chemists in quantitatively measuring many species at once without any separation needed. Rotational spectroscopy's inherent strength in measuring unique spectral features for even the slightest structural changes makes this technique highly useful in identifying and quantifying isotopic impurity levels. As new drugs are designed to have selective positions for deuterium or other isotopes, so long as the position of these isotopic substitutions is set early on in the synthesis in smaller molecules, this technique is in a great position to do these measurements with high confidence. Additionally, for those syntheses that involve adding a deuterium stereo-selectively, the newer technique of chiral tag rotational spectroscopy provides a means to determine absolute configuration and enantiomeric excess as well be described in the next chapter.

Chapter 6 References:

1. Pirali, T.; Serafini, M.; Cargnin, S.; Genazzani, A. A., Applications of Deuterium in Medicinal Chemistry. *J Med Chem* **2019,** *62* (11), 5276-5297.
2. Gant, T. G., Using deuterium in drug discovery: leaving the label in the drug. *J Med Chem* **2014,** *57* (9), 3595-611.
3. Halford, B., The deuterium switcheroo. *C&EN* **2016,** *94* (27), 32-36.
4. Mullard, A., Deuterated drugs draw heavier backing. *Nat Rev Drug Discov* **2016,** *15* (4), 219-21.
5. Czeskis, B.; Elmore, C. S.; Haight, A.; Hesk, D.; Maxwell, B. D.; Miller, S. A.; Raglione, T.; Schildknegt, K.; Traverse, J. F.; Wang, P., Deuterated active pharmaceutical ingredients: A science-based proposal for synthesis, analysis, and control. Part 1: Framing the problem. *J Labelled Comp Radiopharm* **2019,** *62* (11), 690-694.
6. Cambridge Isotope Laboratories, Inc. https://www.isotope.com/.
7. Vang, Z. P.; Reyes, A.; Sonstrom, R. E.; Holdren, M. S.; Sloane, S. E.; Alansari, I. Y.; Neill, J. L.; Pate, B. H.; Clark, J. R., Copper-Catalyzed Transfer Hydrodeuteration of Aryl Alkenes with Quantitative Isotopomer Purity Analysis by Molecular Rotational Resonance Spectroscopy. *J Am Chem Soc* **2021,** *143* (20), 7707-7718.
8. Balle, T. J.; Flygare, W. H., Fabry–Perot cavity pulsed Fourier transform microwave spectrometer with a pulsed nozzle particle source. *Review of Scientific Instruments* **1981,** *52* (1), 33-45.
9. Smith, J. A.; Wilson, K. B.; Sonstrom, R. E.; Kelleher, P. J.; Welch, K. D.; Pert, E. K.; Westendorff, K. S.; Dickie, D. A.; Wang, X.; Pate, B. H.; Harman, W. D., Preparation of cyclohexene isotopologues and stereoisotopomers from benzene. *Nature* **2020,** *581* (7808), 288-293.
10. Neill, J. L.; Yang, Y.; Muckle, M. T.; Reynolds, R. L.; Evangelisti, L.; Sonstrom, R. E.; Pate, B. H.; Gupton, B. F., Online Stereochemical Process Monitoring by Molecular Rotational Resonance Spectroscopy. *Organic Process Research & Development* **2019,** *23* (5), 1046-1051.
11. Brown, G. G.; Dian, B. C.; Douglass, K. O.; Geyer, S. M.; Shipman, S. T.; Pate, B. H., A broadband Fourier transform microwave spectrometer based on chirped pulse excitation. *Rev Sci Instrum* **2008,** *79* (5), 053103.
12. Neill, J. L.; Douglass, K. O.; Pate, B. H.; Pratt, D. W., Next generation techniques in the high resolution spectroscopy of biologically relevant molecules. *Phys Chem Chem Phys* **2011,** *13* (16), 7253-62.
13. Park, G. B.; Field, R. W., Perspective: The first ten years of broadband chirped pulse Fourier transform microwave spectroscopy. *J Chem Phys* **2016,** *144* (20), 200901.
14. BrightSpec How MRR Works. https://www.brightspec.com/how-mrr-works/.
15. Kraitchman, J., Determination of Molecular Structure from Microwave Spectroscopic Data. *American Journal of Physics* **1953,** *21* (1).
16. Grimme, S.; Steinmetz, M., Effects of London dispersion correction in density functional theory on the structures of organic molecules in the gas phase. *Phys Chem Chem Phys* **2013,** *15* (38), 16031-42.
17. Grimme, S.; Schreiner, P. R., Computational Chemistry: The Fate of Current Methods and Future Challenges. *Angew Chem Int Ed Engl* **2018,** *57* (16), 4170-4176.
18. Brown, G. G.; Dian, B. C.; Douglass, K. O.; Geyer, S. M.; Pate, B. H., The rotational spectrum of epifluorohydrin measured by chirped-pulse Fourier transform microwave spectroscopy. *Journal of Molecular Spectroscopy* **2006,** *238* (2), 200-212.
19. Dakermanji, S. J.; Smith, J. A.; Westendorff, K. S.; Pert, E. K.; Chung, A. D.; Myers, J. T.; Welch, K. D.; Dickie, D. A.; Harman, W. D., Electron-Transfer Chain Catalysis of η2-Arene, η2-Alkene, and η2-Ketone Exchange on Molybdenum. *ACS Catalysis* **2019,** *9* (12), 11274-11287.

20. Smith, J. A.; Schouten, A.; Wilde, J. H.; Westendorff, K. S.; Dickie, D. A.; Ess, D. H.; Harman, W. D., Experiments and Direct Dynamics Simulations That Probe eta(2)-Arene/Aryl Hydride Equilibria of Tungsten Benzene Complexes. *J Am Chem Soc* **2020,** *142* (38), 16437-16454.

Chapter 7: Chiral Analysis by Chiral Tag Rotational Spectroscopy on Deuterated Cyclohexene

I'd like to again acknowledge Sarah Brewster for her work within this chapter, which is a continuation of the previous chapter but focused on the chiral aspect of the collaboration with the Harman Group at the University of Virginia. I also thank Justin Weatherford-Pratt of the Harman Group for his synthetic chemistry skills and providing samples for the chiral tag studies and Dr. Reilly Sonstrom, a former member of the Pate Group, who performed many of the quantum chemical calculations and the preliminary experimental work on the parent cyclohexene-PO complex discussed in this chapter.

7.1: *Introduction*:

The difference between deuterium (D) and hydrogen (H), also referred to as protium, might seem very small, but it can cause large changes when deuterium takes the place of protium in a molecule. Protium is composed of just one proton in its nucleus and one electron, while deuterium has an added neutron in its nucleus. This means that deuterium has a mass twice as large as protium. The change in mass affects the vibrational stretching frequency of the bond between other atoms and deuterium or protium, where deuterium bonded to another atom has a lower vibrational stretching frequency.[1, 2] This lowers the zero-point energy of the bond and makes the bond to deuterium more stable than that of protium such that the energy required to break a X-D bond is greater than that of X-H.[1, 2] This effect is called the deuterium kinetic isotope effect (DKIE) and can be measured as the ratio of rate constants, k_H/k_D to get a sense of the impact that deuterium substitution can have for reactions involving the X-D or X-H bonds.[2] Typical values of this ratio range between 1 and 7 where 1 refers to deuterium having no effect on the reaction rate.[2]

How can such a subtle difference as the inclusion of one neutron be important to society, though? Deuterium incorporation has more recently been of interest to drugmakers with FDA

approval of the first deuterated drug, Austedo (deutetrabenazine), in 2017.[3] The selective deuterium modification led to resistance in metabolic degradation allowing the drug to remain longer in the body to perform its intended task.[3] This meant that the benefit of the drug could last longer while using a lower dose and reducing side effects from further metabolism.[3] The advantages of selectively incorporating deuterium into a drug can be summarized to four points:[2]

1) Increased efficacy of the drug due to longer lifetime in the body allowing for lower dosage needed
2) Reduction of toxic metabolites by placing deuterium in 'soft-spots' of the drug where the more stable C-D bond is resistant to oxidative processes and through metabolic shunting of less favorable processes, which aids in the safety of the drug
3) Increase in formation of positive metabolites of therapeutic value through metabolic switching
4) Slowing the racemization of a drug in which a single enantiomer has a positive effect on the body but in which an acidic hydrogen allows for rapid interconversion of enantiomers

The work presented in this chapter is related to the last point. For drugs that are chiral, many are sold as a racemate in which there is a 50:50 mix of the two enantiomers. In many cases, only one of the enantiomers provides a therapeutic effect while the other may only be only slightly active, be completely inactive, or be toxic to the body.[2, 4] While in some cases, synthesis and isolation of the beneficial enantiomer can be done, some have the added challenge that, mainly due to an acidic hydrogen at a chiral center, the enantiomer quickly racemizes in the body to form the other, unwanted enantiomer.[4] By substituting deuterium in the place an acidic hydrogen prone to such racemization, the chemically unstable stereoisomer can be stabilized to greatly reduce

the interconversion rate.[2] A well-known example of this interconversion issue is in the racemization of the drug, thalidomide. [2, 5-7] One enantiomer of the drug was used for its benefits in reducing effects of morning sickness in pregnant women; however, the other enantiomer is linked to causing birth defects.[4-7] Even with the drug being administered in one enantiomeric form, the chiral center bears a hydrogen prone for rapid racemization in the body.[6] In fact, the study to experimentally determine which enantiomer was causing harm was done so by studying the deuterated versions of the enantiomers which reduced the rate of interconversion.[8] Deuterium incorporation at this position has also been done in derivatives of thalidomide that are being used in cancer and inflammatory disease research.[2] Using deuterium to slow or effectively stop racemization takes the place of other practices like replacing the acidic hydrogen of the chiral center with a methyl group or fluorine into a drug. The difference in using deuterium, though, is that the overall structure and pharmacological properties are essentially unchanged, whereas fluorine and other group substitution can drastically change the metabolism and structure of the drug.[4] Characterizing a newly synthesized deuterated chiral species through determination of absolute configuration (AC) and enantiomeric excess (ee, where EE = ee*100%) is therefore important to the field of drug discovery.

In those cases, though, a chiral center already exists, and the acidic hydrogen is exchanged with a deuterium. Current analytic techniques like chiral GC and NMR can typically perform well in this case. However, analyzing species that are chiral merely by deuterium substitution is especially challenging because the change between enantiomers is incredibly subtle. Methods like chiral chromatography struggle to separate these species based on such a small difference without chiral derivatization techniques that are highly specific to the molecular class. NMR can

use chiral derivatizing or solvating agents to distinguish these subtle changes, but spectral overlap and the presence of impurities can make the analysis very challenging and still only work for specific classes of molecules before a new chiral solvating agent is needed.[9] The precise substitution of deuterium to create enantioisotopomers has benefits to society. It has previously been shown that enzymes can notice the small difference of a deuterium and hydrogen at a chiral center through chiral recognition.[10] Designing drugs with deuterium in key locations of the molecule to create chiral centers can aid in the beneficial effects of a drug by designing the drug to better fit key enzymes and receptors in the body, like a proper handshake.[10-12]

We aim to provide a technique that can provide rapid chiral analysis of a complex chemical mixture of deuterated isomers and impurities such that samples directly from the reaction flask can be analyzed with little to no additional work up.[12-16] This technique would need to determine absolute configuration and quantify enantiomeric excess preferably without need of a reference sample, especially in the case of isotopic stereoisomers where references likely do not exist. In general, rotational spectroscopy, which is also referred to as Molecular Rotational Resonance (MRR) spectroscopy, excels in identifying low abundance impurities with subtle changes in molecular structure as is shown in the previous two chapters.[12, 15, 17] However, by itself, MRR spectroscopy cannot tell the difference in enantiomers which have the same distributions of mass and therefore identical rotational spectra.

A new method is being developed in the Pate group at the University of Virginia that breaks this limitation. Using ideas already present in the NMR field in terms of chiral solvating agents, enantiomers can be turned into diastereomers (which have unique rotational spectra) through the addition of an additional chiral center.[13, 18-20] In this case, noncovalent interactions

of the either enantiomer of the analyte with either enantiomer of a small chiral molecule of known AC and EE in the gas phase create weakly bound diastereomeric complexes that rotate as a whole and produce their own unique rotational spectra.[19, 20] This technique is referred to as chiral tag rotational spectroscopy, where the small chiral molecule of known AC and EE is the chiral tag introduced in low concentration in neon to the analyte.[19, 20] Complexation in a pulsed jet expansion forms diastereomeric complexes that fall into two families, the homochiral complexes (+)–(+) or (-)–(-) and the heterochiral complexes (+)–(-) or (-)–(+), where the nomenclature used refers to the optical rotation, (+)- or (-)-, of the each part of the analyte–tag diastereomeric complex.[19] Alternately, for analytes with only one chiral center, the Cahn-Ingold-Prelog nomenclature can also be used, where homochiral complexes are (R)–(R) or (S)–(S) and heterochiral complexes are (S)–(R) or (R)–(S), referring to the chirality of the chiral centers within the analyte-tag complex, respectively.[19]

These diastereomeric complexes produced in a pulsed jet expansion will have unique rotational spectra when subjected to microwave light in a chirped-pulse Fourier transform microwave spectrometer.[21, 22] The technique has unique advantages in that the chiral tag can provide a dipole moment to the analyte if the analyte is not very polar (where the dipole moment determines the intensity of the observed spectral signatures) and that the complexation does not need to occur close in proximity to the chiral center in order to observe the distinct spectra. Additionally, the noncovalent attachment of the tag does not lead to any racemization that can occur through chemically adding in another chiral center in chiral derivatization techniques done for NMR or chiral GC. Several commercially available choices exist for use as a chiral tag and our research group has found that just a select few are needed to work with a wide variety of classes

of molecules. These chiral tags work well through being a hydrogen bond donor or hydrogen bond acceptor to limit the number of docking locations (conformations) that a tag might find in the complexation. To that degree, rotational cooling in the pulsed jet also aids in reducing the number of isomers for the diastereomeric complexes.

To study how well chiral tagging rotational spectroscopy can perform for molecules that are chiral by deuterium substitution, we were able to collaborate with the Harman Group at the University of Virginia. Their group used synthetic techniques discussed in the previous chapter to produce an enantioenriched version of a deuterated isomer of cyclohexene, (S)-3-d1-cyclohexene (Figure 7.1) produced via the stereoselective addition of deuterium and protium to benzene bound to a WTp(NO)(PMe3) dearomatization agent.[12] This agent can be produced as an enantioenriched complex and thereby allow for highly regio- and stereoselective additions due to the ligand structure and exposed faces of the analyte.[12]

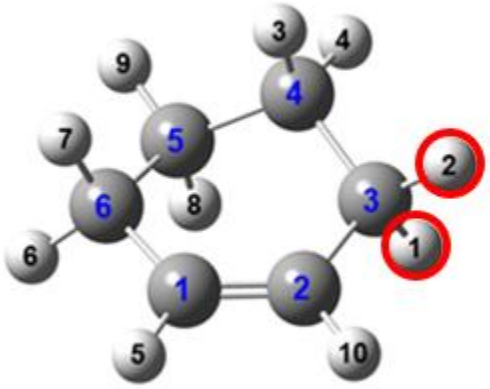

Figure 7.1: Labeling convention for cyclohexene's equilibrium geometry, performed at B3LYP D3BJ/6-311++G(d,p) level of theory. Hydrogen's marked in red pertain to the locations of deuteration for the enantiomers of 3-d1-cyclohexene.

7.2: *Methods*

7.2.1: Synthetic Methods

3-d1-cyclohexene was synthesized by the Harman research group at the University of Virginia. A racemic version and an enantioenriched version were prepared using the synthetic routes discussed in the previous chapter and discussed in the literature.[12] The dearomatizing agent, WTp(NO)(PMe3) with benzene bound to the tungsten, is used to add protium or deuterium in a regio- and stereoselective fashion. The metal complex acts in protecting parts of the benzene as it is reduced to cyclohexene, and by using an enantiomerically enhanced complex, the stereochemistry of the 3-d1-cyclohexene can be controlled. (S)-3-d1-cyclohexene is prepared for these experiments and predicted to have an enantiomer ratio of approximately 9:1 (EE=80) with the (S)-enantiomer in excess. The enantiomer ratio prediction is done indirectly as there is not another technique readily available to directly quantify the EE of 3-d1-cyclohexene. In this case, the dihapto-bound ligand (benzene) is exchanged for one that is chiral such that two diastereomers are formed, one from the enantiomeric complex in excess and one from the minor enantiomeric complex. These diastereomers can then be compared using NMR. Beta-pinene was used in the analysis as it was able to form clear NMR signatures for quantitation.

7.2.2: *Computational Methods and Preliminary Experiments*

Quantum chemistry calculations are performed to predict the structure of the chiral tag complexes by optimizing the electronic energy of the molecular geometry to get rotational constants for the minima of the potential energy surface that can be used to match theory to

experimental rotational constants fit from observed spectra. Optimization only needs to be done for the parent isotopologue species (where cyclohexene with no deuterium substitution, d0-cyclohexene, is referred to as the parent species) because under the Born-Oppenheimer approximation, every deuterated version of the analyte has the same equilibrium geometry. After calculating the lowest energy structures for the complex, one can simply calculate new rotational constants for the deuterated complex species from the structure identified through quantum chemistry by substituting a new mass in for a deuterium position and recalculating just the moments of inertia (and thereby the rotational constants) in the principal axis system for molecular rotation. Gaussian16[23] was used to generate candidate structures through chemical intuition of possible docking sites for PO onto the two faces of the cyclohexene ring, mainly through a weak hydrogen bond. These candidates were optimized at the B3LYP D3BJ / def2TZVP level of theory. Three molecular geometries were identified for the way in which PO noncovalently bonds to cyclohexene and these are displayed in Figure 7.2. Additionally, because the parent isotopologue of cyclohexene is readily available and cheap, the complex spectra for PO with cyclohexene was measured with sensitivity to see the spectra of singly substituted ^{13}C-isotopomers of each of the three isomers of the chiral tag complexes in natural abundance such that Kraitchman analysis could be performed to determine the experimental carbon atom positions.[24] These experimental coordinates are shown in Figure 7.2 as blue spheres within the large grey spheres that are the predicted atom positions. This analysis can often be done in chiral tag rotational spectroscopy to add a higher order of confidence to AC determinations.

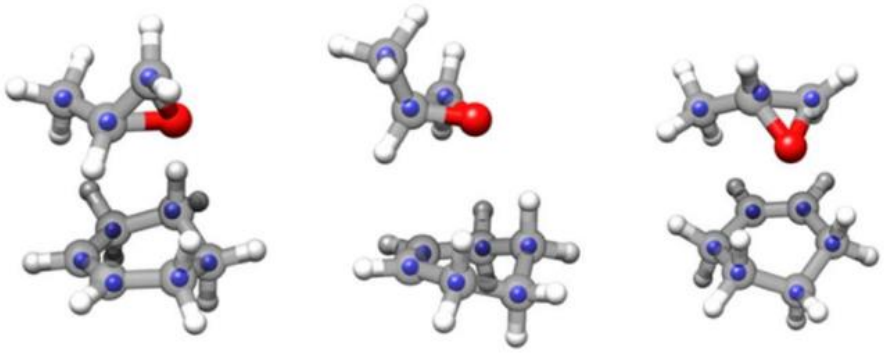

Figure 7.2: Three isomers of the chiral tag complex of d0-cyclohexene and (S)-propylene oxide. Blue spheres indicate the experimentally determined atom positions set inside the grey spheres of the predicted coordinates of the carbon atoms. The left most complex is the lowest energy structure with propylene oxide effectively sitting sideways on the cyclohexene ring.

Table 7.1: *Predicted Rotational Constants (A, B, and C, in MHz) for Chiral Tag Complexes of 3-d1-Cyclohexene with (S)-Propylene Oxide*

Experimental d0*	Theory d0**	Predicted (S)-3-d1-cyclohexene	Predicted (S)-3-d1-cyclohexene	Predicted (R)-3-d1-cyclohexene	Predicted (R)-3-d1-cyclohexene
1876.685(5)	1873.416	1857.581	1854.413	1838.960	1834.847
746.656(2)	772.944	736.005	745.878	743.028	740.234
689.024(2)	710.694	678.762	686.382	683.294	682.005

*Standard error in the experimental rotational constants in parentheses are given in units of the last digit

**B3LYP D3BJ / def2TZVP level of theory is used

The comparison of experimentally fit rotational constants for the d0-cyclohexene complexing with PO can be used to predict and scale the rotational constants for the chiral, deuterated cyclohexene species as shown above in Table 7.1. High-confidence AC determination is done by matching the rotational constants of the experimental spectra to the calculations with accuracy in the predicted constants to be ≤ 0.1 MHz for isotopic isomers of the parent speices.[19] Because the tag can complex from either side of the cyclohexene ring, two spectra are expected

to be observed when the deuterated species is used; this means that in the case of racemic 3-d1-cyclohexene complexing with (S)-PO, four spectra with two coming from each diastereomeric complex family are expected. The lowest energy structure for the complexation of either (R)- or (S)-3-d1-cyclohexene with the chiral tag, (S)-PO, are depicted in Figure 7.3.

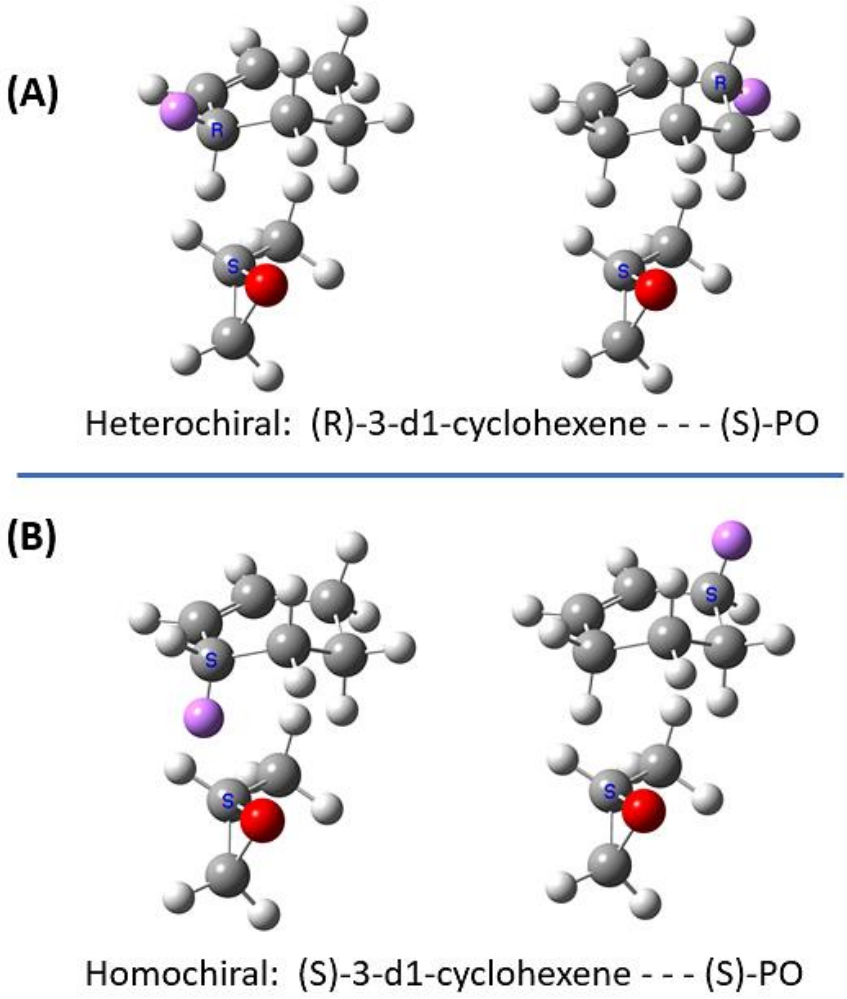

Figure 7.3: The complexation of the enantiomers of the analyte, 3-d1-cyclohexene with the chiral tag, (S)-PO calculated at B3LYP D3BJ / def2TZVP level of theory. Deuterium is labeled in magenta, hydrogen in white, carbon in gray, and oxygen in red. PO can interact with cyclohexene from either face, so each family of chiral tag complexes consists of a pair of structures shown side by side for the heterochiral structure in **(A)** and for the homochiral structure in **(B)**.

7.2.3: *MRR Experimental Details*

The external sample cell discussed in the previous chapter was used for the chiral tag experiments. This sample cell allows us to make small gas mixtures with great control and reproducibility while also greatly increasing the speed at which samples can be introduced to the spectrometer. The cell can easily be purged between measurements using a dry scroll vacuum pump and nitrogen gas source. Two measurements are done to complete the AC and EE determinations in chiral tag rotational spectroscopy. In this case, since a racemic and enantioenriched sample were prepared, one measurement is done using the racemic 3-d1-cyclohexene bound to the metal complex while (S)-PO is used as the tag and the second measurement is done with the enantioenriched sample while still using (S)-PO. Alternatively, if only the enantioenriched sample exists, the measurement can be done using a racemic form of the tag and an enantiopure form of the tag.

Approximately 40 mg of metal complex sample, which was prepared to have enantioenriched 3-d1-cyclohexene bound to it, was placed into the heating crucible. Vacuum was pulled on the sample to remove any highly volatile solvents and then the sample was placed under 1 atm of neon. In order to release the deuterated analyte from the metal complex for analysis, the sample is heated to 250°C for ten minutes to completely release the analyte from the metal (described in detail in the previous chapter). The sample cell's heating crucible is then allowed to cool to 140°C while 40 psig of a 0.5% S-PO in neon gas mixture is added to the cell to reach a final approximate 0.4% S-PO, 0.2% 3-d1-cyclohexene mixture in neon. This concentration of cyclohexene was optimized in the previous chapter, and the higher concentration of PO is used to account for the fact that PO can complex with cyclohexene from either face of the ring. The

mixture is then pulsed with a backing pressure of 15 psig into the instrument's vacuum chamber via three nozzles through 1 mm holes to create supersonic expansions for each nozzle in series. The supersonic expansion and carrier gas aid in rotationally cooling the analyte and tag mixture to allow for stable, freely rotating, noncovalently bound complexes to be studied in the gas phase. The chirped-pulse Fourier transform microwave (CP-FTMW) spectrometer used in the previous chapter was used in these experiments with a 4 μs chirp spanning 2-8 GHz, which captures the peak in Boltzmann distribution of transition intensities of the predicted complex signals. The instrument achieves eight measurements per sample injection where the sample injection runs at 3 Hz, giving an effective repetition rate of 24 Hz. 12,000 FIDs were collected in each trial and coadded before the sample mixture ran out. Following this enantioenriched measurement, the sample cell was purged and the sample holder cleaned. The racemic version of the analyte bound to the metal was loaded and the measurement process was repeated. Each measurement takes approximately 5-10 minutes of sample preparation, 10 minutes of heating, 8 minutes of measurement time, and a variable time for analysis depending on the complexity of the sample. If the experimental rotational constants are already known, AC and EE spectrum analysis can be done in seconds.

7.3: *Results and Discussion*

Measuring the spectrum while using racemic 3-d1-cyclohexene with (S)-PO leads to four new spectra of approximately equal intensity, which account for the four predicted structures shown previously in Figure 7.3 and Table 7.1. Previous spectra of the monomer species, 3-d1-cyclohexene and PO (and any impurities already known from the impurity analysis done in Chapter 6), can be cut out of the spectrum to isolate these new spectra. Experimental spectral fits were done using Pickett's SPCAT/SPFIT[25] spectral analysis program along with Kisiel's AABS[26] program. The spectral assignments are listed in Table 7.2 and compared to the theoretical rotational constants that best match each fit. Percent errors for the deuterated species are on the order of 0.01-0.1% in each case whereas nearest rotational parameters are >0.1%, on the order of 0.2-1.3%.

Table 7.2: *Spectral Assignments for the Chiral Tag Complexes of 3-d1-Cyclohexene and (S)-Propylene Oxide*

Parameter	Experiment[a]	Theory[b]	|% Error|			
	d0-cyclohexene – PO (Parent)					
A / MHz	1876.685(5)	1873.416	0.1745			
B / MHz	746.656(2)	772.944	3.4010			
C / MHz	689.024(2)	710.694	3.0491			
N_{lines}[d]						
μ_a / D		-1.37				
μ_b / D		-0.84				
μ_c / D		0.68				
μ_{total} / D		1.75				
Parameter	**Experiment***	**Theory[c]**	**|% Error|**	**Experiment**	**Theory**	**|% Error|**
		Homochiral 1			**Homochiral 2**	
A / MHz	1857.7642(40)	1857.581	0.0099	1855.51330(98)	1854.413	0.0593
B / MHz	736.20840(66)	736.005	0.0276	746.64760(64)	745.878	0.1032
C / MHz	678.93920(71)	678.672	0.0394	686.89520(62)	686.382	0.0748
N_{lines}	23			31		
|a|/ Å	2.971	2.944		[0][f]	0.299	
|b|/ Å	1.427	1.433		1.629	1.620	
|c|/ Å	0.875	0.886		0.649	0.787	
Parameter	**Experiment**	**Theory**	**|% Error|**	**Experiment**	**Theory**	**|% Error|**
		Heterochiral 1			**Heterochiral 2**	
A / MHz	1838.82000(94)	1838.960	0.0076	1834.69070(79)	1834.847	0.1563
B / MHz	743.31030(55)	743.028	0.0380	740.59600(44)	740.234	0.3620
C / MHz	683.39570(56)	683.294	0.0149	682.06500(44)	682.005	0.0600
N_{lines}	33			32		
|a|/ Å	1.322	1.337		1.838	1.836	
|b|/ Å	2.049	2.019		1.958	1.945	
|c|/ Å	1.172	1.220		1.509	1.558	

[a] Standard error in the experimental rotational constants in parentheses are given in units of the last digits

[b] B3LYP D3BJ / def2TZVP level of theory is used

[c] Theoretical rotational constants for the isotopic isomers are scaled using the error associated with predicting the parent species (using the ratio of experimental and calculated rotational constants for the parent species)

[d] N_{lines} is the number of transitions in the experimental fit

[e] Coordinates for the deuterium position of each species in the principal axis system where experimental values are obtained through Kraitchman analysis.

[f] The a-coordinate is found to be imaginary due to the inertial defect, indicating that this coordinate is small

To determine the AC by this method, an example of the process is shown in Figures 7.4 and 7.5. The strongest transitions for each isomer of each family, where the PO complexes to either side of the cyclohexene ring, are depicted for the measurement using racemic 3-d1-cyclohexene and enantioenriched 3-d1-cyclohexene, respectively. These four transitions are of approximately equal intensity in Figure 7.4, where the (S)-PO tag is equally likely to find an (R)- or (S)- version of the analyte. When switching to the enantioenriched sample, the spectrum in Figure 7.5 shows that the heterochiral complex signals are much weaker and the homochiral complex signals are much stronger. Because we know the AC of the tag and that the homochiral signals went up in the measurement performed with enantioenriched analyte, we can determine that the analyte must be (S)-3-d1-cyclohexene in excess.

Within each of the deuterated complex species listed in Table 7.2, the differences in the rotational constants between each species is much larger than the differences between the scaled theory predictions and experimental constants of each fit. This is vital in the proper assignment of each species and adds a great amount of confidence in the assignment of AC. As an added level of confidence, the coordinates of the deuterium position can be compared from the theoretically calculated geometry to that of the experimentally determined coordinates listed in Table 7.2. The experimental atom positions are determined by Kraitchman analysis of the parent species, in which there was high enough signal-to-noise to fit the spectra observed for singly substituted ^{13}C-isotopologues in natural abundance, with each spectrum at ~1% the intensity of the parent species.[24] Each heavy atom position can then be determined through a series of equations gained from how the isotopic substitution affects the principal moments of inertia.[24] With the carbon skeleton experimentally determined, the H/D atom positions are then

more firm. Table 7.2 lists the magnitude of the atomic coordinates for the deuterium in the experimental results from the Kraitchman analysis and shows that they are very close to the predicted coordinates in the optimized equilibrium geometry. The difference in coordinates between isomers is much more than the difference in the comparison of theory to experiment for the matched spectral assignment. These two features give high confidence in the AC determination done by spectral fitting of the diastereomeric complexes made through the chiral tagging strategy.

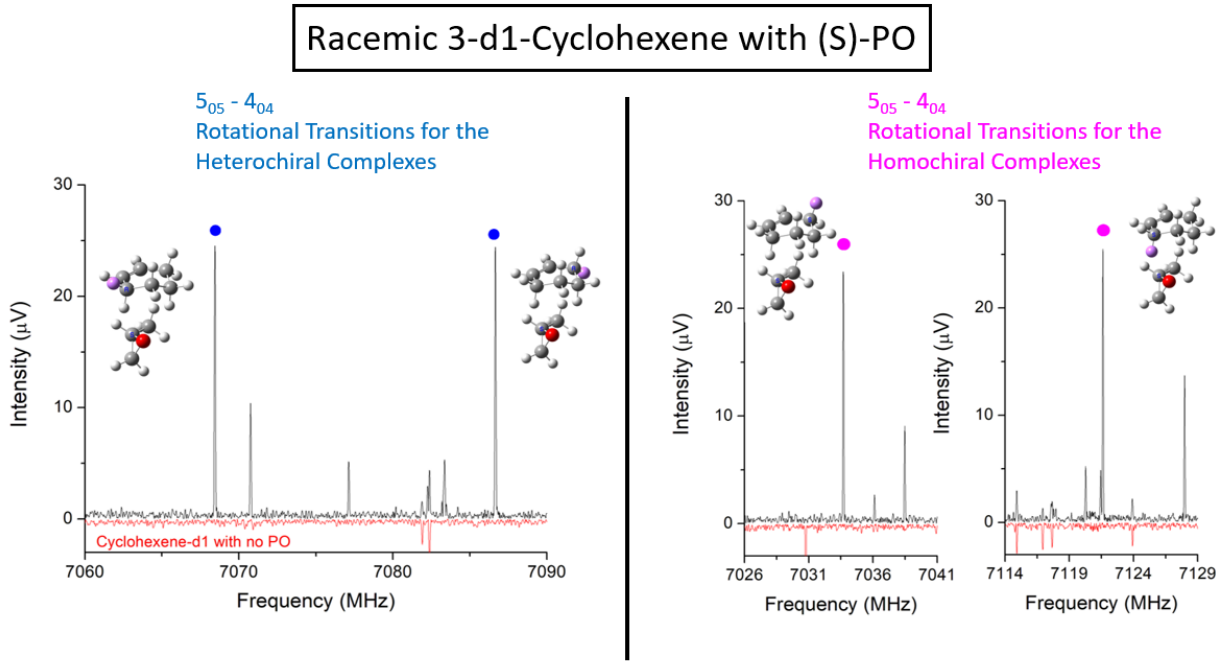

Figure 7.4: Four strongest transitions observed in the measurement with racemic 3-d1-cyclohexene and (S)-propylene oxide. The heterochiral complex signals are shown on the left marked by blue circles, and the homochiral complex signals are marked on the right in magenta circles. Since the propylene oxide can attach from either face of the cyclohexene ring, two isomers give rise to two spectra for each family of complexes. 3-d1-cyclohexene measured without propylene oxide is plotted negative in red to show the presence of new signals from the complex.

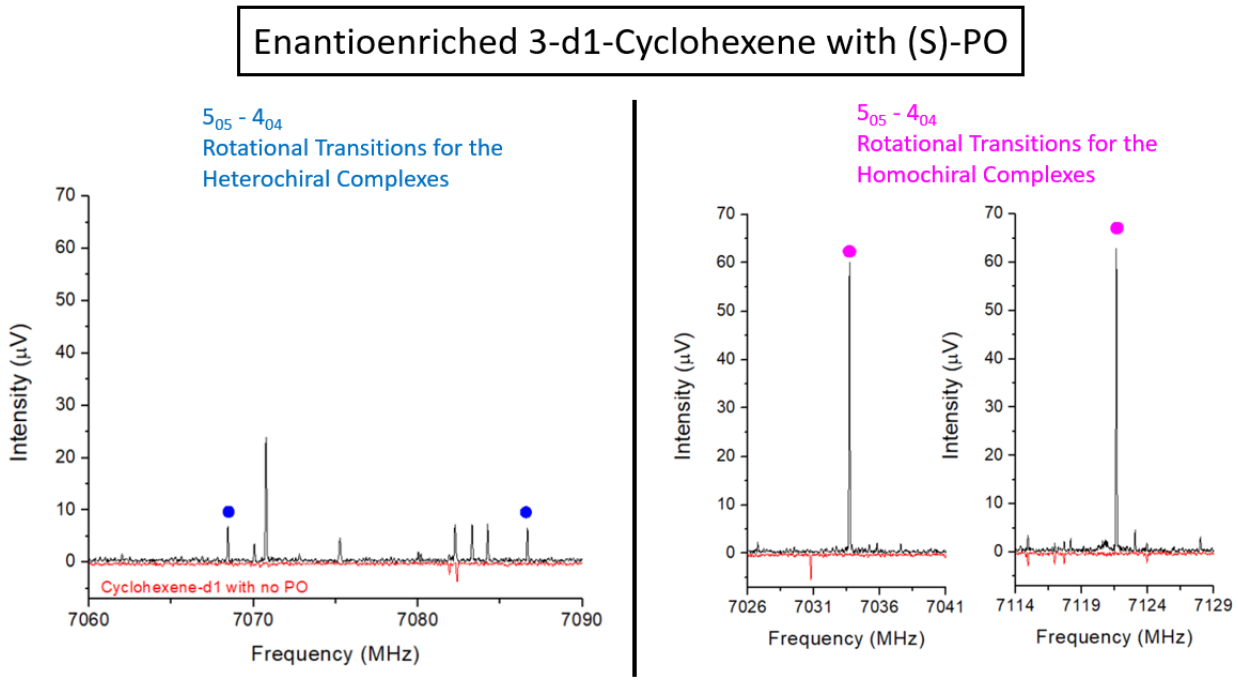

Figure 7.5: Four strongest transitions observed in the measurement with enantioenriched 3-d1-cyclohexene and (S)-propylene oxide. The heterochiral complex signals have decreased in intensity within this measurement whereas the homochiral complex signals have increased. Knowing the AC of the tag, the analyte is determined to be (S)-3-d1-cyclohexene in excess as the homochiral signals increased in this experiment. 3-d1-cyclohexene measured without propylene oxide is plotted negative in red to show the presence of new signals from the complex.

The EE determination is done by first normalizing the signal intensities of the measurement done with enantioenriched analyte by the measurement done with racemic analyte: [20, 27]

$$I_{Norm} = \frac{I_{Enantioenriched}}{I_{Racemic}} \tag{7.1}$$

Next, the heterochiral and homochiral species are compared through the ratio, *R*, of their normalized signal intensities for a given pair of transitions:[20, 27]

$$R = \frac{I_{Norm,Homo}}{I_{Norm,Hetero}} \tag{7.2}$$

A quantity can then be calculated that is related to the EE for the chosen pair of transitions:[20, 27]

$$\frac{R-1}{R+1} = (ee_{Tag})(ee_{Analyte}) \tag{7.3}$$

$$EE = ee_{Analyte} \cdot 100\ \% = \frac{R-1}{R+1} \cdot \frac{1}{ee_{Tag}} \tag{7.4}$$

The EE determination requires a quantitative determination of the EE of the tag used in the measurement. The (S)-PO tag used in these measurements was previously determined to be EE=99.6.[27] Chiral tags are analyzed separately either by what we call "auto tagging" where heterochiral or homochiral dimers are formed or by tagging with one of our other choices in tags. These can then be analyzed by the same method described above.

Since there are typically many pairs of homochiral/heterochiral transitions in the spectrum, the EE can be computed many times using all pairs of transitions, $N_{transitions}$. In this case, the nine strongest transitions ($N_{transitions}$=9) are chosen for the analysis such that there are 81 possible pairs for making EE determinations to acquire a mean value for the final EE determination of the measurement. These determinations can then be used to extract measurement uncertainty. This has been described in detail elsewhere,[19, 20, 27] but the measurement uncertainty is calculated using the standard error, σ_{SE}, which is equal to the standard deviation of the EE determinations(in this case the width of the histogram, $w_{Histogram}$) divided by the square-root of the number of transitions used for the analysis:

$$\sigma_{SE} = \frac{w_{Histogram}}{\sqrt{N_{transitions}}} \tag{7.5}$$

The result is depicted in Figure 7.6, yielding a value of EE = 80.8(4) where the value in parentheses is the uncertainty in the last digit. This is equal to an enantiomer ratio of approximately 9.1 which is in agreement with the predicted enantiomer ratio by the Harman Group. The chiral tagging technique has also been shown to have agreement with chiral GC, the leading technique in chiral analysis.[20, 27]

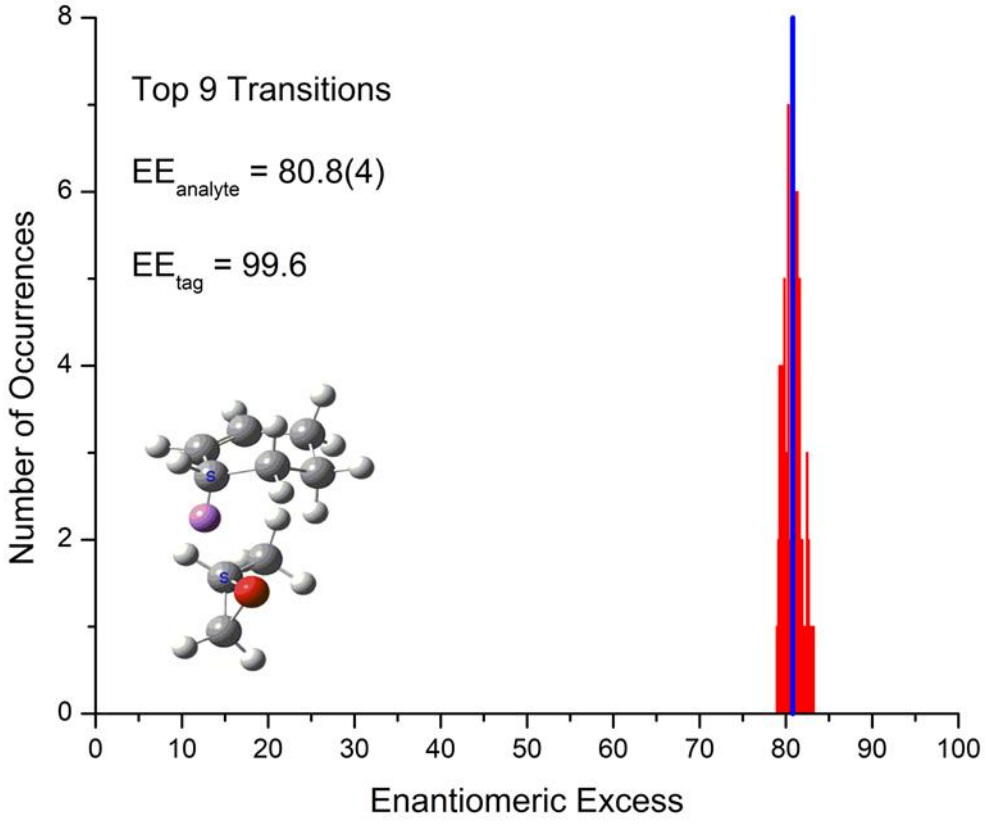

Figure 7.6: Enantiomeric excess determination using the nine strongest transitions for homochiral and heterochiral families of the 3-d1-cyclohexene – propylene oxide complexes. Each transition can be compared to

7.4: *Conclusions*

Racemic and enantioenriched samples of 3-d1-cyclohexene thermally released from a metal complex were analyzed by chiral tag rotational spectroscopy to determine the absolute configuration and enantiomeric excess of the stereoselective deuteration strategy used by the Harman Group at the University of Virginia. A new external sample cell was used to make very reproducible gas mixtures such that a chiral tag could be introduced to an analyte for much faster sampling than previously done with the CP-FTMW instrument. These measurements were done using only 40 mg of sample which consists of the analyte bound to a metal complex such that only ~5 mg of analyte was use in each of the two measurements. Requiring only small amounts of sample for highly analytical results, being able to measure many samples in one day, and with the added benefit of not needing to separate mixtures (detailed in the previous two chapters), this technique has great power in the chemists toolbox.

These AC and EE determinations are not possible by other methods for such a subtle change as introducing chirality by deuterium substitution. However, MRR spectroscopy is well suited for small changes in molecular structure. The chiral tagging strategy in rotational spectroscopy does not require a reference sample of the analyte to determine AC and EE, which is also advantageous to drug discovery where reference samples often do not exist. Additionally, with the high sensitivity of the instrument in these measurements, quantitative EE determinations as high as EE=99.0 and higher are possible, limited by the signal-to-noise ratio of the minor enantiomer.

Chapter 7 References

1. Gant, T. G., Using deuterium in drug discovery: leaving the label in the drug. *J Med Chem* **2014,** *57* (9), 3595-611.
2. Pirali, T.; Serafini, M.; Cargnin, S.; Genazzani, A. A., Applications of Deuterium in Medicinal Chemistry. *J Med Chem* **2019,** *62* (11), 5276-5297.
3. Schmidt, C., First deuterated drug approved. *Nat Biotechnol* **2017,** *35* (6), 493-494.
4. DeWitt, S.; Czarnik, A. W.; Jacques, V., Deuterium-Enabled Chiral Switching (DECS) Yields Chirally Pure Drugs from Chemically Interconverting Racemates. *ACS Med Chem Lett* **2020,** *11* (10), 1789-1792.
5. Blanco, S.; Macario, A.; Lopez, J. C., The structure of isolated thalidomide as reference for its chirality-dependent biological activity: a laser-ablation rotational study. *Phys Chem Chem Phys* **2021,** *23* (24), 13705-13713.
6. Tokunaga, E.; Yamamoto, T.; Ito, E.; Shibata, N., Understanding the Thalidomide Chirality in Biological Processes by the Self-disproportionation of Enantiomers. *Sci Rep* **2018,** *8* (1), 17131.
7. Marianne Reist, P.-A. C., Eric Francotte, Bernard Testa, Chiral Inversion and Hydrolysis of Thalidomide: Mechanisms and Catalysis by Bases and Serum Albumin, and Chiral Stability of Teratogenic Metabolites. *Chemical Research in Toxicology* **1998,** *11* (12), 1521-1528.
8. Takeshi Yamamoto, E. T., Shuichi Nakamura, Norio Shibata, Takeshi Toru, Synthesis and Configurational Stability of (S)- and (R)-Deuteriothalidomides. *Chem. Pharm. Bull* **2010,** *58* (1), 110-112.
9. Yang, L.; Wenzel, T.; Williamson, R. T.; Christensen, M.; Schafer, W.; Welch, C. J., Expedited Selection of NMR Chiral Solvating Agents for Determination of Enantiopurity. *ACS Cent Sci* **2016,** *2* (5), 332-40.
10. B. Belleau, J. B., M. Pindell, J. Reiffenstein, Effect of Deuterium Substitution in Sympathomimetic Amines on Adrenergic Responses. *Science* **1961,** *133* (3446), 102-104.
11. Wilson, K. B.; Smith, J. A.; Nedzbala, H. S.; Pert, E. K.; Dakermanji, S. J.; Dickie, D. A.; Harman, W. D., Highly Functionalized Cyclohexenes Derived from Benzene: Sequential Tandem Addition Reactions Promoted by Tungsten. *J Org Chem* **2019,** *84* (10), 6094-6116.
12. Smith, J. A.; Wilson, K. B.; Sonstrom, R. E.; Kelleher, P. J.; Welch, K. D.; Pert, E. K.; Westendorff, K. S.; Dickie, D. A.; Wang, X.; Pate, B. H.; Harman, W. D., Preparation of cyclohexene isotopologues and stereoisotopomers from benzene. *Nature* **2020,** *581* (7808), 288-293.
13. Neill, J. L.; Yang, Y.; Muckle, M. T.; Reynolds, R. L.; Evangelisti, L.; Sonstrom, R. E.; Pate, B. H.; Gupton, B. F., Online Stereochemical Process Monitoring by Molecular Rotational Resonance Spectroscopy. *Organic Process Research & Development* **2019,** *23* (5), 1046-1051.
14. Christophe, A. L.; Barnes, J. T.; Twagirayezu, S.; Mikhonin, A.; Muckle, M. T.; Neill, J. L., Direct Measurements of Small Polar Impurities in Gasoline Mixtures Using Molecular Rotational Resonance Spectroscopy. *Appl Spectrosc* **2019,** *73* (11), 1334-1339.
15. Vang, Z. P.; Reyes, A.; Sonstrom, R. E.; Holdren, M. S.; Sloane, S. E.; Alansari, I. Y.; Neill, J. L.; Pate, B. H.; Clark, J. R., Copper-Catalyzed Transfer Hydrodeuteration of Aryl Alkenes with Quantitative Isotopomer Purity Analysis by Molecular Rotational Resonance Spectroscopy. *J Am Chem Soc* **2021,** *143* (20), 7707-7718.
16. Joyce, L. A.; Schultz, D. M.; Sherer, E. C.; Neill, J. L.; Sonstrom, R. E.; Pate, B. H., Direct regioisomer analysis of crude reaction mixtures via molecular rotational resonance (MRR) spectroscopy. *Chem Sci* **2020,** *11* (24), 6332-6338.
17. Satterthwaite, L.; Perez, C.; Steber, A. L.; Finestone, D.; Broadrup, R. L.; Patterson, D., Enantiomeric Analysis of Chiral Isotopomers via Microwave Three-Wave Mixing. *J Phys Chem A* **2019,** *123* (14), 3194-3198.

18. Marshall, F. E.; Sedo, G.; West, C.; Pate, B. H.; Allpress, S. M.; Evans, C. J.; Godfrey, P. D.; McNaughton, D.; Grubbs, G. S., The rotational spectrum and complete heavy atom structure of the chiral molecule verbenone. *Journal of Molecular Spectroscopy* **2017,** *342*, 109-115.
19. Brooks H. Pate, L. E., Walther Caminati, Yunjie Xu, Javix Thomas, David Patterson, Cristobal Perez, Melanie Schnell, Quantitative Chiral Analysis by Molecular Rotational Spectroscopy. In *Chiral Analysis*, 2 ed.; 2018; pp 679-729.
20. Sonstrom, R. E.; Neill, J. L.; Mikhonin, A. V.; Doetzer, R.; Pate, B. H., Chiral analysis of pantolactone with molecular rotational resonance spectroscopy. *Chirality* **2022,** *34* (1), 114-125.
21. Brown, G. G.; Dian, B. C.; Douglass, K. O.; Geyer, S. M.; Pate, B. H., The rotational spectrum of epifluorohydrin measured by chirped-pulse Fourier transform microwave spectroscopy. *Journal of Molecular Spectroscopy* **2006,** *238* (2), 200-212.
22. Brown, G. G.; Dian, B. C.; Douglass, K. O.; Geyer, S. M.; Shipman, S. T.; Pate, B. H., A broadband Fourier transform microwave spectrometer based on chirped pulse excitation. *Rev Sci Instrum* **2008,** *79* (5), 053103.
23. Frisch, M. J. T., G. W.; Schlegel, H. B.; Scuseria, G. E.; Robb, M. A.; Cheeseman, J. R.; Scalmani, G.; Barone, V.; Petersson, G. A.; Nakatsuji, H.; Li, X.; Caricato, M.; Marenich, A. V.; Bloino, J.; Janesko, B. G.; Gomperts, R.; Mennucci, B.; Hratchian, H. P.; Ortiz, J. V.; Izmaylov, A. F.; Sonnenberg, J. L.; Williams-Young, D.; Ding, F.; Lipparini, F.; Egidi, F.; Goings, J.; Peng, B.; Petrone, A.; Henderson, T.; Ranasinghe, D.; Zakrzewski, V. G.; Gao, J.; Rega, N.; Zheng, G.; Liang, W.; Hada, M.; Ehara, M.; Toyota, K.; Fukuda, R.; Hasegawa, J.; Ishida, M.; Nakajima, T.; Honda, Y.; Kitao, O.; Nakai, H.; Vreven, T.; Throssell, K.; Montgomery, J. A., Jr.; Peralta, J. E.; Ogliaro, F.; Bearpark, M. J.; Heyd, J. J.; Brothers, E. N.; Kudin, K. N.; Staroverov, V. N.; Keith, T. A.; Kobayashi, R.; Normand, J.; Raghavachari, K.; Rendell, A. P.; Burant, J. C.; Iyengar, S. S.; Tomasi, J.; Cossi, M.; Millam, J. M.; Klene, M.; Adamo, C.; Cammi, R.; Ochterski, J. W.; Martin, R. L.; Morokuma, K.; Farkas, O.; Foresman, J. B.; Fox, D. J. *Gaussian 16*, Revision C.01; Gaussian, Inc, Wallingford CT, 2016.
24. Kraitchman, J., Determination of Molecular Structure from Microwave Spectroscopic Data. *American Journal of Physics* **1953,** *21* (1).
25. Pickett, H. M., The fitting and prediction of vibration-rotation spectra with spin interactions. *J. Mol. Spec.* **1991,** *148*, 371-377.
26. Kisiel, Z., *Assignment and Analysis of Complex Rotational Spectra*. Ed. Kluwer Academic Publishers: 2001.
27. Mayer, K. J. Chiral Analysis by Chiral Tag Rotational Spectroscopy. University of Virginia, Charlottesville, VA, 2022.

Chapter 8: Concluding Remarks and Future Outlook

8.1: *Summary*

Rotational spectroscopy has been around for eighty years or so, largely coming out of the technology advancements in radar during World War II. In that time, rotational spectroscopy has provided vast amounts of knowledge on molecular structure and important physical properties like dipole moments, barriers to internal rotation, and details of noncovalent interactions as well as aiding in the discovery of chemical species in interstellar space.[1] More recently, with the advent of the chirped-pulse Fourier transform microwave spectrometer[2, 3] and with advancements in quantum chemical calculations,[4-6] rotational spectroscopy has developed a set of unique features that set it apart from other techniques commonly used in analytical chemistry.[1] These features are:

1) A unique mass distribution will produce a unique rotational spectrum
2) The instrumentation provides exceptionally high spectral resolution
3) Spectral patterns are predictable to high accuracy with quantum chemistry calculations

The measurement principle mentioned in the first point is different than techniques that can perform molecular identification analysis using total mass or through chromophore-based spectroscopy. While infrared spectroscopy also has the same measurement principle, that technique suffers from large amounts of spectral overlap that rotational spectroscopy does not suffer from. The last point is the most important feature, where it is often the case that high-confidence chemical identity can be determined simply by comparing a measured rotational spectrum with that of the theoretically predicted one. Because of this close comparison to

theory, rotational spectroscopy has a great opportunity to perform direct analysis of complex chemical mixtures without prior separation.

This dissertation described the ongoing development of techniques within rotational spectroscopy to allow it to fit into the toolbox for molecular identification and quantitative analysis in analytical chemistry that showcase how well the technique handles measurements in complex mixtures.

Chapter 1 and 2 provided some of the introductory material for rotational spectroscopy, its history, and one of the first applications to analytical chemistry, in the area of chiral analysis. Within chiral analysis, one of the most difficult measurements to make is the quantitative enantiomeric excess determination for a given sample. A doubly resonant method called three-wave mixing rotational spectroscopy was discussed and how it can provide measurements on absolute configuration and enantiomeric excess and why it is well-suited for analyzing individual components of complex mixtures of chiral molecules.

Chapter 3 assessed the quantitative limits of the three-wave mixing rotational spectroscopy technique and showed that there is a heavy limitation caused by fluctuations in the pulsed jet sample introduction method. Associated error with those fluctuations makes analyzing samples with high enantiomeric excess (highly relevant to drug making) especially challenging.

However, in Chapter 4, a different application was discussed to use the technique for biomarker detection on a rover or probe mission through a collaboration with the Jet Propulsion Laboratory (NASA/Caltech). Homochirality here on Earth might be a good biomarker to use when looking for for signs of past life on places like Mars and the moons of Jupiter and Saturn. The

technique allows for measurements on complex mixtures without separating or cleaning beforehand which is advantageous for space missions. A prototype instrument called ChiralSpec was designed and tested and showed evidence that this technique could provide a way of analyzing small chiral molecules using millimeter-wave technology to reduce size, weight, and power of the instrument.

In Chapter 5, I discussed how rotational spectroscopy can be useful in analyzing mixtures of isotopic isomers. In this case, in a collaboration with Marquette University, we measured "cocktail" mixtures of various ways synthetic chemists could selectively place deuterium or hydrogen in a relevant reaction. With information on the transitions of each of these species, with a library of possibilities, we were then able to increase the screening throughput by using a cavity enhanced instrument.

Chapters 6 and 7 pertain to a collaboration with the Harman group at the University of Virginia and provided another set of examples of where rotational spectroscopy can aid in the quantitative analysis of mixtures of isotopic isomers. High selectivity in the deuterium substitution chemistry is important to synthetic chemists, where post-reaction purification by chromatography is not possible for isotopomers. Here, we were able to help guide a synthesis route to produce target molecules with very little impurities being made due to being able to provide quantitative results on the various impurities and assessing how they might be generated through the mechanism to the target molecule. Additionally, a sample molecule that was chiral merely by deuterium substitution was analyzed for absolute configuration and enantiomeric excess determination using a chiral tagging approach to convert enantiomers into diastereomeric complexes where rotational spectroscopy excels.

8.2: *Future Outlook*

The examples used in this dissertation really showcase how widely applicable rotational spectroscopy can be. With the exceptional performance advantages of the chirped-pulse Fourier transform microwave spectrometer and the recent developments of three-wave mixing and chiral tagging, the number of analytical chemistry problems that rotational spectroscopy can address is expanding. Most recently in the literature, rotational spectroscopy has been used to assess various species (especially low level impurities) in crude reaction mixtures without references,[7] in isotopic isomer impurity analysis,[8, 9] and in chiral analysis.[10, 11]

There are of course some challenges that may arise for the technique. In the case three-wave mixing, there are still issues with the limitation by the pulsed jet sample introduction that introduce larger than expected uncertainties in the measurement. A possibility of overcoming that challenging is by moving to measurements done in a cryogenic buffer gas cell.[12] For chiral tagging, as the analytes get larger and more conformationally flexible, it is unclear how much more difficult the analysis will become when more isomers of the diastereomeric complexes are made. This will need some further research to see what range of molecules will really work with the technique. For isotopic isomer species, rotational spectroscopy really excels at distinguishing subtle changes in molecular geometry, whereas techniques like NMR, mass spectroscopy, and chromatography may lack, especially in distinguishing and quantifying ratios of isotopomers.

The largest possible limitation to rotational spectroscopy is molecular size. As the molecular size increases, the partition function for a given rotational temperature increases which in turn lowers the peak signal levels of spectrum. This is a fundamental physical limitation

to the technique. Secondly, for a typical experiment, approximately 1 Torr of vapor pressure of the analyte is needed. As the molecular size increases, it becomes increasingly difficult to volatilize the sample especially without thermally decomposing the analyte. However, there are ways around this experimental limitation, where laser ablation techniques have been demonstrated.[13-15] Lastly, the accuracy of quantum chemistry needs to be sufficient to predict small, subtle changes in the rotational constants for ever larger systems. This area requires more investigation and benchmarking; however the outlook of quantum chemistry is positive with plenty of room to improve.[5] Even with these potential limitations, rotational spectroscopy has been shown to work up to about 250-300 Da, which covers a wide range of the work in synthetic chemistry where reaction scope is explored and where "building block" strategies in chiral and deuterated molecules are used to develop drug production processes.

At the end of the day, rotational spectroscopy has a bright future as a technique that fits well into the analytical field. Through my time at the University of Virginia, I've been able to work with many collaborators and with undergraduate students in the Physical Chemistry Lab courses to help show just how powerful rotational spectroscopy can be. Many have seen the power of the technique, and I expect that vision to get even more well renowned in time as technology improves.

Chapter 8 References:

1. Pate, B. H., Taking the Pulse of Molecular Rotational Spectroscopy. *Science* **2011,** *333* (6045), 947-948.
2. Brown, G. G.; Dian, B. C.; Douglass, K. O.; Geyer, S. M.; Pate, B. H., The rotational spectrum of epifluorohydrin measured by chirped-pulse Fourier transform microwave spectroscopy. *Journal of Molecular Spectroscopy* **2006,** *238* (2), 200-212.
3. Brown, G. G.; Dian, B. C.; Douglass, K. O.; Geyer, S. M.; Shipman, S. T.; Pate, B. H., A broadband Fourier transform microwave spectrometer based on chirped pulse excitation. *Rev Sci Instrum* **2008,** *79* (5), 053103.
4. Grimme, S.; Steinmetz, M., Effects of London dispersion correction in density functional theory on the structures of organic molecules in the gas phase. *Phys Chem Chem Phys* **2013,** *15* (38), 16031-42.
5. Grimme, S.; Schreiner, P. R., Computational Chemistry: The Fate of Current Methods and Future Challenges. *Angew Chem Int Ed Engl* **2018,** *57* (16), 4170-4176.
6. Puzzarini, C., Rotational spectroscopy meets theory. *Phys Chem Chem Phys* **2013,** *15* (18), 6595-607.
7. Joyce, L. A.; Schultz, D. M.; Sherer, E. C.; Neill, J. L.; Sonstrom, R. E.; Pate, B. H., Direct regioisomer analysis of crude reaction mixtures via molecular rotational resonance (MRR) spectroscopy. *Chem Sci* **2020,** *11* (24), 6332-6338.
8. Smith, J. A.; Wilson, K. B.; Sonstrom, R. E.; Kelleher, P. J.; Welch, K. D.; Pert, E. K.; Westendorff, K. S.; Dickie, D. A.; Wang, X.; Pate, B. H.; Harman, W. D., Preparation of cyclohexene isotopologues and stereoisotopomers from benzene. *Nature* **2020,** *581* (7808), 288-293.
9. Vang, Z. P.; Reyes, A.; Sonstrom, R. E.; Holdren, M. S.; Sloane, S. E.; Alansari, I. Y.; Neill, J. L.; Pate, B. H.; Clark, J. R., Copper-Catalyzed Transfer Hydrodeuteration of Aryl Alkenes with Quantitative Isotopomer Purity Analysis by Molecular Rotational Resonance Spectroscopy. *J Am Chem Soc* **2021,** *143* (20), 7707-7718.
10. Sonstrom, R. E.; Neill, J. L.; Mikhonin, A. V.; Doetzer, R.; Pate, B. H., Chiral analysis of pantolactone with molecular rotational resonance spectroscopy. *Chirality* **2022,** *34* (1), 114-125.
11. Domingos, S. R.; Perez, C.; Marshall, M. D.; Leung, H. O.; Schnell, M., Assessing the performance of rotational spectroscopy in chiral analysis. *Chem Sci* **2020,** *11* (40), 10863-10870.
12. Porterfield, J. P.; Satterthwaite, L.; Eibenberger, S.; Patterson, D.; McCarthy, M. C., High sensitivity microwave spectroscopy in a cryogenic buffer gas cell. *Rev Sci Instrum* **2019,** *90* (5), 053104.
13. Susana Blanco, J. C. L., Alberto Lesarri, Jose L. Alonso, The Gas-Phase Structure of Alanine. *J. Am. Chem. Soc.* **2004,** *126* (37).
14. Blanco, S.; Macario, A.; Lopez, J. C., The structure of isolated thalidomide as reference for its chirality-dependent biological activity: a laser-ablation rotational study. *Phys Chem Chem Phys* **2021,** *23* (24), 13705-13713.
15. Lesarri, A.; Mata, S.; López, J. C.; Alonso, J. L., A laser-ablation molecular-beam Fourier-transform microwave spectrometer: The rotational spectrum of organic solids. *Review of Scientific Instruments* **2003,** *74* (11), 4799-4804.